

Exploring Potential Energy Surfaces in Ground- and Excited States

Dissertation

zur Erlangung des akademischen Grades

doctor rerum naturalium (Dr. rer. nat.)

vorgelegt dem Rat der Chemisch-Geowissenschaftlichen Fakultät

der Friedrich-Schiller-Universität Jena

von

Diplomchemiker Johannes Steinmetzer

geboren am 11.08.1989

in Halle (Saale)

Gutachter:

1. Prof. Dr. Stefanie Gräfe, Friedrich-Schiller-Universität Jena, DE
2. Prof. Dr. Marek Sierka, Friedrich-Schiller-Universität Jena, DE
3. Prof. Dr. Robert Berger, Philipps-Universität Marburg, DE

Tag der Verteidigung: 22.12.2021

“A computer is an educational device, it’s in fact a direct reflection of your own imagination, your own intelligence, your own programming skills and once you’re given the freedom, in which to create things and to see the immediate response on the screen, then it becomes a very enjoyable experience and you go on to involve yourself in many other things.”

Computer store manager[1]

Peer-Reviewed Publications

Included in this Thesis

- Haensch, V. G.; Neuwirth, T.; **Steinmetzer, J.**; Kloss, F.; Beckert, R.; Gräfe, S.; Kupfer, S.; Hertweck, C. Metal-Free Aryl Cross-Coupling Directed by Traceless Linkers. *Chemistry – A European Journal* **2019**, *25*, 16068–16073, DOI: 10.1002/chem.201903582
- **Steinmetzer, J.**; Kupfer, S.; Gräfe, S. pysicsyphus: Exploring potential energy surfaces in ground and excited states. *International Journal of Quantum Chemistry* **2020**, *121*, DOI: 10.1002/qua.26390

Not Included in this Thesis

- G., U. R.; Liu, J.; Hoffmann, P.; **Steinmetzer, J.**; Görls, H.; Kupfer, S.; Askes, S. H. C.; Neugebauer, U.; Gräfe, S.; Schiller, A. Light-responsive paper strips as CO-releasing material with a colourimetric response. *Chemical Science* **2017**, *8*, 6555–6560, DOI: 10.1039/c7sc01692a
- Liu, J.; Hoffmann, P.; **Steinmetzer, J.**; Askes, S. H.; Kupfer, S.; Görls, H.; Gräfe, S.; Neugebauer, U.; Gandra, U. R.; Schiller, A. Visible light-activated biocompatible photo-CORM for CO-release with colorimetric and fluorometric dual turn-on response. *Polyhedron* **2019**, *172*, 175–181, DOI: 10.1016/j.poly.2019.04.031
- Amini, K.; Scalfani, M.; Steinle, T.; Le, A.-T.; Sanchez, A.; Müller, C.; **Steinmetzer, J.**; Yue, L.; Saavedra, J. R. M.; Hemmer, M.; Lewenstein, M.; Moshhammer, R.; Pfeifer, T.; Pullen, M. G.; Ullrich, J.; Wolter, B.; Moszynski, R.; de Abajo, F. J. G.; Lin, C. D.; Gräfe, S.; Biegert, J. Imaging the Renner-Teller effect using laser-induced electron diffraction. *Proceedings of the National Academy of Sciences* **2019**, *116*, 8173–8177, DOI: 10.1073/pnas.1817465116

- Liu, X.; Amini, K.; Steinle, T.; Sanchez, A.; Shaikh, M.; Belsa, B.; **Steinmetzer, J.**; Le, A.-T.; Moshhammer, R.; Pfeifer, T.; Ullrich, J.; Moszynski, R.; Lin, C. D.; Gräfe, S.; Biegert, J. Imaging an isolated water molecule using a single electron wave packet. *The Journal of Chemical Physics* **2019**, *151*, 024306, DOI: 10.1063/1.5100520
- Shillito, G. E.; Preston, D.; Traber, P.; **Steinmetzer, J.**; McAdam, C. J.; Crowley, J. D.; Wagner, P.; Kupfer, S.; Gordon, K. C. Excited-State Switching Frustrates the Tuning of Properties in Triphenylamine-Donor-Ligand Rhenium(I) and Platinum(II) Complexes. *Inorganic Chemistry* **2020**, *59*, 6736–6746, DOI: 10.1021/acs.inorgchem.9b03691
- Belsa, B.; Amini, K.; Liu, X.; Sanchez, A.; Steinle, T.; **Steinmetzer, J.**; Le, A. T.; Moshhammer, R.; Pfeifer, T.; Ullrich, J.; Moszynski, R.; Lin, C. D.; Gräfe, S.; Biegert, J. Laser-induced electron diffraction of the ultrafast umbrella motion in ammonia. *Structural Dynamics* **2021**, *8*, 014301, DOI: 10.1063/4.0000046

The publications listed above correspond to references [2] – [9] in the bibliography.

Contents

I	Introduction	1
1	Introduction	3
1.1	Exploring Potential Energy Surfaces	4
1.2	Photochemistry	7
1.3	Goals and Outline of this Thesis	10
II	Theoretical Background and Methods	13
2	Schrödinger Equation	15
3	Solving the Electronic Schrödinger Equation	16
3.1	Hartree-Fock	17
3.2	Density Functional Theory	19
3.3	Time-Dependent Density Functional Theory	21
3.4	Density Functional Tight-Binding	22
4	Excited State Tracking in Optimizations	25
4.1	Wavefunction Overlaps	26
4.2	Transition Density Overlaps	27
4.3	Natural Transition Orbital Overlaps	28
4.4	Choosing a Reference Cycle	29
5	Obtaining Minima on Potential Energy Surfaces	31
5.1	The Quadratic Approximation	31
5.2	Hessian Update and Initial Choice	32
5.3	Conjugate Gradient and Limited-Memory BFGS	34
5.4	Trust Radius	35
5.5	Line searches	36
5.6	Direct Inversion in the Iterative Subspace	39

6	Internal Coordinates	41
6.1	Definition of Redundant Internal Coordinates	41
6.2	Wilson’s B-Matrix	43
6.3	Internal-Cartesian Back-Transformation	45
6.4	Delocalized Internal Coordinates	46
7	Preconditioning	49
8	Chain-of-States Methods	55
8.1	Nudged Elastic Band	56
8.2	Interpolating Initial Paths	56
8.3	Growing String Method	58
8.4	NEB and String Variants	58
8.5	Optimizing Chain-Of-States	60
8.6	Climbing Image	60
8.7	Highest Energy Image	60
9	Obtaining Transition States on Potential Energy Surfaces	61
10	Dimer Method	63
11	Intrinsic Reaction Coordinate	65
11.1	Gonzalez-Schlegel 2nd-Order Algorithm	66
11.2	Predictor-Corrector Integration	67
III	Results	71
12	Biaryl Cross-Coupling	73
12.1	Introduction	73
12.2	Computational Details	73
12.3	Preferred Ground State Conformation	76
12.4	Ground State Reaction Coordinate and Electronic Structure	82
12.5	Excited State Reaction Mechanism	84
12.6	Summary	86
13	Pysisyphus	89
13.1	Introduction	89

13.2	Benchmarks and Verification	89
13.2.1	Baker Test Set	92
13.2.2	Hobzas S22 Test Set - Noncovalent Interactions	96
13.2.3	External Validation	99
13.2.4	Baker Transition State Test Set	99
13.2.5	Chain-Of-States Test Set	107
13.3	Excited State Optimization	113
13.3.1	Cytosin	114
13.3.2	Ruthenium Nitrosyl Complex	115
13.3.3	Platinum Complexes	117
13.4	Ground State Calculations - Biaryl Cross-Coupling	120
13.5	Implementation	124
13.6	Summary	128
14	Summary	129
15	Zusammenfassung	133
A	Appendix	135
A.1	Numerical integration of the Local Quadratic Approximation	135
A.2	Biaryl Cross-Coupling Results for 1b	137
A.3	S22 Geometries with High root mean square deviations (RMSDs)	138
A.4	Code Listings	139
B	Acknowledgements	145
C	Selbständigkeitserklärung	147
	Bibliography	149

List of Acronyms

ACN acetonitrile	DIIS direct inversion in the iterative sub-space
ANEB adaptive NEB	DLPNO domain based local pair-natural orbital
AO atomic orbital	DM dimer method
ASE Atomic Simulation Environment	DNA desoxyribonucleic acid
BFGS Broyden-Fletcher-Goldfarb-Shanno	DLC delocalized internal coordinates
BDF backward differentiation formula	DWI distance-weighted interpolant
BOA Born-Oppenheimer ansatz	EulerPC Euler predictor-corrector
CAM coulomb attenuated method	ES excited state
CASSCF complete active space self consistent field	FENEB free-end NEB
CBS complete basis set	FEANEB free-end adaptive NEB
CCSD(T) singles and doubles coupled cluster with triples correction	FF force field
CDD charge density difference	GDIIS geometric direct inversion in the iterative subspace
CG conjugate gradient	GEDIIS energy represented direct inversion in the iterative subspace
CI climbing image	GGA generalized gradient approximation
CIS configuration interaction singles	GS ground state
COS chain-of-states	GS2 Gonzalez-Schlegel second-order algorithm
CPCM conductor-like polarizable continuum model	GSM growing string method
CT charge transfer	GTO Gaussian-type orbital
CTS connectivity transition state	HF Hartree-Fock
DFT density functional theory	HEI highest energy image
DFTB density functional tight-binding	

HPC Hessian predictor-corrector	MO molecular orbital
HOMO highest occupied molecular orbital	NA nucleic acid
IC internal conversion	NMC normal mode coordinates
IDPP image dependent pair potential	NTO natural transition orbital
ILCT intra-ligand-charge-transfer	PCA principal component analysis
IM image method	PEC potential energy curve
IRC intrinsic reaction coordinate	PES potential energy surface
KS Kohn-Sham	PRFO partitioned rational function optimization
LBFGS limited-memory BFGS	PSB Powell's symmetric Broyden
LCAO linear combination of atomic orbitals	QC quantum chemistry
LDA local density approximation	QN quasi-Newton
LEPS London-Eyring-Polanyi-Sato	RMSD root mean square deviation
LHS left-hand side	RNA ribonucleic acid
LMCT ligand-to-metal-charge-transfer	RFO rational function optimization
LR linear response	RHS right-hand side
LUMO lowest unoccupied molecular orbital	RIC redundant internal coordinates
LST linear synchronous transit	RI resolution of identity
MB-PES Müller-Brown-PES	RMS root mean square
MEP minimum energy path	RS restricted step
MLCT metal-to-ligand-charge-transfer	RS-IRFO restricted step image method RFO
MP2 Møller-Plesset perturbation theory	RS-RFO restricted step RFO
NEB nudged elastic band	RS-PRFO restricted step partitioned RFO
MH model Hessian	SCC self-consistent charge

Contents

SCF self-consistent field	TD-DFT time-dependent DFT
SD Slater determinant	TDSE time-dependent Schrödinger equation
SM string method	TDEN transition density matrix
SP stationary point	TRIM trust-region image method
SQM semi-empirical quantum chemistry method	TS transition state
SR1 symmetric rank 1	WFO wavefunction overlap
STO Slater-type orbital	XC exchange-correlation
SVD singular value decomposition	XTB extended tight-binding

Part I

Introduction

1 Introduction

Breakthroughs in chemistry have always shaped our world, to the better or the worse. From its prescientific, alchemical origins, chemistry continuously evolved into a modern science. By providing many key technologies, some of them outlined below, chemistry enables our present standard of living.

For most of the human existence, infections with particular bacteria meant certain death, even for the most powerful people of their times.¹ Today, many bacterial infections are routinely treated with a variety of sophisticated antibiotics, e.g., penicillins, discovered by Fleming, Florey and Chain.[13, 14]

Artificial nitrogen fixation through the Haber-Bosch-Process facilitated an unprecedented growth of the world population, by sustaining large-scale fertilizer production.[15]

A main product of the chemical industry are plastics. Ranging from unwanted microplastics in the food we consume,[16–20] to its packaging and many everyday items, plastics are omnipresent in modern society.[21–23]

Chemistry is also expected to play a crucial role in mitigating climate change, by providing new ways to generate and store energy, e.g., in the form of molecular hydrogen, generated via artificial photosynthesis.[24–31]

While early chemical discoveries were predominantly made in classical laboratories, where chemists meticulously carried out experiments by hand, modern chemistry is increasingly supported by computational methods. Nowadays, predictive quantum chemical and derived methods, like force fields[32–39], can be applied to more and more complex systems.[40–48]

The Haber-Bosch process is assumed to consume 1 % of the world's energy production and to account for 1.4 % of global CO₂ emissions.[49] Computational methods are now routinely applied to investigate and evaluate greener alternatives, e.g., by electrocatalysis.[50–53] Similarly, quantum chemical methods enable rational catalyst design for

¹Henry VIII, (1491 – 1547), King of England, presumably died of sepsis.[10, 11] Napoleon Bonaparte (1769 – 1821) and Ivan the Terrible (1530 – 1584) presumably died of syphilis.[12]

plastic manufacturing, e.g., polyurethane materials,[54] and ethylene polymerization.[55] Computational methods are now also commonly used to study degradation pathways of antibiotics,[56–58] or to design and evaluate entirely new drugs.[59–61]

In silico approaches are especially attractive to characterize short-lived species, such as transition states (TSs) or molecular systems in excited states (ESs). Besides the chosen level of theory, two complementary computational approaches can be distinguished: time-dependent and time-independent ones. Time-dependent approaches explicitly propagate the system under study in time, e.g., by integrating Newton’s law of motion (molecular dynamics) or the time-dependent Schrödinger equation (TDSE) (quantum dynamics).[62, 63] In the following, this thesis will outline the time-independent approach in more detail.

1.1 Exploring Potential Energy Surfaces

When not employing molecular or quantum dynamics, computational studies of chemical transformations are conducted by evaluating and comparing energies and molecular properties at stationary points (SPs) of the potential energy surface (PES), where the gradient of the potential $V(\mathbf{x})$ vanishes.

$$\frac{dV(\mathbf{x})}{d\mathbf{x}} = \mathbf{0} \quad (1.1)$$

SPs are distinguished by their index l , given by the number of significant negative eigenvalues of the potential’s Hessian,[64] the matrix of second partial derivatives. Minima on the PES with $l = 0$ represent possible educts, products or stable intermediates of chemical transformations and are connected through TSs with $l = 1$. Involvement of higher index SPs ($l > 1$) is also discussed by some authors.[65–68] The eigenvector belonging to the single negative eigenvalue present at a TS with $l = 1$ is called the transition vector. Going downhill from a TS along the transition vector in both directions yields a minimum energy path (MEP) and leads to the two SPs that are connected by this TS. A common choice for MEP calculation starting from a TS is the intrinsic reaction coordinate (IRC), the path of steepest descent in mass-weighted coordinates.[69] Or, put differently: the gradient component perpendicular to the MEP vanishes, only the parallel component along the MEP remains.

Parts of this chapter are based on:

Steinmetzer, J.; Kupfer, S.; Gräfe, S. pysisyphus: Exploring potential energy surfaces in ground and excited states. *International Journal of Quantum Chemistry* **2020**, *121*, DOI: 10.1002/qua.26390

Open Access publication, licensed under Creative Commons - Attribution 4.0 International (CC BY 4.0).

Instead of initial TS optimization by surface-walking[70] and subsequent MEP calculation, both can be obtained simultaneously by chain-of-states (COS) optimization. A COS can be regarded as approximation of the true MEP and comprises several geometries, called images. The most widespread used COS are the nudged elastic band (NEB) and the string method (SM).[71, 72] COSs methods are especially interesting when no suitable TS guess is available, as they are often started from an interpolated path between two minima on the PES, e.g. known educts and products of a chemical transformation.[73]

Both approaches, surface-walking and COS optimization, are outlined exemplarily for the two-dimensional Müller–Brown-PES (MB-PES) in Figures 1.1 to 1.2.[74] The MB-PES is obtained as linear combination of four Gaussian potentials.

$$V(x, y) = \sum_{i=1}^4 A_i \exp(a_i(x - x_{i,0})^2 + b_i(x - x_{i,0})(y - y_{i,0}) + c_i(z - z_{i,0})^2) \quad (1.2)$$

$$\mathbf{A} = (-200, -100, -170, 15), \quad \mathbf{x}_0 = (1, 0, -0.5, -1), \quad \mathbf{y}_0 = (0, 0.5, 1.5, 1)$$

$$\mathbf{a} = (-1, -1, -6.5, 0.7), \quad \mathbf{b} = (0, 0, 11, 0.6), \quad \mathbf{c} = (-10, -10, -6.5, 0.7)$$

It features three minima, two corresponding TSs of index $l = 1$ and was employed numerous times for benchmarking (reaction path) optimization algorithms.[75–82] Even though the potential is quite simple, it exhibits several characteristics, also found in real chemical systems, e.g., normal modes of highly varying stiffness and TSs with small basins of attraction.[76]

Figure 1.1 outlines the surface-walking approach. Starting from a guess geometry (I), the first SP (II, minimum) is obtained. Modification of II yields TS guess (III), which is subsequently refined to a true TS (IV) of index $l = 1$. IRC integration confirms that TS IV connects II to the formerly unknown SP V. The same process can be repeated, to discover the two remaining SPs (not numbered in Figure 1.1).

PES exploration by COS optimization is shown in Figure 1.2. There, knowledge of a second SP (IV) is required. An initial COS (grey line with dots) is constructed by linear interpolation between II and IV and gradually relaxed towards the true MEP. Later COS optimization cycles are given in a darker shade. In the end, the final COS in Figure 1.2 coincides with the IRC in Figure 1.1. A COS in Cartesian coordinates and an IRC carried out in mass-weighted Cartesians only coincide when all atoms have unit mass, which is usually not true for real molecular systems. While SP geometries are independent of the chosen coordinate system, intermediate geometries along an IRC are not.[83]

1 Introduction

The surface-walking approach is usually computationally less demanding and requires only knowledge of one SP, e.g., II or V in Figure 1.1, but manual construction of a suitable TS guess may be difficult. The COS approach requires knowledge of two SPs, connected by a presumed TS, but manual construction of a TS guess is usually avoided, as the highest energy image (HEI) of a COS can be employed instead. A clear disadvantage of the second approach is its high computational cost, as many energy and gradient evaluations are required for COS optimization.

Reviews on TS searches and COS methods are given by Schlegel, Dewyer and Ásgeirsson.[82, 84, 85]

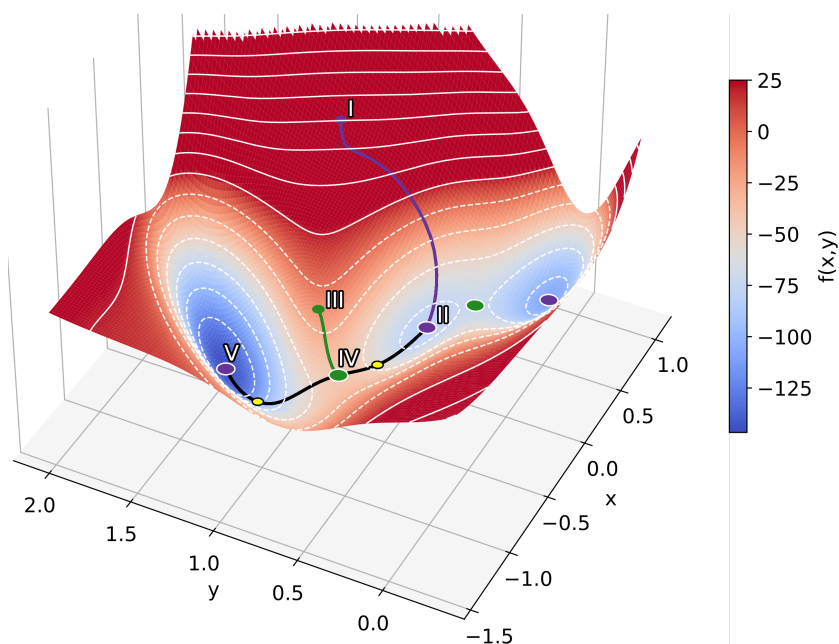


Figure 1.1: Surface-walking approach for exploring the MB-PES.[74] SPs are given as bigger circles (purple = minima, green = TSs; white outline), non-SPs as smaller circles. Initial (TS)-optimizations, starting from non-SPs, are given in the color of the targeted SP. Values $f(x, y) \geq 25$ are shown with the same red color. The order, in which the respective points are obtained, is indicated by roman numerals.

Starting at I, minimum II at $(-0.044, 0.465)$ is obtained by optimization. Based on II, a TS guess (III) is constructed, leading to TS IV at $(-0.822, 0.624)$. Finally, an IRC is integrated, yielding minimum V $(-0.558, 1.442)$. Unit mass was assumed for IRC integration. By passing the inflection points (yellow circles), the curvature of the the PES changes its sign.

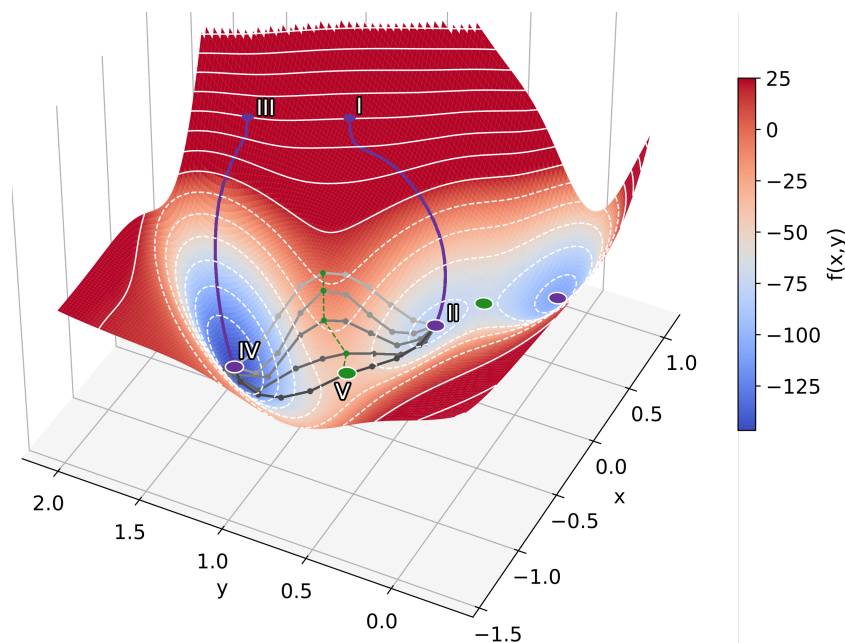


Figure 1.2: PES exploration by COS optimization. Please see the first paragraph of Figure 1.1 for a general comment on the plot and the employed color scheme.

Starting from I and III, minima II and IV are obtained. Subsequently, an initial, interpolated COS is gradually relaxed to the true MEP. Earlier cycles are shown in a lighter shade, COS images are shown as small dots. Evolution of the HEI (small green circle) towards the actual TS is shown by a dashed green line.

1.2 Photochemistry

Traversing the PES of the electronic ground state (GS) by means of surface-walking or COS optimization is usually not hampered by state crossings, as the remaining (excited) electronic states are energetically well separated. This changes in photochemical and photophysical studies, where the state of interest is an electronically ES and multiple electronic states are considered simultaneously.

Although ES-PESs are often explored using molecular or quantum dynamics,[86–89] localizing SPs in ESs is still important, e.g., for Marcus theory or to rationalize ES relaxation pathways for emission (fluorescence, phosphorescence).[8, 90–92]

Typical, competing processes to be taken into account when studying ES-PESs are summarized in Figure 1.3. There, two SPs, for instance, educts and products of a hypothetical reaction, are separated by a barrier in the GS. Depending on its height,

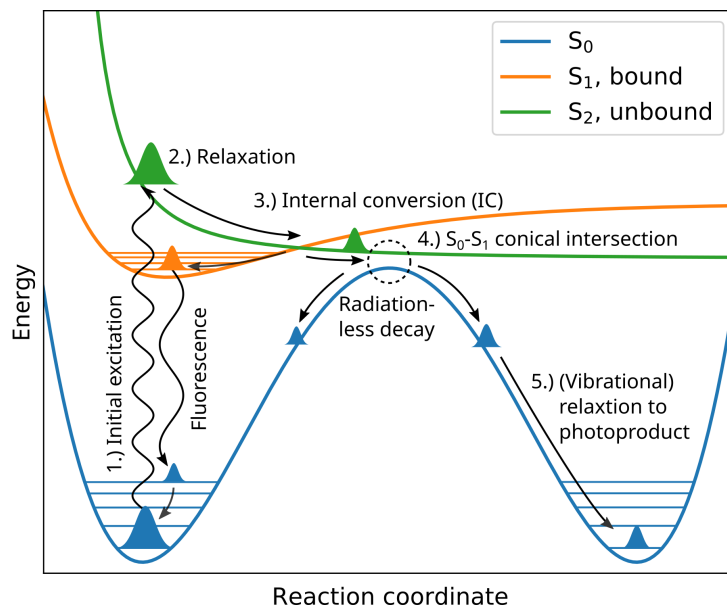


Figure 1.3: Schematic depiction of different photochemical processes that may take place after initial excitation from the vibrational GS at a SP. Same symmetry (spin and wavefunction) is assumed for all electronic states. Arrows indicate possible wavepackage evolution along the different electronic states.

the barrier may not be crossed in the GS, thus the reaction is prevented. By exciting a molecule into a higher lying electronic state, new pathways can become accessible, allowing crossing of otherwise insurmountable barriers.

Starting from the vibrational and electronic GS at an equilibrium geometry, a molecule is excited by light into a higher lying electronic state. According to their electronic structure, ESs may be bound (S_1 in Figure 1.3) or repulsive (S_2 in Figure 1.3). Following the excitation, the molecule begins to evolve on the ES-PES, as it is not at a SP anymore. If another ES comes energetically close, radiationless internal conversion (IC) to this ES may occur. IC takes place at conical intersections, which were found to be important regions in ES relaxation pathways.[93–99] Alternatively, relaxation to the GS can also proceed by photon emission (fluorescence). Compared to the irradiating light, the emitted light is redshifted, as some of the initial energy was already dissipated into the environment or other internal degrees of freedom. If ESs of different multiplicities have to be considered, e.g., because of strong spin-orbit coupling, additional process like intersystem crossing and phosphorescence may take place.[100–103]

A physiologically highly relevant and well studied reaction involving ESs, exhibiting several of the just discussed processes, is the photoisomerization of 11-*cis*-retinal to 11-*trans*-retinal.

11-*cis*-retinal acts as chromophore in the light-sensitive G protein-coupled receptor rhodopsin, which facilitates light perception in dim conditions. Together with photoreceptor proteins photopsins I–III that allow color perception, rhodopsin enables the vision process in vertebrates.

The retinals are conjugated polyenes, covalently bound in their protonated Schiff-base form to a rhodopsin lysine residue. Photoisomerization of 11-*cis*-retinal to 11-*trans*-retinal in rhodopsin occurs very fast in about 200 fs after initial excitation, with a high quantum yield of 0.67.[104, 105] The protein environment greatly facilitates the isomerization reaction, as the same photoisomerization takes place much slower (4 ps), with decreased quantum yield (0.22) in MeOH. It was proposed that the protein modulates the accessibility of different retinal GS conformers.[106]

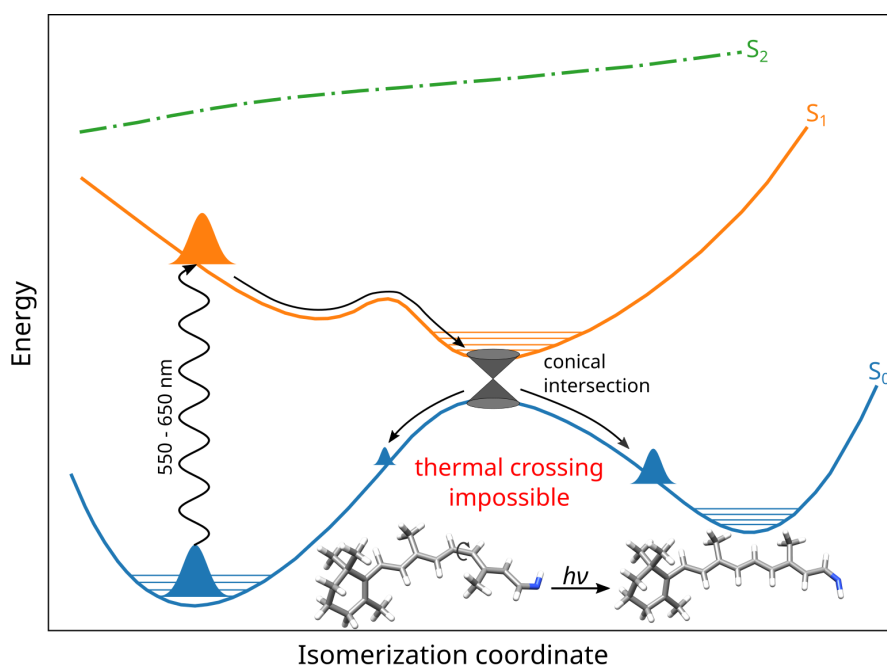


Figure 1.4: Schematic potential energy curves (PECs) for the photoisomerization of 11-*cis*-retinal to 11-*trans*-retinal in their protonated Schiff-base forms. PECs were adapted from fig 2a in [105], licensed under CC BY 4.0.

Rhodopsin exhibits an absorption maximum at $\lambda_{\max} = 498 \text{ nm}$. [107] Following irradiation between 550 nm to 650 nm, a wavepacket is excited from the GS to the S_1 , where it evolves towards a conical intersection (see Figure 1.4). [105, 108–110] Pump-probe

experiments revealed greatly extended ES lifetimes at low temperatures, indicating the presence of a small barrier in the ES.[105]

At the conical intersection, radiationless decay to the S_0 occurs, ultimately yielding 11-*trans*-retinal.[111] The retinal isomerization induces further conformational changes in the rhodopsin photopigment, which activate the G protein transducin. Transducin activates a phosphodiesterase, that degrades and thereby lowers the intracellular cyclic guanosine monophosphate concentration, blocking cation influx into the cell.[104] Finally, the photoreceptor cells are hyperpolarized, leading to neuron excitation and the vision process.[112]

Reviews on photochemistry and calculation of ESs are found in [113–120].

1.3 Goals and Outline of this Thesis

Computational photochemistry often requires effective ES-tracking, as multiple electronic states may be energetically close to a state of interest, e.g., in optimizations. When moving along the PES, root-flips may occur and state-tracking by energy ordering alone becomes unreliable.

Currently, ES-tracking is not universally available in popular quantum chemistry (QC)-packages, or if present, poorly documented and only usable in a black box fashion. ORCA only recently gained ES-tracking capabilities in version 4.1.0.[121] In Turbomole, ES-tracking is available, but undocumented.[122, 123] State-tracking is enabled by default in the Gaussian program suite, but only usable in a black-box fashion, for instance, the reference step in an optimization is restricted to the previous cycle.

All QC packages just mentioned are closed-source program and their source code is not freely available, making changes to them impossible. An attractive route to add the required functionality, is to create wrappers for these packages that expose a common interface and then implement ES-tracking for the common interface. The feasibility of the wrapper approach was already demonstrated impressively by the Atomic Simulation Environment (ASE) project, although ASE is more tailored to solid-state applications and lacks support for internal coordinates, which are required for efficient optimizations.[124]

One goal of this thesis is to implement an external, state of the art optimizer that is aware of ESs and supports efficient and effective ES tracking, for further photochemical applications, e.g., optimization of transition metal complex relaxation pathways. Secondly, this thesis provides computational insights for an elegant biaryl coupling reaction discovered by Kloss et al.[2, 125]

The remainder of this thesis is split in two parts. Part II briefly introduces several approaches to solve the Schrödinger equation and presents the theoretical foundations of ES-tracking, surface-walking, COS methods and internal coordinates.

Results of this thesis are found in Part III. The biaryl coupling reaction is discussed in chapter 12. Implementation of the external optimizer *pysisyphus* and its application in the context of ES optimizations and the biaryl coupling reaction is discussed in chapter 13. Finally, the thesis is summarized in chapter 14.

Part II

Theoretical Background and Methods

2 Schrödinger Equation

Optimizing stationary points on a PES requires, at least, the ability to calculate the energy of a given atomic configuration (system). To this end, many methods have been proposed, most of them are based on solving the TDSE

$$i\hbar \frac{\partial}{\partial t} |\Psi(t, \mathbf{r}, \mathbf{R})\rangle = \hat{\mathcal{H}} |\Theta(\mathbf{r}, \mathbf{R})\rangle . \quad (2.1)$$

The system under study is characterized by its Hamiltonian $\hat{\mathcal{H}}$ and a corresponding wave function $\Psi(t, \mathbf{r}, \mathbf{R})$, depending on time t , electronic coordinates \mathbf{r} and nuclear coordinates \mathbf{R} . For stationary $\hat{\mathcal{H}}$, a time-independent form of eq. (2.1) is derived as

$$\hat{\mathcal{H}} |\Theta(\mathbf{r}, \mathbf{R})\rangle = \mathcal{E}_{\text{tot}} |\Theta(\mathbf{r}, \mathbf{R})\rangle \quad (2.2)$$

with E_{tot} denoting the systems total energy. The Hamiltonian $\hat{\mathcal{H}}$ comprises all interactions between the constituents of the system. For a system of N electrons (subscript e) and M nuclei (subscript nuc) it is

$$\hat{\mathcal{H}} = \hat{\mathcal{T}}_e + \hat{\mathcal{T}}_{\text{nuc}} + \underbrace{\hat{V}_{\text{nuc,nuc}} + \hat{V}_{\text{nuc,e}} + \hat{V}_{e,e}}_{\hat{V}} \quad (2.3)$$

with the kinetic energy operator $\hat{\mathcal{T}}_e$ ($\hat{\mathcal{T}}_{\text{nuc}}$) of the electrons (nuclei). Coulombic interactions are taken into account by the potential energy operator \hat{V} . In atomic units, $\hat{\mathcal{H}}$ is given by

$$\hat{\mathcal{H}} = -\underbrace{\frac{1}{2} \sum_n^N \nabla_n^2}_{\hat{\mathcal{T}}_e} - \underbrace{\frac{1}{2} \sum_m^M \frac{1}{M_m} \nabla_m^2}_{\hat{\mathcal{T}}_{\text{nuc}}} + \underbrace{\sum_{m>m'}^M \frac{q_m q_{m'}}{R_{m,m'}}}_{\hat{V}_{\text{nuc,nuc}}} - \underbrace{\sum_{m,n}^{M,N} \frac{q_m}{r_{m,n}}}_{\hat{V}_{\text{nuc,e}}} + \underbrace{\sum_{n>n'}^N \frac{1}{r_{n,n'}}}_{\hat{V}_{e,e}} . \quad (2.4)$$

A commonly employed approximation for $|\Psi(\mathbf{r}, \mathbf{R})\rangle$ is the Born-Oppenheimer ansatz (BOA), where the electronic wave function $|\Psi_e(\mathbf{r}, \overline{\mathbf{R}})\rangle$ only depends parametrically on the nuclear coordinates \mathbf{R} .^[126]

$$|\Psi(\mathbf{r}, \mathbf{R})\rangle \approx |\Psi_e(\mathbf{r}, \overline{\mathbf{R}})\rangle |\Psi_{\text{nuc}}(\mathbf{R})\rangle \quad (2.5)$$

This approximation is justified, as the light electrons can adapt nearly instantaneously to positional changes of much heavier nuclei. The electronic wave function $\Psi_e(\mathbf{r}, \overline{\mathbf{R}})$ is obtained by solving the electronic Schrödinger equation

$$\hat{H}_e \Psi_e(\mathbf{r}, \overline{\mathbf{R}}) = E |\Psi_e(\mathbf{r}, \overline{\mathbf{R}})\rangle \quad (2.6)$$

with

$$\hat{H}_e = \hat{T}_e + \hat{V} \quad (2.7)$$

where E denotes the electronic energy of the system. In the following, application of the BOA is assumed throughout and nuclear coordinates will be denoted without the overline, just as \mathbf{R} .

3 Solving the Electronic Schrödinger Equation

Eq. (2.6) can be solved analytically only for small systems, like H_2^+ . Treating larger systems requires additional approximations. Given an approximate wave function Ψ_e , a lower bound for its energy E is provided by the Rayleigh-Ritz method (variational principle),^[127] as the expectation value of $\hat{\mathcal{H}}$

$$E = \frac{\langle \Psi_e | \hat{\mathcal{H}} | \Psi_e \rangle}{\langle \Psi_e | \Psi_e \rangle}. \quad (3.1)$$

Based on eq. (3.1), wave function Ψ_e can be varied, until a minimum energy E is obtained. As the wave function Ψ_e describes fermionic particles, it must fulfill the Pauli exclusion principle, which requires the wave function to change sign, under the exchange of two fermions.^[128] Assuming the expansion of Ψ_e into a set of N orthogonal spin orbitals

$\{\phi_i\}$, the Pauli exclusion principle is satisfied, by employing a Slater determinant (SD) as wave function.

$$\Psi_e(1, 2, \dots, N) = \frac{1}{\sqrt{N!}} \begin{vmatrix} \phi_1(\mathbf{x}_1) & \phi_2(\mathbf{x}_1) & \cdots & \phi_N(\mathbf{x}_1) \\ \phi_1(\mathbf{x}_2) & \phi_2(\mathbf{x}_2) & \cdots & \phi_N(\mathbf{x}_2) \\ \vdots & \vdots & \ddots & \vdots \\ \phi_1(\mathbf{x}_N) & \phi_2(\mathbf{x}_N) & \cdots & \phi_N(\mathbf{x}_N) \end{vmatrix} \quad (3.2)$$

Here, $\phi_a(\mathbf{x}_i)$ denotes electron i in spin orbital a . Spin orbitals are composed of a spatial orbital ψ_a and a spin part, depending on spin coordinate ω_i .

$$\phi_a(\mathbf{x}_i) = |\psi_a(\mathbf{r}_i)\rangle \cdot \begin{cases} |\alpha(\omega_i)\rangle \\ |\beta(\omega_i)\rangle \end{cases} \quad (3.3)$$

3.1 Hartree-Fock

The computational bottleneck of solving eq. (2.6) is the accurate treatment of the electron-electron interaction ($\hat{V}_{e,e}$, see eq. 2.4). A basic approximation to $\hat{V}_{e,e}$ is introduced in the Hartree-Fock (HF) method, by considering merely the interaction of electrons with the average field of the remaining electrons.[129] Minimizing the energy of a SD, while requiring the spin orbitals to stay orthonormal, yields the HF equations.

$$\hat{f}(\mathbf{x}_i)\phi_a(\mathbf{x}_i) = \varepsilon_a\phi_a(\mathbf{x}_i) \quad i = 1, 2 \dots N \quad (3.4)$$

The Fock operator $\hat{f}(\mathbf{x}_i)$ comprises a one-electron part $\hat{h}(\mathbf{x}_i)$, describing electron-nuclear attraction and electronic kinetic energy and a two-electron part $\hat{v}^{\text{HF}}(\mathbf{x}_i)$, describing Coulomb interactions between electrons.

$$\hat{f}(\mathbf{x}_i) = \hat{h}(\mathbf{x}_i) + \hat{v}^{\text{HF}}(\mathbf{x}_i) \quad (3.5)$$

Whereas orbital-free, fully numerical solution of the HF equations (3.4) is restricted to small systems up to tri-atomics, [130–133] larger systems can be treated by expanding spatial orbitals ψ_a into atomic orbitals φ_μ (linear combination of atomic orbitals (LCAO)).

$$\psi_a = \sum_{\mu=1}^{\eta} d_{\mu a} \varphi_\mu \quad a = 1, 2 \dots \eta \quad (3.6)$$

3 Solving the Electronic Schrödinger Equation

Parameter η denotes the number of basis functions used in the contraction of spatial orbital ψ_a and d_μ denote contraction coefficients. Historically, Slater-type orbitals (STOs)

$$\varphi_{\text{STO}}(r) \propto e^{-\alpha r} \quad (3.7)$$

have been employed as basis functions, as they are analytical solutions to the hydrogen atom Schrödinger equation. Their use in quantum chemical calculations was superseded by Gaussian-type orbitals (GTOs)

$$\varphi_{\text{GTO}}(r) \propto e^{-\alpha r^2}, \quad (3.8)$$

as Boys recognized that molecular integrals can be calculated much more efficiently using GTOs.[134–138] Compared to GTOs, evaluation of molecular integrals over STOs requires more elaborate algorithms, even for simple integrals like basis function overlaps.[139–144]

In contrast to STOs, GTOs show incorrect asymptotic behavior for big r and their derivative vanishes at the nucleus ($r = 0$), hence multiple GTOs are summed to approximate a STO.[145] Many different GTO basis sets have been proposed until now.[146–148] Basis set choice depends on the chemical nature of the system at hand, as well as on the employed quantum chemical method.[149, 150]

Expanding spatial orbitals into atomic orbitals allows transforming the differential HF equations (3.4) into a set of algebraic equations

$$\hat{f}(\mathbf{r}_i) \sum_{\mu} C_{\mu a} \varphi_{\mu}(\mathbf{r}_i) = \varepsilon_a \sum_{\mu} C_{\mu a} \varphi_{\mu}(\mathbf{r}_i), \quad (3.9)$$

also known as the Roothaan-Hall equations

$$\mathbf{FC} = \mathbf{SC}\varepsilon \quad (3.10)$$

with Fock matrix \mathbf{F} , molecular orbital (MO) coefficients \mathbf{C} , overlap matrix \mathbf{S} and MO energies ε . [151, 152] The Roothaan-Hall equations (3.10) are solved iteratively, until self-consistency of \mathbf{C} is achieved.

If a sufficiently sized basis set is employed, HF is able to account for 99% of the total energy. The difference between the exact, non-relativistic total energy E_{exact} and the HF energy E_{HF} is known as the correlation energy

$$E_{\text{cor}} = E_{\text{exact}} - E_{\text{HF}}. \quad (3.11)$$

Two types of electron correlation are distinguished: static correlation, arising from different, energetically (nearly) degenerate electronic configurations and dynamic correlation, arising from the correlated motion of electrons, as they repel each other.

3.2 Density Functional Theory

Except for the exchange interaction, electron correlation is mostly neglected in HF. A computationally efficient way to partially incorporate dynamical correlation at similar computational cost, is density functional theory (DFT). Whereas a N electron wave function depends on $3N$ spatial and N spin coordinates, the electronic density

$$n(\mathbf{r}) = N \int d\mathbf{r}_2 \dots \int d\mathbf{r}_N \Psi^*(\mathbf{r}, \mathbf{r}_2, \dots, \mathbf{r}_N) \Psi(\mathbf{r}, \mathbf{r}_2, \dots, \mathbf{r}_N) \quad (3.12)$$

depends on only 3 spatial coordinates, independent of N . Hohenberg and Kohn showed that a GS wave function $\Psi_0(\mathbf{r}_1, \mathbf{r}_2, \dots, \mathbf{r}_N)$ is an exact functional of the GS electronic density $n_0(\mathbf{r})$ and that the GS density can be determined from the GS energy functional $E[n_0(\mathbf{r})]$ by the variational principle.[153, 154]

Originally, DFT was formulated orbital-free, thus making it computationally very efficient, as the dimensionality of the electronic density is only 3, but the accurate construction of the electronic kinetic energy functional proved difficult.[155–160] Nowadays, DFT is mostly used in the framework of Kohn and Sham (KS), where orbitals are reintroduced and used to expand the electronic density.[161, 162]

$$n(\mathbf{r}) = \sum_a |\psi_a(\mathbf{r})|^2 \quad (3.13)$$

KS-DFT simplifies the calculation of the electronic kinetic energy

$$T_0[n(\mathbf{r})] = -\frac{1}{2} \sum_a \int d\mathbf{r} \psi_a(\mathbf{r})^* \nabla^2 \psi_a(\mathbf{r}) \quad (3.14)$$

but also increases the computational costs, as the original dimensionality of the problem is restored. The energy functional comprises several terms

$$E[n(\mathbf{r})] = T_0[n(\mathbf{r})] + J[n(\mathbf{r})] + E_{\text{XC}}[n(\mathbf{r})] + V_{\text{ext}}[n(\mathbf{r})] \quad (3.15)$$

with the electron-electron Coulomb potential J , the exchange-correlation (XC) functional E_{XC} and an arbitrary external potential V_{ext} , e.g., the Coulomb potential of the electrons

3 Solving the Electronic Schrödinger Equation

in the field of nuclear charges. The only unknown term in eq. (3.15) is E_{XC} and its choice is crucial for the accuracy of DFT calculations.[163]

The simplest XC functional is given by the local density approximation (LDA), derived from an homogeneous electron gas. It only depends on the electronic density $n(\mathbf{r})$. [164] A first improvement over LDA is given by the generalized gradient approximation (GGA) that also considers the electronic density gradient $\nabla n(\mathbf{r})$. [165] By incorporating exact HF exchange, (global) hybrid functionals are obtained. A popular hybrid functional is B3LYP, [166] consisting of the exchange-functional B88 of Becke and the correlation-functional of Lee, Yang and Parr. [163, 167]

$$E_{\text{xc}}^{\text{B3LYP}} = E_{\text{xc}}^{\text{LDA}} + a_0 (E_{\text{x}}^{\text{HF}} - E_{\text{x}}^{\text{LDA}}) + a_x \Delta E_{\text{x}}^{\text{B88}} + a_c (E_{\text{c}}^{\text{LYP}} - E_{\text{c}}^{\text{VWN-LDA}}) \quad (3.16)$$

Parameters $a_0 = 0.2$, $a_x = 0.72$ and $a_c = 0.81$ were fitted, to reproduce atomization energies and ionization potentials from the G2 data set. [168]

More recent developments include meta-(hybrid)-GGAs, relying also on the second derivative of the electronic density $\nabla^2 n(\mathbf{r})$ and double hybrid functionals, which include a perturbative second-order correlation part. [169–172]

Common XC functionals, like B3LYP, have several shortcomings, especially in the treatment of ESs in time-dependent DFT (TD-DFT) calculations (see section 3.3). Plain GGA and hybrid XC functionals often greatly underestimate excitation energies of charge transfer (CT) states and completely fail in the description of double excitations, based on the single reference nature of DFT. [171, 173–177]

Parts of these deficiencies can be traced to a wrong behavior in the long-range part of the interelectronic exchange potential. In B3LYP, it decays only as $-0.2r_{12}^{-1}$, instead of the correct $-r_{12}^{-1}$ and the amount of exact HF exchange is independent of r_{12} . [178, 179] By making the amount of exact exchange depend on the interelectronic distance r_{12} , greatly improved results for CT states are obtained. To this end, Yanai et al. proposed the coulomb attenuated method (CAM), where r_{12}^{-1} is split into

$$\frac{1}{r_{12}} = \underbrace{\frac{1 - [\alpha + \beta \operatorname{erf}(\mu r_{12})]}{r_{12}}}_{\text{short range}} + \underbrace{\frac{\alpha + \beta \operatorname{erf}(\mu r_{12})}{r_{12}}}_{\text{long range}}. \quad (3.17)$$

Optimal values were determined as $\alpha = 0.19$, $\beta = 0.46$ and $\mu = 0.33$. [179] Eq. (3.17) is used to interpolate the exact exchange ratio between 19 % for short and 65 % for long

interelectronic distances. In the CAM framework B3LYP uses $\alpha = 0.2$ and $\beta = 0.0$. XC functionals incorporating eq. (3.17) are called range-separated hybrids.[180–183]

Alternatively, local hybrid XC functionals, where the amount of exact exchange is real-space position dependent, also show promising performance for CT states.[184–186]

3.3 Time-Dependent Density Functional Theory

Excited states, arising from a time-dependent external potential, e.g., an oscillating electric field with frequency ω , field strength F and dipole operator $\boldsymbol{\mu}$

$$\mathbf{V}_{\text{ext}}(t) = \boldsymbol{\mu}F \cos(\omega t) \quad (3.18)$$

can't be treated by classic Hohenberg-Kohn-Sham DFT, as the Hohenberg-Kohn theorems are restricted to electronic densities, describing time-independent GSs. Runge and Gross extended the time-independent DFT formalism and proved a unique one-to-one correspondence between a time-dependent external potential and the electronic density $n(\mathbf{r}, t)$. [187–189]

The time-dependent electronic density is calculated similar to the Kohn-Sham (KS) ansatz in eq. (3.13) as

$$n(\mathbf{r}, t) = \sum_a |\psi_a(\mathbf{r}, t)|^2, \quad (3.19)$$

in which the orbitals $\psi_a(\mathbf{r}, t)$ are obtained from the time-dependent KS-equations

$$i \frac{\partial}{\partial t} \psi_a(\mathbf{r}, t) = \left[-\frac{1}{2} \nabla^2 + V_s(\mathbf{r}, t) \right] \psi_a(\mathbf{r}, t) \quad (3.20)$$

with the time-dependent KS potential $V_s(\mathbf{r}, t)$.

While there exist real-space formulations of TD-DFT,[190–193] that explicitly propagate the electronic density in time, TD-DFT calculations are mostly conducted in the linear response (LR) formulation.[194, 195] Assuming a small time-dependent perturbation, the electronic density is given as

$$n(\mathbf{r}, t) = n_0(\mathbf{r}) + n_1(\mathbf{r}, t), \quad (3.21)$$

where $n_1(\mathbf{r}, t)$ is the linear response. Its Fourier transformation is given as

$$n_1(\mathbf{r}, \omega) = \int d\mathbf{r}' \chi(\mathbf{r}, \mathbf{r}', \omega) v_1(\mathbf{r}, \omega) \quad (3.22)$$

3 Solving the Electronic Schrödinger Equation

with the density-density response function $\chi(\mathbf{r}, \mathbf{r}', \omega)$, whose poles correspond to the excitation energies of the system under study.[196, 197]

Practically, excitation energies ω and ES wave functions, expressed as linear combination of singly excited SDs, are obtained by solving the Casida equations [194, 195]

$$\begin{bmatrix} \mathbf{A} & \mathbf{B} \\ \mathbf{A}^* & \mathbf{B}^* \end{bmatrix} \begin{pmatrix} \mathbf{X} \\ \mathbf{Y} \end{pmatrix} = \omega \begin{bmatrix} \mathbf{1} & \mathbf{0} \\ \mathbf{0} & -\mathbf{1} \end{bmatrix} \begin{pmatrix} \mathbf{X} \\ \mathbf{Y} \end{pmatrix}. \quad (3.23)$$

Explicit expressions for the matrices \mathbf{A} and \mathbf{B} are found in the literature.[195, 198] The eigenvectors $\begin{pmatrix} \mathbf{X} \\ \mathbf{Y} \end{pmatrix}$ correspond to the transition density matrices (see section 4.2).

3.4 Density Functional Tight-Binding

Naive HF and DFT both scale as N^4 , with N denoting the number of basis functions.[189] This unfavorable scaling makes them unsuitable for quick, explorative calculations and for treating large systems, with thousands of atoms. On the other hand, force fields (FFs) enable molecular dynamic simulations of many nanoseconds for several hundred thousands of atoms.[199–201] Drawbacks are their complicated setup and the absence of a wave function, for further analysis or the calculation of ESs. The realm between high scaling ab initio methods and FFs is given by semi-empirical quantum chemistry methods (SQMs). They allow treating large systems, while still providing a wave function.[202, 203] A SQM closely related to DFT is density functional tight-binding (DFTB).[204–206]

Starting from the DFT energy functional in eq. (3.15) and assuming $n(\mathbf{r})$ is the sum of an unperturbed reference density n_0 and a small fluctuation Δn , the XC energy functional can be expanded in a Taylor series around n_0 . [207]

$$\begin{aligned} E_{\text{XC}}[n_0 + \Delta n] &= E_{\text{XC}}[n_0] + \int \left[\frac{\delta E_{\text{XC}}[n]}{\delta n} \right]_{n_0} \Delta n + \frac{1}{2} \int' \int \left[\frac{\delta^2 E_{\text{XC}}[n]}{\delta n^2} \right]_{n_0, n'_0} \Delta n \Delta n' \\ &+ \frac{1}{6} \int'' \int' \int \left[\frac{\delta^3 E_{\text{XC}}[n]}{\delta n^3} \right]_{n_0, n'_0, n''_0} \Delta n \Delta n' \Delta n'' + \dots \end{aligned} \quad (3.24)$$

For simplicity, the dependence of n on \mathbf{r} has been dropped in eq. (3.24) and integration occurs over \mathbf{r} , \mathbf{r}' and \mathbf{r}'' . Based on the expansion order in eq. (3.24) different DFTB approaches are distinguished, ranging from DFTB1 to DFTB3, with the latter being the most accurate one.[205]

The general energy expression for self-consistent charge (SCC) DFTB comprises three terms[207]

$$E_{\text{SCC-DFTB}} = \underbrace{\sum_{iab} n_i \sum_{\mu \in a} \sum_{\nu \in b} c_{\mu i} c_{\nu i} H_{\mu\nu}^0}_{E^{H0}} + \underbrace{\frac{1}{2} \sum_{ab} \Delta q_a \Delta q_b \gamma_{ab}}_{E^\gamma} + \underbrace{\frac{1}{2} \sum_{ab} V_{ab}^{\text{rep}}}_{E^{\text{rep}}} \quad (3.25)$$

where i runs over all KS orbitals, a and b over all atoms and the greek indices μ and ν over basis functions at the respective atom.

E^{H0} contains energy contributions from an atomic orbital Hamiltonian and depends entirely on precomputed reference densities,[208] making the approach, in combination with a minimal valence basis, computationally extremely efficient. Diagonalization of H^0 is the dominant step in DFTB calculations. Pair-wise repulsive terms are gathered in E^{rep} . Considering only E^{H0} and E^{rep} leads to the non-self consistent DFTB1 method.[205] Including E^γ yields the self-consistent methods (DFTB2, DFTB3). [207, 209] Δq_i is the net charge of atom i

$$\Delta q_i = q_i - q_i^0 \quad (3.26)$$

and γ_{ab} describes the electron-electron interaction. It is given as integral over two normalized Slater-type spherical charge densities.[207] To obtain meaningful geometries, a dispersion correction is often added to eq. (3.25), which also proved crucial for reliable DFT geometries.[210–213]

A major drawback of the DFTB approach is its element-pair-wise parametrization, resulting in a very tedious fitting process.[214, 215] The recently proposed extended tight-binding (XTB) methods by Grimme alleviate the parametrization problem, as they avoid pair-wise parameters and are parametrized up to radon ($Z = 86$).[212, 216, 217]

4 Excited State Tracking in Optimizations

In contrast to GS optimizations, where the state of interest is usually energetically well separated from other electronic states and crossings are unlikely, the picture is different for ES optimizations. Given an initial ES geometry there may be a plethora of energetically close states that may cross with the state of interest over the course of an optimization. To overcome this problem, robust algorithms for ES tracking are of vital importance. Until now, many different techniques for state-tracking have been proposed, i.e., comparison of attachment- and detachment densities,[218] quantified natural transition orbital (NTO) analysis,[219, 220] overlaps between transition density matrices in the MO basis[221, 222] and the NTO basis[223, 224], overlaps between wavefunctions comprised of arbitrarily excited SDs[225] and overlaps between wavefunctions constructed from singly excited SDs.[226] As the latter two methods calculate overlaps between SDs, they are computationally much more expensive than the former methods. Exclusively, actual overlaps between wavefunctions – comprised of arbitrarily excited SDs – can capture crossings between ground- and excited electronic states, as the other methods rely on quantities that are only defined for ESs, like transition density matrices and NTOs derived from the former.[227]

ES tracking in optimizations is realized by calculating excited state overlaps between a given molecular geometry and a reference geometry with the overlaps being stored in an overlap matrix \mathbf{S} . The exact expressions for \mathbf{S} depend on the employed tracking algorithm. In the following, three different methods for ES tracking will be discussed briefly.

Parts of this chapter are based on:

Steinmetzer, J.; Kupfer, S.; Gräfe, S. pysisyphus: Exploring potential energy surfaces in ground and excited states. *International Journal of Quantum Chemistry* **2020**, *121*, DOI: 10.1002/qua.26390

Open Access publication, licensed under Creative Commons - Attribution 4.0 International (CC BY 4.0).

4.1 Wavefunction Overlaps

Wavefunction overlaps (WFO) between two sets of electronic states given by the wavefunctions $\{|\Psi_I\rangle\}$ and $\{|\Psi_J\rangle\}$, calculated at molecular geometries \mathbf{R}_I and \mathbf{R}_J , can be expanded into SDs:

$$S_{IJ} = \langle \Psi_I | \Psi_J \rangle = \sum_{k=1}^{N_{\text{CI},I}} \sum_{l=1}^{N_{\text{CI},J}} d_{Ik} d_{Jl} \langle \Phi_k | \Phi'_l \rangle, \quad (4.1)$$

with d being (configuration interaction) CI-coefficients, N_{CI} their number and $\{|\Phi\rangle\}$ denote SDs. Overlaps between Slater determinants $\langle \Phi_k | \Phi'_l \rangle$ are reduced to MO overlaps.

$$\begin{aligned} & \langle \Phi_k | \Phi'_l \rangle \\ &= \\ & \left| \begin{array}{cccccc} \langle \phi_{k(1)} | \phi'_{l(1)} \rangle & \cdots & \langle \phi_{k(1)} | \phi'_{l(n_\alpha)} \rangle & \langle \phi_{k(1)} | \bar{\phi}'_{l(n_\alpha+1)} \rangle & \cdots & \langle \phi_{k(1)} | \bar{\phi}'_{l(n)} \rangle \\ \vdots & \ddots & \vdots & & \ddots & \vdots \\ \langle \phi_{k(n_\alpha)} | \phi'_{l(1)} \rangle & \cdots & \langle \phi_{k(n_\alpha)} | \phi'_{l(n_\alpha)} \rangle & & & \\ \vdots & & & \langle \bar{\phi}_{k(n_\alpha+1)} | \bar{\phi}'_{l(n_\alpha+1)} \rangle & \cdots & \langle \bar{\phi}_{k(n_\alpha+1)} | \bar{\phi}'_{l(n)} \rangle \\ & & & \vdots & \ddots & \vdots \\ \langle \bar{\phi}_{k(n)} | \phi'_{l(1)} \rangle & \cdots & \langle \bar{\phi}_{k(n)} | \phi'_{l(n_\alpha)} \rangle & \langle \bar{\phi}_{k(n)} | \bar{\phi}'_{l(n_\alpha+1)} \rangle & \cdots & \langle \bar{\phi}_{k(n)} | \bar{\phi}'_{l(n)} \rangle \end{array} \right| \quad (4.2) \\ &= \\ & \left| \begin{array}{cccccc} \langle \phi_{k(1)} | \phi'_{l(1)} \rangle & \cdots & \langle \phi_{k(1)} | \phi'_{l(n_\alpha)} \rangle & & & \\ \vdots & \ddots & \vdots & & & \mathbf{0} \\ \langle \phi_{k(n_\alpha)} | \phi'_{l(1)} \rangle & \cdots & \langle \phi_{k(n_\alpha)} | \phi'_{l(n_\alpha)} \rangle & & & \\ & & & \langle \bar{\phi}_{k(n_\alpha+1)} | \bar{\phi}'_{l(n_\alpha+1)} \rangle & \cdots & \langle \bar{\phi}_{k(n_\alpha+1)} | \bar{\phi}'_{l(n)} \rangle \\ & & & \vdots & \ddots & \vdots \\ & & & \langle \bar{\phi}_{k(n)} | \bar{\phi}'_{l(n_\alpha+1)} \rangle & \cdots & \langle \bar{\phi}_{k(n)} | \bar{\phi}'_{l(n)} \rangle \end{array} \right| \end{aligned}$$

The MO overlap matrix is block diagonal, as MOs of different spin are orthogonal and their overlap vanishes.[225] Overlaps between alpha MOs (\mathcal{S}_{kl}) and beta MOs ($\bar{\mathcal{S}}_{kl}$) can be calculated separately.

$$\langle \Phi_k | \Phi'_l \rangle = \underbrace{\begin{vmatrix} \langle \phi_{k(1)} | \phi'_{l(1)} \rangle & \cdots & \langle \phi_{k(1)} | \phi'_{l(n_\alpha)} \rangle \\ \vdots & \ddots & \vdots \\ \langle \phi_{k(n_\alpha)} | \phi'_{l(1)} \rangle & \cdots & \langle \phi_{k(n_\alpha)} | \phi'_{l(n_\alpha)} \rangle \end{vmatrix}}_{S_{kl}} \times \underbrace{\begin{vmatrix} \langle \bar{\phi}_{k(n_\alpha+1)} | \bar{\phi}'_{l(n_\alpha+1)} \rangle & \cdots & \langle \bar{\phi}_{k(n_\alpha+1)} | \bar{\phi}'_{l(n)} \rangle \\ \vdots & \ddots & \vdots \\ \langle \bar{\phi}_{k(n)} | \bar{\phi}'_{l(n_\alpha+1)} \rangle & \cdots & \langle \bar{\phi}_{k(n)} | \bar{\phi}'_{l(n)} \rangle \end{vmatrix}}_{\bar{S}_{kl}} \quad (4.3)$$

MO overlaps are ultimately obtained in a straightforward fashion from atomic orbital (AO) overlaps

$$\langle \phi_p | \phi'_q \rangle = \sum_{\mu=1}^{N_{\text{MO}}} \sum_{\nu=1}^{N_{\text{MO}}} C_{p\mu} C'_{q\nu} \langle \chi_\mu | \chi'_\nu \rangle, \quad (4.4)$$

with $\{|\phi_p\rangle\}$ and $\{|\phi'_q\rangle\}$ being two distinct sets of MOs with coefficients \mathbf{C} and \mathbf{C}' . The AO sets $\{|\chi_\mu\rangle\}$ and $\{|\chi'_\nu\rangle\}$ are centered at their respective coordinates, \mathbf{R}_I and \mathbf{R}_J , and their overlap matrix \mathbf{S}_{AO} can be obtained from a calculation comprising all basis functions, or, if the difference between both geometries is small, recovered from the MO coefficients \mathbf{C} (\mathbf{C}') at \mathbf{R}_I (\mathbf{R}_J):[228, 229]

$$\mathbf{S}_{\text{AO}} = (\mathbf{C}^{-1})^\top \mathbf{C}'^{-1}. \quad (4.5)$$

Application of eq. (4.5) in geometry optimization is justified, as the geometries between two optimization cycles are very similar. The reader is referred to the original publication for a full discussion of the wavefunction overlap (WFO) algorithm.[225]

4.2 Transition Density Overlaps

Another option for ES tracking are transition density matrix (TDEN) overlaps. Given two MO coefficient matrices \mathbf{C}_I and \mathbf{C}_J obtained at different molecular geometries \mathbf{R}_I and \mathbf{R}_J , their overlap matrix \mathbf{S}_{MO} is defined according to eq. (4.4) as

$$\mathbf{S}_{\text{MO}} = \mathbf{C}_I \mathbf{S}_{\text{AO}} \mathbf{C}_J^\top. \quad (4.6)$$

Assuming N_o occupied and N_v virtual MOs, the overlaps between two one-electron transition density matrices \mathbf{T}_I and \mathbf{T}_J of dimensions $(N_o \times N_o + N_v)$ in their respective

MO bases \mathbf{C}_I and \mathbf{C}_J are calculated as:

$$S_{IJ} = \sum_{\sigma=1}^{N_o} \sum_{\tau=1}^{N_o} \sum_{\mu=1}^{N_o+N_v} \sum_{\nu=1}^{N_o+N_v} T_{I,\tau\mu} T_{J,\sigma\nu} S_{\text{MO},\sigma\tau} S_{\text{MO},\mu\nu} . \quad (4.7)$$

Equation (4.7) is efficiently implemented using matrix-matrix products.

$$S_{IJ} = \sum_{\sigma=1}^{N_o} \sum_{\tau=1}^{N_o} S_{\text{MO},\tau\sigma} \mathbf{T}_I \mathbf{S}_{\text{MO}} \mathbf{T}_J^T \quad (4.8)$$

Compared to WFOs, the evaluation of TDEN overlaps is computationally less challenging, as no determinant calculations are involved.

4.3 Natural Transition Orbital Overlaps

A third option for ES tracking are NTO overlaps.[223] Natural transition orbitals ψ allow a more compact representation of ESs through a basis transformation of the occupied and virtual MOs ϕ and ϕ' .

$$(\psi_1, \dots, \psi_{N_o}) = (\phi_1, \dots, \phi_{N_o}) \mathbf{U} \quad (4.9)$$

$$(\psi'_1, \dots, \psi'_{N_v}) = (\phi'_1, \dots, \phi'_{N_v}) \mathbf{V} \quad (4.10)$$

$$(4.11)$$

Here, the matrices \mathbf{U} and \mathbf{V} are conveniently calculated by a singular value decomposition (SVD) of the one-electron transition density matrix \mathbf{T}

$$\mathbf{T} = \mathbf{U} \mathbf{\Sigma} \mathbf{V}^T , \quad (4.12)$$

with $\mathbf{\Sigma}$ being a diagonal matrix containing the singular values $\{\lambda_i\}$. [227] Often, only a few singular values differ significantly from zero, thus \mathbf{T} is well captured by a low-rank approximation and only few NTOs are needed for the ES description.

Given two one-electron transition density matrices \mathbf{T}_I and \mathbf{T}_J , calculated at nuclear geometries \mathbf{R}_I and \mathbf{R}_J , NTOs $\{\psi_I\}$ and $\{\psi_J\}$, their overlap is calculated as

$$S_{IJ} = \sum_{k=1}^{N_{\text{NTO}}} \lambda_{I,k} \left| \mathbf{C}_{I,k}^{\text{NTO}} \mathbf{S}_{\text{AO}} \mathbf{C}_{J,k}^{\text{NTO},T} \right| , \quad (4.13)$$

with \mathbf{C}^{NTO} containing the respective NTO coefficients for excited state I or J and $\lambda_{I,k}$ being the k -th singular value obtained from the SVD of \mathbf{T}_I . N_{NTO} is determined from the number of singular values above a prescribed threshold (e.g. 0.3). A full derivation of the NTO overlap algorithm is presented in ref.[224].

4.4 Choosing a Reference Cycle

While tracking ESs in geometry optimizations, one of the two nuclear geometries \mathbf{R}_I and \mathbf{R}_J is given by the current optimization cycle, whereas the remaining one is given by a reference cycle. Different types of reference cycles can be chosen. Overlaps between the ESs at the current cycle can either be calculated with the ESs at the first cycle or with the previous optimization cycle. Alternatively, an adaptive algorithm can be employed, where the reference cycle is only updated when two conditions are met. A new reference cycle is only chosen when the highest overlap of the current excited states and the reference state is above a certain threshold (e.g. 0.5), indicating that there is a well defined correspondence between one of the current ESs and the reference ES. Furthermore, the ratio between the second highest and highest overlaps must be between 0.3 and 0.6. Low values indicate easily distinguishable states, therefore no update is needed. High values indicate very similar overlaps, consequentially an update may not be appropriate as multiple states at the current cycle are very similar to the reference state.

5 Obtaining Minima on Potential Energy Surfaces

5.1 The Quadratic Approximation

Searching for minima on PESs is an optimization problem

$$\min_{\mathbf{R} \in \mathbb{R}^n} E(\mathbf{R}) \quad (5.1)$$

with \mathbf{R} denoting a set of (nuclear) coordinates and $E(\mathbf{R})$ the electronic energy. A suitable step \mathbf{p}_k to minimize $E(\mathbf{R})$ at optimization cycle k can be obtained from the Taylor expansion of $E(\mathbf{R})$ to second-order around \mathbf{R}_k , with gradient \mathbf{g}_k and Hessian \mathbf{H}_k

$$E(\mathbf{R}_k + \mathbf{p}_k) = E_k + \mathbf{p}_k^\top \mathbf{g}_k + \frac{1}{2} \mathbf{p}_k^\top \mathbf{H}_k \mathbf{p}_k . \quad (5.2)$$

By differentiating eq. (5.2) with respect to \mathbf{p}_k and equating the result to zero, the step is given as

$$\mathbf{p}_k = -(\mathbf{H}_k)^{-1} \mathbf{g}_k . \quad (5.3)$$

For minimizations it has to be ensured that \mathbf{H}_k has no negative eigenvalues, otherwise eq. (5.3) will result in an erroneous step. Transformed to the Hessian eigenvector basis, eq. (5.3) is rewritten as

$$\tilde{p}_{k,i} = -\frac{\tilde{g}_{k,i}}{\tilde{H}_{k,ii}} \quad (5.4)$$

with i denoting the eigenvector index and the tilde denotes transformed quantities. For negative eigenvalues $\tilde{H}_{k,ii} < 0$, the step produced by eq. (5.4) will be uphill along the gradient, instead of downhill, against the gradient.

Parts of this chapter are based on:

Steinmetzer, J.; Kupfer, S.; Gräfe, S. pysisyphus: Exploring potential energy surfaces in ground and excited states. *International Journal of Quantum Chemistry* **2020**, *121*, DOI: 10.1002/qua.26390

Open Access publication, licensed under Creative Commons - Attribution 4.0 International (CC BY 4.0).

5 Obtaining Minima on Potential Energy Surfaces

Downhill steps can be obtained by determining a suitable shift parameter λ , e.g., from root-finding algorithms.[230]

$$\tilde{p}_{k,i} = -\frac{\tilde{g}_{k,i}}{\tilde{H}_{k,ii} - \lambda} \quad (5.5)$$

Alternatively, valid downhill directions are ensured by rational function optimization (RFO) where

$$E(\mathbf{R}_k + \mathbf{p}_k) = E_k + \frac{\mathbf{p}_k^\top \mathbf{g}_k + \frac{1}{2} \mathbf{p}_k^\top \mathbf{H}_k \mathbf{p}_k}{1 + \mathbf{p}_k^\top \mathbf{S} \mathbf{p}_k} \quad (5.6)$$

instead of eq. (5.2) is minimized.[70, 231, 232] Matrix \mathbf{S} is usually chosen as the unit matrix. The RFO step \mathbf{p}_k for minimizations is obtained by solving the eigenvalue equation

$$\begin{bmatrix} \mathbf{H}_k & \mathbf{g}_k \\ \mathbf{g}_k^\top & 0 \end{bmatrix} \begin{bmatrix} \mathbf{p}_k \\ 1 \end{bmatrix} = \nu \begin{bmatrix} \mathbf{S} & \mathbf{0} \\ \mathbf{0}^\top & 1 \end{bmatrix} \begin{bmatrix} \mathbf{p}_k \\ 1 \end{bmatrix} \quad (5.7)$$

and scaling the eigenvector corresponding to the lowest eigenvalue ν , so its last element equals to 1.

5.2 Hessian Update and Initial Choice

Depending on the Hessian employed to calculate the step \mathbf{p}_k , e.g., by eqs. (5.3) and (5.7), several methods are distinguished. With a simple unit Hessian ($\mathbf{H}_k = \mathbf{I}$) the method of steepest descent is obtained from eq. (5.3), where \mathbf{p}_k is simply given by

$$\mathbf{p}_k = -(\mathbf{H}_k)^{-1} \mathbf{g}_k = -(\mathbf{I})^{-1} \mathbf{g}_k = -\mathbf{g}_k . \quad (5.8)$$

Performance of the steepest descent method is often very poor, as coordinate coupling is fully neglected.[233]

Using the exact Hessian in every cycle eq. (5.3) gives rise to Newton's method.[234] If the PES is well described by a quadratic model, Newton's method shows fast local convergence. Obtaining the exact Hessian in every optimization cycle is often not feasible while searching for SPs, as its calculation is computationally very demanding. A compromise between the computationally cheap, but badly performing method of steepest descent and the performant, but computationally expensive Newton method is provided by quasi-Newton (QN) methods. In QN methods, an approximate Hessian \mathbf{A}_k is used to obtain the step

$$\mathbf{p}_k = -(\mathbf{A}_k)^{-1} \mathbf{g}_k . \quad (5.9)$$

Based on the secant equation

$$\mathbf{A}_{k+1}\mathbf{s}_k = \mathbf{y}_k \quad (5.10)$$

an initial Hessian is updated along the optimization, using only coordinate differences $\mathbf{s}_k = \mathbf{R}_{k+1} - \mathbf{R}_k$ and gradient differences $\mathbf{y}_k = \mathbf{g}_{k+1} - \mathbf{g}_k$, obtained at two successive cycles k and $k+1$. As eq. (5.10) is under-determined, additional constraints like enforcing certain symmetry and positive definiteness of \mathbf{A}_{k+1} are employed, to devise actual update formulas. One of the most popular formulas for minimizations is the Broyden-Fletcher-Goldfarb-Shanno (BFGS) update.[235–238]

$$\mathbf{A}_{k+1} = \mathbf{A}_k - \frac{\mathbf{A}_k\mathbf{s}_k\mathbf{s}_k^\top\mathbf{A}_k}{\mathbf{s}_k^\top\mathbf{A}_k\mathbf{s}_k} + \frac{\mathbf{y}_k\mathbf{y}_k^\top}{\mathbf{y}_k^\top\mathbf{s}_k} \quad (5.11)$$

The need to invert \mathbf{A}_k in every optimization cycle is overcome, by directly updating the inverse of \mathbf{A}_k :

$$\mathbf{A}_k^{-1} = (\mathbf{I} - \rho_k\mathbf{s}_k\mathbf{y}_k^\top)\mathbf{A}_k^{-1}(\mathbf{I} - \rho_k\mathbf{y}_k\mathbf{s}_k^\top) + \rho_k\mathbf{s}_k\mathbf{s}_k^\top \quad (5.12)$$

with $\rho_k = 1/\mathbf{y}_k^\top\mathbf{s}_k$. Other popular update formulas are the symmetric rank 1 (SR1) update, Powell’s symmetric Broyden (PSB) update, and especially for optimizing saddle points, Bofills update.[234, 239, 240] Instead of always updating \mathbf{A}_k the exact Hessian could, if feasible, be recalculated periodically and used as starting point for further Hessian updates, thus mixing Newton and QN steps for improved optimization performance.

Besides the update formula, optimization outcome is greatly affected by the initial Hessian choice (or its inverse). If calculating an initial Hessian is infeasible or not desired, an approximate model Hessian can be estimated. For the purpose of geometry optimization, several model Hessians were proposed, e.g., by Lindh,[241] Fischer[242], and Swart.[243] The only requirement for calculating a model Hessian from the previously mentioned models, is the existence of a set of primitive internal coordinates (stretches, bends, dihedrals, see also Figure 6.1), defining the connectivity of the system under study. See chapter 6 for an overview on internal coordinates.

In the following, Fischers model Hessian is presented exemplarily.[242] By fitting data from reference molecules obtained at the HF/6-31G** level of theory, Fischer gave empirical formulas for the individual force constants k . Eqs. (5.13) to (5.15) are specified using the atomic labels (M, N, O, P) shown in Figure 6.1 on page 42. The bond length between two atoms M and N is denoted by r^{MN} . The sum of their covalent radii is denoted by r_{cov}^{MN} .

$$k_{\text{stretch}} = Ae^{-B(r^{MN} - r_{\text{cov}}^{MN})} \quad (5.13)$$

$$A = 0.3601, B = 1.944$$

$$k_{\text{bend}} = A + \frac{B}{(r_{\text{cov}}^{OM} r_{\text{cov}}^{ON})^D} e^{-C(r^{OM} + r^{ON} - r_{\text{cov}}^{OM} - r_{\text{cov}}^{ON})} \quad (5.14)$$

$$A = 0.089, B = 0.11, C = 0.44, D = -0.42$$

$$k_{\text{dihedral}} = A + \frac{BL^D}{(r^{OP} r_{\text{cov}}^{OP})^E} e^{-C(r^{OP} - r_{\text{cov}}^{OP})} \quad (5.15)$$

$$A = 0.0015, B = 14.0, C = 2.85, D = 0.57, E = 4.00$$

Parameter L in eq. (5.15) denotes the number of bond stretches connected to the central atoms O and P of the dihedral, without the central $O - P$ bond. Calculating a model Hessian by eqs. (5.13) to (5.15) yields a diagonal Hessian in internal coordinates. If the optimization is to be conducted in Cartesian coordinates, the estimated Hessian has to be converted to Cartesian coordinates by eq. (6.10).

5.3 Conjugate Gradient and Limited-Memory BFGS

For big molecules, solving the RFO eigenvalue problem eq. (5.7) may become prohibitively expensive.[244–246] A popular algorithm to determine \mathbf{p}_k , avoiding any matrix operations and requiring minimal storage, is the nonlinear conjugate gradient (CG) method.[75] In CG methods, the search direction is given as

$$\mathbf{p}_{k+1} = -\mathbf{g}_{k+1} + \beta_{k+1}\mathbf{p}_k . \quad (5.16)$$

The algorithm is initialized with a steepest descent step $\mathbf{p}_0 = -\alpha_0\mathbf{g}_0$. Many variants for β have been proposed, a popular one was given by Polak and Ribière[247, 248]

$$\beta_{k+1}^{\text{PR}} = \frac{\mathbf{g}_{k+1}^\top (\mathbf{g}_{k+1} - \mathbf{g}_k)}{\mathbf{g}_k^\top \mathbf{g}_k} . \quad (5.17)$$

Hager and Zhang offered a more complex definition[249]

$$\beta_{k+1}^{\text{HZ}} = \left(\mathbf{y}_k - 2\mathbf{p}_k \frac{\mathbf{y}_k^\top \mathbf{y}_k}{\mathbf{y}_k^\top \mathbf{p}_k} \right)^\top \frac{\mathbf{g}_{k+1}}{\mathbf{y}_k^\top \mathbf{p}_k} . \quad (5.18)$$

As CG methods employ no Hessian information, their performance is expected to be inferior for molecular optimizations.

Limited-memory methods like limited-memory BFGS (LBFGS) offer the best of both worlds: Low storage requirements and computational efficiency similar to CG methods, while implicitly keeping an Hessian approximation.[250] By storing the latest m vector pairs $\{\mathbf{s}_i, \mathbf{y}_i\}$ for $i = k - m, \dots, k - 1$, the matrix-vector product $\mathbf{A}_k^{-1} \mathbf{g}_k$ is calculated in a two-loop recursion, using only vector-vector products (see Algorithm 1).[234, 251]

Algorithm 1 LBFGS two-loop recursion

```

1:  $\mathbf{q} \leftarrow \mathbf{g}_k$ 
2: for  $i = k - 1, \dots, k - m$  do
3:    $\alpha_i \leftarrow \rho_i \mathbf{s}_i^\top \mathbf{q}$  ▷ Store  $\alpha_i$ 
4:    $\mathbf{q} \leftarrow \mathbf{q} - \alpha_i \mathbf{y}_i$ 
5:  $\mathbf{r} \leftarrow (\mathbf{H}_k^0)^{-1} \mathbf{q}$  ▷  $(\mathbf{H}_k^0)^{-1}$  = preconditioner or vector
6: for  $i = k - m, \dots, k - 1$  do
7:    $\beta_i \leftarrow \rho_i \mathbf{y}_i^\top \mathbf{r}$ 
8:    $\mathbf{r} \leftarrow \mathbf{r} + \mathbf{s}_i (\alpha_i - \beta_i)$ 
9: return  $\mathbf{A}_k^{-1} \mathbf{g}_k = \mathbf{r}$ 

```

Two QN optimizations, using either a BFGS update or the LBFGS approach, yield the exact same results for the first m cycles. The LBFGS method usually outperforms CG methods in molecular optimizations, despite slightly increased storage and computational costs.[252, 253]

Care has to be taken that $\mathbf{s}_k \mathbf{y}_k > 0$ is ensured, otherwise \mathbf{A}_k may lose its positive-definiteness. As the Hessian is never explicitly constructed in the LBFGS method, determination of an appropriate shift factor as in eq. (5.5) is not easily achieved. If $\mathbf{s}_k \mathbf{y}_k > 0$ is violated, the Hessian update may be skipped, but this is usually not advised, as valuable curvature information is neglected.[234] By using a damped BFGS update, positive-definiteness of \mathbf{A}_k can be guaranteed.[254] Recently, Goldfarb proposed a double damping procedure that modifies the $(\mathbf{s}_k, \mathbf{y}_k)$ pair (Algorithm 2).[255]

The $\mathbf{A}^{-1} \mathbf{y}$ term in Algorithm 2 is conveniently calculated using the two-loop recursion in Algorithm 1, so double damping is easily utilized in LBFGS optimizations.

5.4 Trust Radius

Given a search direction \mathbf{p}_k , a suitable step length has to be determined. To this end, several approaches exist, with the simplest being the trust radius method. If the length of a proposed step \mathbf{p}_k is below or equal to a prescribed trust radius Δ , it is accepted,

Algorithm 2 Double damping procedure, adapted from [255].

- 1: Given $\mathbf{s} \leftarrow \mathbf{s}_k, \mathbf{y} \leftarrow \mathbf{y}_k, \mathbf{A}^{-1} \leftarrow \mathbf{A}_k^{-1}$ and parameters μ_1, μ_2
 - 2: **if** $\mathbf{s}^\top \mathbf{y} < \mu_1 \mathbf{y}^\top \mathbf{A}^{-1} \mathbf{y}$ **then** $\theta_1 = \frac{(1-\mu_1) \mathbf{y}^\top \mathbf{A}^{-1} \mathbf{y}}{\mathbf{y}^\top \mathbf{A}^{-1} \mathbf{y} - \mathbf{s}^\top \mathbf{y}}$
 - 3: **else** $\theta_1 = 1$
 - 4: $\tilde{\mathbf{s}} = \theta_1 \mathbf{s} + (1 - \theta_1) \mathbf{A}^{-1} \mathbf{y}$
 - 5: **if** $\tilde{\mathbf{s}}^\top \mathbf{y} < \mu_2 \tilde{\mathbf{s}}^\top \tilde{\mathbf{s}}$ **then** $\theta_2 = \frac{(1-\mu_2) \tilde{\mathbf{s}}^\top \tilde{\mathbf{s}}}{\tilde{\mathbf{s}}^\top \tilde{\mathbf{s}} - \tilde{\mathbf{s}}^\top \mathbf{y}}$
 - 6: **else** $\theta_2 = 1$
 - 7: $\tilde{\mathbf{y}} = \theta_2 \mathbf{y} + (1 - \theta_2) \tilde{\mathbf{s}}$
 - 8: **return** $\tilde{\mathbf{s}}, \tilde{\mathbf{y}}$
-

otherwise it can either be simply downscaled or determined from more sophisticated methods like the restricted step (RS) algorithm, as well as the level-shifted Newton method.[232, 256] The trust radius Δ is updated according to the agreement between predicted energy changes ΔE_{pred} , e.g., through eq. (5.6) or eq. (5.2), and actual energy changes ΔE_{act} over the course of an optimization.[234, 239]

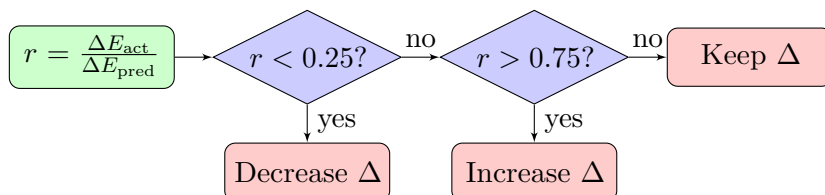


Figure 5.1: Trust radius update flowchart. Depending on the agreement between actual energy changes ΔE_{act} and predicted energy changes ΔE_{pred} , the trust radius Δ is either decreased or increased.

5.5 Line searches

A more rigorous approach for step length determination is given by line searches that may involve multiple energy and gradient evaluations in every optimization cycle. The line search problem is formulated as

$$\min_{\alpha > 0} E(\mathbf{R}_k + \alpha \mathbf{p}_k) \quad (5.19)$$

with the goal to determine α for a given \mathbf{p}_k . Line searches are usually carried out iteratively, until a set of prescribed conditions is satisfied. One popular condition is to require a sufficient decrease of the function value (Armijo condition)[234]

$$E(\mathbf{R}_k + \alpha \mathbf{p}_k) \leq E(\mathbf{R}_k) + c_1 \alpha \mathbf{g}_k^\top \mathbf{p}_k. \quad (5.20)$$

Parameter c_1 controls the degree of required energy decrease and is usually chosen quite small (10^{-4}), thus allowing line search convergence even for minor energy decreases. Enforcing the Armijo condition only requires additional energy calculations. As eq. (5.20) may allow very short steps (depending on c_1), a second condition (curvature condition) can be enforced, guaranteeing that sufficient optimization progress is made:

$$\mathbf{g}(\mathbf{R}_k + \alpha_k \mathbf{p}_k)^\top \mathbf{p}_k \geq c_2 \mathbf{g}_k \mathbf{p}_k . \quad (5.21)$$

Similar to c_1 in eq. (5.20), the parameter $c_2 \in (c_1, 1)$ controls how strongly the left-hand side (LHS) of eq. (5.21) must be reduced, until the curvature condition is satisfied. Typical values for c_2 are 0.9, if \mathbf{p}_k was obtained from a (quasi)-Newton method and 0.1, if \mathbf{p}_k was obtained from a conjugate gradient method. Enforcing the curvature condition requires additional gradient calculations. Applied together, the Armijo and curvature conditions are known as the Wolfe conditions.[234] An example for valid minimizers of a function, obeying the Wolfe conditions, is shown in Figure 5.2. Popular line search algorithms are those provided by Moré and Thuente[257] and by Hager and Zhang.[249]

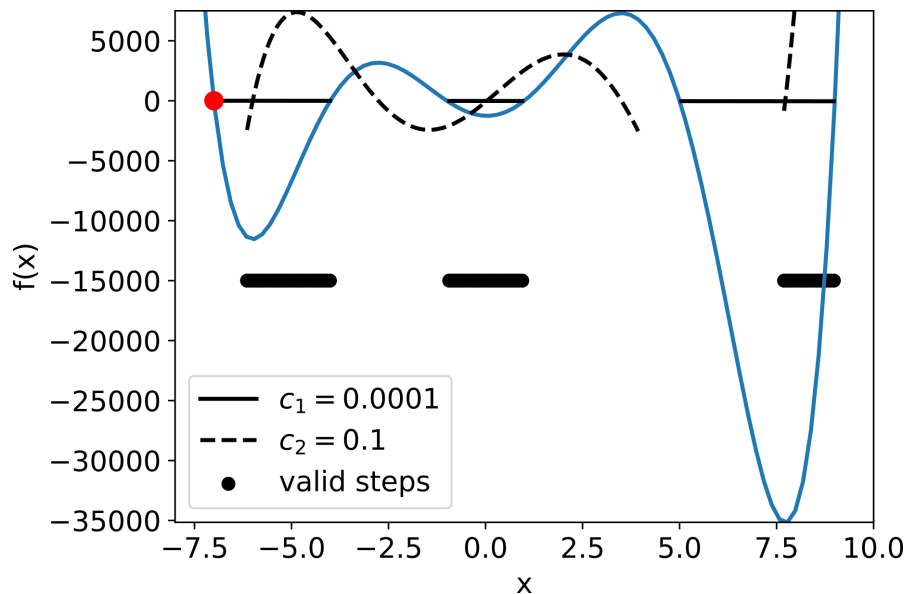


Figure 5.2: Illustration of valid steps from $x_0 = -7$ (red dot) towards a minimizer of $f(x) = (x - 1)(x + 1)(x + 4)(x + 7)(x - 5)(x - 9)$, satisfying the Wolfe conditions. \mathbf{p}_0 was chosen as the direction of steepest descent. The thin black line indicates points that satisfy the Armijo condition ($c_1 = 0.0001$), the dashed black line indicate points that satisfy the curvature condition ($c_2 = 0.1$). Their union, indicated by thick black dots, represent points that satisfy the Wolfe conditions.

Conducting exact line searches satisfying the Wolfe conditions may become computationally very demanding, as additional energy and gradient evaluations are needed in every optimization cycle. Computationally cheaper, albeit less robust, are partial line searches, which are usually employed in the geometry optimizers of QC codes, as additional gradient evaluations are often costly. In practice, partial line searches are performed by fitting a polynomial between two coordinates \mathbf{R}_k and \mathbf{R}_t . Utilizing energies and projected gradients ($\mathbf{g}_k \cdot \alpha_t \mathbf{p}_k$) obtained at \mathbf{R}_k and \mathbf{R}_t , a constrained polynomial of fourth degree, or an unconstrained polynomial of third degree can be fitted.[75] The resulting inter- or extrapolated data (coordinates, energy and gradient) is then used to compute a new step direction \mathbf{p}_{k+1} for the next optimization cycle, so only one energy and gradient evaluation is needed per optimization cycle. Differences between partial and full line searches are illustrated in Figure 5.3.

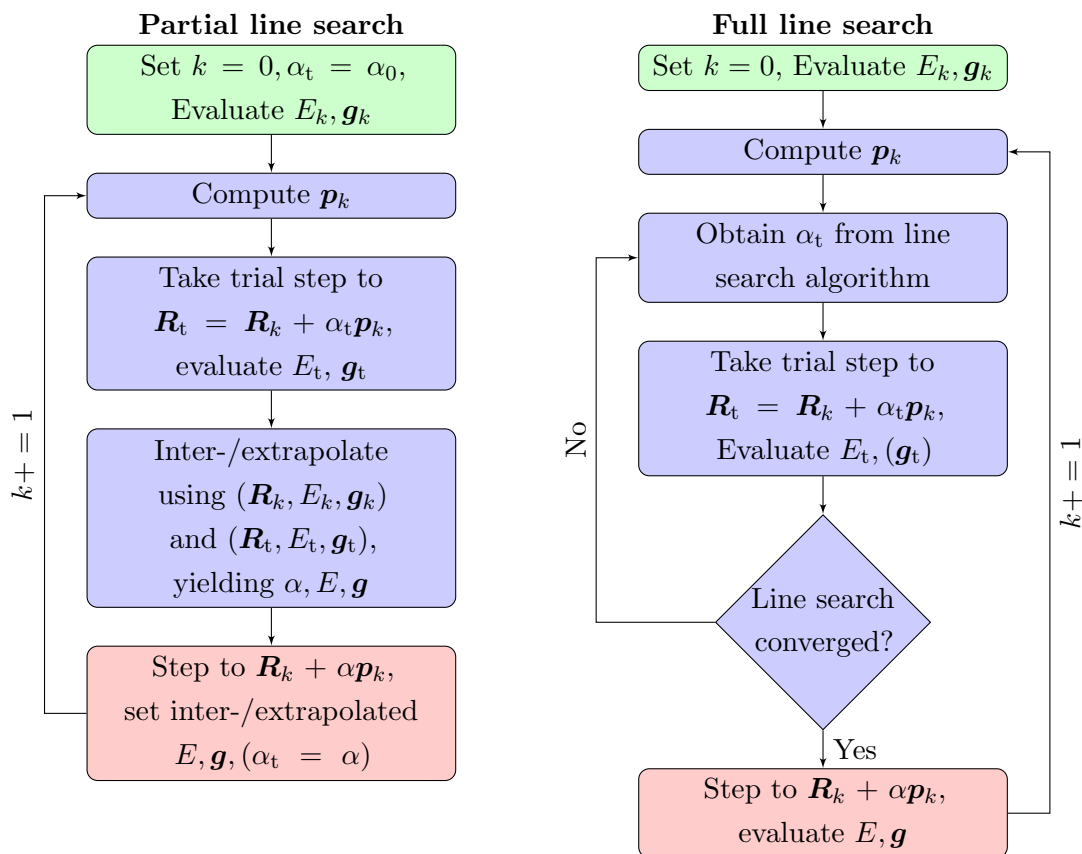


Figure 5.3: Flowcharts for partial (left) and full line searches (right). While partial line searches require only one energy and gradient evaluation per cycle, full line searches may require multiple energy (and gradient) evaluations per cycle, until convergence is achieved.

To the best knowledge of the author, line searches in the context of molecular optimizations are exclusively used for minimizations, but they may also be used for maximizations, e.g., maximizing the energy along the imaginary mode in partitioned rational function optimization (PRFO), presented in chapter 9.

5.6 Direct Inversion in the Iterative Subspace

Instead of fitting polynomials, the geometric direct inversion in the iterative subspace (GDIIS) method can be used for inter- and extrapolation.[258] In GDIIS, a set of k coordinates $\{\mathbf{R}_i\}$ is linearly combined to minimize the length of an error vector $\|\mathbf{x}^*\|_2$.

$$\mathbf{R}^* = \sum_i^k c_i \mathbf{R}_i, \quad \text{with } \sum_i^k c_i = 1 \quad (5.22)$$

The error vector \mathbf{x}^* is obtained as linear combination of respective error vectors \mathbf{e}_i associated with each structure \mathbf{R}_i .

$$\mathbf{x}^* = \sum_i^k c_i \mathbf{e}_i \quad (5.23)$$

Common choices for \mathbf{e}_i are the gradient \mathbf{g}_i , or the predicted quadratic step $-\mathbf{H}_i^{-1}\mathbf{g}_i$, recall eq. (5.3).[246] Coefficients c_i are obtained by solving the least-squares problem

$$\begin{pmatrix} a_{1,1} & \cdots & a_{1,k} & 1 \\ \vdots & \ddots & \vdots & \vdots \\ a_{k,1} & \cdots & a_{k,k} & 1 \\ 1 & \cdots & 1 & 0 \end{pmatrix} \begin{pmatrix} c_1 \\ \vdots \\ c_k \\ \lambda \end{pmatrix} = \begin{pmatrix} 0 \\ \vdots \\ 0 \\ 1 \end{pmatrix} \quad (5.24)$$

with $a_{i,j} = \mathbf{e}_i^T \mathbf{e}_j$ and the Lagrangian multiplier λ .[259] As regular GDIIS is prone to converge to the nearest SP or an inflection point, several safeguards have been proposed by Farkas and Schlegel, yielding the controlled GDIIS method.[259]

Similar to \mathbf{R}^* , a corresponding gradient \mathbf{g}^* is obtained that can be used to predict new coordinates for the next optimization cycle.

$$\mathbf{R}_{k+1} = \mathbf{R}^* - \mathbf{H}^{-1}\mathbf{g}^* \quad (5.25)$$

In GDIIS, coefficients $|c_i| > 1$ are possible, thus allowing extrapolation. Far from convergence, extrapolation may yield erroneous steps. A closely related method allowing

5 Obtaining Minima on Potential Energy Surfaces

only interpolation, is the energy represented direct inversion in the iterative subspace (GEDIIS).[260] Based on a first-order energy expansion

$$E(\mathbf{R}^*) = E_k + (\mathbf{R}^* - \mathbf{R}_k)^\top \mathbf{g}_k , \quad (5.26)$$

the GEDIIS energy expression is obtained by multiplying with c_i and summing over N points

$$E(\mathbf{R}^*) = \sum_{i=1}^N c_i [E(\mathbf{R}_i) + \sum_{j=1}^N c_j \mathbf{R}_j \mathbf{g}_i - \mathbf{R}_i \mathbf{g}_i] . \quad (5.27)$$

Coefficients c_i are obtained by direct minimization of eq. (5.27) under the constraint $0 \leq c_i \leq 1$. Compared to GDIIS, GEDIIS can be enabled earlier in an optimization and has been shown to result in smooth optimizations, with less erroneous, energy increasing steps.[260]

6 Internal Coordinates

Coordinate system choice greatly affects the outcome of geometry optimizations. The simplest choice are Cartesian coordinates, as they are, disregarding translation and rotation, unambiguously defined and always available. A big disadvantage, preventing efficient optimizations in Cartesians, is their strong coupling, exemplified in a strongly non-diagonal Hessian.[261] By employing an optimizer that utilizes Hessian information, the coupling can be taken into account to some degree. For this, the Hessian would have to be calculated, as it is not possible to estimate an approximate Hessian using Cartesian coordinates alone (see section 5.2).

An improved coordinate choice is given by normal mode coordinates (NMC), obtained from diagonalizing the mass-weighted Hessian.[262, 263] While keeping the big advantage of being unambiguously defined, they are orthogonal to each other and don't couple. Nonetheless, a Hessian is needed for their definition.

A third choice is given by redundant internal coordinates (RIC), composed of bond stretches, bends, linear bends and dihedrals.[232, 239, 264–266] In the following, the definition and usage of RICs for molecular optimizations is summarized. Many more coordinate systems have been proposed over the years, including the Z-Matrix[75], natural internal coordinates,[267–269], delocalized internal coordinates (DLC),[270] hybrid DLC,[271] and translation-rotation internal coordinates,[272] from which only DLC will be briefly discussed.

6.1 Definition of Redundant Internal Coordinates

Redundant internal coordinates for a set of atoms are assigned, based on atomic connectivity.[232] See Figure 6.1 for an illustration, how common internal coordinates are defined. A bond stretch q_s between two atoms is assigned, when their distance is equal or smaller than the scaled sum of their covalent radii. A factor of 1.2 or 1.3 is usually employed for scaling. For every pair of bond stretches sharing an atom, a bend q_b is defined. Similarly, a dihedral q_d is defined for every consecutively bonded set of four atoms. Care has to be taken that no dihedral is defined, when three of the four atoms

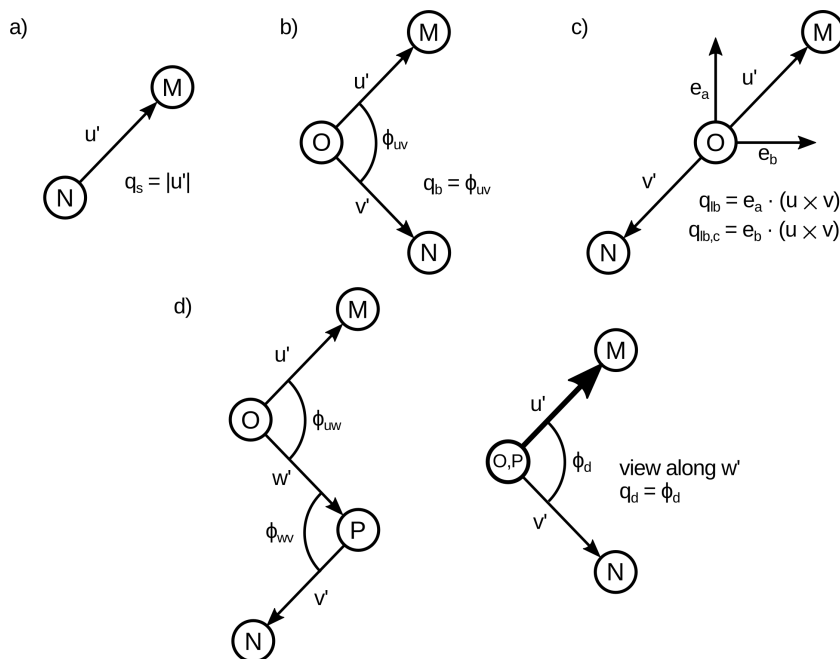


Figure 6.1: Definition of commonly used primitive internal coordinates: a) bond stretch q_s , b) bend q_b c) linear bend q_{lb} and its orthogonal complement $q_{lb,c}$ d) dihedral q_d .

are (nearly) collinear, as then q_d becomes undefined. For a set of three (nearly) collinear atoms, a linear bend q_{lb} and its orthogonal complement can be defined.[273–275]. In contrast to regular bends, the second derivative of a linear bend, with respect to the Cartesian coordinates making it up, is defined even for collinear atomic arrangements. If several disconnected fragments are present, it has to be ensured that coordinates connecting them are defined.

Furthermore, additional coordinates can be defined, e.g., explicit hydrogen bonds, out-of-plane angles,[276] and/or auxiliary bond stretches that use an increased scaling factor for the summed covalent radii.[232]

The choice of the initial scaling factor in the bond stretch definition and the different types of internal coordinates actually used, make their overall definition highly ambiguous. It was recognized that including too many (auxiliary) bond stretches is detrimental for the optimization outcome and hampers the back-transformation of a step in internal coordinates to Cartesian coordinates (vide infra).[232, 277]

6.2 Wilson's B-Matrix

The central quantity when working with internal coordinates, is the Wilson \mathbf{B} matrix. It relates changes in Cartesian coordinates \mathbf{R} , to changes in internal coordinates \mathbf{q} . [232, 278]

$$B_{ij} = \frac{\partial q_i}{\partial R_j} \quad (6.1)$$

Matrix \mathbf{B} is rectangular, with one row per internal coordinate q_i and one column per Cartesian coordinate R_j .

$$\begin{array}{c}
 q_1 \\
 q_2 \\
 \vdots \\
 \vdots \\
 \vdots \\
 q_n
 \end{array}
 \begin{pmatrix}
 R_1 & R_2 & \cdots & R_n \\
 \text{stretches} \\
 \cdots \\
 \text{bends} \\
 \cdots \\
 \text{dihedrals}
 \end{pmatrix}
 \quad (6.2)$$

Explicit expressions for eq. (6.1) are given, e.g., by Wilson and Bakken. [232, 278] With \mathbf{B} , small Cartesian displacements are transformed to displacements in internal coordinates.

$$\mathbf{B}\delta\mathbf{R} = \delta\mathbf{q} \quad (6.3)$$

As the matrix inverse is only defined for quadratic matrices, the pseudo-inverse \mathbf{B}^+ is used for the inverse operation.

$$\delta\mathbf{R} = \mathbf{B}^+\delta\mathbf{q} \quad (6.4)$$

\mathbf{B}^+ is readily obtained from a SVD of $\mathbf{G} = \mathbf{B}\mathbf{B}^\top$ by inverting only singular values above a certain threshold.

$$\mathbf{G} = \mathbf{B}\mathbf{B}^\top = \mathbf{U}\mathbf{\Sigma}\mathbf{V}^\top \quad (6.5)$$

$$\mathbf{B}^+ = \mathbf{B}^\top(\mathbf{V}'\mathbf{\Sigma}'^{-1}\mathbf{U}'^\top) \quad (6.6)$$

The prime indicates that only singular values above a threshold and corresponding singular vectors are used for the inversion. A suitable threshold for the singular values is 3.16×10^{-4} , when \mathbf{G} was calculated in atomic units (corresponding to a threshold of 1×10^{-7} for the eigenvalues of \mathbf{G}). [264]

6 Internal Coordinates

Similar to the coordinates, the Cartesian gradient \mathbf{g}_R and the gradient in internal coordinates \mathbf{g}_q are transformed.

$$\mathbf{g}_R = \mathbf{B}^\top \mathbf{g}_q \quad (6.7)$$

$$\mathbf{g}_q = (\mathbf{B}^\top)^+ \mathbf{g}_R \quad (6.8)$$

Transforming the Cartesian Hessian \mathbf{H}_R and the Hessian in internal coordinates \mathbf{H}_q requires \mathbf{g}_q and derivatives of \mathbf{B} , with respect to Cartesian coordinates.

$$\mathbf{H}_R = \mathbf{B}^\top \mathbf{H}_q \mathbf{B} + \mathbf{K} \quad (6.9)$$

$$\mathbf{H}_q = (\mathbf{B}^\top)^+ (\mathbf{H}_R - \mathbf{K}) \mathbf{B}^+ \quad (6.10)$$

$$K_{jk} = \sum_i [\mathbf{g}_q]_i B'_{ijk} = \sum_i [\mathbf{g}_q]_i \frac{\partial^2 q_i}{\partial R_j \partial R_k} \quad (6.11)$$

When the chosen set of internal coordinates is redundant, matrix \mathbf{B} is rank-deficient and has linearly dependent rows. To ensure a step is only taken in the non-redundant subspace of \mathbf{B} , the gradient \mathbf{g}_q is projected by \mathbf{P} .

$$\mathbf{P} = \mathbf{B} \mathbf{B}^+ \quad (6.12)$$

$$\tilde{\mathbf{g}}_q = \mathbf{P} \mathbf{g}_q \quad (6.13)$$

Additionally, the elements of \mathbf{H}_q belonging to the redundant subspace $(\mathbf{I} - \mathbf{P})$ orthogonal to \mathbf{P} , are shifted to high values ($\alpha = 1000$).

$$\tilde{\mathbf{H}}_q = \mathbf{P} \mathbf{H}_q \mathbf{P} + \alpha (\mathbf{I} - \mathbf{P}) \quad (6.14)$$

Constraints are easily implemented by means of a projector \mathbf{P}' . [265] Given a diagonal matrix \mathbf{C} , with ones on the diagonal for the constrained primitives and zeros elsewhere, \mathbf{P} can be modified to

$$\mathbf{P}' = \mathbf{P} - \mathbf{P} \mathbf{C} (\mathbf{C} \mathbf{P} \mathbf{C})^{-1} \mathbf{C} \mathbf{P}. \quad (6.15)$$

This approach even allows constraining Cartesian coordinates of (single) atoms, which may appear counterintuitive at first. But Cartesian coordinates are well supported in the framework of internal coordinates, as their first and second derivatives with respect to Cartesian coordinates are easily calculated ($\partial q_i / \partial R_j = \delta_{ij}$, $\partial^2 q_i / \partial R_j \partial R_k = 0$). Alternatively, constraints can be implemented by means of Lagrange multipliers or penalty functions. [84, 279–281]

6.3 Internal-Cartesian Back-Transformation

A step in internal coordinates has to be iteratively transformed to a step in Cartesian coordinates.[232] Starting from internals \mathbf{q}_0 and step $\Delta\mathbf{q}_0$, the desired target coordinates $\mathbf{q}_T = \mathbf{q}_0 + \Delta\mathbf{q}_0$ are obtained from multiple evaluations of

$$\mathbf{R}_{l+1} = \mathbf{R}_l + \mathbf{B}^+ \Delta\mathbf{q}_l, \quad (6.16)$$

as eq. (6.4) is only valid for small displacements $\delta\mathbf{q}$. Figure 6.2 shows the flowchart for the iterative back-transformation.

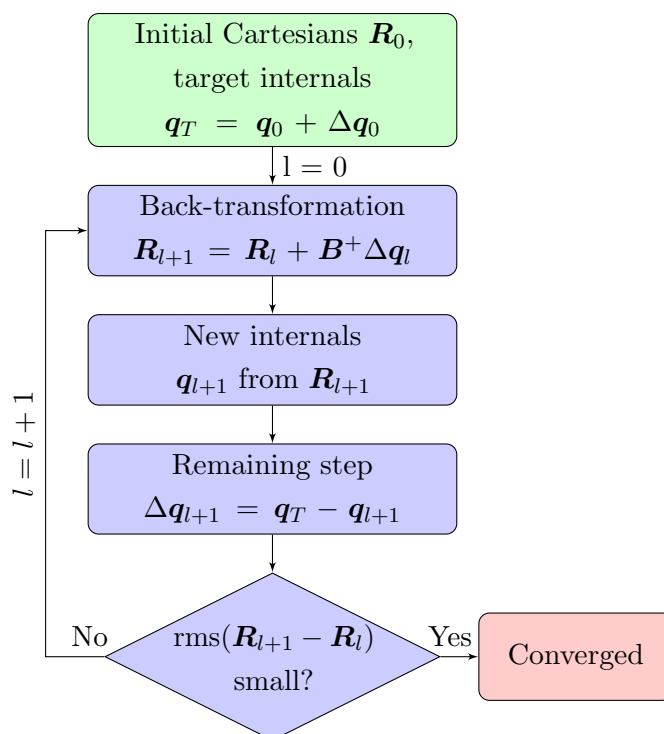


Figure 6.2: Flowchart for the iterative back-transformation of a desired step in internal coordinates $\Delta\mathbf{q}_0$, starting from Cartesian coordinates \mathbf{R}_0 and corresponding internals \mathbf{q}_0 .

It has to be noted that not all possible sets of internal coordinates \mathbf{q} have a valid Cartesian representation. The triangle equality states for every triangle that the summed length of two sides must be greater or equal to the third side. It is easy to propose three bond stretches between three atoms that violate the triangle equality, thus this set of internals can't have a Cartesian representation.[282] Given the restriction of eq. (6.4) to small displacements and the possibility of invalid internals, the back-transformation in

Figure 6.2 occasionally fails. In such cases, optimizations are continued with \mathbf{R}_1 , the Cartesian coordinates obtained in the first cycle of the back-transformation. A more robust approach for the back-transformation using high-order derivatives of \mathbf{B} based on automatic differentiation was proposed by Rybkin.[283]

6.4 Delocalized Internal Coordinates

With a computationally cheap method to evaluate energies and gradients, handling RIC can become the computational bottleneck for big molecules. Especially the number of possible dihedrals grows immensely with the molecular size, leading to big Hessians and Wilson’s B-matrices. Matrix diagonalization and inversion scale cubically with matrix size ($\mathcal{O}(n^3)$). Both operations are needed, e.g., to calculate a RFO step in internal coordinates and back-transform it to Cartesians. Furthermore, RIC still show some coupling, even though it is greatly reduced compared with Cartesian coordinates.

Both problems are overcome with DLC. Diagonalizing $\mathbf{G} = \mathbf{B}\mathbf{B}^\top$ yields two sets of eigenvectors. For nonlinear molecules, a set of $3N - 6$ eigenvectors \mathbf{U} with eigenvalues $\lambda > 0$ spanning the non-redundant subspace of internals and the remaining eigenvectors \mathbf{V} with vanishing eigenvalues spanning the redundant subspace, is obtained.[270]

$$\mathbf{G}(\mathbf{UV}) = (\mathbf{UV}) \begin{pmatrix} \boldsymbol{\Sigma} & \mathbf{0} \\ \mathbf{0} & \mathbf{0} \end{pmatrix} \quad (6.17)$$

Eigenvectors \mathbf{U} (active set) are used to obtain the active (DLC) coordinates \mathbf{q}^{DLC} and for transforming the original \mathbf{B} matrix.

$$\mathbf{q}^{\text{DLC}} = \mathbf{U}^\top \mathbf{q} \quad (6.18)$$

$$\mathbf{B}^{\text{DLC}} = \mathbf{U}^\top \mathbf{B} \quad (6.19)$$

When substituting \mathbf{B}^{DLC} for \mathbf{B} in eqs. (6.8), (6.11) and (6.16), the same equations can be used to transform Cartesian gradient and Hessian as well as for the iterative back-transformation.[270] For a nonlinear molecule of N atoms with $m = 3N - 6$ internal degrees of freedom, the DLC Hessian has size $(m \times m)$. Thus, Hessian diagonalization will be much faster in DLC compared to RIC for big N . As the eigenvectors \mathbf{U} are orthogonal to each other, DLCs show no coupling, at least for the coordinates at which they were obtained.

DLCs have two drawbacks. First, they are complicated linear combinations of RIC and not easily interpretable. Second, they are only strictly orthogonal at the geometry

they were defined at. Consequently, DLCs defined at the beginning may not be suitable in later stages of an optimization, requiring repeated diagonalization of \mathbf{G} , therefore defeating the purpose of avoiding expensive operations on big matrices. Usually \mathbf{G} is only calculated once and the same set of eigenvectors \mathbf{U} is used throughout an optimization.

For a set of small molecules, DLC and RIC showed similar performance with respect to required optimization cycles.[270] Choosing DLCs may become favorable for big molecules, when matrix operation (diagonalization of \mathbf{H} , inversion of \mathbf{B}) become costly and the overall optimization time is considered.

7 Preconditioning

The optimization problem

$$\min_{\mathbf{R} \in \mathbb{R}^n} E(\mathbf{R}) \quad (7.1)$$

is well conditioned, if its solution is not greatly perturbed by small changes of its input values.[234] Molecular optimizations are often ill-conditioned, as molecular degrees of freedom (e.g. bond stretches, dihedrals, interfragment stretches) have force constants of different magnitudes. While a small change of a bond length greatly affects the energy, a small rotation around a dihedral leaves the energy nearly unaffected.

As already discussed in section 5.1, $E(\mathbf{R})$ can be linearized and minimized by solving $\mathbf{H}_k \mathbf{p}_k = -\mathbf{g}_k$ for \mathbf{p}_k . Ill-conditioning makes \mathbf{p}_k susceptible to small inaccuracies in \mathbf{H}_k and \mathbf{g}_k , e.g., arising from numerical integration in DFT, impeding efficient optimizations.[284] Furthermore, step restriction may become difficult, as steps for the different internal coordinates may be of different magnitudes, preventing the use of a simple maximum value for all step elements.

The conditioning of a problem or a matrix is measured by its condition number κ . For a normal matrix,¹ e.g., the Hessian, κ is defined as

$$\kappa = \frac{|\lambda_{\max}|}{|\lambda_{\min}|}, \quad (7.2)$$

with λ_{\max} (λ_{\min}) being the greatest (smallest) matrix eigenvalue.[285]

Preconditioning can be seen as transformation to a set of coordinates $\mathbf{R}' = \mathbf{P}^{1/2} \mathbf{R}$, where the corresponding Hessian has an improved eigenvalue distribution $\{\lambda'_i\}$, through a preconditioner matrix \mathbf{P} . [286] The eigenvalues of the preconditioned Hessian $\{\lambda'_i\}$ are defined as

$$\lambda'_i = \frac{\mathbf{u}_i^\top \mathbf{H}_k \mathbf{u}_i}{\mathbf{u}_i^\top \mathbf{P}_k \mathbf{u}_i}, \quad (7.3)$$

with \mathbf{u}_i denoting the i -th eigenvector of the unconditioned Hessian \mathbf{H}_k . Well-conditioned optimizations are expected to converge much faster, compared to ill-conditioned optimizations.[234, 287] The effect of preconditioning for a quadratic potential is shown in Figure 7.1.

¹Matrix \mathbf{A} is normal if $\mathbf{A}\mathbf{A}^* = \mathbf{A}^*\mathbf{A}$

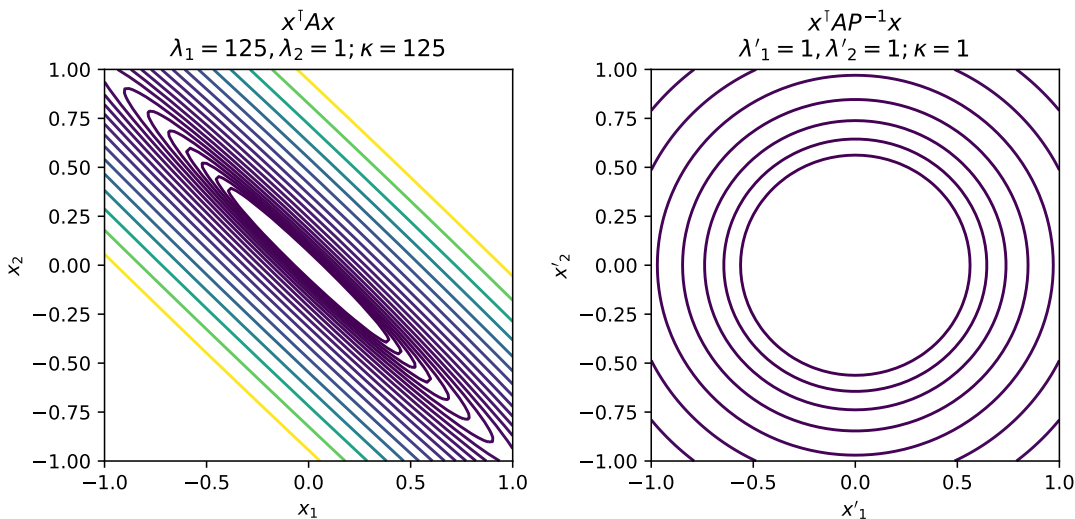


Figure 7.1: Effect of preconditioning for an ill conditioned quadratic potential obtained from $\mathbf{x}^T \mathbf{A} \mathbf{x}$ with $\mathbf{A} = \begin{bmatrix} 63 & 62 \\ 62 & 63 \end{bmatrix}$ (eigenvalues $\lambda_1 = 125, \lambda_2 = 1$) and $\mathbf{x} = \begin{bmatrix} x_1 \\ x_2 \end{bmatrix}$. Left: Original problem. Progress along the valley towards the minimizer requires large step sizes, as the potential is shallow, but small steps perpendicular to this direction lead to steep potential increases, making step scaling difficult. Right: Preconditioned problem with optimal condition number $\kappa = 1$, allowing easy step scaling, as the potential is isotropic. In the present case the “optimal” preconditioner $\mathbf{P} = \mathbf{A}^{-1}$ was used, which is usually not available in real applications, e.g., searches for SPs on molecular PESs.

Optimizations are then carried out in the new coordinate system, e.g., using the method of steepest descent.

$$\mathbf{R}'_{k+1} = \mathbf{R}'_k - \alpha_k \mathbf{g}'_k \quad (7.4)$$

$$\mathbf{P}^{1/2} \mathbf{R}_{k+1} = \mathbf{P}^{1/2} \mathbf{R}_k - \alpha_k \mathbf{P}^{-1/2} \mathbf{g}_k \quad (7.5)$$

Back-transformation of eq. (7.5) to the original coordinate system recovers the equation for a quasi-Newton step, as already given in eq. (5.9). In this sense, steepest descent in the transformed coordinate system and a QN in the original coordinate system are identical, when $\mathbf{P} = \mathbf{A}_k$.

$$\mathbf{R}_{k+1} = \mathbf{R}_k - \alpha_k \mathbf{P}^{-1} \mathbf{g}_k \quad (7.6)$$

For $\mathbf{P} = \mathbf{I}$ the steepest descent method in the original coordinates \mathbf{R} is recovered, and for $\mathbf{P} = \mathbf{H}_k$, eq. (7.6) yields the original Newton step.[286] Similarly, preconditioning can

be applied to a QN method, e.g., the LBFGS algorithm (see line 5 in Algorithm 1 on page 35), for improved optimization performance compared to preconditioned steepest descent.[234, 288]

A useful preconditioner \mathbf{P} must fulfill several requirements: a) it must be easy to construct, b) cheap to invert, e.g., by exploiting sparsity, and c) must be positive definite to ensure a descent direction is obtained, see eq. (5.4).[287]

Mones et al. proposed a force field based scheme to construct effective preconditioners \mathbf{P} for molecular systems, fulfilling the above requirements.[286] Starting from a surrogate force field potential V_{FF}

$$V_{\text{FF}} = \sum_i V_i(q_i(\mathbf{R})) \quad (7.7)$$

comprising individual potential energy terms V_i , e.g., quadratic potentials

$$V_{i,\text{Quadratic}} = \frac{1}{2}k_i(q_i - q_{i,0})^2 \quad (7.8)$$

the corresponding Hessian

$$\mathbf{H}_{\text{FF}} = \frac{\partial^2 V_{\text{FF}}}{\partial \mathbf{R}^2} = \sum_i \frac{\partial^2 V_i}{\partial \mathbf{R}^2} = \sum_i \mathbf{H}_i \quad (7.9)$$

is calculated. When long-range interactions are neglected while constructing V_{FF} , e.g., only bonding interactions are considered, \mathbf{H}_{FF} will be sparse and is easily stored and inverted. Depending on \mathbf{R} and the actual potential energy terms $\{V_i\}$, \mathbf{H}_{FF} may not be positive definite. Mones suggested modifying the local Hessian contributions to ensure overall positivity.[286]

$$\mathbf{H}_i = \frac{\partial^2 V_i}{\partial \mathbf{R}^2} = \underbrace{\frac{\partial q_i}{\partial \mathbf{R}} \otimes \frac{\partial q_i}{\partial \mathbf{R}} \frac{\partial^2 V_i}{\partial q_i^2}}_{\mathbf{H}_i^{(1)}} + \underbrace{\frac{\partial^2 q_i}{\partial \mathbf{R}^2} \frac{\partial V_i}{\partial q_i}}_{\mathbf{H}_i^{(2)}} \quad (7.10)$$

For quadratic potentials $\partial^2 V_i / \partial q_i^2 = k_i > 0$, so $\mathbf{H}_i^{(1)}$ will be positive-semi-definite, whereas the definiteness of $\mathbf{H}_i^{(2)}$ is ambiguous. By dropping the second term $\mathbf{H}_i^{(2)}$ and using the absolute value of $\partial^2 V_i / \partial q_i^2$, positive-definiteness of \mathbf{P} is ensured even for non-quadratic potentials and the following, general formula for \mathbf{P} is obtained:

$$\mathbf{P} = \sum_i \tilde{\mathbf{H}}_i^{(1)} = \frac{\partial q_i}{\partial \mathbf{R}} \otimes \frac{\partial q_i}{\partial \mathbf{R}} \left| \frac{\partial^2 V_i}{\partial q_i^2} \right|. \quad (7.11)$$

7 Preconditioning

The $\partial q_i / \partial \mathbf{R}$ terms are elements of Wilson's B-Matrix discussed in section 6.2 and are easily computed. A particular attractive, black-box way, for calculating $\partial^2 V_i / \partial q_i^2$ was given by Lindh.[241]

$$V_{\text{Lindh}}(\mathbf{q}) = V_{\text{linear}}(\mathbf{q}) + V_{\text{stretch}}(\mathbf{q}) + V_{\text{bend}}(\mathbf{q}) + V_{\text{dihedral}}(\mathbf{q}) \quad (7.12)$$

The linear term assumes the availability of energy and gradient at a newly computed point \mathbf{q}_0 .

$$V_{\text{linear}}(\mathbf{q}) = V_{\text{Lindh}}(\mathbf{q}_0) + (\mathbf{q} - \mathbf{q}_0) \frac{\partial V_{\text{Lindh}}(\mathbf{q}_0)}{\partial \mathbf{q}} \quad (7.13)$$

Quadratic expressions are used for the remaining terms.

$$V_{\text{stretch}} = \frac{1}{2} \sum_{j>i} k_{ij} (q_{ij} - q_{0,ij})^2 \quad (7.14)$$

$$V_{\text{bend}} = \frac{1}{2} \sum_{k>j>i} k_{ijk} (q_{ijk} - q_{0,ijk})^2 \quad (7.15)$$

$$V_{\text{dihedral}} = \frac{1}{2} \sum_{l>k>j>i} k_{ijkl} (q_{ijkl} - q_{0,ijkl})^2 \quad (7.16)$$

Depending on the number of subscript indices, different internal coordinates are distinguished (2: stretches, 3: bends, 4: dihedrals). Lindh suggested to use all possible terms, besides repeated and reversed index combinations. Force constants k are calculated from the equations below.

$$\rho_{ij} = \exp(\alpha_{ij} (q_{\text{ref},ij}^2 - q_{ij}^2)) \quad (7.17)$$

$$k_{ij} = k_s \rho_{ij} \quad (7.18)$$

$$k_{ijk} = k_b \rho_{ij} \rho_{jk} \quad (7.19)$$

$$k_{ijkl} = k_d \rho_{ij} \rho_{jk} \rho_{kl} \quad (7.20)$$

Parameters $\{\alpha_{ij}, q_{\text{ref},ij}, k_s, k_b, k_d\}$, obtained from calculations on water and hydroxysulphane at the HF/STO-3G level of theory, are given in Table 7.1. Figure 7.2 shows the effect of preconditioning using the Lindh model Hessian for 2-pentene. Improved preconditioners may be estimated from more sophisticated force fields like Amber,[32] CHARMM[33], or the universal force field (UFF),[289] at the cost of having to provide a suitable molecular topology to the force field engine.

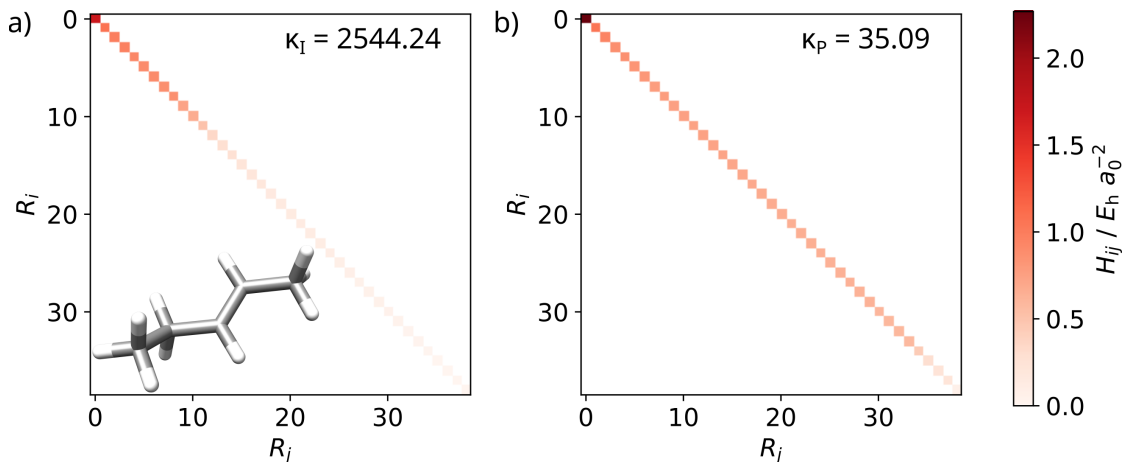


Figure 7.2: Effect of preconditioning on force constants and condition number κ . a) Unconditioned Cartesian Hessian and b) preconditioned Cartesian Hessian for 2-pentene, obtained at the HF/def2-SVP level of theory. The preconditioner was obtained as outlined in [286], using the Lindh model Hessian (vide infra).[241]. Preconditioning leads to a markedly improved eigenvalue distribution and greatly reduced condition number κ_P . The six smallest eigenvalues belonging to the eigenvectors describing translational and rotational motions have been removed.

Table 7.1: Lindh model Hessian parameters in atomic units for the first three periods of the periodic table. The parameter for an atom pair depends entirely on their periods i, j in the periodic table. Force constants $k_s = 0.45$, $k_b = 0.15$ and $k_d = 0.005$ are employed in eqs. (7.18) to (7.20).[241]

$\alpha_{ij} \begin{matrix} \backslash j \\ i \end{matrix}$	1	2	3	$q_{\text{ref},ij} \begin{matrix} \backslash j \\ i \end{matrix}$	1	2	3
1	1.0000	0.3949	0.3949	1	1.35	2.10	2.53
2	0.3949	0.2800	0.2800	2	2.10	2.87	3.40
3	0.3949	0.2800	0.2800	3	2.53	3.40	3.40

8 Chain-of-States Methods

Computational studies of reaction mechanism are conducted by locating SPs on the PES of the reactants and the MEPs connecting them. Whereas educts and products of a reaction may be known beforehand and are easily optimized, the TSs connecting them are often less accessible. Unfortunately, the comprehensive description of reaction energetics requires the TS, as it is essential for the prediction of reaction barriers.

Optimizing TSs poses several challenges: Most methods like PRFO[290] or the image method (IM)[256] require a computationally demanding Hessian calculation and the Hessian must have at least one significant negative eigenvalue with a corresponding eigenvector, suitable for the description of the reaction under study. Costly Hessian calculations may be sped up by employing techniques like resolution of identity (RI)[291, 292], however, providing a good initial guess geometry is far more difficult. Often, guesses for TSs are constructed manually, nevertheless such TS guesses may yield Hessians with wrong eigenvalue structure, or without a suitable eigenvector to describe the reaction coordinate, resulting in a laborious process of trial and error. Suitable TS guesses for further refinement can be obtained from COS methods.

In COS methods, a MEP is discretized by a set of tangents $\{\boldsymbol{\tau}_i\}$ defined at a set of molecular geometries (images) given by coordinates $\{\mathbf{R}_i\}$. The simplest tangent is given by the normalized distance vector between two adjacent images

$$\boldsymbol{\tau}_i = \frac{\mathbf{R}_{i+1} - \mathbf{R}_i}{|\mathbf{R}_{i+1} - \mathbf{R}_i|}, \quad (8.1)$$

but often a more sophisticated definition like an upwinding tangent is used.[72, 293, 294] A COS is usually spanned between two pre-optimized minima on the PES, while passing through a point close to the TS.[73]

Parts of this chapter are based on:

Steinmetzer, J.; Kupfer, S.; Gräfe, S. pysisyphus: Exploring potential energy surfaces in ground and excited states. *International Journal of Quantum Chemistry* **2020**, *121*, DOI: 10.1002/qua.26390

Open Access publication, licensed under Creative Commons - Attribution 4.0 International (CC BY 4.0).

The initial path is iteratively refined until it coincides with a MEP, or represents a sufficient approximation to it. An image i is considered converged to the MEP, when the perpendicular component \mathbf{f}_i^\perp of the force \mathbf{f}_i acting on it vanishes or is below a prescribed threshold

$$\mathbf{f}_i^\perp = \mathbf{f}_i - (\mathbf{f}_i \cdot \boldsymbol{\tau}_i)\boldsymbol{\tau}_i \approx \mathbf{0} \quad (8.2)$$

that is, the remaining force \mathbf{f}_i acts only along the tangent $\boldsymbol{\tau}_i$.

Common examples for COS methods are the NEB and the growing string method (GSM).[71, 295] Both methods differ in how the image distribution along the path is achieved and in their initial path setup (see section 8.2).

8.1 Nudged Elastic Band

The NEB method introduces artificial spring forces, acting parallel to the path

$$\mathbf{f}_i^\parallel = k_i(|\mathbf{R}_{i+1} - \mathbf{R}_i| - |\mathbf{R}_{i-1} - \mathbf{R}_i|)\boldsymbol{\tau}_i, \quad (8.3)$$

so the total force $\mathbf{f}_i^{\text{NEB}}$ acting on image i is given by

$$\mathbf{f}_i^{\text{NEB}} = \mathbf{f}_i^\perp + \mathbf{f}_i^\parallel. \quad (8.4)$$

If the same spring constant k_i is used throughout all images, an equal image distribution along the band is achieved, as \mathbf{f}_i^\parallel vanishes for equidistant images.

8.2 Interpolating Initial Paths

An initial COS path is generated by interpolation between two minima. The quality of the initial path is crucial for the successful outcome of COS optimizations.[296] Given two images \mathbf{R}_0 and \mathbf{R}_{N-1} , intermediate images \mathbf{R}_i are linearly interpolated as

$$\mathbf{R}_i = \mathbf{R}_0 + i \frac{\mathbf{R}_{N-1} - \mathbf{R}_0}{N - 1} \quad (8.5)$$

with N denoting the desired total number of images in the path and i is running from 0 to $N - 1$. Linear interpolation in Cartesian coordinates often yields poor paths, as the curvilinear nature of bends and dihedrals is neglected, leading to artificially compressed bonds and frequent atom clashes.

Improved paths are obtained from interpolating atomic distance matrices \mathbf{D}_0 and \mathbf{D}_{N-1} , defined at \mathbf{R}_0 and \mathbf{R}_{N-1} . The distance between atoms j and k for Cartesian coordinates \mathbf{R} is

$$D_{jk} = \sqrt{\sum_{\sigma} (R_{j\sigma} - R_{k\sigma})^2} \quad (8.6)$$

with σ running over the Cartesian axes x, y, z . Analogous to eq. (8.5), interpolated distance matrices are obtained as

$$\mathbf{D}_i = \mathbf{D}_0 + i \frac{\mathbf{D}_{N-1} - \mathbf{D}_0}{N-1}. \quad (8.7)$$

Typically, there are many more atomic distances than internal degrees of freedom, so a desired distance matrix \mathbf{D}_i can only be approximated by a set of Cartesian coordinates in a least-squares sense. Halgren and Lipscomb proposed the linear synchronous transit (LST) method, to determine a suitable set of Cartesian coordinates via minimization of an objective function S^{LST} .^[297–299]

$$S_i^{\text{LST}}(\mathbf{R}_i) = \underbrace{\sum_{k>j} \frac{(D_{jk} - D_{jk}^{(i)})^2}{(D_{jk}^{(i)})^4}}_{S^{\text{IDPP}}} + 10^{-6} \underbrace{\sum_{j,\sigma} (R_{i,j\sigma} - R_{i,j\sigma}^{(i)})^2}_{S^{\text{TR}}} \quad (8.8)$$

Indices j and k denote atoms. Terms $\mathbf{D}^{(i)}$ and $\mathbf{R}_i^{(i)}$, determined from eq. (8.7) and eq. (8.5), remain fixed throughout the minimization of S_i^{LST} . The small term S^{TR} in eq. (8.8) was introduced to penalize excessive translation and rotation, with respect to a reference geometry. Full LST paths are obtained by subsequent minimizations of S_i^{LST} for all intermediate images ($0 < i < N - 1$).

The LST approach was improved by Smidstrup in the image dependent pair potential (IDPP) method. By only using the first term S^{IDPP} from eq. (8.8) and optimizing all images simultaneously as a NEB, overall convergence is improved.^[296]

While LST and IDPP usually greatly improve upon naive linear interpolation, both methods can yield discontinuous paths, as the minimization(s) may fail to converge. The computational effort to evaluate the objective function S and its gradient ∇S is usually negligible, compared to the actual electronic structure calculations in the subsequent COS optimizations.

If it is feasible to define internal coordinates at \mathbf{R}_0 and \mathbf{R}_{N-1} , then linear interpolation in DLC is the preferred interpolation method, as the curvilinear nature of bends and dihedrals is correctly taken into account, while lengthy minimization as in LST and

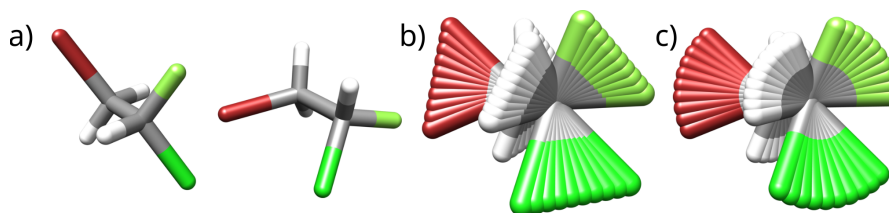


Figure 8.1: Different interpolated paths for rotation around the central dihedral in $\text{CH}_2\text{BrCHFCl}$. a) Initial and final geometries, b) linearly interpolated Cartesians and c) linearly interpolated DLCs. Linearly interpolated Cartesians yield artificially compressed bond lengths, as the curvilinear nature of dihedrals is neglected, while linearly interpolated DLCs take it correctly into account.

IDPP are avoided.[300] A discussion of the different interpolation algorithms is given by Zhu.[301] Figure 8.1 illustrates the differences between linear interpolation in Cartesian and internal coordinates.

8.3 Growing String Method

If none of the former interpolation methods yields a reasonable initial path, a growing COS method like the GSM can be used.[300] In this case, initial construction of a full path is avoided and new images are added on-the-fly, when sufficient convergence is achieved on the innermost images of the two disconnected sub-strings. In string methods (SMs), a prescribed image distribution along the string is achieved by periodical reparametrization. Depending on the employed coordinate system of the string images, a cubic spline is used for Cartesian coordinates and linear interpolation is done for delocalized internal coordinates.[300, 302] No spring constants are needed in the string method, and the forces acting on the images in a string are given by eq. (8.2).

8.4 NEB and String Variants

When the initial path is poor, tight convergence is required or many images are employed, COS optimizations can become computationally very costly, as one gradient evaluation per image is needed in every optimization cycle. To this end, several COS variants have been developed.

If the goal is to obtain a suitable TS guess, there is no need to tightly converge images far from the HEI. Rather, it may be beneficial, to increase the resolution around the HEI by zooming-in around it.

Originally proposed by Maragakis, this is implemented in the adaptive NEB (ANEb) variant.[303] The full NEB is optimized until a looser convergence threshold is fulfilled, then all but the energetically highest lying images are dropped and new images are interpolated between. This strategy can be applied recursively, zooming in further and further, until the ANEB is converged. Maragakis reported computational savings of up to 60%.[303] An illustration of the ANEB method is given in Figure 8.2.

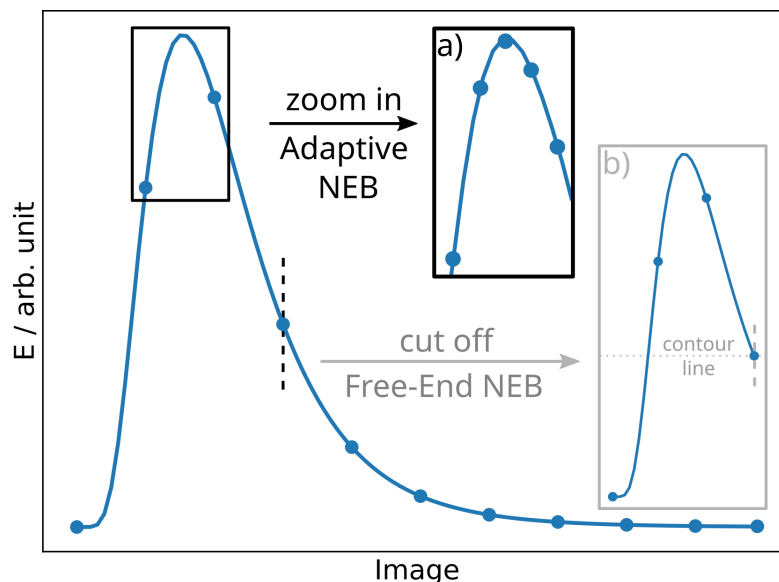


Figure 8.2: Illustration of NEB variants, aiming at reducing the computational costs of NEB optimizations. The original NEB has poor resolution around the presumed TS and features a long tail with only minor energetic differences between the images. a) Black inset in the upper part: adaptive NEB. Only the highest energy images are kept and new images are interpolated in between, leading to increased resolution around the TS. b) Grey inset in the lower part: free-end NEB. Images in the long tail are cut off and only the previous images are relaxed further. The frontier image is constrained to a contour line of the PES.

Similarly, if the NEB exhibits a long tail of energetically close images, computational resources may be wasted. Zhu suggested the free-end NEB (FENEb) variant, where the path is cut off after a selected image and the image is constrained to an isocontour line of the energy.[304] Both variants, ANEB and FENEb were later combined by Zhang into to free-end adaptive NEB (FEANEb) method.[305]

8.5 Optimizing Chain-Of-States

As briefly mentioned in section 8.1, COS paths are optimized by minimizing f^\perp . Many different algorithms have been employed for COS optimizations, with CG and LBFGS appearing most promising (see section 5.3).[306, 307]. Sheppard and Henkelman recognized a global version of LBFGS as especially effective.[306] By optimizing the whole COS as one super-molecule with LBFGS, the inter-image coupling via the tangents τ is included to some degree.

It was shown by Melander and Herbol that removal of translational and rotational degrees of freedom, either via quaternions or the Kabsch algorithm, is crucial for the success of COS optimizations.[307, 308]

8.6 Climbing Image

Improved TS guesses can be obtained by employing either one or two climbing images (CIs).[309, 310] After a few optimization cycles, the HEI can be converted to a CI. When two CIs are desired, the two images bracketing the HEI are converted. The force acting on CI i is reversed along its tangent τ_i , so a CI moves uphill along the COS-path and eventually converges to the true TS.

$$\mathbf{f}_i^{\text{CI}} = \mathbf{f}_i - 2(\mathbf{f}_i^\top \boldsymbol{\tau}_i) \boldsymbol{\tau}_i \quad (8.9)$$

8.7 Highest Energy Image

Given a converged COS, its HEI can be selected and used as guess in a subsequent TS-optimization. If the chosen TS-optimizer employs Hessian information and the Hessian has multiple negative eigenvalues, the HEI tangent can be used to select the initial eigenvector to follow uphill by an overlap criterion.

Starting TS searches in internal coordinates from a previous COS calculation also provides an additional benefit that is easily overlooked: By considering the union of internal coordinates from the first and last image in a COS, an improved set of internal coordinates can be generated for the TS search, compared to automated procedures that only consider the molecular geometry at the TS guess. As broken or not yet formed bonds are common in TSs, automated procedures can easily miss some bond definitions, resulting in an artificial restriction of the geometries degrees of freedom.

Overall, the choice of the coordinate system is extremely important for the success of (TS) optimizations, as can also be seen from Table III in ref. [270]. Depending on the chosen coordinate system, a TS guess may or may not have an imaginary frequency.

9 Obtaining Transition States on Potential Energy Surfaces

Given a suitable guess, e.g., the HEI from a COS optimization, TSs are obtained most efficiently by optimizers utilizing Hessian information. In contrast to minimizations, where the energy is minimized along all Hessian eigenvectors, the energy along one mode (transition vector) is maximized, when searching for first-order saddle points.

Suitable steps for TS optimizations are obtained from the PRFO method, where two eigenvalue equations similar to eq. (5.7) are solved. By transforming gradient \mathbf{g}_k and Hessian \mathbf{H}_k into the eigenvector basis of the latter, the two eigenvalue equations are

$$\begin{bmatrix} \tilde{H}_{k,11} & \tilde{g}_{k,1} \\ \tilde{g}_{k,1} & 0 \end{bmatrix} \begin{bmatrix} \tilde{p}_{k,1} \\ 1 \end{bmatrix} = \nu_{\max} \begin{bmatrix} \tilde{p}_{k,1} \\ 1 \end{bmatrix} \quad (9.1)$$

$$\begin{bmatrix} \tilde{H}_{k,22} & & 0 & \tilde{g}_{k,2} \\ & \ddots & & \vdots \\ 0 & & \tilde{H}_{k,nn} & \tilde{g}_{k,n} \\ \tilde{g}_{k,2} & \cdots & \tilde{g}_{k,n} & 0 \end{bmatrix} \begin{bmatrix} \tilde{p}_{k,2} \\ \vdots \\ \tilde{p}_{k,n} \\ 1 \end{bmatrix} = \nu_{\min} \begin{bmatrix} \tilde{p}_{k,2} \\ \vdots \\ \tilde{p}_{k,n} \\ 1 \end{bmatrix}, \quad (9.2)$$

with the tilde denoting transformed quantities and assuming the energy is to be maximized along eigenvector 1. Whereas the eigenvector with the smallest eigenvalue is scaled in eq. (9.2), the eigenvector belonging to the largest eigenvalue is scaled in eq. (9.1). As both eigenvalue equations are solved independently, PRFO neglects the coupling between both subspaces.

This problem is solved by the image method (IM). Given the Taylor expansion $E(\mathbf{R})$ in eq. (5.2), an image function $\bar{E}(\mathbf{R})$ is constructed in a way, such that the TSs of $E(\mathbf{R})$

Parts of this chapter are based on:

Steinmetzer, J.; Kupfer, S.; Gräfe, S. pysisyphus: Exploring potential energy surfaces in ground and excited states. *International Journal of Quantum Chemistry* **2020**, *121*, DOI: 10.1002/qua.26390

Open Access publication, licensed under Creative Commons - Attribution 4.0 International (CC BY 4.0).

9 Obtaining Transition States on Potential Energy Surfaces

coincide with the minima of $\bar{E}(\mathbf{R})$. [232, 256] By applying a Householder transformation

$$\mathbf{P} = \mathbf{I} - 2v_i v_i^\top, \quad (9.3)$$

with identity matrix \mathbf{I} and transition vector v_i , to gradient and Hessian at cycle k

$$\bar{\mathbf{g}}_k = \mathbf{P} \mathbf{g}_k \quad (9.4)$$

$$\bar{\mathbf{H}}_k = \mathbf{P} \mathbf{H}_k \quad (9.5)$$

$$(9.6)$$

the image function $\bar{E}(\mathbf{R})$ is defined as

$$\bar{E}(\mathbf{R}_k + \mathbf{p}_k) = E_k + \mathbf{p}_k^\top \bar{\mathbf{g}}_k + \frac{1}{2} \mathbf{p}_k^\top \bar{\mathbf{H}}_k \mathbf{p}_k. \quad (9.7)$$

Now minima of $\bar{E}(\mathbf{R})$ can be obtained according to the approach outlined in section 5.1 using RFO, while correctly taking into account the coupling between both subspaces.

10 Dimer Method

When Hessian calculations become computationally infeasible, e.g., for large systems, or when analytical Hessian implementations are unavailable, TSs can be obtained by means of the dimer method (DM).[311] As it only utilizes first derivatives, any unfavorable $\mathcal{O}(N^3)$ -scaling matrix operations like diagonalization or inversion are avoided.

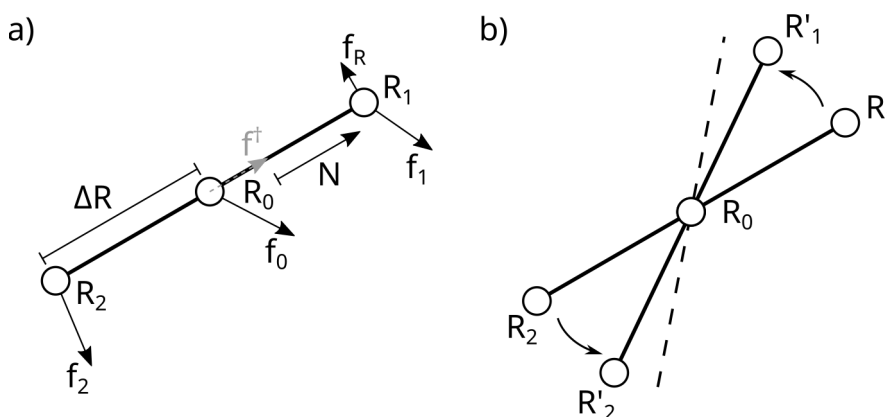


Figure 10.1: Illustration of the DM: a) The dimer comprises two images, \mathbf{R}_1 and \mathbf{R}_2 , displaced by ΔR from a common midpoint \mathbf{R}_0 along \mathbf{N} (dimer orientation). The rotational force \mathbf{f}^\perp acts on image \mathbf{R}_1 . Midpoint \mathbf{R}_0 is displaced uphill, against the parallel force \mathbf{f}^\parallel , towards the TS. b) One dimer rotation step: images \mathbf{R}_1 and \mathbf{R}_2 are rotated around \mathbf{R}_0 towards the lowest curvature mode, indicated by a dashed line.

A dimer consists of two images \mathbf{R}_1 and \mathbf{R}_2 , displaced into opposite directions by ΔR from a common midpoint \mathbf{R}_0 , along an orientation vector \mathbf{N} . The dimer is optimized towards a TS by repeated application of two steps: rotation and translation. Dimer rotation is achieved by minimizing the rotational force

$$\mathbf{f}_R = (\mathbf{f}_1 - \mathbf{f}_2) - ((\mathbf{f}_1 - \mathbf{f}_2)\mathbf{N})\mathbf{N} \quad (10.1)$$

and aims at bringing its orientation \mathbf{N} into maximum coincidence with the lowest curvature mode of the system, thus approximating the imaginary mode to follow uphill.

Several approaches for minimization of \mathbf{f}_R have been proposed, ranging from direct minimization through LBFGS[312], the constrained Broyden method[313], or direct inversion in the iterative subspace (DIIS)[314], to rotations based on a Fourier series expansion of the curvature C . [290] The curvature is calculated numerically as

$$C = \frac{(\mathbf{f}_2 - \mathbf{f}_1)\mathbf{N}}{2\Delta\mathbf{R}}. \quad (10.2)$$

Dimer translation moves it closer towards the TS. Similar to climbing images in COS optimizations, a modified force \mathbf{f}^\dagger is employed: In the convex region of positive curvature ($C > 0$), the dimer is translated using only the reversed force component along \mathbf{N} , whereas in regions of negative curvature ($C < 0$) the perpendicular component of \mathbf{f}_0 is minimized simultaneously.

$$\mathbf{f}^\dagger = \begin{cases} -(\mathbf{f}_0^\top \mathbf{N})\mathbf{N} & C > 0 \\ \mathbf{f}_0 - 2(\mathbf{f}_0^\top \mathbf{N})\mathbf{N} & C < 0 \end{cases} \quad (10.3)$$

While Hessian-based TS-optimizers require only one gradient evaluation per optimization cycle, multiple evaluations are needed for the DM, as repeated rotations may be necessary. Kästner reported an average of 2.81 gradient calculations per dimer cycle for converging the Baker-TS benchmark set.[312, 315] Depending on the system, increased costs of additional gradient evaluations may be offset by not having to calculate the Hessian. In a comparison between PRFO and DM,[290] Heyden et al. determined the DM to be computationally more efficient for systems consisting of $1.5X$ atoms, when the exact Hessian is calculated every X cycles in the PRFO method.¹

¹If the Hessian is calculated every 10th cycle, the DM becomes more efficient than PRFO for molecules with ≥ 15 atoms.[290]

11 Intrinsic Reaction Coordinate

Given a successfully optimized TS, it may not be obvious which reactants it connects on the PES, e.g., just by examining the imaginary mode, or when the optimized TS is quite different from the initial guess structure. Actually connected reactants can be obtained by integrating a MEP, originating from the TS.

An uniquely defined MEP is the IRC,[316] the path of steepest descent in mass-weighted coordinates \mathbf{x} , along reaction coordinate s :

$$\frac{d\mathbf{x}(s)}{ds} = -\frac{\mathbf{g}(\mathbf{x})}{|\mathbf{g}(\mathbf{x})|}. \quad (11.1)$$

Starting at the educts with $s = -\infty$, the reaction coordinate s passes the TS at $s = 0$ and becomes $s = +\infty$ for the products. Calculating an IRC can also be regarded as integrating Newton's equations of motion with fully damped kinetic energy, yielding an infinitely slow moving, imaginary minimum energy trajectory.[317] The resulting IRC does not exhibit any complicated rotational or vibrational motions and is easily interpreted.[69, 318] As the kinetic energy is fully neglected, dynamical effects like PES-bifurcations are not captured by an IRC,[318, 319] although multiple techniques have been developed to capture such events along an IRC.[320–322]

The TS is a stationary point with vanishing gradient, therefore eq. (11.1) cannot be used to define a direction of steepest descent at the TS. An initial step towards a geometry with non-vanishing gradient is done by displacing the TS along its imaginary mode (transition vector) by a prescribed length Δx . Alternatively, Δx can be calculated from a quadratic potential, by requiring a certain energy lowering ΔE (e.g. $5 \times 10^{-4} E_h$)

$$\Delta E = \frac{1}{2}q\Delta x^2, \quad (11.2)$$

with q being the force constant of the transition vector.

Parts of this chapter are based on:

Steinmetzer, J.; Kupfer, S.; Gräfe, S. pysisyphus: Exploring potential energy surfaces in ground and excited states. *International Journal of Quantum Chemistry* **2020**, *121*, DOI: 10.1002/qua.26390

Open Access publication, licensed under Creative Commons - Attribution 4.0 International (CC BY 4.0).

Eq. (11.1) is a stiff differential equation (see chapter 7), making its accurate integration difficult.[323–325] Algorithms to solve eq. (11.1) can be broadly categorized in explicit and implicit methods. Explicit methods require only evaluation of quantities (e.g. energy and gradient) at the initial point, whereas implicit methods also require quantities evaluated at intermediate points of the integration.[325] The simplest explicit scheme is the Euler method

$$\mathbf{x}_{k+1} = \mathbf{x}_k - \alpha \mathbf{g} . \quad (11.3)$$

For stiff problems, the Euler method allows only small integration lengths, before the accuracy degrades. Implicit methods allow for greater integration step lengths at increased computational costs, as multiple energy and gradient evaluations are needed in every IRC cycle.[326, 327] Two examples for implicit methods will be briefly discussed in the following. Historical surveys of different integration algorithms are given by Melissas, Deng and Gonzalez,[328–330] while a more recent overview is presented by Maeda.[318]

11.1 Gonzalez-Schlegel 2nd-Order Algorithm

A widely implemented IRC integrator, utilizing Hessian information and sustaining longer step lengths was proposed by Gonzalez and Schlegel.[83, 331] Starting at point \mathbf{x}_k , a half-step of length $\frac{1}{2}\Delta s$ is taken against the gradient towards pivot point \mathbf{x}_{k+1}^*

$$\mathbf{x}_{k+1}^* = \mathbf{x}_k - \frac{1}{2}\Delta s \frac{\mathbf{g}_k}{|\mathbf{g}_k|} . \quad (11.4)$$

Subsequently, a constrained optimization is carried out on a hypersphere of radius $\frac{1}{2}\Delta s$, by minimizing the Lagrangian function

$$L(\lambda) = E'_{k+1} + \Delta \mathbf{x}'^\top \mathbf{g}'_{k+1} + \frac{1}{2}\Delta \mathbf{x}'^\top \mathbf{H}'_{k+1} \Delta \mathbf{x}' - \frac{1}{2}\lambda[\mathbf{p}'_k{}^\top \mathbf{p}'_k - (\frac{1}{2}\Delta s)^2] . \quad (11.5)$$

No energy and gradient evaluation is needed at the pivot point, but at the successive points on the hypersphere $\{\mathbf{x}'_{k+1}\}$. Primes indicate quantities evaluated on the hypersphere, \mathbf{p}'_k denotes a vector pointing from the pivot point towards \mathbf{x}'_{k+1} . See Figure 11.1 for an illustration. The Hessian is updated using BFGS.[235–238] Depending on the chosen step length, multiple additional energy and gradient evaluations are needed in every IRC cycle.

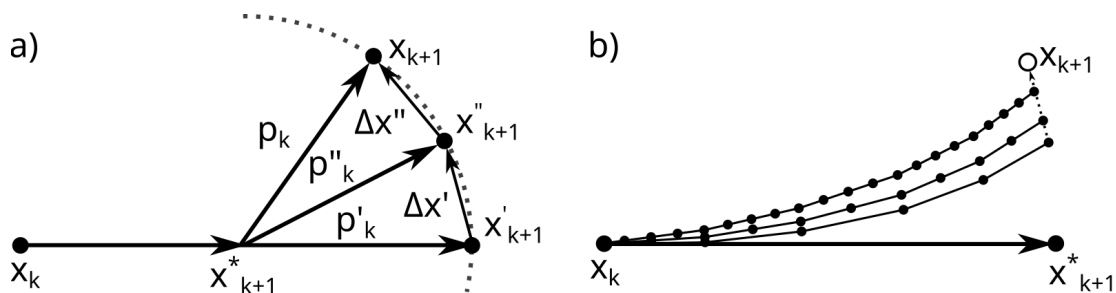


Figure 11.1: IRC step determination in the Gonzalez-Schlegel second-order algorithm (GS2) and Hessian predictor-corrector algorithms.[83, 325, 331–333] Large, filled circles indicate points, where energy and gradients are evaluated. a) Gonzalez-Schlegel 2: After an initial half step from \mathbf{x}_k to a pivot point \mathbf{x}_{k+1}^* , a constrained optimization is carried out on a hypersphere with radius $\frac{1}{2}\Delta s$, yielding the next point on the IRC \mathbf{x}_{k+1} . b) Hessian predictor-corrector integrator: After an initial predictor step to \mathbf{x}_{k+1}^* , an analytical surface is fitted by distance-weighted interpolants (DWIs) using energy, gradient and Hessian data. Multiple corrector integrations with decreasing step sizes are carried out on the DWIs surface and their results are combined using Richardson extrapolation, yielding the the next point on the IRC. In cycle k no energy and gradient evaluation is needed at \mathbf{x}_{k+1} .

11.2 Predictor-Corrector Integration

Expanding $\mathbf{g}(\mathbf{x})$ to first-order around \mathbf{x}_0 and substituting into eq. (11.1) yields

$$\frac{d\mathbf{x}(s)}{ds} = -\frac{\mathbf{g}(\mathbf{x}_0) + \mathbf{H}(\mathbf{x}_0)\Delta\mathbf{x}}{|\mathbf{g}(\mathbf{x}_0) + \mathbf{H}(\mathbf{x}_0)\Delta\mathbf{x}|}. \quad (11.6)$$

Introducing an independent variable t allows separation of eq. (11.6) into

$$\frac{d\mathbf{x}(t)}{dt} \frac{dt}{ds} = -(\mathbf{g}(\mathbf{x}_0) + \mathbf{H}(\mathbf{x}_0)\Delta\mathbf{x}) \cdot \frac{1}{|\mathbf{g}(\mathbf{x}_0) + \mathbf{H}(\mathbf{x}_0)\Delta\mathbf{x}|} \quad (11.7)$$

yielding the equations[325, 334, 335]

$$\frac{d\mathbf{x}}{dt} = -(\mathbf{g}(\mathbf{x}_0) + \mathbf{H}(\mathbf{x}_0)\Delta\mathbf{x}) \quad (11.8)$$

and

$$\frac{ds}{dt} = |\mathbf{g}(\mathbf{x}_0) + \mathbf{H}(\mathbf{x}_0)\Delta\mathbf{x}|. \quad (11.9)$$

11 Intrinsic Reaction Coordinate

For quadratic potentials, eq. (11.8) is solved by

$$\mathbf{x}(t) = \mathbf{x}_0 + \mathbf{A}(t)\mathbf{g}(\mathbf{x}_0) . \quad (11.10)$$

Matrix $\mathbf{A}(t)$ is defined as

$$\mathbf{A}(t) = \mathbf{U}_0\boldsymbol{\alpha}(t)\mathbf{U}_0^\top \quad (11.11)$$

with \mathbf{U}_0 being the eigenvector matrix of $\mathbf{H}(\mathbf{x}_0)$ and the diagonal matrix $\boldsymbol{\alpha}(t)$ with elements

$$\alpha_{ii} = \frac{e^{-\lambda_i t} - 1}{\lambda_i} , \quad (11.12)$$

where $\{\lambda_i\}$ are the eigenvalues of $\mathbf{H}(\mathbf{x}_0)$. Eq. (11.9) is integrated until a t is obtained that produces the desired step length $\Delta s = s - s_0$. The integration is carried out in the basis of the Hessian eigenvectors by the Euler method.

$$\frac{ds}{dt} = \sqrt{\sum_i \mathbf{g}'_{0i}{}^2 e^{-2\lambda_i t}} \quad (11.13)$$

Please see Appendix A.1 for a full derivation of eq. (11.13). An initial step size for the Euler integration is calculated as

$$\delta t = \frac{1}{N_{\text{Euler}}} \frac{s - s_0}{|\mathbf{g}(\mathbf{x}_0)|} , \quad (11.14)$$

with $N_{\text{Euler}} = 5000$. Given a suitable t , corresponding coordinates are obtained from eq. (11.10).

Based on eqs. (11.6) to (11.14), Hratchian proposed the Hessian predictor-corrector (HPC) method.[325, 336]

Starting from \mathbf{x}_k , an initial predictor step to \mathbf{x}_{k+1}^* is determined by the procedure just outlined and the gradient is evaluated. Subsequently, the predictor step is refined by modified Bulirsch-Stoer integration.[337–339]

As the corrector integration requires many energy and gradient evaluations, actual electronic structure calculations would be too costly. Instead, corrector integrations are carried out, using an analytical DWI surface, obtained from energies and derivatives at \mathbf{x}_k and \mathbf{x}_{k+1}^* .[340–344]

The DWI energy is defined as

$$E_{\text{DWI}} = \sum_i^N w_i T_i \quad (11.15)$$

with T_i being a Taylor expansion to second-order

$$T_i(\Delta \mathbf{x}_i) = E(\mathbf{x}_i) + \Delta \mathbf{x}_i^\top \mathbf{g}(\mathbf{x}_i) + \frac{1}{2} \Delta \mathbf{x}_i^\top \mathbf{H}(\mathbf{x}_i) \Delta \mathbf{x}_i, \quad (11.16)$$

and $\Delta \mathbf{x}_i = \mathbf{x} - \mathbf{x}_i$. Assuming $N = 2$, e.g., interpolation between two geometries, coordinate dependent weights w_1 and w_2 are given as

$$w_1(\mathbf{x}) = \frac{|\Delta \mathbf{x}_2|^n}{|\Delta \mathbf{x}_1|^n + |\Delta \mathbf{x}_2|^n}, \quad w_2(\mathbf{x}) = \frac{|\Delta \mathbf{x}_1|^n}{|\Delta \mathbf{x}_1|^n + |\Delta \mathbf{x}_2|^n}. \quad (11.17)$$

Integer n is commonly chosen as 4.[345] The DWI energy expression eq. (11.15) can be differentiated with respect to Cartesian coordinates, allowing fast energy and gradient calculations in $\mathcal{O}(N^2)$ operations. Explicit expressions for the gradient of E_{DWI} are given by Meisner.[346, 347]

The Bulirsch-Stoer method comprises repeated cycles of numerical integrations with decreasing step sizes and subsequent Richardson extrapolation to zero step size, until a prescribed extrapolation error is satisfied, e.g. $1 \times 10^{-6} a_0$. Given a function that returns the corrector integration endpoint \mathbf{x}_{k+1} for a given integration step size $\Delta s = \Delta s_0/2^j$, depending on integer j

$$R(j, 0) = \mathbf{x}_{k+1}(\Delta s_0/2^j), \quad (11.18)$$

an extrapolation table can be formulated (see Table 11.1).[348–350] Entries in the first

Table 11.1: Richardson extrapolation table for function $R(j, k)$. Entries in the first column $R(j, k = 0)$ are obtained by Euler integration on a DWI surface with step size $\Delta s = \Delta s_0/2^j$. All remaining entries $R(j, k > 0)$ can be calculated from the recursion defined in eq. (11.19).

$R(0, 0)$				
$R(1, 0)$	$R(1, 1)$			
$R(2, 0)$	$R(2, 1)$	$R(2, 2)$		
$R(3, 0)$	$R(3, 1)$	$R(3, 2)$	$R(3, 3)$	
...
$\mathcal{O}(\Delta s_0)$	$\mathcal{O}(\Delta s_0^2)$	$\mathcal{O}(\Delta s_0^3)$	$\mathcal{O}(\Delta s_0^4)$	

column ($k = 0$) are obtained by actual corrector integrations with decreasing step sizes. All remaining entries with $k > 0$ are obtained by extrapolation, based on the recursion

$$R(j, k) = \frac{2^k R(j, k-1) - R(j-1, k-1)}{2^k - 1} \quad (11.19)$$

and previously calculated values. See Figure 11.1 for an illustration of the step determination in the HPC method.

While modified-midpoint integration is employed in the original Bulirsch-Stoer method, it was found to magnify the stiff character of eq. (11.1).[325] Instead, Hratchian proposed to use simple Euler integration, resulting in a modified Bulirsch-Stoer method.[325] Additionally, the backward differentiation formula (BDF) and Radau IIA methods were found to be suitable corrector integrators.[3, 351, 352]

Determining the corrector step requires a $\mathcal{O}(N^3)$ -scaling Hessian diagonalization, which may become a computational bottleneck for large molecules. To this end, Hratchian also suggested the simplified Euler predictor-corrector (EulerPC) integrator,[332, 333] where the predictor step is obtained as

$$\mathbf{x}_{k+1}^* = \mathbf{x}_k - \Delta s \frac{\mathbf{g}_k}{|\mathbf{g}_k|} . \quad (11.20)$$

Alternatively, Hessian information can be considered in the predictor step by directly integrating

$$\frac{d\mathbf{x}}{ds} = - \frac{\mathbf{g}_0 + \Delta \mathbf{x} \mathbf{H}_0}{|\mathbf{g}_0 + \Delta \mathbf{x} \mathbf{H}_0|} , \quad (11.21)$$

while avoiding matrix diagonalization, which was already recognized by Page and McIver and pointed out again by Meisner.[335, 346] Compared to GS2, HPC and EulerPC only need two energy and gradient evaluations per IRC cycle.

Part III

Results

12 Biaryl Cross-Coupling

12.1 Introduction

Biaryl motifs play a key role in many pharmaceutical compounds[353] like antihypertensive sartans[354], non-steroidal anti-inflammatory drugs[355, 356], natural products[357] like cannabino[358] and many alkaloids.[359–361]. Selective cross-coupling of aryl-residues is usually achieved by employing transition metal catalysts.[362–369] As transition metal catalysts are often toxic and expensive, metal-free aryl cross-coupling reactions have been proposed, as more sustainable alternatives.[370–379]

Recently, Kloss reported a novel metal-free cross-coupling reaction, where two phenyl groups tethered by a sulfonamide linker can be fused with high regio- and chemoselectivity in a single coupling product through irradiation by ultraviolet light.[2, 125]

This chapter presents computational insights and suggests an ES reaction mechanism for the biaryl cross-coupling reaction. Computational investigations were carried out for two substrates: **1a**, a *p*-methyl carboxylate substituted biaryl-sulfonamide, affording good reaction yields and the unsubstituted reference biaryl-sulfonamide **1b**, for which only traces of the biphenyl photoproduct are detected (Figure 12.1).

For each substrate a conformer search was conducted, to identify important GS conformations. Subsequently, GS TSs were obtained and the corresponding IRCs were integrated. ESs of both substrates were calculated and analyzed for several geometries along the IRC.

12.2 Computational Details

Ground state potential energy surfaces of **1a** and **1b** were sampled by means of relaxed scans and conformer analysis. All ground state DFT calculations were carried out, using

Parts of this chapter are based on:

Haensch, V. G.; Neuwirth, T.; **Steinmetzer, J.**; Kloss, F.; Beckert, R.; Gräfe, S.; Kupfer, S.; Hertweck, C. Metal-Free Aryl Cross-Coupling Directed by Traceless Linkers. *Chemistry – A European Journal* **2019**, *25*, 16068–16073, DOI: 10.1002/chem.201903582

Open Access publication, licensed under Creative Commons - Attribution 4.0 International (CC BY 4.0).

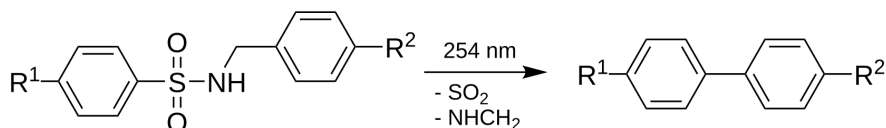


Figure 12.1: General scheme for the biaryl cross-coupling photoreaction, starting from biaryl-sulfonamides and yielding coupled biaryls, after irradiation at 254 nm (4.88 eV). Two substrates were investigated: **1a** ($R^1 = \text{Me}$, $R^2 = \text{COOMe}$) and the unsubstituted biaryl-sulfonamide **1b** ($R^1 = R^2 = \text{H}$), yielding the photoproducts **2a** and **2b**. The species NHCH_2 can hydrolyze to ammonia and formaldehyde.[125, 380]

the range-separated XC functional CAM-B3LYP[179] and the all-electron def2-TZVP triple- ζ basis set.[381] Dispersion interactions were taken into account by Grimme's D3-model with Becke-Johnson damping.[382, 383]

Relaxed scans were performed with Gaussian 16, Revision B.01[384] at the DFT level (CAM-B3LYP/def2-TZVP) by varying the central (C-N-S-C)-dihedral angle in the sulfonamide-linker from -180° to 180° with a step size of 10° , while equilibrating the remaining degrees of freedom at each step.

Possible conformers of the biaryl sulfonamide substrates were generated by a simulated annealing procedure, as implemented in Grimme's extended tight binding code GFN-XTB 5.8 using the GFN2-parametrization.[212] Effects of solvation by acetonitrile (ACN) on the conformer geometries were taken into account by the generalized Born solvent area (GBSA) continuum solvation model.[217]

Improved energies[385] for the conformers (generated by XTB) were calculated with domain based local pair-natural orbital (DLPNO) singles and doubles coupled cluster with triples correction (CCSD(T)), as implemented in ORCA 4.0.1.2.[386–388] The def2-QZVPP and corresponding auxiliary basis sets were utilized.[381, 389, 390] Solvent effects (ACN, $\epsilon = 36.6$, $n = 1.344$) on the coupled cluster single point energies were considered by the conductor-like polarizable continuum model (CPCM).[391, 392] Tight criteria were used for convergence and truncation thresholds in the DLPNO procedure (*TightPNO*, $T_{\text{CutPairs}} = 1 \times 10^{-5}$, $T_{\text{CutPNO}} = 1 \times 10^{-7}$, $T_{\text{CutMKN}} = 1 \times 10^{-4}$).[393]

To visualize the correlation between conformer bonding parameters and their coupled cluster energies, a principal component analysis (PCA) was conducted, using a set of eight primitive internal coordinates as features, describing the relative orientation of the two phenyl rings. All features were shifted to zero mean and scaled to unit variance. Conformers above a certain energy threshold (30.0 kJ mol^{-1} higher, than the minimum energy conformer, based on the DLPNO-CCSD(T) energies) were excluded from the

PCA. The PCA was carried out using the python package `scikit-learn`.^[394, 395] Care has to be taken when dealing with dihedrals, as they are periodic.¹ Dihedrals were correctly taken into account for the PCA by employing their sine and cosine values.^[396]

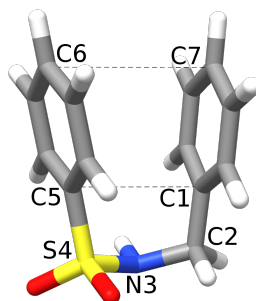


Figure 12.2: Atom labels, used for defining the internal coordinate features of the PCAs for the conformers of **1a** and **1b**.

Table 12.1: Employed internal coordinates in the PCA.

#	Coordinate type	Indices
1	Bond	C6 – C7
2	Bond	C5 – C1
3	Bend	C5 – S4 – N3
4	Bend	S4 – N3 – C2
5	Bend	N3 – C2 – C1
6	Bend	C5 – N3 – C2
7	cos(Dihedral)	C5 – S4 – N3 – C2
8	sin(Dihedral)	C5 – S4 – N3 – C2
9	cos(Dihedral)	S4 – N3 – C2 – C1
10	sin(Dihedral)	C5 – S4 – N3 – C2

Transition state optimizations, subsequent vibrational analysis, and reaction path calculations were carried out at the DFT level. The nature of the first-order saddle points was confirmed by vibrational analysis. Minimum energy paths were obtained by IRC integration using the HPC method,^[325, 336] as implemented in Gaussian, to verify that the optimized TSs connect the presumed educts and products of the biaryl coupling reaction. Exact Hessians were recalculated every seventh IRC step. Equally spaced geometries were sampled from both sides of the IRC every sixth step, yielding reaction paths for subsequent ES calculations.

¹Two dihedrals of 179° and -179° are nearly identical, even though their naively calculated (Euclidean) distance is big.

All ES calculations were carried out in Gaussian 16, using TD-DFT along the sampled IRC geometries. The same basis set and dispersion correction model as for the preliminary ground state DFT calculations was applied. This computational setup allows a balanced description of local, as well as of CT excitations among the π -systems of educt and product states.[397] Vertical excitation energies and oscillator strengths of the six lowest singlet ESs were calculated for the sampled geometries along the IRC. Solvent effects (ACN) on the vertical excitation energies and oscillator strengths were taken into account by the CPCM. Excited state characters were interpreted in terms of NTOs (see section 4.3), as calculated by Multiwfn 3.5.[227, 398] All calculations were carried out, assuming neutral charge and singlet multiplicity. If not noted otherwise, all orbital plots were created using an isovalue of 0.04 au.

12.3 Preferred Ground State Conformation

Molecules possess many different internal degrees of freedom. Rigid degrees, like the framework of (covalent) bonds, are not easily altered and stay close to their equilibrium values. Flexible degrees, like dihedrals, are altered more easily and may span a broad range of values, some of them far from equilibrium values, e.g., obtained at a stationary point.

This high flexibility can give rise to many different conformers, each one corresponding to a local minimum on the molecular PES. Naive calculation of full, $3N - 6(5)$ dimensional PESs and subsequent determination of all local minima is infeasible for all, except the smallest molecules. Efficient conformer search is a topic of ongoing research and to this date, many different methods have been proposed.[399–407]

Presence of multiple, energetically accessible and interconvertible conformers complicates computational studies, as their results may depend strongly on the studied conformers. Whereas determining energetically low-lying conformers may be feasible by one of the methods mentioned above, studying their interconversion is usually out of scope, as this would require $\sum_i^{N-1} i$ additional TS optimizations, for N conformers.

In the present study, energetically low-lying conformers of **1a** and **1b** have been obtained by means of simulated annealing and were interpreted in terms of corrected energies from coupled cluster calculations and PCA (see section 12.2).

1a

Simulated annealing conformer search yielded 38 geometries for the educt **1a**, 34 remained below 30.0 kJ mol^{-1} above the minimum energy conformer (see Figure 12.3 and Figure 12.5). Two conformer motifs could be identified: linear conformers with increased C1 – C5 distances (e.g. Figure 12.3e) and horseshoe conformers featuring decreased C5 – C1 distances and (nearly) parallel phenyl rings (e.g. Figure 12.3a) facing each other.

The minimum energy geometry for **1a** (conformer 2) belongs to the horseshoe motif with a C5 – C1 distance of 310 pm. In typical linear conformers, e.g., conformer 19, the C5 – C1 distance is about 500 pm. Small C5 – C1 distances are expected to facilitate the bond formation, between these two carbon atoms.

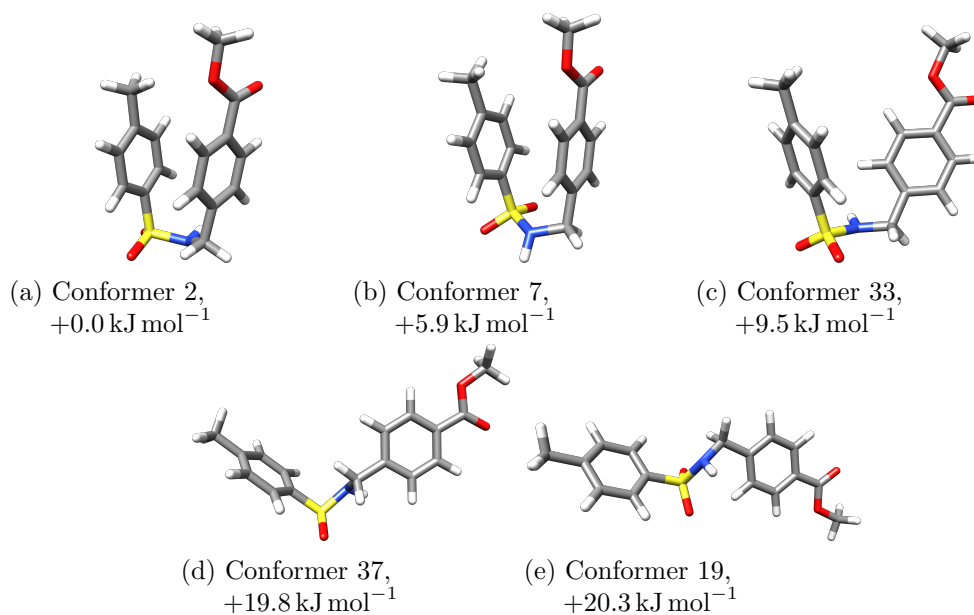


Figure 12.3: Selected **1a** conformers and energies obtained at the DLPNO-CCSD(T)/def2-QZVPP/CPCM(ACN) level of theory, with respect to minimum energy at conformer 2.

PCA results for **1a** are shown in Figure 12.5. The first two principal components PC1 and PC2 capture 54.7% of the total variance. PC1 corresponds mainly to reduced C – C distances in both, C6 – C7 (-0.49) and C5 – C1 (-0.52) (see Table 12.2), allowing to distinguish between linear (negative PC1 contribution, increased distances) and horseshoe motifs (positive PC1 contribution, decreased distances). Similarly, decreases of the angle C5 – N3 – C2 (-0.52) contribute to PC1. Indeed, conformers 1 to 7, 12 and 33 in Figure 12.5 with strong positive contributions of PC1 correspond to the horseshoe motif,

while conformers 19 and 16 with strong negative contributions of PC1 correspond to the linear motif (see also Figure 12.3). A more detailed depiction of conformers 2 and 19 including values of selected internal coordinates is found in Figure 12.4.

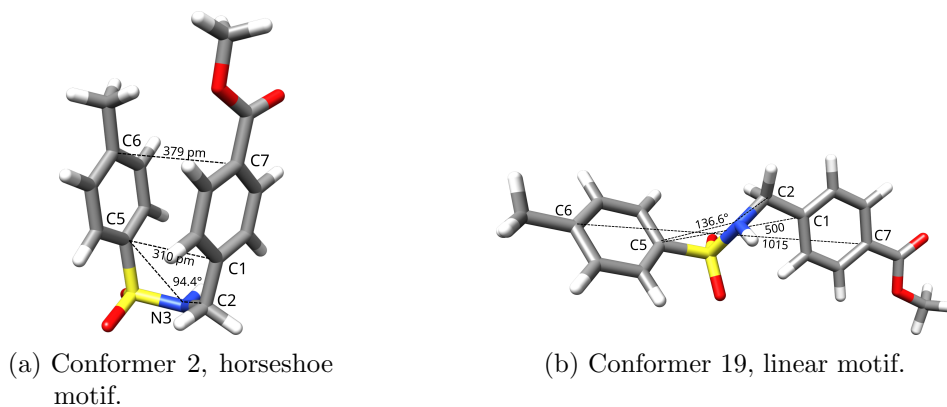


Figure 12.4: Detailed display of prototypical horseshoe and linear motifs for **1a**, including structural parameters that make up the first principal component PC1 (C5 – C1, C6 – C7 and C5 – N3 – C2). The units in conformer 19 (pm) have been omitted for clarity.

Table 12.2: First two principal components PC1 and PC2 in terms of scaled and shifted internal coordinates for conformers of **1a** and **1b**.

#	Coordinate	1a		1b	
		PC1	PC2	PC1	PC2
1	C6 – C7	–0.49	–0.08	–0.44	–0.01
2	C5 – C1	–0.52	–0.07	–0.49	–0.04
3	C5 – S4 – N3	–0.03	0.52	–0.05	0.56
4	S4 – N3 – C2	–0.06	0.48	–0.07	0.53
5	N3 – C2 – C1	0.29	–0.20	0.39	–0.03
6	C5 – N3 – C2	–0.52	–0.04	–0.49	–0.03
7	cos(C5 – S4 – N3 – C2)	0.21	0.50	0.17	–0.03
8	sin(C5 – S4 – N3 – C2)	–0.05	–0.11	–0.08	–0.43
9	cos(S4 – N3 – C2 – C1)	0.26	–0.40	0.34	0.21
10	sin(C5 – S4 – N3 – C2)	–0.10	–0.15	0.15	–0.42

1b

Simulated annealing conformer search yielded 17 geometries for **1b** that can similarly be assigned to either linear or horseshoe motifs. In contrast to **1a**, the minimum energy

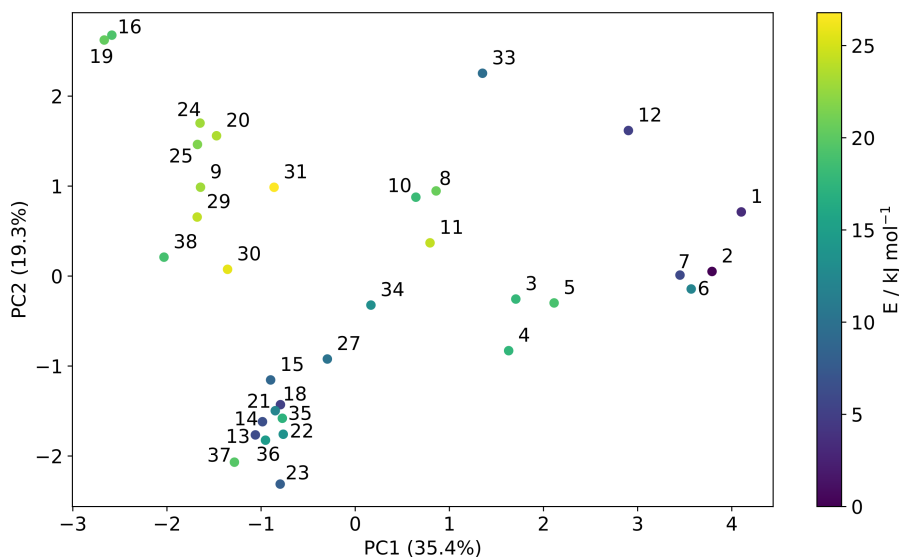


Figure 12.5: Scatter plot of DLPNO-CCSD(T)/def2-QZVPP/CPCM(ACN) energies for the first two principal components (PC1, PC2), obtained from a PCA on a subset of primitive internal coordinates of **1a**. All energies are given with respect to the minimum energy at conformer 2. The first principal component PC1 allows distinguishing between horseshoe and linear motif. Conformers 33, 12, 2, 1, 7, and 6 exhibit a horseshoe motif, whereas conformers 19, 16, 25, and 29 belong to the linear motif.

geometry is linear for **1b** (conformer 8) with a high C5 – C1 distance of 471 pm. Horseshoe conformers have slightly higher energies: +4.6 kJ mol^{-1} for conformer 1 and +8.0 kJ mol^{-1} for conformer 4 (see Figure 12.7 and Figure 12.6).

By considering the first two principal components PC1 and PC2, 58.2% of the total variance is captured. As expected, this is slightly more compared with **1a**, as **1b** has overall fewer degrees of freedom. The analysis of the **1a** PCA also applies to the **1b** PCA, as PC1 and PC2 are very similar in both cases (see Table 12.2). Notably, as the minimum conformer 8 does not belong to the horseshoe motif, contribution of PC1 is negligible (Figure 12.7).

12 Biaryl Cross-Coupling

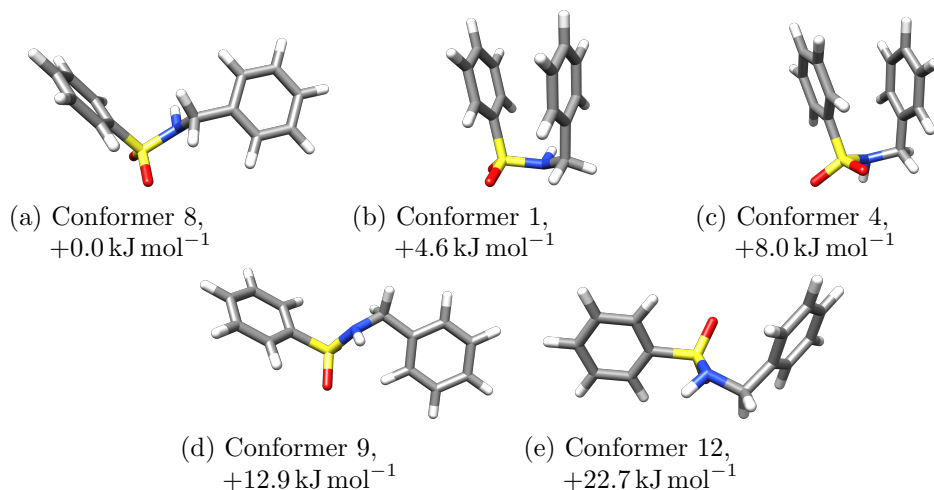


Figure 12.6: Selected **1b** conformers and energies obtained at the DLPNO-CCSD(T)/def2-QZVPP/CPCM(ACN) level of theory with respect to minimum energy conformer 8.

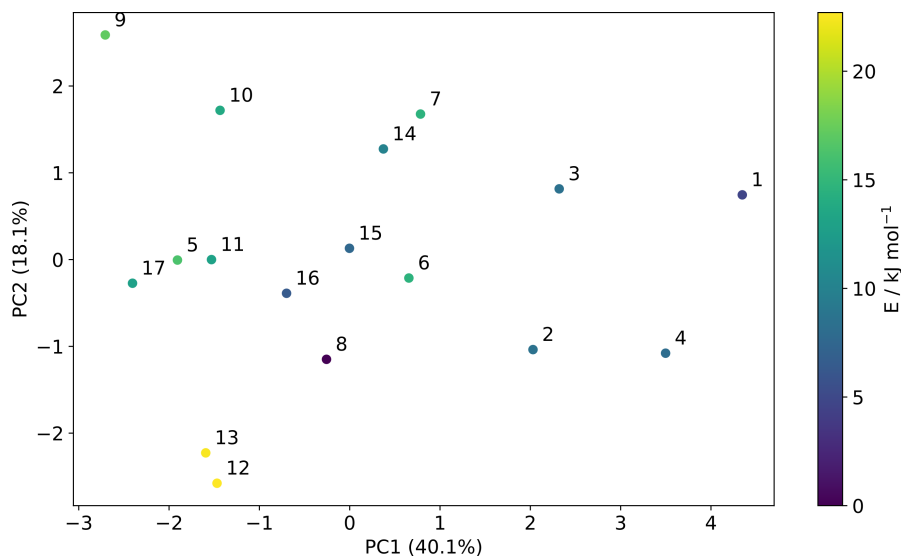


Figure 12.7: Scatter plot of DLPNO-CCSD(T)/def2-QZVPP/CPCM(ACN) energies for the first two principal components (PC1, PC2) obtained from a PCA on a subset of primitive internal coordinates of **1b**. All energies are given with respect to the minimum energy at conformer 8. The first principal component PC1 allows distinguishing between horseshoe and linear motif. Conformers 1–4 exhibit a horseshoe motif, whereas conformers 9, 12, 13, and 17 belong to the linear motif.

In summary, the conformer search results for **1a** and **1b** give a first hint on the different photoreaction yields. The minimum energy conformer **2** for **1a** belongs to the horseshoe motif, exhibiting a small C5 – C1 distance (310 pm), which facilitates efficient C – C bond formation. However, the minimum energy conformer **8** for **1b** belongs to the linear motif exhibiting an increased C5 – C1 distance (471 pm), hindering efficient bond formation in the photoreaction, while its lowest horseshoe conformer was predicted at slightly higher energy (4.4 kJ mol⁻¹).

Relaxed Scan Around the Central Dihedral Angle

Additionally, the GS PES of **1a** and **1b** were sampled by relaxed scans around the central dihedral angle $\phi(\text{C5} - \text{S4} - \text{N3} - \text{C2})$ at the DFT (CAM-B3LYP/def2-TZVP) level of theory.

For **1a**, results from the relaxed scan are in line with the conformer search. Both approaches predict a horseshoe conformer as minimum energy geometry (see Figure 12.8). The horseshoe conformer at $\phi = -80^\circ$ exhibits a small C5 – C1 distance of only 326 pm and is 10 kJ mol⁻¹ more stable, compared to the linear conformer at $\phi = 70^\circ$, with an increased C5 – C1 distance of 480 pm.

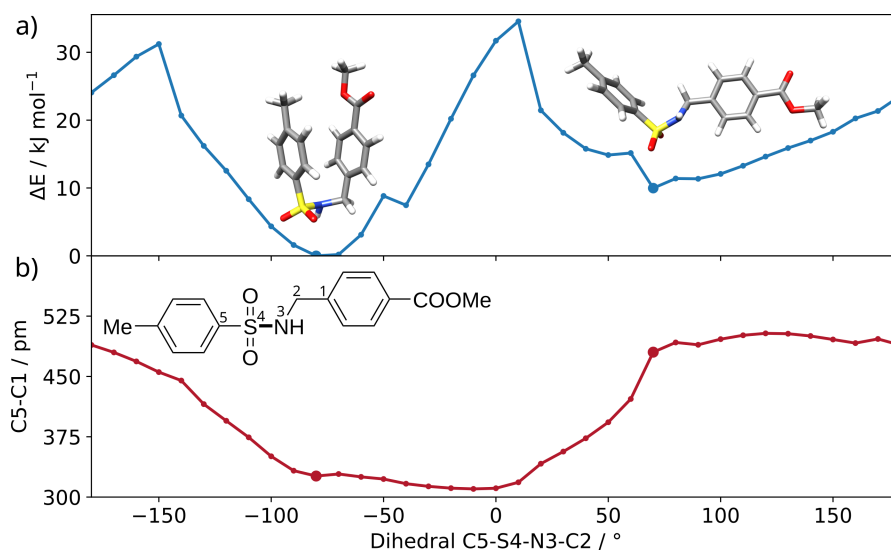


Figure 12.8: Energy differences and C5 – C1 distances for the relaxed scan around the central dihedral (C5 – S4 – N3 – C2) in **1a** at the CAM-B3LYP/def2-TZVP level of theory. A horseshoe conformer is predicted as minimum energy geometry at a) $\phi = -80^\circ$ with b) a C5 – C1 distance of 326 pm. The second marked minimum corresponds to a linear conformer with increased C5 – C1 distance.

In contrast to the conformer search, the relaxed scan predicts a horseshoe conformer as minimum for **1b**, but it is only 5.2 kJ mol^{-1} more stable, compared to the linear conformer at $\phi = 70^\circ$ (see Figure A.1).

Overall, sampling the GS PES of **1a** and **1b** revealed two distinct, structural motifs: horseshoe conformations with shorter C5 – C1 distances, pivotal for efficient bond formation and linear conformations with increased C5 – C1 distances, rendering efficient bond formation unlikely.

12.4 Ground State Reaction Coordinate and Electronic Structure

To evaluate the potential course of the biaryl coupling, formation of photoproducts **2a** and **2b** (fig. 12.1) was assessed along a GS IRC, obtained at the CAM-B3LYP/def2-TZVP/CPCM(ACN) level of theory. The IRC connects educt and product states via a cyclic (C1 – C2 – N3 – S4 – C5)-containing TS (see Figure 12.9a).

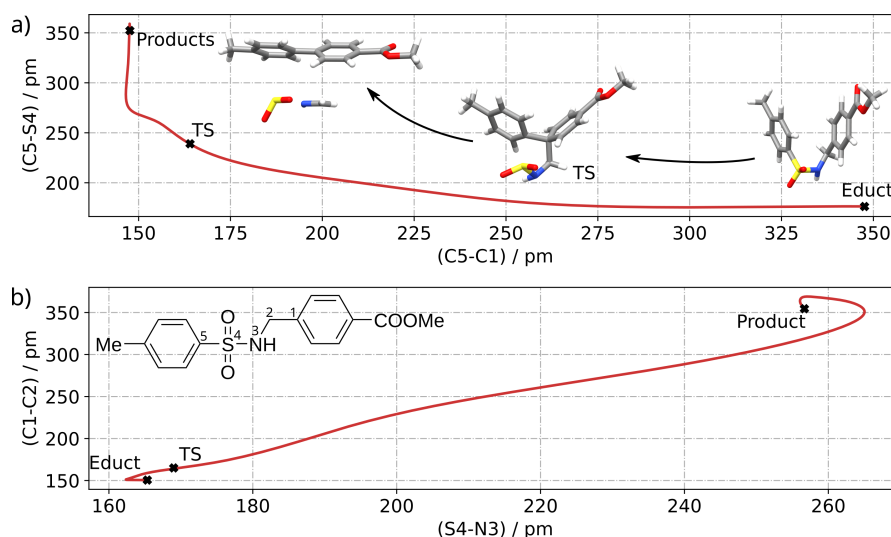


Figure 12.9: Selected distances along the IRC, describing the formation of **2a** from **1a** by photosplicing, obtained at the CAM-B3LYP/def2-TZVP/CPCM(ACN) level of theory. a) Atomic distances with significant changes when going from the educt to the TS and b) distances that change significantly in the second IRC half, when going from TS to the photoproducts.

Towards the five-membered TS of the reaction from **1a** to **2a**, the C5 – C1 distance decreases from 348 pm to 164 pm, which is associated with C5 – C1 bond formation.

Simultaneously, partial cleavage of the C5 – S4 bond is indicated by a distance increase from 176 pm to 239 pm (see Figure 12.9). In stark contrast, changes within the sulfonamide linker are less pronounced until the TS is reached. Only on relaxation towards the product state and thus formation of photoproduct **2a** increased S4 – N3 (169 pm to 257 pm) as well as C1 – C2 distances (165 pm to 355 pm) are observed, indicating extrusion of SO₂ and NHCH₂. The latter species can hydrolyze to ammonia and formaldehyde.[125, 380]

Similar results are obtained for the formation of **2b** from **1b**, which are omitted here (see Figure A.2 on page 138). Selected atomic distances for educts, TSs and products of both photoreactions are given in Table 12.3.

Table 12.3: Selected distances in educts, transition states and products in the biaryl coupling reactions of **1a** and **1b** in pm. While the C5 – C1 bond is formed along the IRC, the remaining bonds are broken.

Bond	Change	1a			1b		
		Educt	TS	Products	Educt	TS	Products
		Distance / pm			Distance / pm		
C5 – C1	formed	348	164	148	340	170	148
C5 – S4	broken	176	239	352	177	241	354
S4 – N3	broken	165	169	257	164	170	256
C1 – C2	broken	150	165	355	151	163	347

According to the calculations, TS-formation requires an activation energy of 4.08 eV in the GS for **1a**, and 4.07 eV for **1b**. Irradiation of the biaryl sulfonamides is carried out at 254 nm (4.88 eV), energetically well above the obtained GS barrier heights of about 4.0 eV. Even though the barriers are presumably not crossed in the electronic GS, but in an ES, the obtained pathways are consistent with the experimental conditions and energetically feasible, as the GSs barrier heights are below the irradiation energy.

The electronic structure of the biaryl sulfonamides is briefly discussed, at the example of a **1a** horseshoe conformer. Its frontier MOs (HOMO–3 to LUMO+3) have mainly π and π^* character (see Figure 12.12) and are expected to be major contributors, to the low-lying ESs of **1a**. Whereas, the orbital lobes at C5 and C1 in the HOMO of **1a** have opposite signs and thus, are antibonding, the C5 – C1 interaction is bonding in the LUMO. A simplified scheme is shown in Figure 12.11. All investigated biaryl sulfonamides have high HOMO-LUMO gaps of about 8.0 eV. In contrast to **1b**, the conjugated π -system in **1a** is extended by a methyl carboxylate residue, nearly coplanar to the connected phenyl

ring (rotated by 2.3°). Extending π -systems is known to modulate excitation energies and oscillator strengths, usually resulting in redshifted and brighter excitations.[408–412]

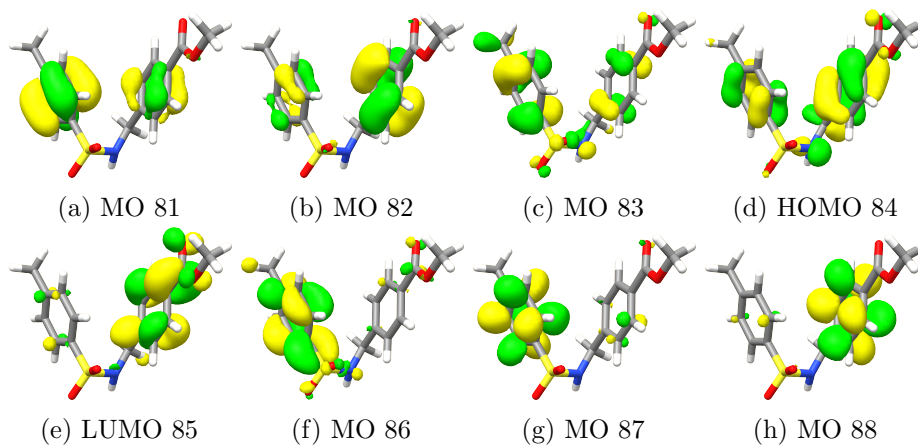


Figure 12.10: Isocontour plots of the frontier MOs of **1a** obtained at the CAM-B3LYP/def2-TZVP/CPCM(ACN) level of theory.

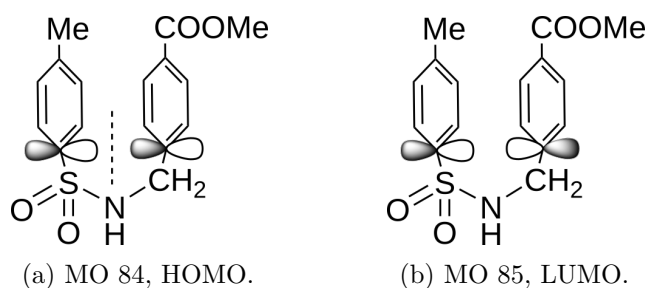


Figure 12.11: Simplified illustration of the orbital lobes centered at C5 and C1 for HOMO and LUMO in **1a**. Whereas the interaction in the HOMO is antibonding, it is bonding in the LUMO. The nodal plane between C5 and C1 in the HOMO is indicated by a dashed line.

12.5 Excited State Reaction Mechanism

To elucidate a potential reaction mechanism, low-lying ESs in the Franck-Condon region of **1a** and **1b** were calculated. In the following, π -orbitals located on the S-linked phenyl residue are denoted by a S-subscript (π_S), and π -orbitals located on the CH_2 –NH-linked phenyl residue are denoted with a N-subscript (π_N).

The simulated absorption spectrum of **1a** (see Figure 12.13a and Table 12.4) shows several bright ESs in the vicinity of the irradiating light source centered at 4.88 eV

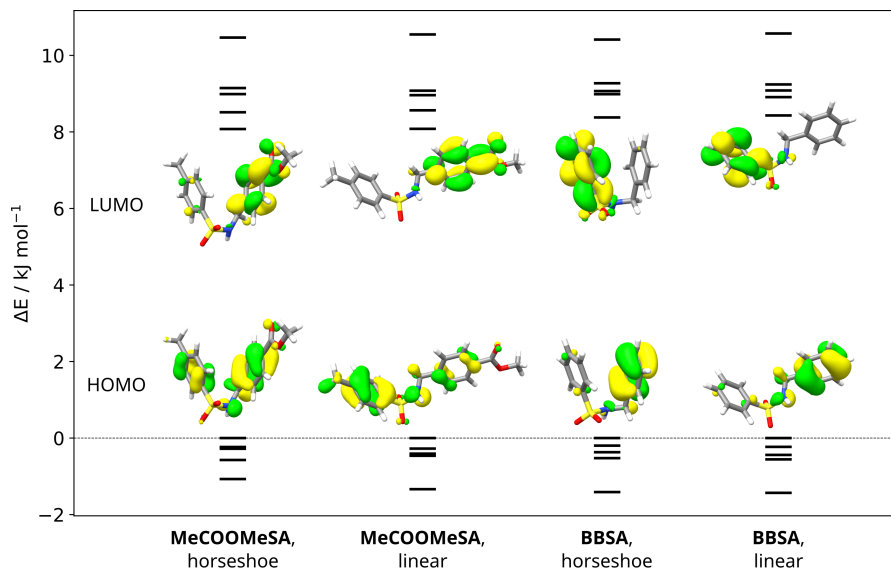


Figure 12.12: Energies and isocontour plots of the HOMO and LUMO for horseshoe and linear conformations of **1a** and **1b**, obtained at the CAM-B3LYP/def2-TZVP/CPCM(ACN) level of theory.

(254 nm) that is S_2 at 5.30 eV (234 nm, oscillator strength $f = 0.0664$) and S_3 at 5.40 eV (230 nm, $f = 0.3611$). In terms of NTOs, the S_3 is well described by one π_N/π_N^* NTO pair with a contribution of 70%. Considering the original MO basis, the biggest contribution (41%) to the S_3 arises from a HOMO-LUMO transition (MOs 84 and 85 in Figure 12.10), corresponding to depopulation of a C5 – C1 antibonding orbital and subsequent population of a C5 – C1 bonding orbital.

Similar ESs are obtained for **1b**, albeit hypsochromically blue-shifted and with lower oscillator strengths. Compared to the S_3 in **1a** at 5.30 eV, the similar S_4 in **1b** is found at 6.02 eV with a decreased oscillator strength $f = 0.0550$ (see Figure 12.13). It is well described by one NTO pair (74%) and corresponds to a transition from a π_N into a strongly C5 – C1 bonding π orbital. The brighter S_3 of **1b** at 5.81 eV with $f = 0.1169$ is also well captured by one π_S/π_S^* NTO pair (86% contribution). It is not expected to participate effectively in the photoreaction, as the transition density is constrained to the S-linked phenyl residue. Due to a mismatch between the energetic location of S_3 and S_4 with the available irradiation energy (centered at 4.88 eV), population of these ESs is unlikely. Therefore, disadvantageous ES properties at the Franck-Condon geometry of **1b** prevent an efficient photoreaction at 254 nm irradiation, which is in agreement with the experiment, as only traces of the photoproduct biphenyl are detected for **1b**.

Table 12.4: Calculated low-lying excited singlet states, excitation wavelengths (λ/nm), excitation energies ($\Delta E/\text{eV}$), oscillator strengths f and leading NTO pairs of **1a** for a horseshoe conformation at the educt side of the IRC, obtained at the CAM-B3LYP/def2-TZVP/CPCM(ACN) level of theory.

State	λ/nm	$\Delta E/\text{eV}$	f	NTOs	Weight / %
S_1	242	5.12	0.0157	$\pi_{\text{N}} \rightarrow \pi_{\text{N}}^*$	74
				$\pi_{\text{N}} \rightarrow \pi_{\text{N}}^*$	25
S_2	234	5.30	0.0664	$\pi_{\text{S}} \rightarrow \pi_{\text{S}}^*, \sigma_{\text{CC}}^*$	57
				$\pi_{\text{S}} \rightarrow \pi_{\text{S}}^*$	28
S_3	230	5.40	0.3611	$\pi_{\text{N}} \rightarrow \pi_{\text{N}}^*$	70
				$\pi_{\text{S}} \rightarrow \pi_{\text{S}}^*$	16
S_4	228	5.44	0.0158	$n_{\text{O}} \rightarrow \pi_{\text{N}}^*$	98
S_5	217	5.73	0.2116	$\pi_{\text{S}} \rightarrow \pi_{\text{S}}^*$	82
S_6	196	6.33	0.0444	$\pi_{\text{S}} \rightarrow \pi_{\text{N}}^*, \sigma_{\text{CC}}^*$	58
				$\pi_{\text{S}}, \pi_{\text{N}} \rightarrow \pi_{\text{S}}^*$	24

Analyzing the ESs of **1a** along the GS IRC (Figure 12.13) corroborates the results obtained at the Franck-Condon geometry. Product formation in the GS is prevented by a high barrier (4 eV) that is reduced to only 0.69 eV in the S_1 at 5.12 eV. Assuming a most likely initial population of the energetically higher lying, bright S_3 (5.40 eV) and subsequent adiabatic evolution, the barrier is further reduced to 0.41 eV,² allowing efficient product formation. The calculated excitation energy of the S_3 also coincides with the experimentally determined maximum substrate turnover at 5.32 eV (233 nm).[125]

Noteworthy, an even further reduced activation energy or even a barrier-free reaction is expected along a suitable excited state reaction pathway; however, determining such coordinate is far from trivial.

In contrast to **1a**, the ES barrier height in the S_1 of **1b** is slightly higher (0.77 eV). However, efficient photoreaction is already prevented by the hypsochromically shifted ESs and low oscillator strengths, as reflected by the photochemical experiment yielding merely traces of photoproduct **2b** at the applied conditions.

12.6 Summary

The computational results are in full accordance with the experimental observations and thus allowed elucidating the mechanism of photosplicing. Quantum chemical simulations show that electron-withdrawing and electron-donating groups are a prerequisite for the

² $\Delta E(S_1) + \text{ES barrier height} - \Delta E(S_3) = 5.12 \text{ eV} + 0.69 \text{ eV} - 5.40 \text{ eV} = 0.41 \text{ eV}$

Table 12.5: Calculated low-lying excited singlet states, excitation wavelengths (λ/nm), excitation energies ($\Delta E/\text{eV}$), oscillator strengths f and leading NTO pairs of **1b** for a horseshoe conformation at the educt side of the IRC, obtained at the CAM-B3LYP/def2-TZVP/CPCM(ACN) level of theory.

State	λ/nm	$\Delta E/\text{eV}$	f	NTOs	Weight / %
S_1	231	5.38	0.0125	$\pi_S \rightarrow \pi_S^*$	67
				$\pi_S \rightarrow \pi_S^*$	33
S_2	227	5.47	0.0007	$\pi_N \rightarrow \pi_N^*$	52
				$\pi_N \rightarrow \pi_N^*$	48
S_3	213	5.81	0.1169	$\pi_S \rightarrow \pi_S^*$	86
S_4	206	6.02	0.0550	$\pi_N \rightarrow \pi_N^*, \pi_S^*, \sigma_{CC}^*$	74
				$\pi_N \rightarrow \pi_N^*$	19
S_5	200	6.19	0.0028	$\pi_N \rightarrow \pi_S^*$	87
S_6	195	6.37	0.0172	$\pi_N \rightarrow \pi_S^*$	94

photoreaction, because these substituents control the energy of the ESs and determine the overlap with the applied light source. The course of the photoreaction can be illustrated by means of the frontier orbitals of **1a** (Figure 12.11) contributing to S_3 . Specifically, the HOMO exhibits antibonding character between C5 and C1, whereas the LUMO shows bonding character between these two carbon atoms. The photoinduced population of the LUMO lowers the activation energy substantially and enables the photochemical formation of **2a**. The small energy gap (1.0 eV) between GS and ES S_1 in the vicinity of the TS facilitates the relaxation into the product state.

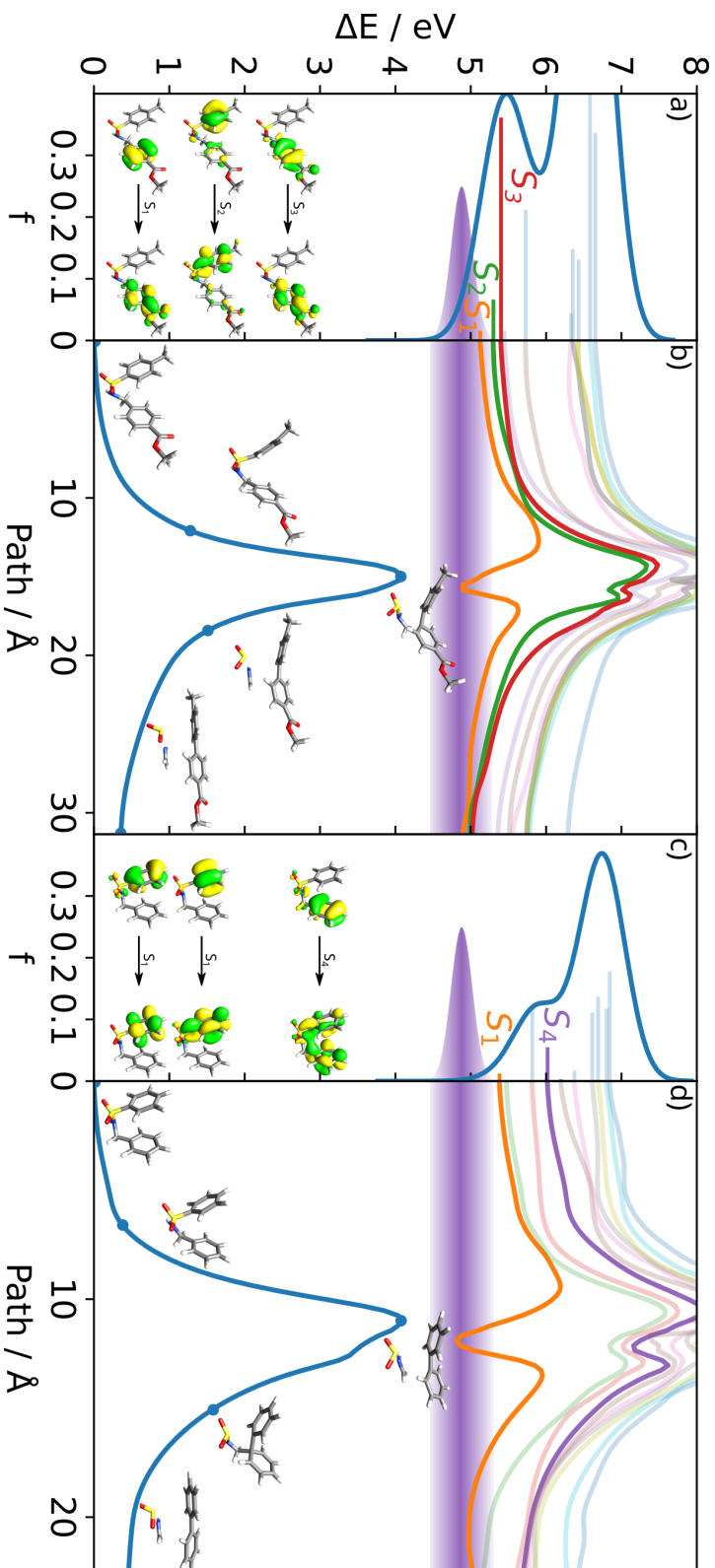


Figure 12.13: Calculated absorption spectrum at the Franck-Condon point (panels a and c), and energies of relevant electronic states for the photochemical reaction along the IRCs for **1a** and **1b** (panels b and d). Emission of the light source centered at 4.88 eV (254 nm) is highlighted purple. Higher lying and non-participating electronic states are shown with reduced opacity.

13 Pysisyphus

13.1 Introduction

This chapter discusses the implementation of pysisyphus, an external optimizer written in python,[413, 414] that also accounts for ESs. Pysisyphus allows localizing SPs in ground- and excited states, using surface-walking, COS methods and IRC calculations. Several algorithms for effective state-tracking are available. Although already several external optimizers with impressive functionalities like ASE or DL-FIND exist,[124, 415] none of them is tailored to the optimization of ESs. Only recently, García et al. presented their SDNTO[223] approach for localizing minima in ESs, but the program is restricted to a steepest descent optimizer and a rather limited selection of QC packages for ES gradient calculations, e.g., the programs ORCA and Gaussian.[121, 384]

The chapter is organized as follows: section 13.2 verifies the correct implementation of pysisyphus and analyzes its performance by optimizing several test sets. Pysisyphus' ES tracking capabilities are demonstrated exemplarily for ES optimizations of cytosin and three transition metal complexes in section 13.3. The process of obtaining full reaction paths starting from only educts and products is shown in section 13.4 exemplarily for a GS reaction coordinate. Section 13.5 gives the list of QC programs, interfaced by pysisyphus and contains a short comment on its general structure. Implementation of RIC is discussed briefly.

13.2 Benchmarks and Verification

Effectiveness and efficiency of a geometry optimizer depend strongly on the careful selection of employed algorithms and the tuning of many parameters. Considering only initial Hessian choice and subsequent Hessian update in pysisyphus (see Table 13.1),

Parts of this chapter are based on:

Steinmetzer, J.; Kupfer, S.; Gräfe, S. pysisyphus: Exploring potential energy surfaces in ground and excited states. *International Journal of Quantum Chemistry* **2020**, *121*, DOI: 10.1002/qua.26390

Open Access publication, licensed under Creative Commons - Attribution 4.0 International (CC BY 4.0).

already gives rise to $7 \cdot 8 = 56$ possible algorithmic combinations. Also including convergence accelerators, which are either enabled or disabled, yields a total of $2^3 \cdot 56 = 448$ possible combinations. If further important decisions, like coordinate system or initial, minimum and maximum trust radius are considered, scanning the full space of possible algorithm and parameter combinations quickly becomes infeasible. Therefore, only some appropriate combinations are usually tested.[245]

To this date, several molecular benchmark sets have been put forward, allowing unambiguous evaluation of optimizer performance and its specific implementation. The most frequently employed test set for ground state optimizations was proposed by Baker and comprises 30 small molecules, containing 3 to 29 atoms (Figure 13.1).[268] The intended level of theory is HF/STO-3G, although often different basis sets are employed.[159, 232, 241, 246, 416, 417]

Subsequently, Baker also released a test set for evaluating TS optimizers at the HF/3-21G level of theory.[315] It includes 25 geometries from 3 to 16 atoms, close to a TS geometry. Notably, two cases (10 and 11) start in the convex region of the PES and exhibit no imaginary frequencies at the given geometry.

Accompanying the test sets, Baker proposed the following convergence criteria: no gradient component greater than $3.0 \times 10^{-4} E_h \cdot a_0^{-1}$ (rad^{-1}) and either an energy difference, compared to the previous cycle, below $1.0 \times 10^{-6} E_h$, or no step component greater than $3.0 \times 10^{-4} a_0$ (rad).¹

In the following, correct implementation of pysisyphus and its performance for molecular and reaction path optimization is verified for several benchmark sets and compared, if possible, to established optimizers and literature data.

¹Using RIC usually results in different units for individual coordinates, e.g., lengths for stretches, and radians for angles (bends, dihedrals). Certain definitions for out-of-plane angles and linear bends even result in unitless coordinates.[276] Mixed units are denoted as a_0 (rad) in the present work.

Table 13.1: Possible keywords, controlling the behavior of the default optimizer for minimizations and TS searches in pysisyphus.

Keyword	Comment	Reference
Initial Hessian		
calc	Calculate exact Hessian. Expensive, not available always.	-
unit	Unit matrix.	-
simple	Fixed force constants: 0.5 for bonds, 0.2 for bends and 0.1 for dihedrals.	[232]
fischer	MH, parametrized against HF/6-31G**, <i>default</i> (see eqs. (5.13) to (5.15)).	[242]
lindh	MH, parametrized against HF/STO-3G.	[241]
swart	MH, similar to lindh.	[243]
xtb/xtb1	Calculation at GFN2/GFN1-xtb level of theory.	[418]
Hessian update		
bfgs	<i>Default</i> , see eq. (5.11).	[235–238]
damped_bfgs	Modifies gradient difference \mathbf{y} , when curvature condition is not satisfied ($s\mathbf{y} < 0$).	[234]
sr1	Suitable for TS-optimization.	[419]
psb	Suitable for TS-optimization.	[420]
bofill	Suitable for TS-optimization, combines SR1 and PSB.	[240]
flowchart	Switches between SR1, BFGS and PSB.	[239]
(hessian_recalc)	See calc, recalculation of exact Hessian every n -th cycle.	-
Convergence acceleration/stabilization		
gediis	<i>Disabled by default</i> .	[260]
gdiis	<i>Enabled by default</i> . At most 5 gradients are used as error vectors.	[258, 259]
line_search	Fitting of 1d quartic/cubic polynomials, <i>enabled by default</i> . Fallback if GDIIS/GEDIIS failed or disabled.	[75]

13.2.1 Baker Test Set

Aiming at determining most suitable default options for the pysisyphus optimizer, different choices for initial Hessian, its update, and convergence acceleration (Table 13.1) have been tested. A similar survey was already conducted by Bakken.[232]

Energies and gradients were obtained with ORCA 4.2.1 at the HF/STO-3G level of theory, enforcing tight self-consistent field (SCF) convergence criteria (keyword `tightscf`), to reduce numerical noise in the gradients.[388] Neutral charge and singlet multiplicity were assumed throughout. Optimizations were conducted by RFO in RIC. If the proposed RFO step exceeded a prescribed trust radius (initial value $0.5 a_0$ (rad), maximum value $1.0 a_0$ (rad)), it was scaled to the trust radius.

Table 13.2: Required cycles to converge Baker’s test set using pysisyphus, for different keyword choices (see Table 13.1). If not noted otherwise, the initial Hessian is calculated according to Fischer, updated by the BFGS formula and convergence is accelerated by partial line searches and GDIIS.

Initial Hessian		Cycles
fischer		207
lindh		212
simple		254
swart		228
Hessian update		Cycles
bfgs		207
damped_bfgs		207
flowchart		225
bofill		232
Convergence acceleration		
line_search	gdiis	Cycles
yes	yes	207
no	yes	208
no	no	208

Results of the initial survey are shown in Table 13.2. The smallest number of required cycles (207), to converge Baker’s test set at the HF/STO-3G level of theory, is achieved by combining Fischers model Hessian,[242] BFGS updating, partial line searches, and GDIIS.[75, 258, 259] In the following, this combination is referred to as the standard method.

Initial Hessian choice has the biggest influence on the number of cycles. The highest number of cycles (254) is obtained with a simple model Hessian, using fixed values of 0.5/0.2/0.1 for stretches, bends and dihedrals. Only 228 cycles are required with Swarts model Hessian.[243] Using Lindh's model Hessian yields results (212 cycles) close to the optimal choice (Fischer, 207 cycles).[241]

Whether the BFGS Hessian update is damped or not, has no influence for the Baker test set. Damping is only important when the curvature condition is violated, which is never the case for these well behaved optimizations. Using the flowchart update, which selects between SR1, BFGS and PSB updates, requires 225 cycles.[239] Bofills update, originally proposed for TS optimizations, needs even more cycles (232).

Disabling convergence accelerators like partial line searches and GDIIS, leaves the number of required cycles nearly unaffected, which is consistent with the findings of Bakken.[232] As the test set geometries are already close to a stationary point, the local quadratic expansion seems to approximate the true PES well and produces reasonable, hardly improvable steps. GDIIS is only activated, after the root mean square (RMS) of the step falls below $2.5 \times 10^{-3} a_0$ (rad), which usually happens quite late in the course of an optimization, so GDIIS is employed only a few times.[259] Enabling GEDIIS led to inferior results in many cases, even though it appears to be correctly implemented. It is disabled by default in pysisyphus.[260]

The number of 207 cycles in pysisyphus compares favorably to the original 240 cycles reported by Baker,[268] but is slightly higher than the 185 cycles reported by Fischer.[232] Bakken's result was obtained using a set of extra-redundant coordinates, which may lead to problems in the internal-Cartesian back-transformation (see section 6.3) of the optimization step, even though no such problems were reported by Bakken. Similar results are obtained when the bigger 6-31G* basis is employed. Bakken reported 198 cycles, whereas 215 cycles are needed in pysisyphus. Distributed over the whole test set, most optimizations differ only in one or two cycles. Recently, Raggi reported 262 cycles for Baker's test set using RFO, without any step size restriction at the HF/6-31G level of theory in OpenMolcas.[417, 421, 422] Using the same convergence criteria, pysisyphus needs only 209 cycles, showing a marked improvement. Especially, three cases converged slowly in Raggis work: histidine (case 27, 29 cycles), 2,3-dimethylpentane (case 28, 27 cycles) and menthone (case 30, 32 cycles). This highlights the fact that optimization performance is probably highly sensitive to numerous (implementation) details and can differ greatly from software to software, even for simple cases. The present implementation is also competitive with results reported by Meyer (232 cycles, Baker's convergence criteria), who used a novel Gaussian process regression approach and internal coordinates.[159]

Table 13.3: Optimization cycles, required to converge the Baker test set (Figure 13.1), according to Baker’s criteria (see section 13.2) for different basis sets.[268] Convergence to the correct geometry was ensured by comparing the final energy to the published values (only for STO-3G basis). Bakken’s results correspond to their most efficient method, using extra-redundant internal coordinates, as presented in Table X in [232]. Code to reproduce the results of this work is given in Listing A.1 on page 139.

#	Molecule	HF/STO-3G			HF/6-31G*	
		This work	Baker [268]	Bakken [232]	This work	Bakken [232]
1	Water	4	6	4	4	5
2	Ammonia	7	6	5	7	5
3	Ethane	4	5	3	4	4
4	Acetylene	4	6	4	4	4
5	Allene	4	5	4	5	5
6	Hydroxysulphane	7	8	7	8	6
7	Benzene	3	4	3	3	3
8	Methylamine	5	6	4	5	5
9	Ethanol	6	6	4	6	5
10	Acetone	6	6	4	6	4
11	Disilyl ether	10	8	8	14	11
12	1,3,5-Trisilacyclohexane	8	8	9	7	8
13	Benzaldehyde	6	6	4	7	5
14	1,3-Difluorobenzene	6	5	4	7	5
15	1,3,5-Trifluorobenzene	5	5	4	4	5
16	Neopentane	4	5	4	4	4
17	Furan	7	8	5	7	5
18	Naphthalene	6	5	5	6	5
19	1,5-Difluoronaphthalene	7	6	5	7	5
20	2-Hydroxybicyclopentane	10	15	9	11	9
21	ACHTAR10	8	12	8	9	9
22	ACANIL01	8	8	7	7	6
23	Benzidine	8	9	9	9	9
24	Pterin	9	10	8	8	9
25	Difuropyrazine	8	9	6	8	7
26	Mesityl oxide	6	7	5	6	5
27	Histidine	14	19	16	16	16
28	Dimethylpentane	10	12	9	8	9
29	Caffeine	7	12	6	7	7
30	Menthone	10	13	12	11	13
	Sum	207	240	185	215	198

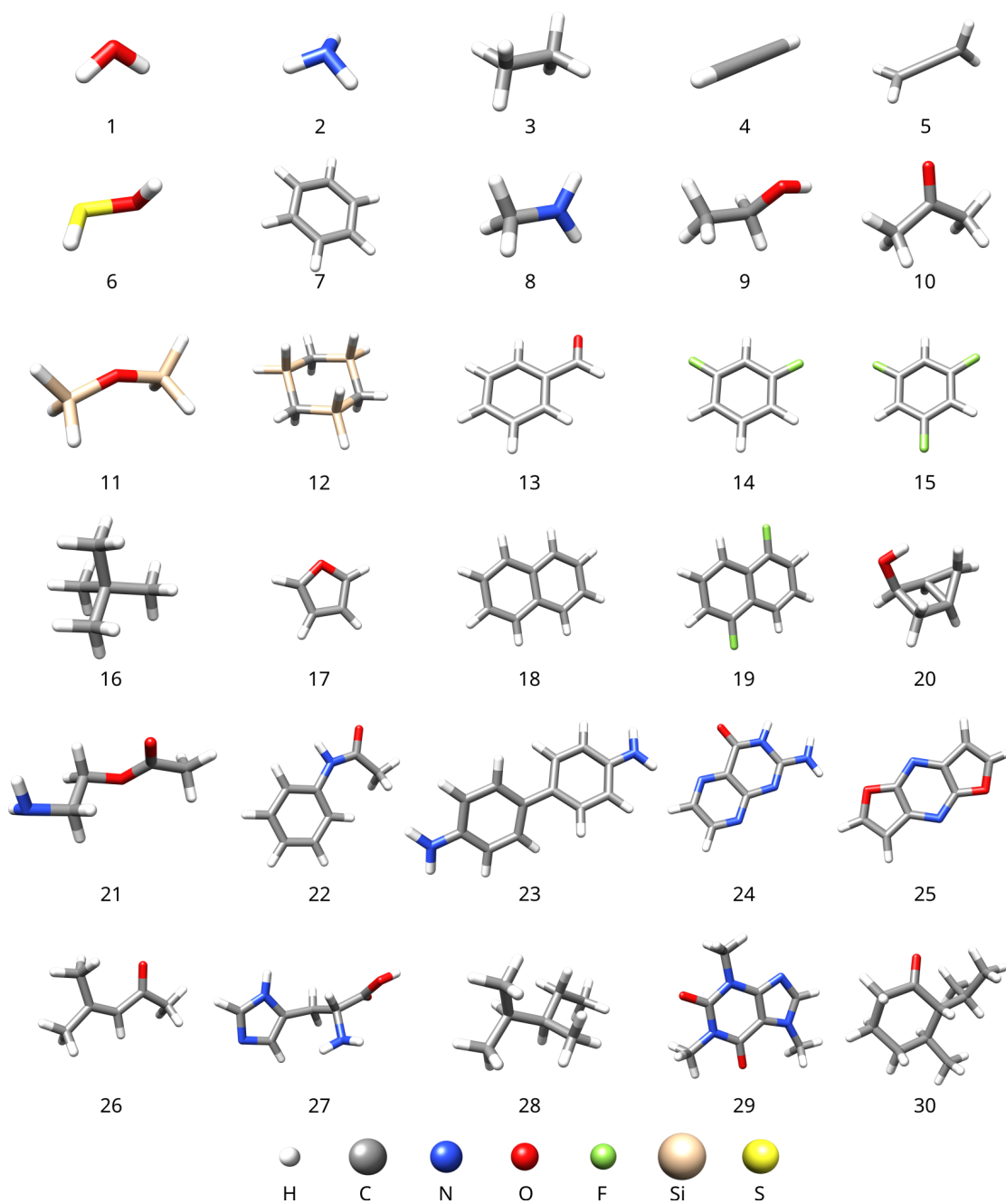


Figure 13.1: Initial geometries, contained in Baker's test set, comprising 30 small molecules.[268] A color code is given in the last row.

13.2.2 Hobzas S22 Test Set - Noncovalent Interactions

Compared to Baker's test set, the more challenging S22 set (Figure 13.2) was proposed by Hobza and coworkers.[423] Originally, it was compiled to provide reference energies at the Møller-Plesset perturbation theory (MP2) and CCSD(T) levels of theory in the complete basis set (CBS) limit, for benchmarking lower level computational methods.[424]

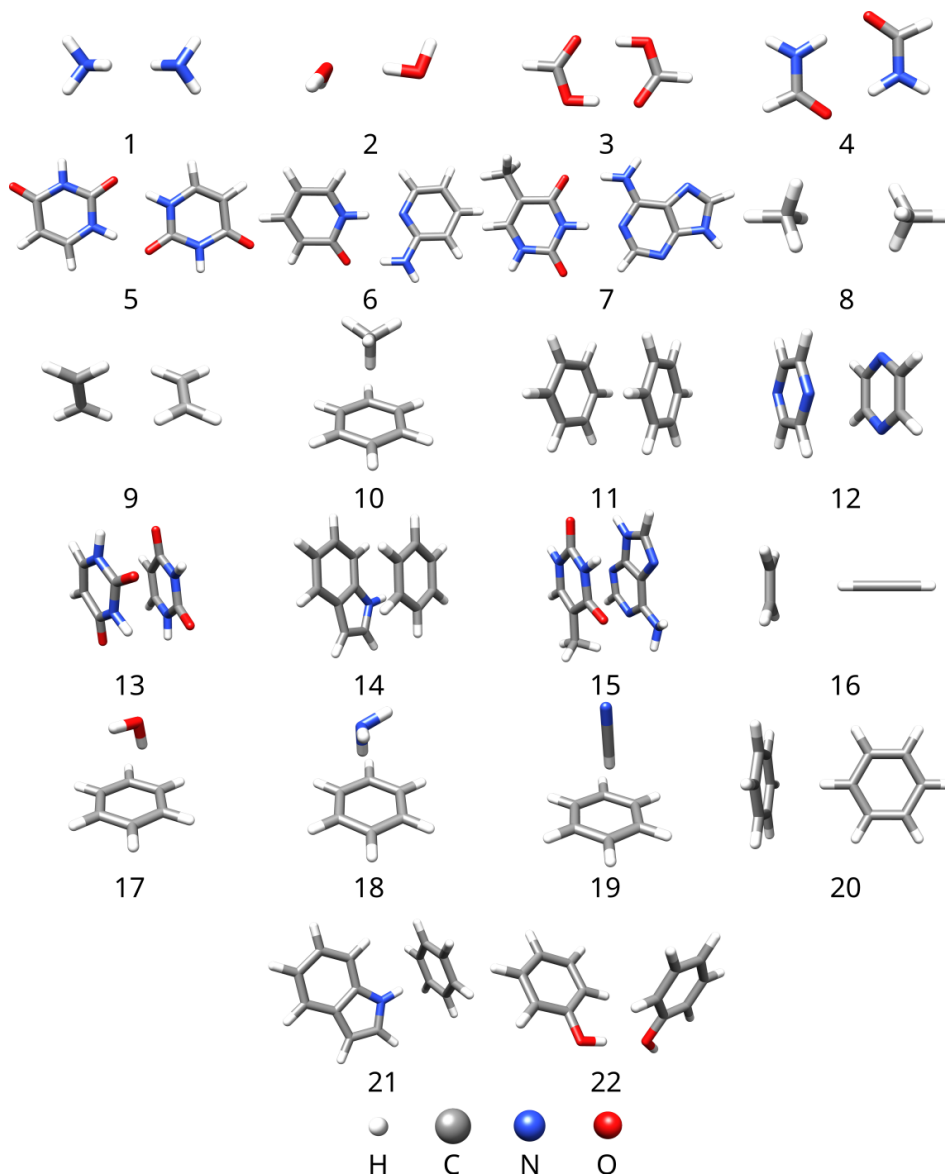


Figure 13.2: Initial geometries, contained in the S22 test set, comprising 22 dimers.[423]
A color code is given in the last row.

S22 comprises 22 small molecule dimers, dominated by hydrogen bonds and dispersion interactions, see Table 13.4. Such interactions give rise to very flat PESs that are often insufficiently described by simple quadratic approximations (eq. (5.2) and eq. (5.6) on page 31). As molecular optimizers are usually based on quadratic models, searching SPs on flat PESs is especially challenging. For this reason, optimizing the S22 set should be a better test of optimizer robustness, compared to Baker’s test set.[268]

Energies and gradients were obtained from ORCA 4.2.1 at the RI-MP2/6-31G** level of theory. [388, 425–429] As no correlation fitting basis, explicitly optimized for 6-31G** is available, the def2-SVP/C correlation fitting basis set was used instead.[430] Tight SCF convergence criteria were enforced (keyword `tightscf`), to reduce numerical noise in the gradients. Neutral charge and singlet multiplicity were assumed throughout. Optimizations were carried out with `pysisyphus`, using the standard method outlined in section 13.2.1. Initial geometries of the S22 set were taken from the original publication.[423]

Convergence was indicated when all absolute values of the gradient were equal or less than $4.5 \times 10^{-4} E_h \cdot a_0^{-1}$ (rad^{-1}), the RMS of the gradient was equal or less than $3.0 \times 10^{-4} E_h \cdot a_0^{-1}$ (rad^{-1}), all absolute values of the proposed step were equal or less than $1.8 \times 10^{-3} a_0$ (rad) and the RMS of the step was equal or less than $1.2 \times 10^{-3} a_0$ (rad). These thresholds conform to the defaults in the Gaussian program suite and will be denoted as Gaussian convergence criteria from now on.[384]

Results for the S22 set are given in Table 13.4 and compared to reference results published by Lindh.[417] Optimization success was judged according to the RMSD between the final geometries of this work and Lindh’s work. Some geometries in the latter work exhibit a different atom ordering with respect to the original geometries of Hobza employed in this work, therefore, complicating the RMSD calculation. Before the RMSD calculations, the atoms were automatically reordered using the Hungarian method, trying to bring both atom orderings into maximum coincidence.[431, 432] `Pysisyphus` implements the Hungarian method according to Allen and Wagner.[433, 434] Cases 2, 8, 9, 11, 17 and 18 exhibit high RMSD values ($> 0.1 a_0$, corresponding to > 5.3 pm), even after resorting. They were examined and aligned manually in the visualization system UCSF Chimera (Figure A.3).[435]

`Pysisyphus` obtains SPs for all cases of the S22 set. All geometries, beside case 17 (benzene · water dimer) are virtually indistinguishable from the reference geometries, as evident from small RMSDs ($\ll 0.1 a_0$) or perfect superposition in Figure A.3. The benzene · water dimer converged to a higher lying (0.2 kJ mol^{-1}) SP.[417] `Pysisyphus` required only 310 energy and gradient evaluations, whereas Lindh reported 358 evaluations. Without

case 17, pysisyphus required 260 evaluations, a marked improvement over Lindh’s 323 evaluations. Overall, pysisyphus shows a promising performance for the S22 test set, even though one case converged to an energetically, slightly higher lying SP.

Table 13.4: Number of optimization cycles required to converge the S22 test set (Figure 13.2) at the RI-MP2/6-31G** level of theory.[423] Lindh’s results are taken from the restricted step RFO (RS-RFO) column of Table 3 in [417]. Convergence to the correct geometry was ensured by calculating the RMSD with geometries published by Lindh.[417, 436] Code to reproduce the results of this work is given in Listing A.2 on page 140.

#	Molecule	This work	Lindh [268]	RMSD / a_0
Hydrogen bonded complexes				
1	ammonia dimer	5	5	0.0034
2	water dimer	13	6	1.0579 ^a
3	formic acid dimer	9	7	0.0045
4	formamide dimer	5	7	0.0090
5	uracil dimer	5	7	0.0105
6	2-pyridoxine · 2-aminopyridine	16	15	0.0097
7	adenine · thymine WC	6	18	0.0981
Dispersion dominated complexes				
8	methane dimer	7	20	1.4933 ^a
9	ethene dimer	3	5	2.8812 ^a
10	benzene · methane	4	4	0.0054
11	benzene dimer C _{2h}	9	7	0.1071 ^a
12	pyrazine dimer	10	8	0.0144
13	uracil dimer stack	18	24	0.0196
14	indole · benzene	44	61	0.0247
15	adenine · thymine stack	33	29	0.0177
Mixed complexes				
16	ethene · ethine	4	6	0.0077
17	benzene · water	50	35	0.1383 ^{a,b}
18	benzene · ammonia	17	33	0.7585 ^a
19	benzene · hydrogen cyanide	14	31	0.0245
20	benzene dimer C _{2v}	7	5	0.0218
21	indole · benzene, T-shape	12	4	0.0073
22	phenole dimer	19	21	0.0690
Sum		310	358	

^a Overlays of both geometries are given in Figure A.3 at page 138.

^b Converged to a higher lying SP

13.2.3 External Validation

The RFO implementation of pysisyphus was also employed by Ahuja et al., as one of multiple references, in an effort to benchmark a new reinforcement-learning-based optimization approach.[437] Starting from a set of perturbed organic molecules, they found their approach to be superior, requiring on average 94 cycles until convergence, whereas pysisyphus required 105. The next best optimizer (LBFGS) already required 129 cycles on average. In a second test set, pysisyphus seemed competitive with their new method, as it required the fewest cycles for 2 out of 12 cases, and the same cycle number for one case (table 1 in [437]).²

13.2.4 Baker Transition State Test Set

Compared to the optimizations just described, where the energy was minimized along all Hessian eigenvectors, TS searches are more challenging, as they require energy maximization along one eigenvector. Foremost, this necessitates selecting an appropriate eigenvector and keeping track of it, along the optimization.

Besides a test set for GS minimizations, Baker also proposed a set, concerning TS searches.[315] This section investigates the performance of pysisyphus for the Baker TS test set, using two different approaches: Hessian based TS optimization and TS optimizations using only first-derivatives, by means of the DM (see chapter 10).

Hessian-based Optimizer

All calculations were carried out using ORCA 4.2.1 at the HF/3-21G level of theory.[388] Singlet multiplicity was assumed throughout, except for cases 4, 5 and 8, which were calculated as doublets. Total charges were chosen according to Table 13.6. The initial (maximum) trust radius was decreased to 0.1 a_0 (rad) (0.3 a_0 (rad)). Analytical Hessian were calculated in the first optimization cycle and the imaginary mode belonging to the most negative eigenvalue, if present, was followed uphill. The Hessian was subsequently updated with Bofills formula.[240]

Converging cases 10 and 11 (Figure 13.3), which start in the convex region of the PES, requires additional measures. Case 10 is supposed to yield a TS for the dissociation of 1,2,4,5-tetrazine into two HCN molecules and N₂, whereas case 11 is supposed to yield the TS for the isomerization of *trans*-butadiene to *cis*-butadiene. Even though various authors reported successful optimizations for one or both cases, they never discussed how the initial root was obtained.[232, 256, 315]

²The author of this thesis did not contribute in any way to the work by Ahuja et al.

13 Pysisyphus

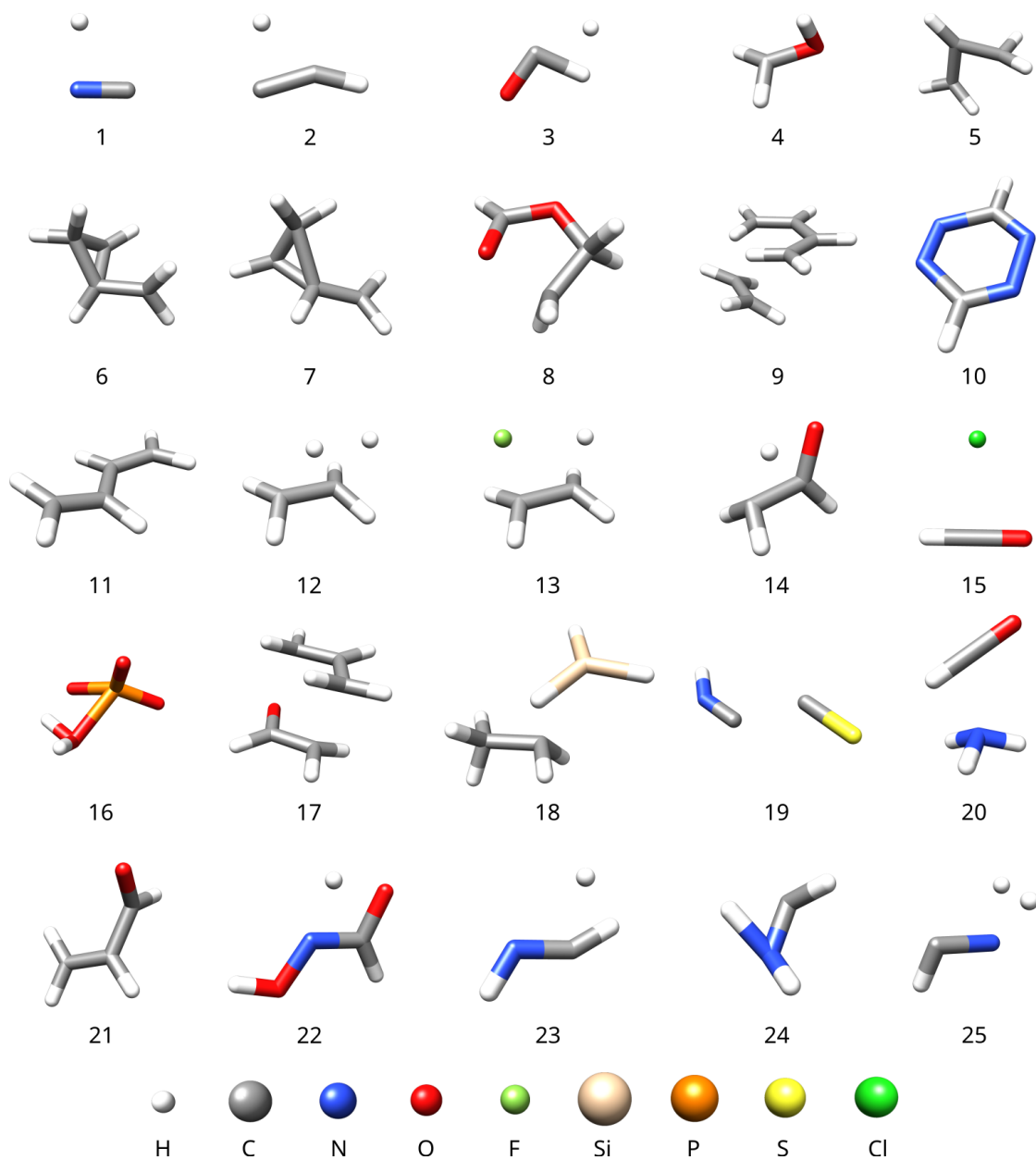


Figure 13.3: Initial geometries of the Baker TS test set, comprising 25 small molecules and ions.[315] A color code is given in the last row.

Pysisyphus offers an elegant way (keyword `rx_mode`), for initial root selection, requiring minimal user input. By specifying a list of primitive internals and an additional number, an approximate eigenvector is constructed. For tetrazine (Figure 13.4) `rx_mode: [[[0, 2], 1], [[1, 3], 1]]` yields a vector, suitable for describing in-phase change of the two CN-bonds, stretched at the TS.

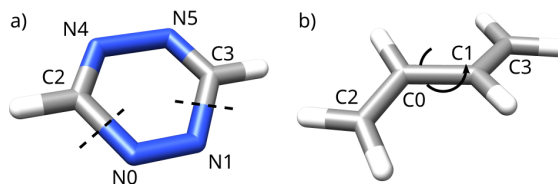


Figure 13.4: Starting geometries for cases 10 and 11 from Baker’s TS test set. a) 1,2,4,5-tetrazine and b) *trans*-butadiene. Bonds, stretched at the TS, are crossed by a dashed line. Atom labels start at 0, to be consistent with the actual pysisyphus input.

In this example, the exact signs of the additional numbers do not matter, as long as both are the same. Swapping one sign to a negative number would result in a vector, describing stretching of one and compression of the other bond. After normalization, overlaps between the approximate mode and Hessian eigenvectors are calculated and the eigenvector corresponding to the highest overlap is select as initial root (Listing 13.1). Care has to be taken that only overlaps within the non-redundant subspace are considered. In the present implementation, pysisyphus defines 28 primitive internals for tetrazine.

Listing 13.1: Python code for the `rx_mode` root selection algorithm.

```
def root_select(eigvals, eigvecs, rx_mode, thresh=1e-8):
    # Construct approximate mode/eigenvector
    mode = np.zeros_like(eigvals) # Initialize zero-vector
    for prim_coord, number in rx_mode: # Loop over rx_mode input
        # Determine location of primitive internal in mode
        index = get_index_of_prim_coord(prim_coord)
        mode[index] = number # Set number at appropriate location
        mode /= np.linalg.norm(mode) # Normalize to unit length

    # Take absolute value of overlaps, because eigenvector sign is ambiguous.
    ovpls = np.abs(np.einsum("ij,i->j", eigvecs, mode))
    # Only consider overlaps in non-redundant subspace by zeroing overlaps
    # in the redundant subspace.
    small_inds = np.abs(eigvals) < thresh
    ovpls[small_inds] = 0.0
    root = ovpls.argmax() # Select root with highest overlap
    return root
```

Using the aforementioned `rx_mode` input, the algorithm determines the 16th Hessian eigenvector for maximization. If a TS for a bond breaking reaction is sought one cannot just blindly maximize along the lowest (first) Hessian eigenvector, as the lowest modes usually describe dihedrals motions. For the *cis-trans* isomerization of butadiene (case 11), specification of one dihedral is enough (`rx_mode: [[2, 0, 1, 3], 1]`), see

Figure 13.4). In this case, maximization is actually carried out along the first Hessian eigenvector, with a non-vanishing eigenvalue.

Overall, the presented approach allows easy, initial root selection. By controlling the sign of the additional number, even complicated phase relationships between different internal coordinates can be expressed, if required.

Pysisyphus implements three TS optimizers that utilize Hessian information: restricted step partitioned RFO (RS-PRFO), restricted step image method RFO (RS-IRFO), and the trust-region image method (TRIM) (see eq. (9.7) on page 62 and eq. (5.7) on page 32). TRIM combines the IM with step determination through eq. (5.5). [256, 438] All three optimizers were applied to Baker’s TS test set. Additionally, the use of line searches, that is maximization in one subspace and minimization in the other, was investigated for RS-PRFO.

Contrary to the published value of $-242.255\ 29\ E_h$, a lower final energy of $-242.256\ 96\ E_h$ is used as reference energy for case 22. The former value corresponds to a planar, symmetry constrained solution, which relaxes to the latter value without constraints.

Results for the different optimizers are shown in Table 13.5. RS-PRFO, with enabled line search is the only optimizer that converged all 25 investigated test cases, requiring 325 cycles. Disabling line search yields a failure for case 2 and a total of 326 cycles are required to converge the remaining 24 test cases. RS-IRFO fails for case 15 and requires a total of 297 cycles. TRIM fails for five cases (10, 11, 14, 16, 22), while the remaining cases require 254 cycles.

Considering only the 18 cases that converged for all optimizers (excludes 2, 10, 11, 15, 14, 16, 22), then RS-IRFO needs the fewest cycles (221), closely followed by RS-PRFO with enabled line search (224). Disabling line search increases the required cycles to 238 for RS-PRFO. TRIM requires a total of 227 cycles.

Table 13.5: Performance of different TS optimizers in pysisyphus for converging Baker’s TS test set. The numbers in parentheses give the required cycles, to converge the 18 cases that did not fail with any optimizer (excludes cases 2, 10, 11, 14, 15, 16 and 22), recall Figure 13.3.

Optimizer	Converged	Failed cases	Cycles
RS-PRFO with line search	25	-	325 (224)
RS-PRFO without line search	24	2	326 (238)
RS-IRFO	24	15	297 (221)
TRIM	20	10, 11, 14, 16, 22	254 (227)

Table 13.6: Number of optimization cycles required to converge Baker’s TS test set (Figure 13.3), according to Baker’s criteria (see section 13.2).[315] Convergence to the correct geometry was ensured by comparing the final energy to the published values. Bakken’s results correspond to their most efficient method, as presented in Table XV in [232]. Besalu’s results correspond to the RS-PRFO column in Table 1 in [256], whereas Baker’s original results are taken from Table IV in [315]. Code to reproduce the results of this work is given in Listing A.3 on page 141.

#	Reaction	This work	Bakken [232]	Besalu [256]	Baker [268]
1	$\text{HCN} \rightleftharpoons \text{HNC}$	12	9	-	9
2	$\text{HCCH} \rightleftharpoons \text{CCH}_2$	13	7	-	8
3	$\text{H}_2\text{CO} \rightleftharpoons \text{H}_2 + \text{CO}$	13	13	-	13
4	$\text{CH}_3\text{O} \rightleftharpoons \text{CH}_2\text{OH}$	9	-	-	11
5	cyclopropyl ring opening	20	-	-	11
6	bicyclo[1.1.0]butane ring opening	8	-	-	7
7	bicyclo[1.1.0]butane ring opening	11	-	-	9
8	1,2-migration (formyloxy)ethyl	10	-	-	26
9	butadiene + ethylene \rightleftharpoons cyclohexene	18	15	x	13
10	s-tetrazine \rightleftharpoons 2 HCN + N ₂	11	9	32	14
11	<i>trans</i> -butadiene \rightleftharpoons <i>cis</i> -butadiene	10	-	-	8
12	$\text{CH}_3\text{CH}_3 \rightleftharpoons \text{CH}_2\text{CH}_2 + \text{H}_2$	11	8	15	12
13	$\text{CH}_3\text{CH}_2\text{F} \rightleftharpoons \text{CH}_2\text{CH}_2 + \text{HF}$	15	15	-	11
14	vinyl alcohol \rightleftharpoons acetaldehyde	23	19	-	13
15	$\text{HCOCl} \rightleftharpoons \text{HCl} + \text{CO}$	15	-	-	12
16	$\text{H}_2\text{O} + \text{PO}_3^- \rightleftharpoons \text{H}_2\text{PO}_4^-$	15	-	-	23
17	Claisen rearrangement	13	-	36	8
18	$\text{SiH}_2 + \text{CH}_3\text{CH}_3 \rightleftharpoons \text{SiH}_3\text{CH}_2\text{CH}_3$	12	12	-	7
19	$\text{HNCCS} \rightleftharpoons \text{HNC} + \text{CS}$	13	13	-	10
20	$\text{HCONH}_3^+ \rightleftharpoons \text{NH}_4^+ + \text{CO}$	15	-	14	10
21	rotational TS in acrolein	5	5	-	4
22	$\text{HCONHOH} \rightleftharpoons \text{HCOHNHO}$	14	5	10	5
23	$\text{HNC} + \text{H}_2 \rightleftharpoons \text{H}_2\text{CNH}$	7	8	22	8
24	$\text{H}_2\text{CNH} \rightleftharpoons \text{HCNH}_2$	23	18	20	14
25	$\text{HCNH}_2 \rightleftharpoons \text{HCN} + \text{H}_2$	9	8	56	9
	Sum	325	162	205	275

A more detailed listing of the RS-PRFO results with enabled line search is given in Table 13.6. Compared with Baker's original work, the most efficient method in this work requires more cycles (325 cycles versus 275 cycles).[315] However, the present implementation can be used mostly in a black box way, whereas Baker's results were obtained with manually constructed Z-matrices. Comparisons with other published results is difficult, as often only results for a subset of the 25 cases are reported. In contrast to the present work, Bakken found TRIM to provide the best performance for 15 tested cases. Similarly, Besalu found the IM based optimizers more stable (see Table 13.5).[256] But it must be kept in mind that both studies employed only a subset of Baker's TS test set. Considering only cases that converged for all optimizers in this work, then RS-IRFO also compares favorably to RS-PRFO (221 versus 224 cycles).

In summary, RS-PRFO with enabled line searches shows robust performance on Baker's TS test set. In case, a TS search is started from a convex region on the PES, pysisyphus offers a simple way to select an appropriate root for uphill following, by means of the `rx_mode` keyword.

Dimer method

While utilizing Hessian information enables efficient and effective TS optimization, computational demand of obtaining and handling Hessian matrices (diagonalization/inversion, see chapter 10) grows quickly with system size.[439] Recently, Hermes showed that QN-methods easily lose track of the leftmost Hessian eigenvector and accumulate significant error in the Hessian, when standard update methods (SR1, BFGS) are employed.[440] Only one Hessian calculation at the beginning may be sufficient to converge well-behaved TS optimizations, as in Baker's TS set. But more challenging TS searches may require additional, intermediate Hessian calculations, to circumvent aforementioned error accumulation, which may become prohibitive for big systems.

Pysisyphus implements the DM, which requires only gradients, thus avoiding the problems outlined above. In every optimization cycle, the dimer is converged onto the leftmost Hessian eigenvector, up to a prescribed tolerance, by means of dimer rotations. Translation steps move the whole dimer closer towards the TS.

Energies and gradients were calculated at the same level of theory as previously outlined. The DM (chapter 10) was employed for converging dimer orientation \mathbf{N} to the leftmost Hessian eigenvector, corresponding to the smallest eigenvalue, in every optimization cycle. A reasonable choice for the initial dimer orientation \mathbf{N} is crucial for a successful outcome of the TS search. Starting from optimized TSs, obtained with a Hessian based optimizer, IRCs were integrated towards the educts and products, connected by the TSs. Initial

guesses for \mathbf{N} were calculated as normalized difference between the Cartesian coordinates of aligned educt and product geometries. If no initial \mathbf{N} is provided to pysisyphus, a random orientation is chosen. In general, picking a random orientation should be avoided, as the dimer rotations may fail to converge for bad initial guesses. An example for this is found in Table 1 of [312], where even simple cases like the HCN isomerization failed to converge for a random initial orientation.

A dimer separation of $\Delta R = 0.0189 a_0$ was chosen (Figure 10.1 on page 63). Rotations were carried out as described by Kästner, with a tolerance of $\phi_{\text{tol}} = 5^\circ$ and steps obtained from a LBFGS optimizer.[312] Performance of LBFGS has proven superior to the CG and steepest descent approaches outlined elsewhere.[290, 311] For cases 10 and 11, starting in the convex PES region, dimer rotations were disabled until the convex region was left and the curvature became negative. In contrast to the original proposal by Jonsson,[311] it was critical for the convergence of case 10, to use parallel and perpendicular force components, even in the convex PES region, recall eq. (10.3). These choices correspond to the default settings for the DM in pysisyphus.

Dimer translation was carried out by a (preconditioned) LBFGS optimizer. Preconditioners \mathbf{P} were constructed as outlined in chapter 7, using Lindh’s model Hessian.[241, 286] All stretches, bends and dihedrals, automatically defined by the internal coordinate setup algorithm in pysisyphus, are used for constructing \mathbf{P} . The present implementation utilizes the sparse linear algebra capabilities of the SciPy package.[441] As some of the molecules are quite small, using all primitive internals resulted in dense preconditioners. For large molecules, care has to be taken for \mathbf{P} to be actually sparse, otherwise the computational benefits of preconditioning may not be realized.

Gas-phase Hessians are at least six fold degenerate, so \mathbf{P} was regularized ($\mathbf{P} \rightarrow \mathbf{P} + c\mathbf{I}$) with $c = 0.103 E_h a_0^{-2}$. [286] If the absolute value of any element in the proposed step exceeded $0.25 a_0$, the whole step was scaled accordingly, so the absolute values are equal to or less than the threshold. Cartesian coordinates and Baker’s convergence criteria were used throughout.

Results obtained with and without preconditioner are given in Table 13.7. The DM in combination with (preconditioned) LBFGS, as implemented in pysisyphus, managed to converge 24 out of 25 cases from Baker’s TS set. Only case 11 failed, regardless of whether a preconditioner was used. Employing preconditioning is clearly superior, as only 358 optimization cycles (dimer translations) are needed, while 577 cycles are required without preconditioner. Disregarding the additional energy and gradient evaluations required for dimer rotations, the present implementation nearly rivals the performance of optimizations that utilized Hessian information (325 cycles, Table 13.6). For a total of

1092 evaluations, an average of 46 energy and gradient evaluations are needed to converge 24 cases with preconditioner. Without preconditioner, the total (average) is significantly higher 1706 (71).

Table 13.7: Number of optimization cycles required to converge Baker's TS test set (Figure 13.3) according to Baker's criteria (see section 13.2), using the DM and (preconditioned) LBFGS.[234, 251, 286, 315] Required energy and gradient evaluations are given in parentheses. Convergence to the correct geometry was ensured by comparing the final energy to the published values. Code to reproduce these results is given in Listing A.4 on page 142.

#	Reaction	Preconditioning	
		yes	no
1	$\text{HCN} \rightleftharpoons \text{HNC}$	12 (42)	13 (44)
2	$\text{HCCH} \rightleftharpoons \text{CCH}_2$	13 (45)	11 (36)
3	$\text{H}_2\text{CO} \rightleftharpoons \text{H}_2 + \text{CO}$	10 (32)	12 (38)
4	$\text{CH}_3\text{O} \rightleftharpoons \text{CH}_2\text{OH}$	10 (25)	10 (24)
5	cyclopropyl ring opening	14 (46)	32 (95)
6	bicyclo[1.1.0]butane	12 (40)	25 (79)
7	ring opening bicyclo[1.1.0]butane	14 (49)	42 (131)
8	ring opening 1,2-migration (formyloxy)ethyl	18 (47)	34 (73)
9	butadiene + ethylene \rightleftharpoons cyclo- hexene	17 (57)	31 (105)
10	s-tetrazine \rightleftharpoons 2 HCN + N ₂	12 (43)	21 (63)
11	<i>trans</i> -butadiene \rightleftharpoons <i>cis</i> -butadiene	-	-
12	$\text{CH}_3\text{CH}_3 \rightleftharpoons \text{CH}_2\text{CH}_2 + \text{H}_2$	12 (29)	16 (37)
13	$\text{CH}_3\text{CH}_2\text{F} \rightleftharpoons \text{CH}_2\text{CH}_2 + \text{HF}$	14 (35)	19 (45)
14	vinyl alcohol \rightleftharpoons acetaldehyde	17 (51)	29 (80)
15	$\text{HCOCl} \rightleftharpoons \text{HCl} + \text{CO}$	12 (50)	29 (114)
16	$\text{H}_2\text{O} + \text{PO}_3^- \rightleftharpoons \text{H}_2\text{PO}_4^-$	15 (50)	31 (104)
17	Claisen rearrangement	19 (58)	38 (113)
18	$\text{SiH}_2 + \text{CH}_3\text{CH}_3 \rightleftharpoons \text{SiH}_3\text{CH}_2\text{CH}_3$	23 (53)	43 (109)
19	$\text{HNCCS} \rightleftharpoons \text{HNC} + \text{CS}$	22 (67)	29 (90)
20	$\text{HCONH}_3^+ \rightleftharpoons \text{NH}_4^+ + \text{CO}$	16 (61)	21 (74)
21	rotational TS in acrolein	11 (36)	22 (69)
22	$\text{HCONHOH} \rightleftharpoons \text{HCOHNHO}$	27 (75) ^a	18 (56) ^b
23	$\text{HNC} + \text{H}_2 \rightleftharpoons \text{H}_2\text{CNH}$	12 (30)	16 (42)
24	$\text{H}_2\text{CNH} \rightleftharpoons \text{HCNH}_2$	18 (52)	22 (56)
25	$\text{HCNH}_2 \rightleftharpoons \text{HCN} + \text{H}_2$	8 (19)	13 (29)
	Sum	358 (1092)	577 (1706)

^a Final energy $-242.256\,96 E_h$, relaxed TS geometry.

^b Final energy $-242.255\,30 E_h$, published value.[315]

Comparison to other implementations is difficult. Heyden also used the DM for Baker’s TS set, but the starting geometries were obtained as interpolated HEI from a previous GSM run.[290] Kästner directly started from the test set geometries, but used a random initial dimer orientation \mathbf{N} , resulting in failures for several cases. He reported between 2211 to 2689 energy and gradient evaluations to converge on average 22 of the 25 test cases.[312] Shang et al. employed a different level of theory³, direct dimer rotation using constrained Broyden minimization, a more complex force definition, and different convergence criteria. They achieved an average of 35 energy and gradient evaluations, while converging all 25 cases, which appears superior to the present implementation.[313] But it has to be noted that looser convergence criteria were employed in this study, as convergence was already indicated, when the maximum absolute value of the gradient entries fell below $6.9 \times 10^{-3} E_h a_0^{-1}$.

13.2.5 Chain-Of-States Test Set

Pysisyphus offers several ways for obtaining TS guesses, e.g., by means of COS methods like NEB or the GSM. Here, the performance of the GSM implementation in pysisyphus is investigated for a diverse test set, comprising 20 reactions (Figure 13.5).

The set is mostly based on a set presented by Birkholz and Schlegel.[265, 315, 442–444] It includes educt, TS and product geometries obtained at the PM6[445] and B3LYP/6-31G(d,p) level of theory.[446–449] For the present benchmark, the given TSs were reoptimized at the GFN2-XTB level of theory, using pysisyphus. Subsequently, IRCs were integrated towards educts and products of the reactions, to obtain a consistent set of structures. The IRC endpoints were then employed as initial geometries for the GSM. Two cases were excluded from the original set: the S_N2 reaction of fluoride and methyl chloride (case 19) does not have a TS at the GFN2-XTB level of theory, which was also noted by Birkholz for the B3LYP/6-31G(d,p) PES. Similarly, explorative calculations for the addition of difluorocarbene to ethylene (case 9) revealed the same absence of a TS at the tight-binding level of theory. These cases were replaced by two hydride shift reactions (cases 14 and 30) from the MOBH35 test set (metal-organic barrier heights with 35 members).[450]

The ability of the GSM to yield useful TS guesses for the MOBH35 set was recently probed by Grimme, using the original GSM implementation of Zimmerman.[300, 451] Unfortunately, no details on the GSM calculations (number of images, optimization algorithm, threshold for growing images, among others) were reported by Grimme.

³Numerical double- ζ basis and GGA-PBE XC-functional

13 Pysisyphus

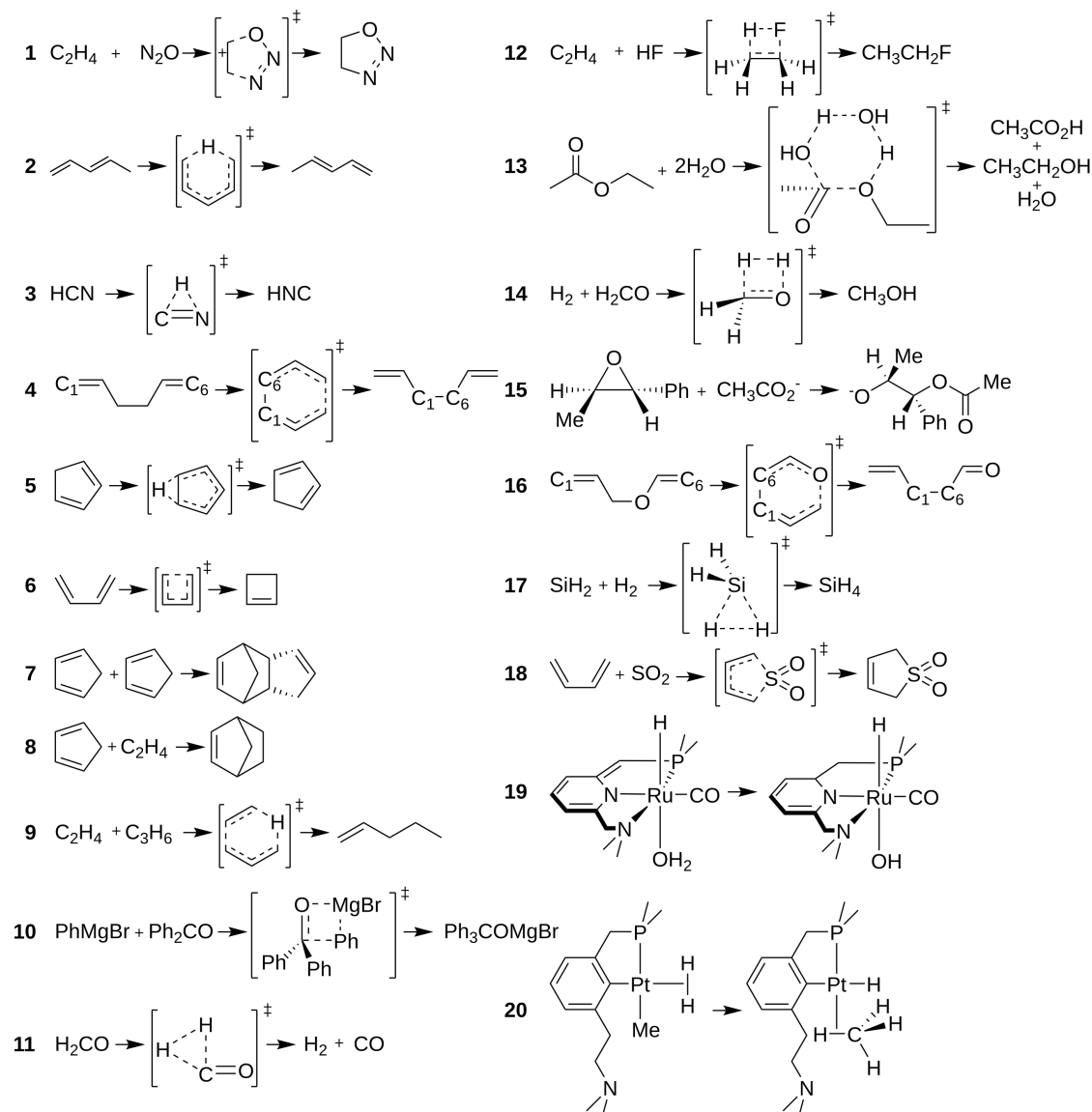


Figure 13.5: Investigated reactions in the COS test set.

Some geometries in the present set differ significantly from the originals. Notably, the educts for the two Cope-rearrangements (cases 4 and 16 in Figure 13.5) exhibit a different conformation (see Figure 13.6). When a GSM is initiated from the original conformers, subsequent optimization of the HEI yields a wrong TS. If the GSM is initiated from the IRC endpoints, the correct TS is obtained. Starting from reasonable conformers is crucial for the successful outcome of COS optimizations, as already noted by Birkholz and others.[442, 451]

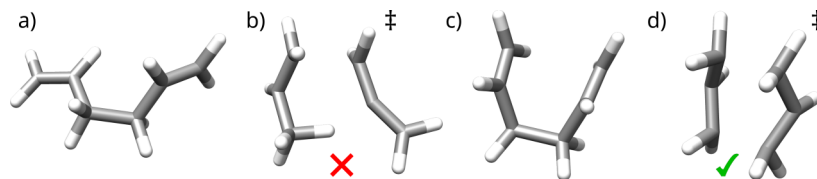


Figure 13.6: Different educt (a, c) and TS geometries (b, d) for the Cope rearrangement of 1,4-hexadiene (case 4 in the COS test set). a) Conformer, as published in [442], b) (wrong) TS, obtained from GSM started from a) and subsequent TS optimization. c) Conformer used in this benchmark and d) correct TS, obtained when starting GSM from the conformer c).

Likewise, the high symmetry of HCN and CNH (case 3) was broken slightly, to allow successful interpolation. A similar approach was recently discussed by Palenik.[282] Interestingly, correct TSs are obtained by the connectivity transition state (CTS) approach, also available in pysisyphus, even when starting from the original conformers (see Listing A.6).[442]

Energies and gradients were obtained at the GFN2-XTB level of theory using XTB 6.3.3.[212] Singlet multiplicity and neutral charge was assumed throughout, except for case 15 (charge -1). Initial educt and product geometries were preoptimized for a maximum of 5 cycles, using the standard method in pysisyphus (see section 13.2.1). Starting from the preoptimized geometries, a string in DLC was grown to a total of 12 images (10 inner images).[300] New images were added, when the RMS of the perpendicular force acting on the frontier images fell below $0.05 E_h \cdot a_0^{-1}$ (rad^{-1}). String reparametrization occurred every other cycle during the growth phase, and every third cycle after the string was fully grown. Originally, Behn and Zimmerman proposed a reparametrization approach, where every image is shifted many times along the string using very small steps.[299, 300] Pysisyphus uses a different approach: The required step is estimated and taken directly for every image that needs reparametrization. This is repeated iteratively, until the desired string parametrization is achieved. Usually, only one or two steps are needed per image and thus, excessive internal-Cartesian back-transformations are avoided. While still in the growth phase, the DLC were reset after every reparametrization, and a new active set \mathbf{U} was calculated for every image (see section 6.4). Resetting of DLCs was stopped after the string was fully grown, to not interfere with the LBFGS optimizer, which relies on a history of previous steps and gradient differences.

When the RMS of the perpendicular force dropped below $0.0075 E_h \cdot a_0^{-1}$ (rad^{-1}) and the string was fully grown, the HEI was converted to a CI, aimed at yielding an improved TS guess. During the growth phase, string optimization was achieved via

steepest descent steps after reparametrizations and CG (Fletcher-Reeves) otherwise. [234, 300] After the string was fully grown, optimization continued with LBFGS. A history of 10 previous cycles was retained and a doubly damped BFGS update was used (Algorithm 2 on page 36).[255] To the best knowledge of the author, a doubly damped BFGS update was not yet applied in the context of COS optimization. The whole step vector was scaled accordingly, if the absolute value of any element in it exceeded $0.2 a_0$ (rad). All optimizers were employed in their global variant, that is the whole COS was optimized as super-molecule, instead of optimizing every image on its own. While this makes no difference for steepest descent, as image-coupling is neglected, Sheppard found global LBFGS superior over per-image LBFGS.[306]

GSM convergence was signaled, when the RMS of the perpendicular force fell below or was equal to $0.005 E_h \cdot a_0^{-1}$ (rad^{-1}). In the present study, GSM is employed to obtain a reasonable TS guess, so there is no need for overly tight convergence. Finally, after convergence an interpolated HEI was obtained by means of cubic splining, which is superior over just picking the HEI without interpolation.[309] It was ensured that all primitive bond stretches that are either present in the educt or the product geometry, are also defined for the HEI derived TS guess. In the following and in the context of COS optimizations, this approach will be referred as the standard method.

Two of the twenty cases required slight adjustments, to ensure convergence: The GSM for case 3 (HCN isomerization) was optimized in Cartesian coordinates instead of DLC and for case 20, the convergence criterion was tightened to $0.003 E_h \cdot a_0^{-1}$ (rad^{-1}).

Subsequent TS optimizations were started from the splined HEI in RIC, using RS-IRFO. An exact Hessian was calculated before the first optimization cycle and the eigenvector for energy maximization was selected according to its overlap with the HEI tangent. The trust radius was restricted to $0.5 a_0$ (rad), to avoid overly long steps, which can result in a loss of the correct eigenvector.[440] Convergence of the TS optimization was indicated when the standard Gaussian criteria were fulfilled (see section 13.2.2). A Hessian was calculated at the final geometry to verify the nature of the SP as first-order TS. Success of the TS optimizations was verified by calculating the RMSD with a reference TS geometry.

Results for the COS test set are summarized in Table 13.8. The correct TS is obtained for all twenty cases in the test set by the standard method with only two minor adjustments. Similarly, all previous GSM optimizations converged. String optimizations of cases 11 (formaldehyde decomposition) and 14 (H_2 addition to formaldehyde) required the most cycles (26 and 22) until convergence, even though they belong to the smallest test cases. Overall, a total of 204 GSM cycles are required, each cycle comprising multiple energy and gradient evaluations. Subsequent TS optimizations required a total of 228 cycles

(minimum 2, median 10, maximum 26 cycles). In nearly all cases, the overlap of the HEI tangent with the eigenvector, belonging to the most negative eigenvalue of the HEI Hessian, was close to 1.

Disabling LBFGS and relying only on steepest descent and CG steps for string optimization, leads to a failure in the subsequent TS optimizations of cases 11 and 19. For case 11, already the GSM optimization failed, as it did not converge in 50 cycles. For case 19 it required only 7 cycles, but converged to a wrong TS, as the eigenvector selection fails and the vector belonging to the second, most negative eigenvalue is chosen for uphill following. Compared to the standard method disabling LBFGS results in 54 additional COS optimization cycles (225 vs. 171), if the two failing cases are neglected.

Turning off the doubly damped BFGS update leads to 45 additional COS optimization cycles (249), compared to the standard method. COS optimization of case 11 terminates prematurely, as the coordinates of two images became too similar. The number of required TS optimization cycles increases to 278, corresponding to 50 additional cycles, compared to the standard method. Nonetheless, all 20 TS optimizations converged to the correct TSs.

Only the combination of LBFGS and doubly damped update appears to sustain long optimization step lengths (maximum absolute element $0.2 a_0$ (rad)). The influence of whether LBFGS with double damping is enabled or not, could probably be decreased by using smaller step lengths, at the cost of additional energy and gradient evaluations.

The present setup also allows to investigate the influence of the chosen primitive internals at the TS guess, on the outcome of the TS optimization. When bends and dihedrals, defined at educt and product geometries, are also included in the coordinate set at the TS guess, 2 additional cycles (230) are required compared to the standard method that only considers the bonding skeleton. Fully neglecting, which primitives are defined at educt and product, leads to deteriorated TS optimization performance, as overall 256 cycles are required. Care must be taken, not to include superfluous linear bends at the TS guess, which can lead to spurious eigenvectors with strongly negative eigenvalues, as observed for case 1 in Figure 13.7. Even though the Cartesian Hessian at the TS guess has one significant imaginary mode, retaining the linear bend results in two imaginary modes in RIC (Table 13.9). If the linear bend is omitted at the TS guess, only one imaginary mode is present. At least for this case, the spurious eigenvector is easily detected, as its overlap with the HEI tangent is basically zero (Table 13.9).

In summary, the present GSM implementation offers a robust way to obtain TS guesses in a black-box fashion, while requiring only educt and product geometries as input. By

Table 13.8: Results for the COS test set, comprising 20 reactions (Figure 13.5). Optimization cycles to converge the growing string and subsequent TS optimization started from the HEI, RMSD values with a reference TS geometry, number of imaginary modes at the HEI and overlap between HEI tangent τ and the Hessian eigenvector, belonging to the most negative eigenvalue. Code to reproduce these results is given in Listing A.5 on page 143.

#	Reaction	Opt. cycles			Imaginary mode(s)		
		GSM	TS	RMSD/ a_0	N	Overlap	
1	NO addition to ethylene	6	4	0.0018	1	0.97	
2	1,5-H-transfer in 1,3-pentadiene	8	7	0.0012	1	0.97	
3	HCN isomerization ^a	16	2	0.0001	1	0.99	
4	Cope rearrangement of 1,4-hexadiene	9	19	0.0012	2	0.91	
5	H-shift in 1,3-CpH	8	6	0.0005	1	0.99	
6	Cyclization of 1,3-butadiene	10	6	0.0017	1	0.96	
7	Diels-Alder endo addition of CpH to CpH	5	10	0.0039	2	0.98	
8	Diels-Alder addition of CpH to ethylene	5	4	0.0015	1	0.98	
9	Ene reaction of ethylene and propene	9	14	0.0036	3	0.90	
10	PhMeBr addition to benzophenone	5	13	0.0060	1	0.96	
11	Formaldehyde decomposition	26	9	0.0005	1	0.86	
12	HF addition to ethylene	14	6	0.0007	1	0.97	
13	H ₂ O assisted ethyl acetate hydrolysis	10	15	0.0124	2	0.94	
14	H ₂ addition to formaldehyde	22	10	0.0012	2	0.95	
15	2-Methyl-3-phenyloxirane ring opening	5	14	0.0000	1	0.95	
16	Oxy-Cope rearrangement to 1-pentene-5-one	11	26	0.0014	2	0.92	
17	H ₂ addition to silylene	14	12	0.0031	2	0.93	
18	SO ₂ addition to butadiene	5	8	0.0213	1	0.91	
19	H-shift in Ru-complex (MOBH35 case 14)	7	20	0.0156	3	0.61	
20	H-shift in Pt-complex (MOBH35 case 30) ^c	9	23	0.0366	3	0.84	
Sum		204	228				

^a GSM with Cartesians instead of DLC

^c GSM convergence tightened to $0.003 E_h \cdot a_0^{-1}$ (rad⁻¹)

Table 13.9: Negative eigenvalues and overlaps of the corresponding eigenvectors with the HEI tangent, depending on whether a linear bend is defined at the HEI or not (see Figure 13.7).

#	linear bend		no linear bend	
	eigenvalue	overlap	eigenvalue	overlap
1	-0.371532	0.000041	-0.019199	0.974726
2	-0.016751	0.974867		

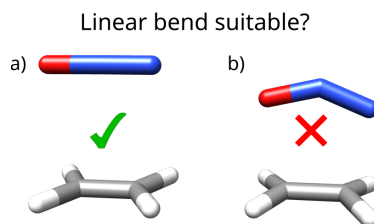


Figure 13.7: Case 1 from the COS test set. Whereas a linear bend is a suitable coordinate for the educt a) ($\angle_{\text{ONN}} = 179.6^\circ$), it isn't suitable anymore at TS geometry b) ($\angle_{\text{ONN}} = 143.7^\circ$). Including the linear bend at b) leads to a spurious imaginary mode.

taking into account the union of bonds defined at educt and product geometries for the TS guess, improved optimization performance is achieved. LBFGS combined with double damping appears to be a promising strategy for COS optimization, whereas using plain LBFGS seems less suitable.

13.3 Excited State Optimization

The performance of pysisyphus for optimizing and tracking ESs is verified against two previously published systems: the optimizations of the first two excited singlet states of cytosin (**Cy**) and the S_0 of the ruthenium nitrosyl complex $cis-(\text{Cl}, \text{Cl})[\text{RuCl}_2](\text{NO})(\text{tpy})^+$ (**RuNO**).^[223] Additionally, two exemplary optimizations of excited triplet states for two platinum complexes ($[\text{Pt}(\text{C}\equiv\text{C-Tol})_2(\text{phen-TPA-R})]$; R = OMe, CN) investigated by Shillito et al., are presented.^[8] Structural formulas for all compounds are given in Figure 13.8.

All optimizations were carried out in RIC using the standard method outlined in section 13.2.1, with enabled GDIIS and quartic line search. Initial Hessians were estimated according to Fischer and updated with the BFGS formula.^[234, 242] ESs were tracked by the WFO approach. The reference cycle for the overlap calculation was updated using

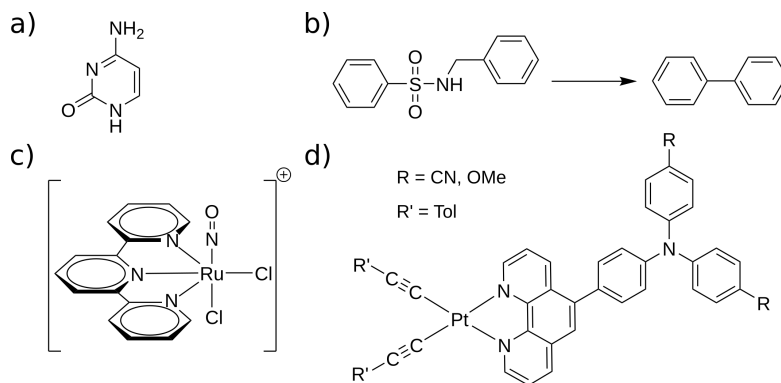


Figure 13.8: Compounds investigated in this chapter. a) 1H-amino-keto tautomer of cytosin (**Cy**), b) reaction of *N*-benzylbenzenesulfonamide (**1b**) to biphenyl (**2b**), c) ruthenium nitrosyl complex *cis*-(Cl, Cl)[RuCl₂](NO)(tpy)]⁺ (**RuNO**) and d) two platinum complexes [Pt(C≡C-Tol)₂(phen-TPA-R)] (**Pt-TPA-OMe** with R = OMe, **Pt-TPA-CN** with R = CN).

the adaptive formalism described in section 4. Convergence was indicated when the Gaussian criteria were fulfilled (see section 13.2.2).

13.3.1 Cytosin

As one of the five canonical nucleobases making up nucleic acids (NAs), the photochemistry of cytosin received considerable scientific interest.[452–458] Absorption of ultraviolet light through nucleic acids may lead to their degradation and can induce harmful processes like cell apoptosis.[458, 459] Extensive photo-degradation of nucleic acids is avoided by very fast nonradiative decay, as the excitation energy is dissipated in the surroundings.[460–462] Cytosin shows fast IC from a bright $\pi \rightarrow \pi^*$ to a dark $n \rightarrow \pi^*$ state.[456] Its small size makes it suitable for benchmarking ES tracking algorithms, as shown by García et al.[223] Here, similarly the performance of pysisyphus for optimizing the first two singlet ES of the 1H-amino-keto-tautomer of cytosin (**Cy**, Figure 13.8a) was investigated.

All calculations at the DFT and TD-DFT level of theory were carried out via Turbomole V7.3.[122] Excited state properties (such as vertical excitation energies and oscillator strengths) for the first two excited singlet states were obtained from TD-DFT calculations at the PBE0/def2-SVP[381, 463] level of theory, using the starting geometry provided by García.[223] The RIJ approximation with corresponding auxiliary basis set was used to speed up the calculations.[389, 464]

Optimization results are shown in Figure 13.9. Pysisyphus successfully optimizes both ESs to SPs, while correctly tracking their diabatic character. In both cases,

the state crossings occur shortly after the start of optimization. The charge density differences (CDDs) along the optimization paths stay nearly constant. García reported 160 steps for the S_1 optimization and ca. 324 steps for the S_2 optimization, until a SP was reached. In pysisyphus only 9 (10) gradient calculations are needed for the S_1 (S_2) optimization, showing a remarkable, although unsurprising, improvement. Enhanced performance of internal coordinates in combination with an optimizer, utilizing Hessian information, was already recognized many years ago by Schlegel.[75]

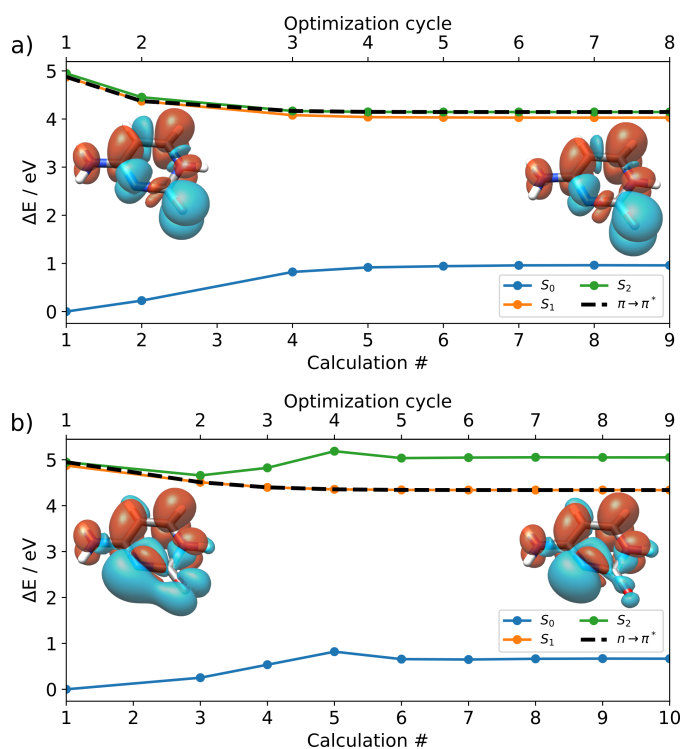


Figure 13.9: Electronic energies of the ground and the first two excited singlet states of cytosin (**Cy**) along the optimization of the a) bright S_1 and b) dark S_2 , with respect to the ground state energy at the first cycle. The tracked excited state is indicated by a dashed black line. Every marker corresponds to an optimization cycle and missing markers indicate root flips. CDDs illustrate the excited state character at the start and the end of the optimization; electron density is excited from blue to red.

13.3.2 Ruthenium Nitrosyl Complex

Besides carbon monoxide and hydrogen sulfide, nitric oxide (NO) is an important physiologically relevant gasotransmitter.[465] In the human body, NO acts as strong

vasodilator and can activate macrophages.[466–470] Even long before its important physiological role was understood, NO-precursor drugs like nitroglycerin and amyl nitrate were in wide use.[471, 472] Direct and targeted application of gaseous NO in humans is difficult, resulting in the development of transition metal complexes, where the NO release can be triggered by light.[473–478] Transition metal nitrosyls exhibit a complex photochemistry, as NO may undergo either photo-release or photo-isomerization.[479–481] By computing the relaxation pathways of ESs, the photochemistry of transition metal nitrosyls can be rationalized.[482–484]

As a challenging example, García recently presented the optimization of the bright S_9 of **RuNO** (see Figure 13.8c) using NTO overlaps.[223] Similar to the **Cy** example, the performance of pysisyphus in the scope of ES optimizations in the singlet manifold is investigated.

All calculations at the DFT and TD-DFT level of theory were carried out by Turbomole V7.3.[122] Excited state properties for the first ten excited singlet states were obtained from TD-DFT calculations using the BHandLYP exchange-correlation functional and the starting geometry provided by García.[163, 223, 447, 485]. The double- ζ basis 6-31G(d)[486] was employed for hydrogen, carbon, oxygen and nitrogen, the augmented 6-31+G(d)[487, 488] basis set for chlorine and the LANL2DZ basis with corresponding effective core potential for ruthenium.[489, 490] The RIJ approximation with corresponding auxiliary basis set was used to speed up the calculations.[389, 464] Initial and maximum trust radius Δ were set to $0.3 a_0$ (rad).

The optimization was started in the bright S_9 state ($\Delta E = 4.08 \text{ eV}$, $f = 0.1251$), corresponding to a ligand-to-metal-charge-transfer (LMCT) excitation from π_{tpy} and $p_{\text{Cl,ax}}$ orbitals into an antibonding $\pi_{\text{Ru,NO}}^*$ orbital; results are shown in Figure 13.10. The NO group tilts down, and the Ru-N-O angle decreases from 176.4° to 145.5° along the optimization. Several root flips occur and the final ES, e.g., the respective LMCT at the SP is the S_6 . García reported the need for 619 optimization cycles, whereas pysisyphus only needs 28 cycles to reach a SP, while overachieving on the RMS (maximum) of the Cartesian gradient with $3 \times 10^{-6} E_h a_0^{-1}$ ($1.9 \times 10^{-5} E_h a_0^{-1}$), again showing a marked improvement.[223]

Just by visually inspecting, the CDDs of the initial S_9 and the final S_6 in Figure 13.10, seem quite different and it may be assumed that the ES tracking failed. But analyzing the overlaps reveals that they never drop below 0.85 and are usually well above 0.90, confirming a successful state-tracking. This example clearly shows that small differences in ES character between successive optimization cycles may amount to big differences

between the first and the final cycle, highlighting again the need for a robust automated state tracking procedure.

If desired, pysisyphus offers easy CDD visualization along the optimization, as it is also interfaced to Multiwfn[491] and Jmol[492], allowing automated calculation and rendering of CDDs for Gaussian, ORCA and Turbomole.[121, 122, 384]

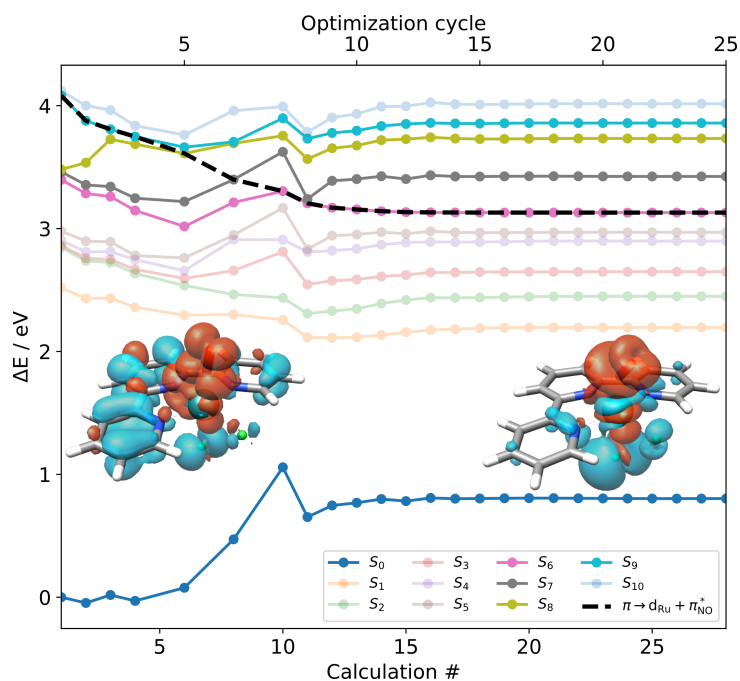


Figure 13.10: Electronic energies of the ground and the first ten excited singlet states of a ruthenium nitrosyl complex (**RuNO**) along the optimization of the bright S_9 , with respect to the ground state energy at the first cycle. The tracked excited state is indicated by a dashed black line. Excited states that do not cross with the state of interest are shown with reduced opacity. Every marker corresponds to an optimization cycle, and missing markers indicate root flips. CDDs illustrate the excited state character at the start and the end of the optimization; electron density is excited from blue to red.

13.3.3 Platinum Complexes

Modifying ligands in transition metal complexes, e.g., by substitution with electron-donating or electron-withdrawing groups, influences their photophysical properties considerably. By adding such electron donating or withdrawing groups to the triphenylamine (TPA) moiety in a rhenium complex, Larsen reported the effective emission energy

tuning from a short-lived $^1\text{ILCT}$ state (intra-ligand-charge-transfer).[493] In an effort to adjust the interaction of ILCT and metal-to-ligand-charge-transfer (MLCT) states in *fac*-[Re(L)(CO) $_3$ (α -diimine)] $^{n+}$, Shillito investigated the role of the ancillary ligand L.[494] The α -diimine ligand corresponds to 1,10-phenanthroline, with TPA appended in 5 position (phen-TPA). Recently, the effect of further modifying TPA in the phen-TPA ligand by electron-donating methoxy or electron-withdrawing cyano-groups on the photophysics of two rhenium and platinum complexes was analyzed by a combined experimental and computational study.[8]

Herein, optimizations of two excited triplet states for the two platinum complexes **Pt-TPA-OMe** and **Pt-TPA-CN** (see Figure 13.8d) are presented, thus, expanding the application of pysisyphus to excited state optimizations of triplet nature.

All quantum chemical calculations were performed using Gaussian 16.[384] Ground state equilibrium structures were obtained at the DFT level of theory utilizing the B3LYP35 functional,[495–498] comprising 35 % of exact-exchange, 58.5 % of non-local B88[163] exchange and the LYP correlation.[447] The effective core potential MWB-60[499] and its corresponding valence basis set were used for platinum, the 6-31G(d) basis set was employed for all other atoms.[486] Excited state properties for the first 10 triplet states of **Pt-TPA-OMe** and the first 25 triplet states of **Pt-TPA-CN** were obtained by TD-DFT from a singlet reference state. Solvent effects (CH_2Cl_2 $\epsilon = 8.93$, $n = 1.4070$) were considered by means of the integral equation formalism of the polarizable continuum model.[500] Dispersion interactions were taken into account by the D3-model with Becke-Johnson damping.[382, 383] The initial (maximum) trust radius Δ was set to $0.05 a_0$ (rad) ($0.3 a_0$ (rad)).

Results of both optimizations are shown in Figure 13.11. Optimizing the T_9 of **Pt-TPA-CN** to a SP took 43 optimization cycles, as the initial ES becomes the T_8 at the SP. Compared to **RuNO** with 34 atoms and 384 basis functions, where only the first 10 excited states were considered, **Pt-TPA-CN** is a much larger system with 89 atoms, 872 basis functions and 15 additional excited states, showing that pysisyphus in conjunction with WFOs can also be employed to optimize sizeable molecular systems. Optimizing the T_3 of **Pt-TPA-OMe** to a SP point took 35 cycles, and no state switching occurred. Successful state tracking is confirmed by the CDDs shown in Figure 13.11, as they are very similar between the start and the end of the optimizations in both cases.

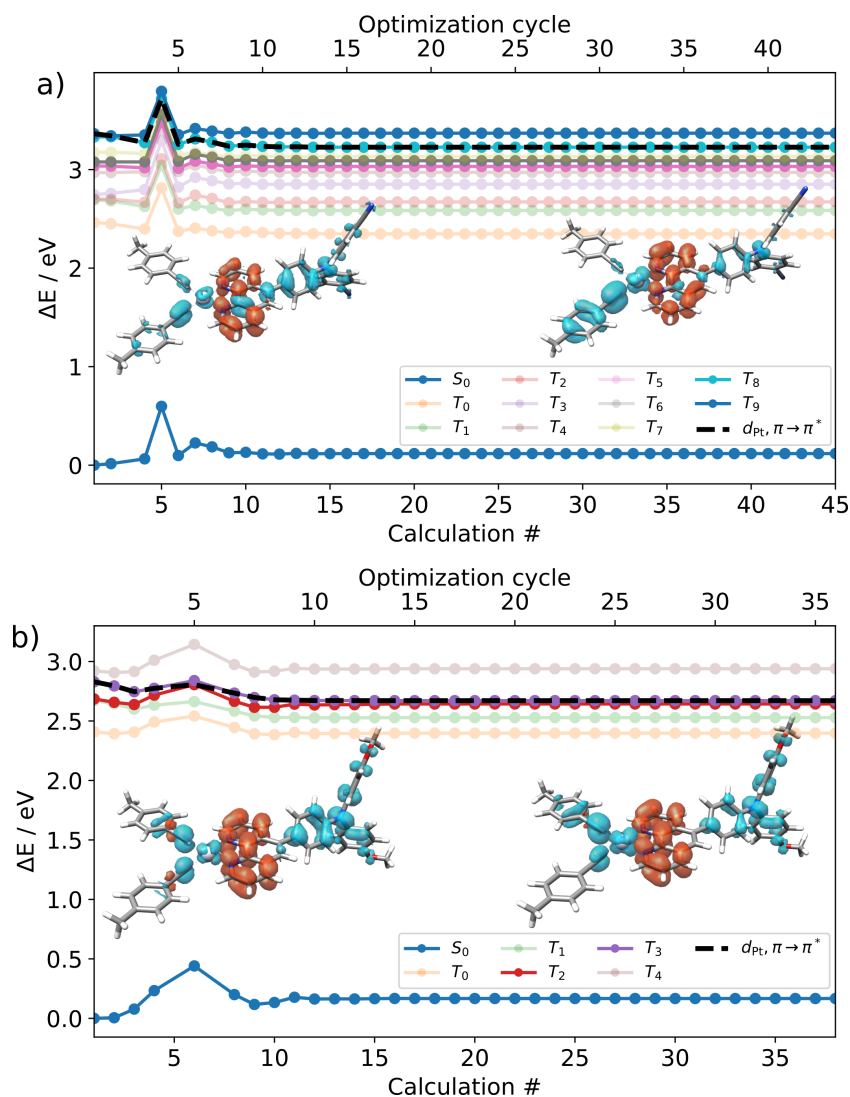


Figure 13.11: Electronic energies of the singlet ground state and a) the first ten triplet states of **Pt-TPA-CN** along the optimization of the T_9 and b) the first five triplet states of **Pt-TPA-OMe** along the optimization of the T_3 , with respect to the ground state energy at the first cycle. The tracked excited state is indicated by a dashed black line. Excited states that do not cross with the state of interest are shown with reduced opacity. Every marker corresponds to an optimization cycle, and missing markers indicate root flips. CDDs illustrate the excited state character at the start and the end of the optimization; electron density is excited from blue to red.

13.4 Ground State Calculations - Biaryl Cross-Coupling

Pysisyphus' capabilities to obtain reaction coordinates was already outlined in section 13.2.5. Here, the calculation of a GS reaction coordinate for the photoreaction discussed in chapter 12 is presented, as it is an example for a complex and computationally challenging reaction, where three bonds are broken and one bond is formed. Even though the true reaction coordinate involves ESs, the GS coordinate is a good approximation to it. The unsubstituted *N*-benzylbenzenesulfonamide **1b** (compound **1p** in [2]) was chosen, as this allows all calculations to be performed in a timely manner, even on common desktop hardware.

All DFT calculations were performed in ORCA 4.2.0[121] with the range-separated exchange correlation functional CAM-B3LYP and the def2-SVP double- ζ basis set.[381, 501] The RIJCOSX approximation was employed to speed up the calculations.[291] Dispersion interactions were taken into account by the D3-model with Becke-Johnson damping.[382, 383] To reduce noise in the calculated gradients arising from the numerical integration in DFT, tight convergence criteria for the self consistent field iterations and finer integration grids were used (keywords `tightscf`, `grid4`, `finalgrid5`, `gridx6`).

The GSM in DLC, as implemented in *pysisyphus*, was used to obtain a suitable TS guess for the biaryl cross-coupling reaction (see Figure 13.8b). Initial molecular geometries for the GSM were taken from the endpoints of an IRC, calculated in an earlier study[2] of the system at the CAM-B3LYP/def2-TZVP level of theory. Both molecular geometries were pre-optimized for 5 cycles in RIC using the standard method, outlined in section 13.2.1. A conjugate gradient optimizer[300] was employed to relax the string to the MEP. The string was grown to a total length of 13 images (11 inner images). First and last image of the string remained fixed over the course of the optimization. After the string was fully grown, optimization was terminated and the HEI was used as initial guess for a TS optimization.

Subsequent TS optimization in RIC was carried out using RS-IRFO. Analytical Hessians were recalculated at every 5th optimization cycle. The nature of the obtained TS as first-order saddle point was verified by a Hessian calculation.

IRCs in mass-weighted Cartesian coordinates were traced from the TS to confirm that the TS connects presumed educts and products of the biaryl cross-coupling reaction. A predictor-corrector integrator utilizing Hessian information was used to integrate an IRC (eq. (11.1)) with a step length of $0.1 a_0$. [332, 346] Corrector integration on the DWI surface was carried out using the Radau integrator, as provided by `SciPy`. [352, 441]

Analytical Hessians were recalculated every 10th IRC cycle. After the IRCs converged to a Cartesian gradient RMS of $1.0 \times 10^{-3} E_h a_0^{-1}$, its endpoints were optimized to SPs. Along the IRC towards the products of the reaction, the TS fragments into three separate molecules. If requested by the user, pysisyphus can automatically detect the fragments and optimize them separately after convergence of the IRC is achieved.

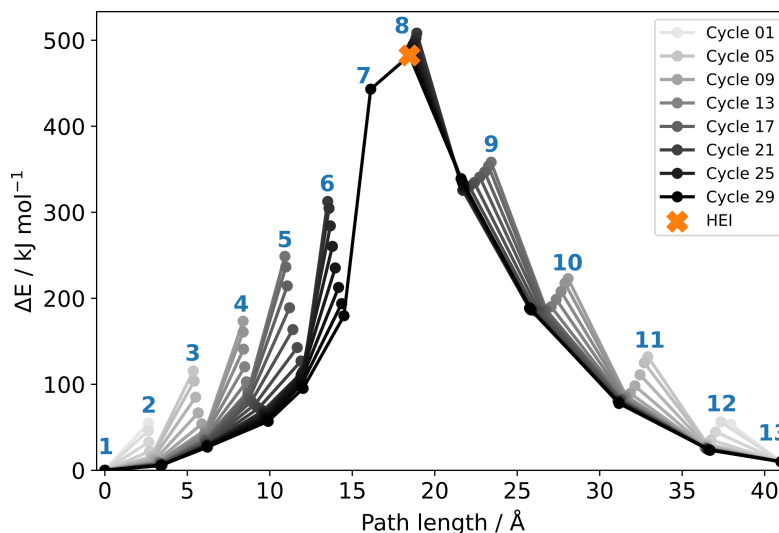


Figure 13.12: Image energies of the growing string, describing the biaryl cross-coupling reaction over the course of the string optimization, with respect to the energy of the first image in the first cycle. Earlier cycles are shown in a lighter shade, later cycles in a darker shade. Images are enumerated by blue numbers. Inner images are introduced (grown) in later cycles. Image 1 and 13 remained fixed, while the other images were allowed to relax. The HEI was employed as guess for a subsequent TS optimization and is highlighted in orange.

Results of the calculations are shown in Figures 13.12 to 13.14. The two starting images were pre-optimized for 5 cycles, lowering their RMS Cartesian gradient from $6.4 \times 10^{-3} E_h a_0^{-1}$ to $2.0 \times 10^{-4} E_h a_0^{-1}$ for image 1 and from $6.8 \times 10^{-3} E_h a_0^{-1}$ to $3.9 \times 10^{-4} E_h a_0^{-1}$ for image 13. As educts and products will be optimized later on, starting from the IRC endpoints, it is not necessary to optimize the starting images tightly. If one of the starting images consists of multiple weakly bound fragments, the optimization may even fail, as such optimizations are notoriously difficult to converge.[272] Figure 13.12 displays the energy profile of the string images over the course of the optimization. The RMS of the DLC gradient of the string images quickly drops from $7.7 \times 10^{-3} E_h a_0^{-1}$ in the first cycle and never exceeds $6.0 \times 10^{-3} E_h a_0^{-1}$ after cycle 6, showing that the

gradual growing of new images avoids any high energy geometries. Image 7 is the last one to be grown and image 8 is finally selected as HEI and used for the TS optimization.

Calculation of a Hessian in RIC at the HEI revealed three significant negative eigenvalues. The overlap between the HEI tangent τ and the eigenvector belonging to the most negative eigenvalue was 0.93, indicating that the string was converged well enough for τ to be a good approximation to the reaction coordinate. In this case, the DM would also be expected to allow a successful TS optimization, as τ would be a very good guess for the initial dimer orientation N .^[290] An overlay of the HEI geometry and the optimized TS is given in Figure 13.13a, confirming that the HEI is already a good approximation to the true TS. The TS optimization converged in 16 cycles; besides the initial Hessian at the HEI, three additional Hessians were calculated. An optimization starting from the same HEI without additional Hessian calculations took 50 cycles to converge the correct TS, but still needed roughly 10% less computational time compared to the optimization with Hessian recalculations (73 min vs. 65 min). If analytical Hessians are available for the chosen level of theory, it is usually beneficial to recalculate them periodically for effective optimizations.

Starting from the TS, an IRC calculation (see Figure 13.14) confirmed that the optimized TS indeed connects the sulfonamide **1b** educt and the biaryl coupling product. Without taking into account any thermochemical corrections, the reaction barrier in the GS, as calculated in the IRC, is 335 kJ mol⁻¹ and thus the cross-coupling reaction cannot proceed in the GS. If the involvement of ESs is considered, the barrier height is substantially lowered in the S_1 and the coupling reaction can take place. A full discussion of the reaction mechanism is found in chapter 12 and reference [2].

The example presented here exemplifies that full reaction paths can be obtained in pysisyphus with minimal user intervention, by using robust and efficient algorithms. Starting from the pre-optimization and ending with the optimization of the IRC endpoints, all calculations took 9.6 h on a desktop computer equipped with 8 physical CPU cores (Ryzen 1700X CPU).

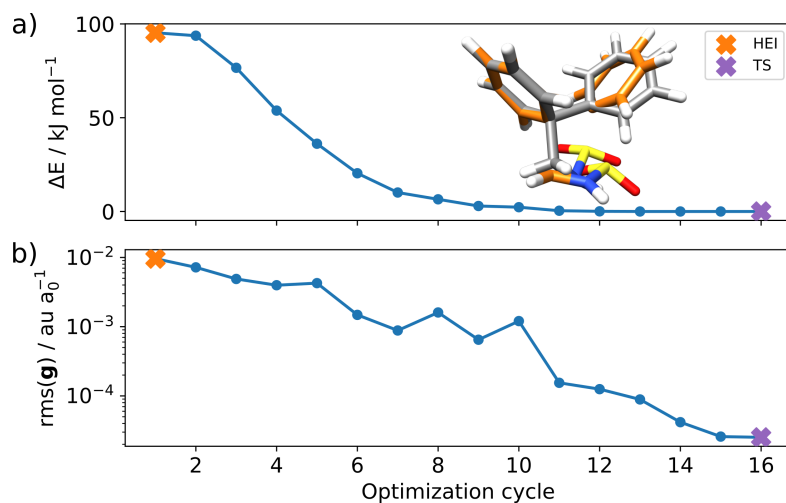


Figure 13.13: TS optimization of the biaryl cross-coupling reaction started from HEI guess using RS-IRFO: a) Energy change between HEI and optimized TS and b) RMS of the Cartesian gradient over the course of the optimization. The molecular geometries of HEI guess (in orange) and the optimized TS is shown in the upper panel.

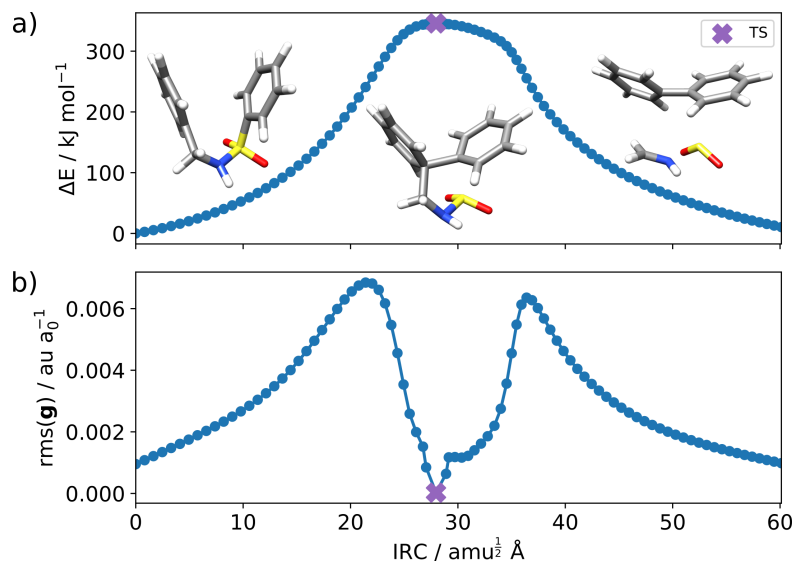


Figure 13.14: Forward and backward IRCs of the biaryl cross-coupling reaction started from the optimized TS, using a predictor-corrector integrator: a) Energy profile with respect to the educt energy at the start of the IRC and b) RMS of the Cartesian gradient along the IRC.

13.5 Implementation

Pysisyphus is licensed under GNU GPL 3 and implemented in python 3.[413, 414, 502] Python is a popular, interpreted, high-level programming language that found widespread adoption in the chemistry community.[124, 272, 503–507] It features a rich ecosystem of mature, well tested and versatile libraries for scientific computing.[441, 508]

Inputs to pysisyphus can be given via simple to create YAML files or it can be used as a python library, to implement custom workflows, tailored to the users needs.

Required electronic energies and their derivatives are not calculated by pysisyphus itself, but by calling external QC packages. ES gradients and ES-tracking are currently available for Gaussian 16[384], ORCA 4[121], TURBOMOLE 7[122] PySCF[504] and the tight-binding code DFTB+.[206] GS calculations are possible with the already mentioned packages, Psi 4[503] and the fast semiempirical packages MOPAC2016[509] and xtb.[418] An even broader variety of QC packages is available through the QCEngine project, however with varying degree of supported features.[510] QCEngine provides basic wrappers for many additional codes, for instance NWChem,[511] GAMESS[512] and Q-Chem[513]. Advanced features like reusing wavefunction information from previous calculations and ES tracking is currently only possible with native pysisyphus calculators, nonetheless the applicability of pysisyphus is greatly increased through QCEngine. Parallel execution of the many required gradient calculations for COS methods is possible through the dask library, thus available resources like HPC clusters can be utilized efficiently.[514]

Quick testing and rapid prototyping of new methods in pysisyphus is possible through analytical implementations of many potentials like the Lennard-Jones potential or the London-Eyring-Polanyi-Sato (LEPS) method, as their evaluation time is negligible compared to ab initio calculations and even semiempirical methods.[71] New 2D-potentials for testing can be easily specified just by their energy expression. First and second derivatives are then automatically determined by the *sympy* computer algebra system.[515]

Using internal coordinates requires the calculation of the so called Wilson- \mathbf{B} matrix that relates changes of Cartesian coordinates to changes in internal coordinates.[232, 278] Transforming a Cartesian Hessian to internal coordinates also requires derivatives of the \mathbf{B} matrix-elements with respect to the Cartesian coordinates. Pysisyphus uses code generation to avoid error-prone hand coding of these lengthy expressions. Algebraic expressions for the first and second derivatives of stretches, (linear) bends and dihedrals with respect to Cartesian coordinates were generated with *sympy*, simplified using common subexpression elimination and translated in a python module. Figure 13.15

shows valid python code that generates all expressions for the first and second derivatives of a dihedral coordinate with respect to Cartesian coordinates of the atoms making up the dihedral. Linear bends are implemented as given by Hoy.[273–275]

```
import sympy as sym
from sympy.vector import CoordSys3D

m0, m1, m2, n0, n1, n2, o0, o1, o2, p0, p1, p2 = sym.symbols("m:3 n:3 o:3 p:3")

Sys = CoordSys3D("Sys")

M = Sys.origin.locate_new("M", m0*Sys.i + m1*Sys.j + m2*Sys.k)
N = Sys.origin.locate_new("N", n0*Sys.i + n1*Sys.j + n2*Sys.k)
O = Sys.origin.locate_new("O", o0*Sys.i + o1*Sys.j + o2*Sys.k)
P = Sys.origin.locate_new("P", p0*Sys.i + p1*Sys.j + p2*Sys.k)

U = M.position_wrt(O)
V = N.position_wrt(P)
W = P.position_wrt(O)

U_ = U.normalize()
W_ = W.normalize()
V_ = V.normalize()

phi_u = sym.acos(U_.dot(W_))
phi_v = sym.acos(-W_.dot(V_))
q_d = sym.acos(U_.cross(W_).dot(V_.cross(W_))/(sym.sin(phi_u)*sym.sin(phi_v)))

dx_d = (m0, m1, m2, o0, o1, o2, p0, p1, p2, n0, n1, n2)
deriv1 = sym.derive_by_array(q_d, dx_d) # deriv1.shape == (12,)
deriv2 = sym.derive_by_array(deriv1, dx_d) # deriv2.shape == (12, 12)
```

Figure 13.15: Python code for the sympy computer algebra system to generate first and second derivatives for a primitive dihedral coordinate with respect to the Cartesian coordinates of the atoms making up the dihedral.

The code is developed mainly in an object-oriented way with superclasses for (TS) optimizations, IRC calculations, COS methods, line searches and interpolation, providing commonly needed functionality. Actual algorithms like optimizers and IRC integrators are implemented as subclasses, specifying only the functionality specific to the respective method. This way, pysisyphus is extended easily with new methods, as the existing infrastructure from the superclasses can be reused.

Interoperability with the well-established ASE package is possible by an automated conversion of the central `Geometry` class from pysisyphus to the central `Atoms` class in ASE.[124] Hence, functionality unique to pysisyphus, e.g., ES-tracking can be combined with ASE optimizers, increasing the applicability of pysisyphus.

While interfacing to ASE requires the user to write additional python code, pysisyphus also offers a socket-interface, supporting a superset of the `i-PI` communication protocol.[516, 517] The original protocol is restricted to simultaneous sending of energy and forces. Pysisyphus extends it to also support sending Hessians or energies only, as required for TS-optimizations and line searches. According to the ASE documentation, a

variety of quantum chemical codes implement the (original) i -PI protocol, e.g., Quantum Espresso,[518, 519] Siesta,[520] DFTB+[206] and NWChem.[511, 521] Communication via sockets was successfully tested with DFTB+, for which *pysisyphus* can act as external optimizer.

The present ES-tracking functionality is easily accessible, as interfaces to new programs only have to provide the MO coefficients and the one-electron transition density matrix. Care was taken to allow a quick and easy visualization of running and completed calculations via the `pysisplot` command. A subset of possible visualizations is shown in Figure 13.16.

Fully automated interpolation of molecular geometries with the methods discussed in section 8.2, including interpolation in DLC, is available through a simple to use command line interface. This way interpolated paths, e.g. for Marcus theory, are easily obtained.[90]

Pysisyphus is developed using continuous integration and features an extensive test suite, to ensure that further code development does not break existing functionality and introduces new bugs.[522] The code is fully available at <https://github.com/eljost/pysisyphus> and is easily installed from the python Package index with `pip install pysisyphus`. Comprehensive documentation and examples are found online.⁴ Contributions and bug reports are welcome. To this date, *pysisyphus* already received a code contribution from an external researcher.[523]

⁴ <https://pysisyphus.readthedocs.io>

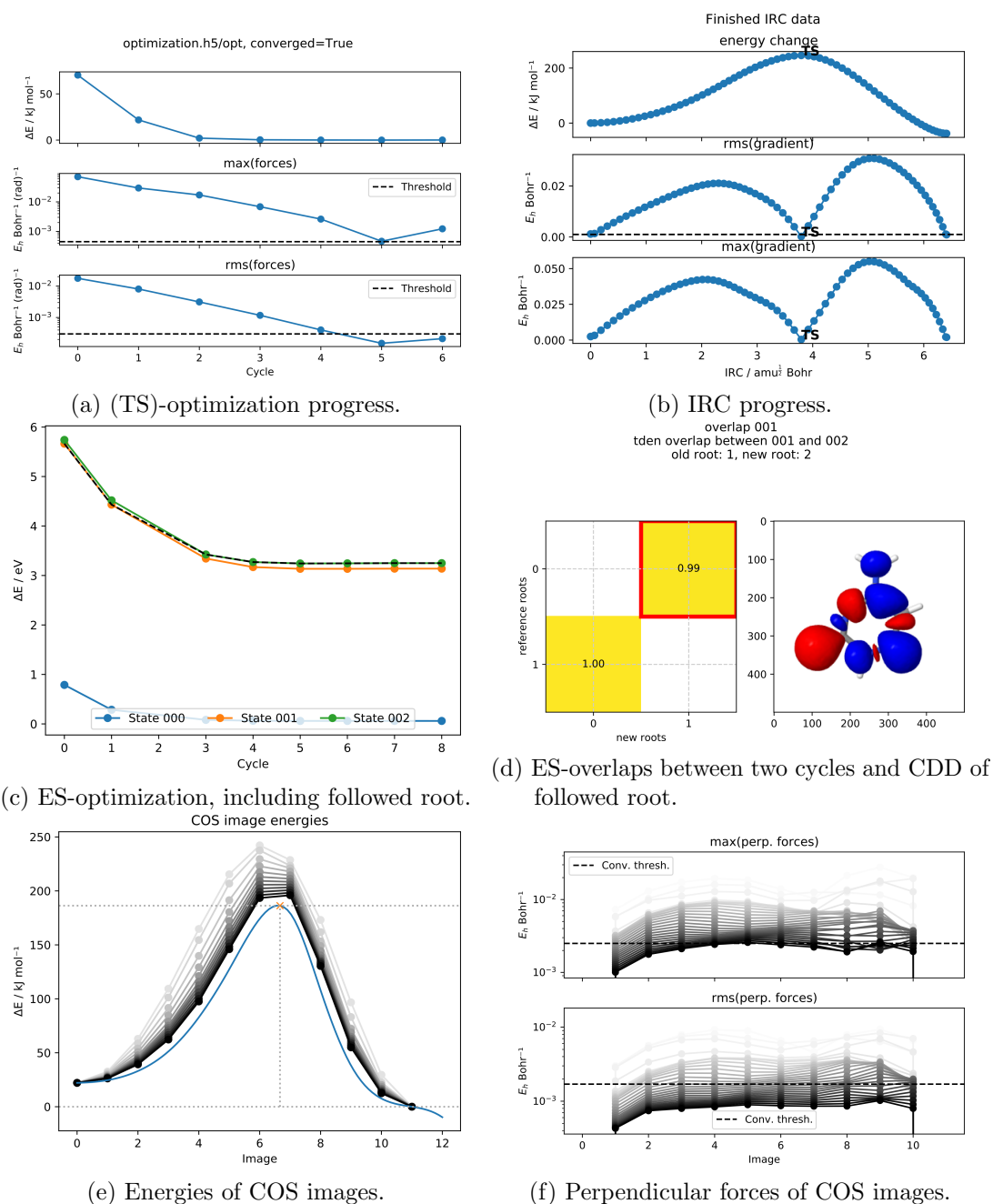


Figure 13.16: Selection of possible visualizations available via the `pysisplot` command. Besides removing superfluous whitespace, figures were used, as produced by `pysisyphus`. While not intended for direct inclusion into publications, these visualizations allow a quick control of (running) calculations.

13.6 Summary

This chapter described the capabilities and implementation of *pysisyphus* – an external optimizer for stationary points and reaction coordinates in ground and ESs. By providing ES tracking capabilities and optimization in internal coordinates, *pysisyphus* allows highly efficient ES optimizations. The performance of *pysisyphus* was verified extensively against several test sets and previously published results for ES optimizations of cytosin and a ruthenium nitrosyl complex. Furthermore, it was applied to the optimization of excited triplet states of two sizeable platinum complexes, (long-lived) key states in their ES relaxation cascades.[8] The ability of *pysisyphus* to obtain full reaction paths by means of COS methods and IRC calculations was demonstrated for a real world example in the electronic ground state, but all presented methods are also applicable in ES calculations. Besides the already mentioned platinum complexes, *pysisyphus* was already successfully applied for elucidating the reaction mechanisms of (metal-free) biaryl cross-couplings and iron(0) mediated (3+2) cycloaddition of thiochalcones.[2, 524]

Possible extensions of *pysisyphus* would be the generalization of ES tracking to arbitrary multiplicities and support for wavefunctions beyond CIS, as they occur in complete active space self consistent field (CASSCF) calculations. By combining the interpolation and ES optimization capabilities of *pysisyphus*, the automated calculation of rate constants, e.g. in the scope of electron transfer processes using semi-classical Marcus theory, could be realized. A pure python implementation of Plassers *wfoverlap*[225] program is already underway.[525] By incorporating changes of the WFO algorithm proposed by Sapunar, overlap calculations for configuration interaction singles (CIS) type wavefunction could be made even more efficient.[226]

14 Summary

Chemical reactivity of atoms, molecules and ions is governed by their underlying potential energy surface (PES). N atoms in the gas-phase give rise to a PES with $3N - 6$ degrees of freedom ($3N - 5$ for linear arrangements). Calculating the whole PES within reasonable bounds, is impossible for all but the smallest N . Usually, only parts of the full PES can be studied, namely stationary points (SPs) and the minimum energy paths (MEPs) connecting them. By comparing energies of SPs and their separating barriers, conclusions regarding possible reactions mechanism, or their infeasibility, can be drawn. Taking excited states (ESs) into account leads to further complications, as now multiple PESs have to be considered and root flips between different ESs may occur, requiring effective ES-tracking.

Part II describes the required methods to locate SPs and MEPs on PESs, by using surface-walking, chain-of-states (COS) optimization and intrinsic reaction coordinate (IRC) integration.

Special focus was set on ES-tracking in chapter 4, where three approaches are outlined and an adaptive formalism to update the reference cycle is presented. State-tracking by wavefunction overlaps is the most general approach, but computationally also the most demanding, as many determinant calculations may be required.

Different coordinate systems, including their advantages and disadvantages are discussed in chapter 6. The most promising coordinates for molecular optimizations are redundant internal coordinates (RIC), as they usually exhibit small coupling and allow easy estimation of initial model Hessians. Drawbacks of internal coordinates in general, are that they are not unambiguously defined and their need for an iterative internal-Cartesian back-transformation that may fail to converge.

Chapter 7 briefly reviews preconditioning. Preconditioning shows a different route to the omnipresent Newton step (eq. (5.3) on page 31) in molecular optimizations, apart from the usual derivation via Taylor expansion. Convergence of optimizations carried out in Cartesian coordinates is often greatly improved by preconditioning. Optimizing Baker's transition state (TS) set using the dimer method (DM) and preconditioned

limited-memory BFGS (LBFGS) (section 13.2.4, Table 13.7) showed that preconditioning can rival the performance of optimizations carried out in internal coordinates.

A COS comprises several images, discretizing a MEP, onto which it can be gradually relaxed. The highest energy image (HEI) of a relaxed COS is often a good guess for subsequent TS optimizations. If converged tightly, a COS may even be a good approximation to the true MEP. Commonly employed COS methods (nudged elastic band (NEB) and string method (SM)), including their variants are discussed in chapter 8. Obtaining TSs by utilizing Hessian information is outlined in chapter 9. TS optimization using only first derivatives of the energy by means of the DM is reviewed in chapter 10. Chapter 11 describes how to integrate an IRC, the path of steepest descent in mass-weighted Cartesian coordinates. IRCs are usually easily interpreted, as they don't exhibit complicated rotational and vibrational motions. Similar to normal optimizations, IRC integrators (Gonzalez-Schlegel second-order algorithm (GS2) and Euler predictor-corrector (EulerPC)) utilizing Hessian information can sustain longer step lengths, compared to integrators relying only on the energy gradient.

Results of this thesis are presented in Part III. This thesis makes two contributions to the field of photochemistry: chapter 12 provides a possible ES reaction mechanism for the biaryl cross-coupling reaction shown in Figure 14.1 and offers a plausible explanation for its high regioselectivity.

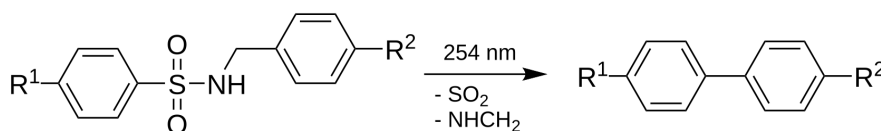


Figure 14.1: Biaryl cross-coupling photoreaction.

The coupling reaction was investigated for two substrates: **1a**, affording significant photoproduct yields and the unsubstituted **1b**, providing only photoproduct traces. Their ground state (GS) PESs were sampled by simulated annealing conformer searches and relaxed scans, leading to the identification of two major structural motifs: Linear conformers, characterized by increased distances between the C5 – C1 carbons supposed to couple and horseshoe conformers exhibiting decreased C5 – C1 distances. According to the conformer search, the horseshoe motif is preferred for **1a**, while a linear minimum energy conformer is predicted for **1b**. A five-membered TS in the GS was obtained for both substrates. IRC integration revealed high barriers, preventing a GS reaction. ES calculations along selected IRC geometries confirmed the existence of several ESs

that facilitate the photoreaction with greatly reduced barriers. Compared to **1a**, the relevant ESs in **1b** are shifted hypsochromically and exhibit lower oscillator strengths, thus impeding the photoreaction which is in full accordance with the experimental results.

The second contribution is the development pysisyphus (chapter 13), an external optimizer implemented in python, aware of ESs and thus the core of this thesis. Besides the recently proposed SDNTO program by García et al.,[223] which is restricted to a steepest descent optimizer and does not support RIC, the author of this thesis is not aware of other external optimizers tailored to deal with ESs. All ES-tracking approaches outlined in chapter 4 (wavefunction overlaps, transition density matrix (TDEN) overlaps and natural transition orbital (NTO) overlaps) are implemented in pysisyphus.

Pysisyphus features comprehensive documentation and is developed using contemporary practices like continuous integration and unit testing, to assert the correctness of the software.

Chapter 13 presents extensive benchmarks, confirming that pysisyphus is ahead of, or at least competitive with similar implementations. Optimization of minima was benchmarked for Baker’s test set and the more challenging S22 set of Hobza.[268, 423] TS optimization performance was investigated for Baker’s TS test set,[315] using two different approaches: utilizing-Hessian information and utilizing only first derivatives, by means of the DM. Finally, pysisyphus’ ability to obtain TSs from preceding COS optimizations was verified against a diverse test set, containing educts and products of 20 reactions.

Results for several ES optimizations are presented in section 13.3. Compared to SDNTO, pysisyphus shows greatly improved performance for ES optimizations. Optimizing the bright S_9 of **RuNO** required only 28 cycles, compared to 619 cycles reported for SDNTO.[479] Applicability of the ES-optimizer to triplet states of sizable systems was demonstrated for two Pt-complexes in section 13.3.3.

Care was taken to integrate pysisyphus into the bigger ecosystem of computational chemistry software, by providing an Atomic Simulation Environment (ASE) interface and supporting an extended version of the i-PI socket protocol, allowing users to leverage the many thousand development hours already spent on these projects.

Internal coordinates were implemented using code generated by the sympy computer algebra system, to avoid error prone manual coding of the lengthy but necessary internal coordinate derivatives.

Besides the calculation of energies and their derivatives, which are carried out using external quantum chemistry (QC) software, pysisyphus is self-contained. It does not rely

14 Summary

on optimization algorithms implemented in the QC packages, thus offering full control, if required by the user. Pysisyphus implements a multitude of relevant algorithms for surface-walking, COS optimizations and IRC integration. All algorithms discussed in chapters 5 to 11, and many more, are available in pysisyphus. Further development of pysisyphus is especially attractive, as it would expand the applicability of all interfaced QC packages.

15 Zusammenfassung

Die chemische Reaktivität von Atomen, Molekülen und Ionen wird durch ihre unterliegende Potentialhyperfläche (PES) bestimmt. N Atome in der Gasphase werden durch eine PES mit $3N - 6$ Freiheitsgraden beschrieben ($3N - 5$ für lineare Anordnungen). Berechnung der vollständigen PES, in angemessenen Grenzen, ist nur für kleinste Systeme möglich. Überlicherweise können nur Ausschnitte der PES untersucht werden: Stationäre Punkte (SPs) und die sie verbindenden Minimal-Energie-Pfade (MEPs). Durch Vergleich der Energien von SPs und der sie trennenden Barrieren können Aussagen über die Möglichkeit, oder Unmöglichkeit, von Reaktionsmechanismen getroffen werden. Werden zum elektronischen Grundzustand noch zusätzlich angeregte Zustände (ESs) berücksichtigt, verkompliziert sich die Interpretation der PESs, da nun auch Wechsel zwischen verschiedenen elektronischen Zuständen auftreten können.

Die vorliegende Arbeit beschäftigt sich mit der Implementierung von Methoden zur PES-Aufklärung in Grund- und angeregten Zuständen, sowie ihrer Anwendung auf photochemische Fragestellungen.

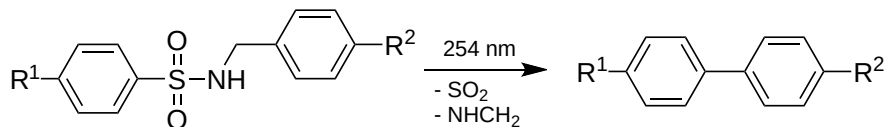
Der Theorieteil diskutiert die benötigten theoretischen Grundlagen, um SPs und MEPs auf PESs zu finden. Dabei können drei Algorithmenklassen unterschieden werden:

- Schreiten entlang der PES (*surface walking*): Eine vermutete Startgeometrie wird zum nächstgelegenen SP (Minimum oder Sattelpunkt) optimiert.
- Optimierung einer Kette von Zuständen (*chain-of-states*, COS): Eine Kette von mehreren Geometrien approximiert einen MEP und wird gemeinsam optimiert, bis alle Geometrien auf dem MEP liegen.
- Integration einer intrinsischen Reaktionskoordinate (IRC): Pfad des steilsten Abstieges in massengewichteten, kartesischen Koordinaten, üblicherweise ausgehend von einem Sattelpunkt, hin zu Edukt(en) und Produkt(en).

Ein besonderer Fokus der Arbeit liegt auf Methoden, um einen initial gewählten ES entlang einer Optimierung zu verfolgen (*state-tracking*), auch über Kreuzungen mit anderen Zuständen hinweg. Der Ergebnisteil diskutiert die Resultate der vorliegenden Dissertation in zwei Kapiteln.

Biaryl-Kopplungs-Photoreaktion

Kapitel 12 beschäftigt sich mit der Aufklärung des Reaktionsmechanismus einer Biaryl-Kopplungs-Photoreaktion. Mittels Konformerensuche und Optimierungen unter Nebenbe-



dingungen (*relaxed scans*) konnten zwei wichtige Struktur motive identifiziert werden, welche die Sulfonamid-Edukte einnehmen: lineare Geometrien, mit großem Abstand zwischen den zu koppelnden Kohlenstoffatomen und Hufeisen-Geometrien, mit stark verringertem Abstand. Für den elektronischen Grundzustand wurde ein fünf-gliedriger Übergangszustand gefunden, welcher die Reaktion vermittelt. Eine IRC-Integration zeigte jedoch die Existenz einer hohen Barriere, welche die Reaktion im Grundzustand unmöglich macht. Durch Berechnungen von ESs entlang des IRCs wurden verschiedene Zustände erhalten, in denen die Barrierehöhe stark reduziert ist, so dass die Reaktion effizient stattfinden kann. Die Ergebnisse der Berechnungen zeigen eine gute Überstimmung mit experimentellen Messungen.

Pysisyphus

Kapitel 13 stellt die Software pysisyphus vor, einen externen Optimierer mit spezieller Unterstützung für die Verfolgung von ESs. Pysisyphus erlaubt *state-tracking* mittels Überlapps zwischen Wellenfunktionen, Übergangsdichte-Matrizen oder *natural transition orbitals*. Für verschiedene ES-Optimierungen zweier Referenzsysteme (Cytosin und ein Ruthenium-Nitrosyl-Komplex) konnte der benötigte Rechenaufwand im Vergleich zur Literatur auf 3.1% bis 5.6% reduziert werden. Die Anwendbarkeit der vorliegenden Implementierung für Optimierungen von Triplett-Zuständen wurde für zwei Platin-Komplexe gezeigt.

Weiterhin implementiert pysisyphus eine Vielzahl von Algorithmen für *surface-walking*, COS-Optimierung und IRC-Integration. Die Korrektheit der vorliegenden Implementierungen wurde ausgiebig gegen eine Vielzahl von Referenzsystemen verifiziert. Neben den untersuchten Referenzsystemen wurde die Anwendbarkeit von pysisyphus für die Sattelpunktsuche auch für die o.g. Biaryl-Kopplungs-Reaktion gezeigt.

Pysisyphus wurde mittels moderner Praktiken wie *unit-tests*, *continuous integration* und Code-Generierung entwickelt.

A Appendix

A.1 Numerical integration of the Local Quadratic Approximation

The IRC

$$\frac{d\mathbf{x}(s)}{ds} = -\frac{\mathbf{g}(\mathbf{x})}{|\mathbf{g}(\mathbf{x})|} \quad (\text{A.1})$$

is parametrized by the arc length s . Assuming $3N$ mass-weighted Cartesians the arc length is calculated as[335]

$$ds^2 = \sum_{i=1}^{3N} dx_i^2 . \quad (\text{A.2})$$

Pechukas noted that integrating

$$\frac{d\mathbf{x}(t)}{dt} = -\mathbf{g}(\mathbf{x}) \quad (\text{A.3})$$

yields the same paths, as integration of eq. (A.1).[334] Eq. (A.3) can be related to eq. (A.1) via

$$\frac{d\mathbf{x}}{dt} = \frac{d\mathbf{x}}{ds} \frac{ds}{dt} \quad (\text{A.4})$$

Expanding $\mathbf{g}(\mathbf{x})$ to first-order around \mathbf{x}_0 and substituting into eq. (A.3) yields

$$\frac{d\mathbf{x}(t)}{dt} = -\mathbf{g}(\mathbf{x}_0) - \mathbf{H}(\mathbf{x}_0)(\mathbf{x} - \mathbf{x}_0) . \quad (\text{A.5})$$

For quadratic potentials eq. (A.5) is solved by

$$\mathbf{x}(t) = \mathbf{x}_0 + \mathbf{A}(t)\mathbf{g}(\mathbf{x}_0) . \quad (\text{A.6})$$

Matrix $\mathbf{A}(t)$ is defined as

$$\mathbf{A}(t) = \mathbf{U}_0\boldsymbol{\alpha}(t)\mathbf{U}_0^\top \quad (\text{A.7})$$

A Appendix

with \mathbf{U}_0 being the eigenvector matrix of $\mathbf{H}(\mathbf{x}_0)$ and $\boldsymbol{\alpha}(t)$ is a diagonal matrix with elements

$$\alpha_{ii} = \frac{e^{-\lambda_i t} - 1}{\lambda_i} \quad (\text{A.8})$$

where $\{\lambda_i\}$ are the eigenvalues of $\mathbf{H}(\mathbf{x}_0)$. From now on, $\mathbf{g}(\mathbf{x}_0)$ and $\mathbf{H}(\mathbf{x}_0)$ will be denoted as \mathbf{g}_0 and \mathbf{H}_0 . Substituting Eq. (A.6) in the right-hand side (RHS) of eq. (A.5) and multiplying from the left with \mathbf{U}_0^\top yields:

$$\mathbf{U}_0^\top \frac{d\mathbf{x}}{dt} = -\mathbf{U}_0^\top \mathbf{g}_0 - \mathbf{U}_0^\top \mathbf{H}_0 (\mathbf{x}_0 + \mathbf{A}(t)\mathbf{g}_0 - \mathbf{x}_0) \quad (\text{A.9})$$

$$= -\mathbf{U}_0^\top \mathbf{g}_0 - \mathbf{U}_0^\top \mathbf{H}_0 \mathbf{A}(t)\mathbf{g}_0 \quad (\text{A.10})$$

$$= -\mathbf{U}_0^\top \mathbf{g}_0 - \mathbf{U}_0^\top \mathbf{H}_0 \mathbf{U}_0 \boldsymbol{\alpha}(t) \mathbf{U}_0^\top \mathbf{g}_0 \quad (\text{A.11})$$

$$= -\mathbf{U}_0^\top \mathbf{g}_0 - \boldsymbol{\lambda}_0 \boldsymbol{\alpha}(t) \mathbf{U}_0^\top \mathbf{g}_0 . \quad (\text{A.12})$$

$\boldsymbol{\lambda}_0$ denotes a diagonal matrix containing the eigenvalues of \mathbf{H}_0 . Eq. (A.12) is further simplified to

$$\mathbf{U}_0^\top \frac{d\mathbf{x}}{dt} = -(\boldsymbol{\lambda}_0 \boldsymbol{\alpha}(t) + 1) \mathbf{U}_0^\top \mathbf{g}_0 \quad (\text{A.13})$$

$$\frac{d\mathbf{x}'}{dt} = -(\boldsymbol{\lambda}_0 \boldsymbol{\alpha}(t) + 1) \mathbf{g}'_0 \quad (\text{A.14})$$

where the prime denotes quantities transformed to the basis of the Hessian eigenvectors \mathbf{U}_0 . Matrix $\boldsymbol{\lambda}_0 \boldsymbol{\alpha}(t)$ is diagonal with elements

$$(\boldsymbol{\lambda}_0 \boldsymbol{\alpha}(t))_{ii} = \lambda_i \frac{e^{-\lambda_i t} - 1}{\lambda_i} \quad (\text{A.15})$$

$$= e^{-\lambda_i t} - 1 . \quad (\text{A.16})$$

Substituting eq. (A.16) into eq. (A.14) yields

$$\left(\frac{d\mathbf{x}'}{dt} \right)_i = -(e^{-\lambda_i t} - 1 + 1) g'_{0i} \quad (\text{A.17})$$

$$= -e^{-\lambda_i t} g'_{0i} . \quad (\text{A.18})$$

Arc length s satisfies the equation

$$\frac{ds}{dt} = \sqrt{\frac{d\mathbf{x}}{dt} \frac{d\mathbf{x}}{dt}} . \quad (\text{A.19})$$

A.2 Biaryl Cross-Coupling Results for **1b**

Together with eq. (A.18) and the fact that the (unitary) transformation $\mathbf{x}' = \mathbf{U}_0^\top \mathbf{x}$ is norm conserving ($\mathbf{x}'^\top \mathbf{x}' = \mathbf{x}^\top \mathbf{x}$), the final equation for integrating $\frac{ds}{dt}$ in the basis of the Hessian eigenvectors is obtained.

$$\frac{ds}{dt} = \sqrt{\sum_i g_{0i}'^2 e^{-2\lambda_i t}} \quad (\text{A.20})$$

A.2 Biaryl Cross-Coupling Results for **1b**

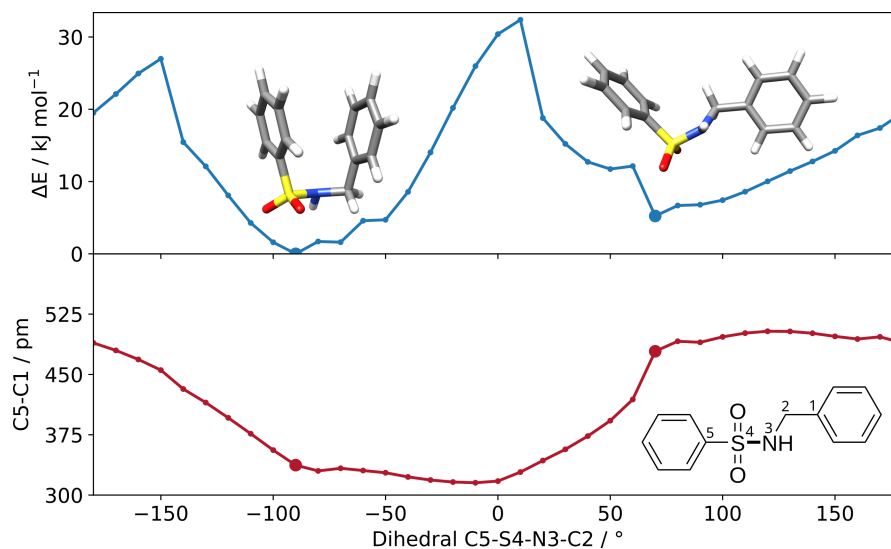


Figure A.1: Energy differences and C5 – C1 distances for the relaxed scan around the central dihedral (C5 – S4 – N3 – C2) in **1b** at the CAM-B3LYP/def2-TZVP level of theory. A horseshoe conformer is predicted as minimum energy geometry at $\phi = -90^\circ$ with a C5 – C1 distance of 337 pm.

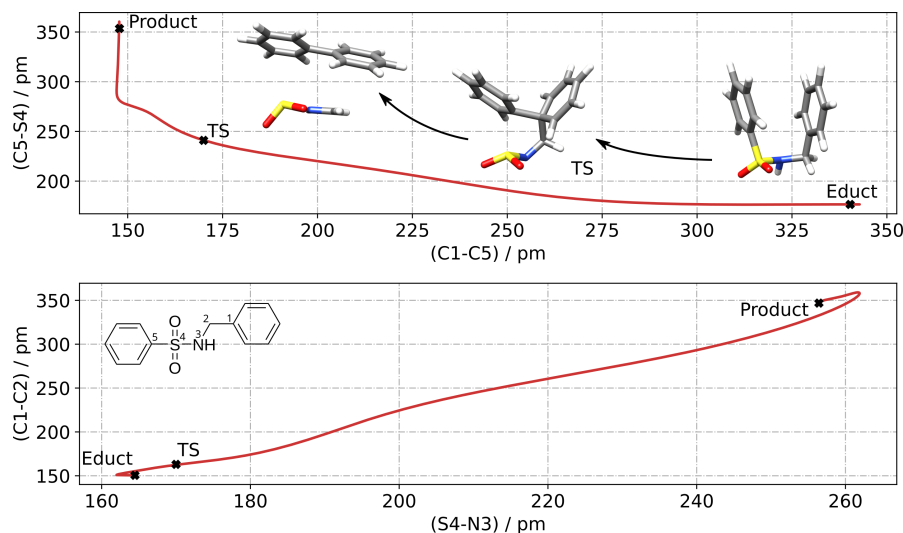


Figure A.2: Selected distances along the IRC, describing the formation of **2b** from **1b** by photosplicing, obtained at the CAM-B3LYP/def2-TZVP/CPCM(ACN) level of theory. a) Atomic distances with significant changes when going from the educt to the TS and b) distances that change significantly in the second IRC half, when going from TS to the photoproducts.

A.3 S22 Geometries with High root mean square deviations (RMSDs)

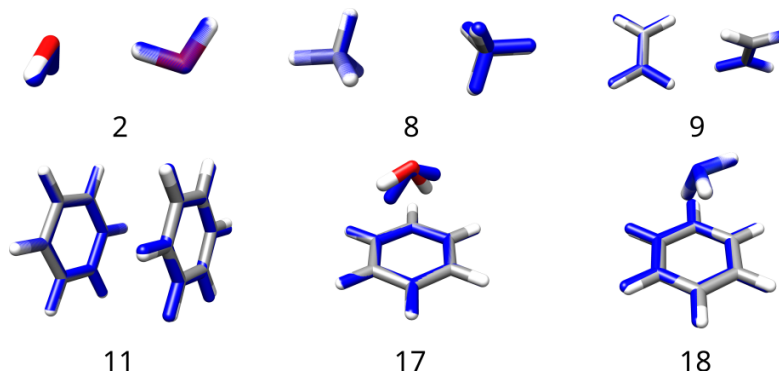


Figure A.3: Overlay of selected, optimized geometries from the S22 test set, as discussed in section 13.2.2.[417, 423] The numbering is consistent with Table 13.4. Reference geometries as provided by Lindh are given in blue, whereas the geometries obtained from pysisyphus (this work) are colored by element. All geometries, beside case 17 (benzene · water dimer) are virtually indistinguishable, from the reference geometries, even though they show high RMSDs, in spite of resorting the atoms with the Hungarian algorithm.[433, 434]

A.4 Code Listings

This section contains several python code listings, allowing to reproduce (part of) the results presented in this thesis. Listings are provided in the form of unit tests, that can be executed by the `pytest` python package. [526–529] Exact git commits are given as docstring below the function header.

Listing A.1: *test.baker.py*, Optimization of Bakers test set in 207 cycles at the HF/STO-3G level of theory, as discussed in section 13.2.1.

```
import pytest

from pysisyphus.benchmarks import Benchmark
from pysisyphus.calculators.ORCA import ORCA
from pysisyphus.optimizers.RFOptimizer import RFOptimizer

def calc_getter(charge, mult):
    return ORCA(keywords="hf_sto-3g", pal=6, charge=charge, mult=mult)

BakerBm = Benchmark("baker", coord_type="redund", calc_getter=calc_getter)

@pytest.mark.parametrize("fn, _geom, _ref_energy", BakerBm)
def test_baker(fn, geom, ref_energy):
    """pysisyphus @ 7cc0a296493b797ae934dfe891109414f9f8afc6"""
    opt_kwargs = {
        "thresh": "baker",
        "hessian_init": "fischer",
        "hessian_update": "bfgs",
        "line_search": True,
        "gdiis": True,
    }
    opt = RFOptimizer(geom, **opt_kwargs)
    opt.run()

    assert opt.is_converged
    assert geom.energy == pytest.approx(ref_energy)
```

Listing A.2: *test_s22_set.py*, Optimization of S22 TS test set in 310 cycles at the RI-MP2/6-31G** level of theory, as discussed in section 13.2.2.

```

import pytest

from pysisyphus.benchmarks import Benchmark
from pysisyphus.calculators import ORCA
from pysisyphus.optimizers.RFOptimizer import RFOptimizer
from pysisyphus.testing import using

S22Bm = Benchmark("s22", coord_type="redund")

@using("orca")
@pytest.mark.parametrize(
    "fn, _geom, _charge, _mult, _ref_energy",
    S22Bm.geom_iter
)
def test_s22_set(fn, geom, charge, mult, ref_energy):
    """ pysisyphus @ e56df2973cdcf3140216637b4ae4b5dbf2f30542 """
    calc = ORCA(
        keywords="RI-MP2-6-31G**_def2-SVP/C_tightscf",
        pal=4,
        mem=1500,
        charge=charge,
        mult=mult,
    )
    geom.set_calculator(calc)
    opt_kwargs = {
        "thresh": "gau",
        "dump": True,
    }
    opt = RFOptimizer(geom, **opt_kwargs)
    opt.run()

    assert opt.is_converged

```

Listing A.3: *test_baker_ts.py*, Optimization of Bakers TS test set in 304 cycles at the HF/3-21G level of theory, as discussed in section 13.2.4, using restricted step partitioned RFO (RS-PRFO) with enabled line search.

```

import pytest

from pysisyphus.benchmarks import Benchmark
from pysisyphus.calculators.ORCA import ORCA
from pysisyphus.tsoptimizers import RSPRFOptimizer

def calc_getter(charge, mult):
    return ORCA(keywords="HF_3-21g", pal=6, mem=500, charge=charge,
                 mult=mult)

BakerTSBm = Benchmark(
    "baker_ts",
    coord_type="redund",
    calc_getter=calc_getter,
)

@pytest.mark.parametrize("fn, _geom, _ref_energy", BakerTSBm)
def test_baker_ts(fn, geom, ref_energy):
    """pysisyphus @ 1ce48d3eb95715111b4758c3e6a1f0da4e7319d4"""
    if fn == "22_hconhoh.xyz":
        ref_energy = -242.25695787 # Unconstrained solution

    opt_kwargs = {
        "thresh": "baker",
        "trust_radius": 0.1,
        "trust_max": 0.3,
        "min_line_search": True,
        "max_line_search": True,
    }
    # Cases 10 & 11 start in the convex region of the PES, so we must
    # designate an initial mode/root/direction.
    if fn == "10_tetrazine.xyz":
        opt_kwargs["rx_mode"] = (((0, 2), 1), ((1, 3), 1))
    elif fn == "11_trans_butadiene.xyz":
        opt_kwargs["rx_mode"] = (((2, 0, 1, 3), 1), )
    opt = RSPRFOptimizer(geom, **opt_kwargs)
    opt.run()

    assert opt.is_converged
    assert geom.energy == pytest.approx(ref_energy)

```

Listing A.4: *test_baker_ts_dimer.py*, Optimization of Bakers TS test set in 358 cycles (1092 gradient evaluations in total) at the HF/3-21G level of theory, using the DM and preconditioned LBFGS, as discussed in section 13.2.4 and summarized in Table 13.7.

```

import pickle
import pytest

from pysisyphus.benchmarks import Benchmark
from pysisyphus.calculators import Dimer, ORCA
from pysisyphus.optimizers.PreconLBFGS import PreconLBFGS

BTS = Benchmark(
    "baker_ts",
    coord_type="cart",
    exclude=(10,),
)

@pytest.mark.parametrize(
    "fn, _geom, _charge, _mult, _ref_energy",
    BTS.geom_iter
)
def test_baker_ts_dimer(fn, geom, charge, mult, ref_energy):
    """pysisyphus @ 6d9c004d"""
    with open("Ns", "rb") as handle:
        N_INITS = pickle.load(handle) # Load initial orientations

    calc = ORCA("hf_3-21g_tightscf", charge=charge, mult=mult, pal=6)
    dimer_kwargs = {
        "rotation_method": "fourier",
        "calculator": calc,
        "N_raw": N_INITS[fn[:2]],
        "length": 0.0189,
        "rotation_tol": 5,
        "rotation_disable_pos_curv": True,
        "trans_force_f_perp": True,
    }
    dimer = Dimer(**dimer_kwargs)
    geom.set_calculator(dimer)
    opt_kwargs = {
        "thresh": "baker",
        "precon": True,
        "max_step_element": 0.25,
        "max_cycles": 50,
        "c_stab": 0.103,
        "dump": True,
    }
    opt = PreconLBFGS(geom, **opt_kwargs)
    opt.run()
    assert opt.is_converged
    assert geom.energy == pytest.approx(ref_energy)

```

Listing A.5: *test_xtb_rx.py*, TS optimizations for the COS test set at the GFN2-XTB level of theory, using the GSM and restricted step image method RFO (RS-IRFO), as discussed in section 13.2.5.

```

from pathlib import Path
import tempfile

import pytest

from pysisyphus.benchmarks import Benchmark
from pysisyphus.xyzloader import write_geoms_to_trj
from pysisyphus.run import run_from_dict

@pytest.mark.parametrize(
    "fn, _geoms, _charge, _mult, _ref_energy", Benchmark("xtb_rx").geom_iter
)
def test_xtb_rx(fn, geoms, charge, mult, ref_energy):
    """pysisyphus @ 3779c3485bb5048dc6b58fa6f035e9cb493c1ec6"""
    start, ts_ref_org, end = geoms
    id_ = fn[:2]
    with tempfile.TemporaryDirectory() as tmp_dir:
        tmp_path = Path(tmp_dir)
        inp_trj = str(tmp_path / "gs.inputs.trj")
        write_geoms_to_trj((start, end), inp_trj)
        run_dict = {
            "geom": {
                "type": "dlc" if (id_ != "02") else "cart",
                "fn": inp_trj,
            },
            "calc": {
                "type": "xtb", # GFN2-XTB 6.3.3
                "pal": 1,
                "mem": 750,
                "charge": charge,
                "mult": mult,
            },
            "preopt": {"max_cycles": 5},
            "cos": {
                "type": "gs",
                "climb": True,
                "climb_rms": 0.0075,
            },
            "opt": {
                "type": "string",
                "max_step": 0.2,
                "rms_force": 0.005 if (id_ != "19") else 0.003,
                "rms_force_only": True,
            },
            "tsopt": {
                "type": "rsirfo",
                "thresh": "gau",
                "trust_max": 0.5,
                "do_hess": True,
            },
        }
        results = run_from_dict(run_dict)
        assert results.ts_opt.is_converged

```

Listing A.6: *test_birkholz_interpolation.py*, TS optimizations for the HCN isomerization and the Cope rearrangement of 1,4-hexadiene using the connectivity transition state (CTS) method, as mentioned in section 13.2.5.

```

import pytest

from pysisyphus.calculators.PySCF import PySCF
from pysisyphus.helpers import (
    geom_loader,
    do_final_hessian,
    highlight_text
)
from pysisyphus.tsoptimizers import RSPRFOptimizer, birkholz_interpolation
from pysisyphus.testing import using

@using("pyscf")
@pytest.mark.parametrize(
    "name, _fn, _ref_energy",
    [
        ("hcn", "lib:birkholz_rx/02_hcn_original.trj", -91.56485102),
        ("cope", "lib:birkholz_rx/03_cope.trj", -230.06026151),
    ],
)
def test_birkholz_interpolation(name, fn, ref_energy):
    """pysisyphus @ f67a70a2a565c42c7d422190288aac96d4fa6fd2"""
    geoms = geom_loader(fn)

    def calc_getter():
        return PySCF(basis="sto3g", verbose=0)

    ts_guess = birkholz_interpolation(geoms, calc_getter)

    print(highlight_text("TS-Optimization"))
    tsopt_kwargs = {
        "dump": True,
        "thresh": "gau",
        "trust_max": 0.3,
        "prefix": name,
    }
    tsopt = RSPRFOptimizer(ts_guess, **tsopt_kwargs)
    tsopt.run()

    do_final_hessian(ts_guess, write_imag_modes=True)
    assert ts_guess.energy == pytest.approx(ref_energy)

```


B Acknowledgements

My sincerest gratitude goes to everyone that supported me and allowed this thesis to become reality. First and foremost I'd like to thank Prof. Dr. Stefanie Gräfe for supervising my thesis and giving me the opportunity to be part of her group, while still providing the freedom to pursue my scientific interests.

This thesis would not have been possible without the guidance of Dr. Stephan Kupfer. Thank you for the many collaborations and insights. I appreciate the many stimulating discussions with Philipp Traber and Phillip Seeber. They really broadened my horizon. The good work atmosphere greatly facilitated working on this thesis. I also wish to thank Philipp Traber and fellow colleagues Clara Zens and Alexander Schwab for continued use and testing of pysisyphus and providing me with invaluable feedback.

I'd like to thank Prof. Dr. Christian Hertweck for the ability to collaborate on the biaryl cross-coupling project and Veit Hänsch for the associated experimental measurements and the continued scientific exchange on this topic.

I would like express my deepest gratitude to my wife Agnes, for keeping up with our two daughters, in times of the COVID-19 pandemic and closed kindergartens. Alma and Josephine, you kept us always on our toes, which made this endeavor not easier but your presence makes everything much more worthwhile.

A heartfelt thank you goes to my parents and my grandmother for continued support and spending countless hours with Alma.

Finally I'd like to thank my friends for the rare and enjoyable encounters, that were possible in these times. Better times are on their way.

C Selbständigkeitserklärung

Ich erkläre, dass ich die vorliegende Arbeit selbständig und unter Verwendung der angegebenen Hilfsmittel, persönlichen Mitteilungen und Quellen angefertigt habe.

Jena, 16.02.2022

Bibliography

- (1) Hoffman, D. 1979 Computer Store Manager Predicts Future Youtube, <https://www.youtube.com/watch?v=eNT1L3jGjbA>.
- (2) Haensch, V. G.; Neuwirth, T.; **Steinmetzer, J.**; Kloss, F.; Beckert, R.; Gräfe, S.; Kupfer, S.; Hertweck, C. Metal-Free Aryl Cross-Coupling Directed by Traceless Linkers. *Chemistry – A European Journal* **2019**, *25*, 16068–16073, DOI: 10.1002/chem.201903582.
- (3) **Steinmetzer, J.**; Kupfer, S.; Gräfe, S. pysisyphus: Exploring potential energy surfaces in ground and excited states. *International Journal of Quantum Chemistry* **2020**, *121*, DOI: 10.1002/qua.26390.
- (4) G., U. R.; Liu, J.; Hoffmann, P.; **Steinmetzer, J.**; Görls, H.; Kupfer, S.; Askes, S. H. C.; Neugebauer, U.; Gräfe, S.; Schiller, A. Light-responsive paper strips as CO-releasing material with a colourimetric response. *Chemical Science* **2017**, *8*, 6555–6560, DOI: 10.1039/c7sc01692a.
- (5) Liu, J.; Hoffmann, P.; **Steinmetzer, J.**; Askes, S. H.; Kupfer, S.; Görls, H.; Gräfe, S.; Neugebauer, U.; Gandra, U. R.; Schiller, A. Visible light-activated biocompatible photo-CORM for CO-release with colorimetric and fluorometric dual turn-on response. *Polyhedron* **2019**, *172*, 175–181, DOI: 10.1016/j.poly.2019.04.031.
- (6) Amini, K.; Sclafani, M.; Steinle, T.; Le, A.-T.; Sanchez, A.; Müller, C.; **Steinmetzer, J.**; Yue, L.; Saavedra, J. R. M.; Hemmer, M.; Lewenstein, M.; Moshhammer, R.; Pfeifer, T.; Pullen, M. G.; Ullrich, J.; Wolter, B.; Moszynski, R.; de Abajo, F. J. G.; Lin, C. D.; Gräfe, S.; Biegert, J. Imaging the Renner-Teller effect using laser-induced electron diffraction. *Proceedings of the National Academy of Sciences* **2019**, *116*, 8173–8177, DOI: 10.1073/pnas.1817465116.
- (7) Liu, X.; Amini, K.; Steinle, T.; Sanchez, A.; Shaikh, M.; Belsa, B.; **Steinmetzer, J.**; Le, A.-T.; Moshhammer, R.; Pfeifer, T.; Ullrich, J.; Moszynski, R.; Lin, C. D.; Gräfe, S.; Biegert, J. Imaging an isolated water molecule using a single electron

- wave packet. *The Journal of Chemical Physics* **2019**, *151*, 024306, DOI: 10.1063/1.5100520.
- (8) Shillito, G. E.; Preston, D.; Traber, P.; **Steinmetzer, J.**; McAdam, C. J.; Crowley, J. D.; Wagner, P.; Kupfer, S.; Gordon, K. C. Excited-State Switching Frustrates the Tuning of Properties in Triphenylamine-Donor-Ligand Rhenium(I) and Platinum(II) Complexes. *Inorganic Chemistry* **2020**, *59*, 6736–6746, DOI: 10.1021/acs.inorgchem.9b03691.
- (9) Belsa, B.; Amini, K.; Liu, X.; Sanchez, A.; Steinle, T.; **Steinmetzer, J.**; Le, A. T.; Moshhammer, R.; Pfeifer, T.; Ullrich, J.; Moszynski, R.; Lin, C. D.; Gräfe, S.; Biegert, J. Laser-induced electron diffraction of the ultrafast umbrella motion in ammonia. *Structural Dynamics* **2021**, *8*, 014301, DOI: 10.1063/4.0000046.
- (10) Chalmers, C.; Chaloner, E. 500 years later: Henry VIII, leg ulcers and the course of history. *J R Soc Med* **2009**, *102*, 514–517, DOI: 10.1258/jrsm.2009.090286.
- (11) Bonkat, G. Syphilis und Heinrich VIII. *Urologe* **2018**, *57*, 1433–1435, DOI: 10.1007/s00120-018-0798-9.
- (12) Weissfeld, A. S. Infectious Diseases and Famous People Who Succumbed to Them. *Clinical Microbiology Newsletter* **2009**, *31*, 169–172, DOI: 10.1016/j.clinmicnews.2009.10.002.
- (13) Fleming, A. On the Antibacterial Action of Cultures of a Penicillium, with Special Reference to their Use in the Isolation of B. influenzae. *British journal of experimental pathology* **1929**, *10*, PMC2048009, 226–236.
- (14) Bennett, J. W.; Chung, K.-T. In *Advances in Applied Microbiology*; Elsevier: 2001, pp 163–184, DOI: 10.1016/s0065-2164(01)49013-7.
- (15) Leigh, G. J. In *Catalysts for Nitrogen Fixation*; Springer Netherlands: 2004, pp 33–54, DOI: 10.1007/978-1-4020-3611-8_2.
- (16) Andrady, A. L. Microplastics in the marine environment. *Marine Pollution Bulletin* **2011**, *62*, 1596–1605, DOI: 10.1016/j.marpolbul.2011.05.030.
- (17) Law, K. L.; Thompson, R. C. Microplastics in the seas. *Science* **2014**, *345*, 144–145, DOI: 10.1126/science.1254065.
- (18) Andrady, A. L. The plastic in microplastics: A review. *Marine Pollution Bulletin* **2017**, *119*, 12–22, DOI: 10.1016/j.marpolbul.2017.01.082.

- (19) Cox, K. D.; Covernton, G. A.; Davies, H. L.; Dower, J. F.; Juanes, F.; Dudas, S. E. Human Consumption of Microplastics. *Environ. Sci. Technol. Technology* **2019**, *53*, 7068–7074, DOI: 10.1021/acs.est.9b01517.
- (20) Hale, R. C.; Seeley, M. E.; Guardia, M. J. L.; Mai, L.; Zeng, E. Y. A Global Perspective on Microplastics. *J. Geophys. Res. Oceans* **2020**, *125*, DOI: 10.1029/2018jc014719.
- (21) Andrady, A. L.; Neal, M. A. Applications and societal benefits of plastics. *Phil. Trans. R. Soc. B* **2009**, *364*, 1977–1984, DOI: 10.1098/rstb.2008.0304.
- (22) Thompson, R. C.; Swan, S. H.; Moore, C. J.; vom Saal, F. S. Our plastic age. *Phil. Trans. R. Soc. B* **2009**, *364*, 1973–1976, DOI: 10.1098/rstb.2009.0054.
- (23) Haider, T. P.; Völker, C.; Kramm, J.; Landfester, K.; Wurm, F. R. Plastics of the Future? The Impact of Biodegradable Polymers on the Environment and on Society. *Angew. Chem. Int. Ed.* **2018**, *58*, 50–62, DOI: 10.1002/anie.201805766.
- (24) Dogutan, D. K.; Nocera, D. G. Artificial Photosynthesis at Efficiencies Greatly Exceeding That of Natural Photosynthesis. *Acc. Chem. Res.* **2019**, *52*, 3143–3148, DOI: 10.1021/acs.accounts.9b00380.
- (25) House, R. L.; Iha, N. Y. M.; Coppo, R. L.; Alibabaei, L.; Sherman, B. D.; Kang, P.; Brennaman, M. K.; Hoertz, P. G.; Meyer, T. J. Artificial photosynthesis: Where are we now? Where can we go? *Journal of Photochemistry and Photobiology C: Photochemistry Reviews* **2015**, *25*, 32–45, DOI: 10.1016/j.jphotochemrev.2015.08.002.
- (26) Zhang, B.; Sun, L. Artificial photosynthesis: opportunities and challenges of molecular catalysts. *Chem. Soc. Rev.* **2019**, *48*, 2216–2264, DOI: 10.1039/c8cs00897c.
- (27) Su, J.; Vayssieres, L. A Place in the Sun for Artificial Photosynthesis? *ACS Energy Lett. Energy Letters* **2016**, *1*, 121–135, DOI: 10.1021/acsenergylett.6b00059.
- (28) Butburee, T.; Chakthranont, P.; Phawa, C.; Faungnawakij, K. Beyond Artificial Photosynthesis: Prospects on Photobiorefinery. *ChemCatChem* **2020**, *12*, 1873–1890, DOI: 10.1002/cctc.201901856.
- (29) Kim, D.; Sakimoto, K. K.; Hong, D.; Yang, P. Artificial Photosynthesis for Sustainable Fuel and Chemical Production. *Angew. Chem. Int. Ed.* **2015**, *54*, 3259–3266, DOI: 10.1002/anie.201409116.

Bibliography

- (30) El-Khouly, M. E.; El-Mohsnawy, E.; Fukuzumi, S. Solar energy conversion: From natural to artificial photosynthesis. *Journal of Photochemistry and Photobiology C: Photochemistry Reviews* **2017**, *31*, 36–83, DOI: 10.1016/j.jphotochemrev.2017.02.001.
- (31) Ye, S.; Ding, C.; Liu, M.; Wang, A.; Huang, Q.; Li, C. Water Oxidation Catalysts for Artificial Photosynthesis. *Adv. Mater.* **2019**, *31*, 1902069, DOI: 10.1002/adma.201902069.
- (32) Wang, J.; Wolf, R. M.; Caldwell, J. W.; Kollman, P. A.; Case, D. A. Development and testing of a general amber force field. *Journal of Computational Chemistry* **2004**, *25*, 1157–1174, DOI: 10.1002/jcc.20035.
- (33) Vanommeslaeghe, K.; Hatcher, E.; Acharya, C.; Kundu, S.; Zhong, S.; Shim, J.; Darian, E.; Guvench, O.; Lopes, P.; Vorobyov, I.; Mackerell, A. D. CHARMM general force field: A force field for drug-like molecules compatible with the CHARMM all-atom additive biological force fields. *Journal of Computational Chemistry* **2009**, NA–NA, DOI: 10.1002/jcc.21367.
- (34) Van Duin, A. C. T.; Dasgupta, S.; Lorant, F.; Goddard, W. A. ReaxFF: A Reactive Force Field for Hydrocarbons. *J. Phys. Chem. A* **2001**, *105*, 9396–9409, DOI: 10.1021/jp004368u.
- (35) Clark, M.; Cramer, R. D.; Opdenbosch, N. V. Validation of the general purpose tripos 5.2 force field. *J. Comput. Chem.* **1989**, *10*, 982–1012, DOI: 10.1002/jcc.540100804.
- (36) Cornell, W. D.; Cieplak, P.; Bayly, C. I.; Gould, I. R.; Merz, K. M.; Ferguson, D. M.; Spellmeyer, D. C.; Fox, T.; Caldwell, J. W.; Kollman, P. A. A Second Generation Force Field for the Simulation of Proteins, Nucleic Acids, and Organic Molecules. *J. Am. Chem. Soc.* **1995**, *117*, 5179–5197, DOI: 10.1021/ja00124a002.
- (37) Harder, E.; Damm, W.; Maple, J.; Wu, C.; Reboul, M.; Xiang, J. Y.; Wang, L.; Lupyan, D.; Dahlgren, M. K.; Knight, J. L.; Kaus, J. W.; Cerutti, D. S.; Krilov, G.; Jorgensen, W. L.; Abel, R.; Friesner, R. A. OPLS3: A Force Field Providing Broad Coverage of Drug-like Small Molecules and Proteins. *J. Chem. Theory Comput.* **2015**, *12*, 281–296, DOI: 10.1021/acs.jctc.5b00864.
- (38) Nerenberg, P. S.; Head-Gordon, T. New developments in force fields for biomolecular simulations. *Current Opinion in Structural Biology* **2018**, *49*, 129–138, DOI: 10.1016/j.sbi.2018.02.002.

- (39) Doherty, B.; Zhong, X.; Gathiaka, S.; Li, B.; Acevedo, O. Revisiting OPLS Force Field Parameters for Ionic Liquid Simulations. *J. Chem. Theory Comput.* **2017**, *13*, 6131–6145, DOI: 10.1021/acs.jctc.7b00520.
- (40) Senn, H. M.; Thiel, W. QM/MM Methods for Biomolecular Systems. *Angewandte Chemie International Edition* **2009**, *48*, 1198–1229, DOI: 10.1002/anie.200802019.
- (41) Perilla, J. R.; Goh, B. C.; Cassidy, C. K.; Liu, B.; Bernardi, R. C.; Rudack, T.; Yu, H.; Wu, Z.; Schulten, K. Molecular dynamics simulations of large macromolecular complexes. *Current Opinion in Structural Biology* **2015**, *31*, 64–74, DOI: 10.1016/j.sbi.2015.03.007.
- (42) Marrink, S. J.; Corradi, V.; Souza, P. C.; Ingólfsson, H. I.; Tieleman, D. P.; Sansom, M. S. Computational Modeling of Realistic Cell Membranes. *Chem. Rev.* **2019**, *119*, 6184–6226, DOI: 10.1021/acs.chemrev.8b00460.
- (43) Ingólfsson, H. I.; Arnarez, C.; Periole, X.; Marrink, S. J. Computational ‘microscopy’ of cellular membranes. *J Cell Sci* **2016**, *129*, 257–268, DOI: 10.1242/jcs.176040.
- (44) Feig, M.; Yu, I.; Wang, P.-h.; Nawrocki, G.; Sugita, Y. Crowding in Cellular Environments at an Atomistic Level from Computer Simulations. *J. Phys. Chem. B* **2017**, *121*, 8009–8025, DOI: 10.1021/acs.jpcc.7b03570.
- (45) Lagardère, L.; Jolly, L.-H.; Lipparini, F.; Aviat, F.; Stamm, B.; Jing, Z. F.; Harger, M.; Torabifard, H.; Cisneros, G. A.; Schnieders, M. J.; Gresh, N.; Maday, Y.; Ren, P. Y.; Ponder, J. W.; Piquemal, J.-P. Tinker-HP: a massively parallel molecular dynamics package for multiscale simulations of large complex systems with advanced point dipole polarizable force fields. *Chem. Sci.* **2018**, *9*, 956–972, DOI: 10.1039/c7sc04531j.
- (46) Kmiecik, S.; Gront, D.; Kolinski, M.; Wieteska, L.; Dawid, A. E.; Kolinski, A. Coarse-Grained Protein Models and Their Applications. *Chem. Rev.* **2016**, *116*, 7898–7936, DOI: 10.1021/acs.chemrev.6b00163.
- (47) Li, C.; Strachan, A. Molecular scale simulations on thermoset polymers: A review. *J. Polym. Sci. Part B: Polym. Phys.* **2014**, *53*, 103–122, DOI: 10.1002/polb.23489.
- (48) Suter, J. L.; Anderson, R. L.; Greenwell, H. C.; Coveney, P. V. Recent advances in large-scale atomistic and coarse-grained molecular dynamics simulation of clay minerals. *J. Mater. Chem.* **2009**, *19*, 2482, DOI: 10.1039/b820445d.

Bibliography

- (49) Kyriakou, V.; Garagounis, I.; Vourros, A.; Vasileiou, E.; Stoukides, M. An Electrochemical Haber-Bosch Process. *Joule* **2020**, *4*, 142–158, DOI: 10.1016/j.joule.2019.10.006.
- (50) Abghoui, Y.; Garden, A. L.; Hlynsson, V. F.; Björgvinsdóttir, S.; Ólafsdóttir, H.; Skúlason, E. Enabling electrochemical reduction of nitrogen to ammonia at ambient conditions through rational catalyst design. *Physical Chemistry Chemical Physics* **2015**, *17*, 4909–4918, DOI: 10.1039/c4cp04838e.
- (51) Zhao, J.; Chen, Z. Single Mo Atom Supported on Defective Boron Nitride Monolayer as an Efficient Electrocatalyst for Nitrogen Fixation: A Computational Study. *Journal of the American Chemical Society* **2017**, *139*, 12480–12487, DOI: 10.1021/jacs.7b05213.
- (52) Li, Q.; He, L.; Sun, C.; Zhang, X. Computational Study of MoN₂ Monolayer as Electrochemical Catalysts for Nitrogen Reduction. *J. Phys. Chem. C* **2017**, *121*, 27563–27568, DOI: 10.1021/acs.jpcc.7b10522.
- (53) Guo, X.; Huang, S. Tuning nitrogen reduction reaction activity via controllable Fe magnetic moment: A computational study of single Fe atom supported on defective graphene. *Electrochimica Acta* **2018**, *284*, 392–399, DOI: 10.1016/j.electacta.2018.07.168.
- (54) Muuronen, M.; Deglmann, P.; Tomovic, Z. Design Principles for Rational Polyurethane Catalyst Development. *The Journal of Organic Chemistry* **2019**, *84*, 8202–8209, DOI: 10.1021/acs.joc.9b01319.
- (55) Chen, M.; Chen, C. Rational Design of High-Performance Phosphine Sulfonate Nickel Catalysts for Ethylene Polymerization and Copolymerization with Polar Monomers. *ACS Catal. Catalysis* **2017**, *7*, 1308–1312, DOI: 10.1021/acscatal.6b03394.
- (56) Dou, M.; Wang, J.; Gao, B.; Xu, C.; Yang, F. Photocatalytic difference of amoxicillin and cefotaxime under visible light by mesoporous g-C₃N₄: Mechanism, degradation pathway and DFT calculation. *Chemical Engineering Journal* **2020**, *383*, 123134, DOI: 10.1016/j.cej.2019.123134.
- (57) Yin, R.; Guo, W.; Wang, H.; Du, J.; Zhou, X.; Wu, Q.; Zheng, H.; Chang, J.; Ren, N. Selective degradation of sulfonamide antibiotics by peroxymonosulfate alone: Direct oxidation and nonradical mechanisms. *Chemical Engineering Journal* **2018**, *334*, 2539–2546, DOI: 10.1016/j.cej.2017.11.174.

- (58) Pelalak, R.; Alizadeh, R.; Ghareshabani, E.; Heidari, Z. Degradation of sulfonamide antibiotics using ozone-based advanced oxidation process: Experimental, modeling, transformation mechanism and DFT study. *Science of The Total Environment* **2020**, *734*, 139446, DOI: 10.1016/j.scitotenv.2020.139446.
- (59) Abbas, A. M.; Faisal, S. R.; Orabi, A. S. Novel β -lactam antibiotic derivative and its complexes: DFT, frontier energy levels, DNA interaction, docking, physicochemical and antimicrobial properties. *Journal of Molecular Structure* **2020**, *1218*, 128487, DOI: 10.1016/j.molstruc.2020.128487.
- (60) Abdel-Rahman, L. H.; Abdelhamid, A. A.; Abu-Dief, A. M.; Shehata, M. R.; Bakheet, M. A. Facile synthesis, X-Ray structure of new multi-substituted aryl imidazole ligand, biological screening and DNA binding of its Cr(III), Fe(III) and Cu(II) coordination compounds as potential antibiotic and anticancer drugs. *Journal of Molecular Structure* **2020**, *1200*, 127034, DOI: 10.1016/j.molstruc.2019.127034.
- (61) Rajamanikandan, S.; Soundarya, S.; Paramasivam, A.; Prabhu, D.; Jeyakanthan, J.; Ramasamy, V. Computational identification of potential lead molecules targeting rho receptor of *Neisseria gonorrhoeae*. *Journal of Biomolecular Structure and Dynamics* **2021**, 1–11, DOI: 10.1080/07391102.2021.1885491.
- (62) Adcock, S. A.; McCammon, J. A. Molecular Dynamics: Survey of Methods for Simulating the Activity of Proteins. *Chem. Rev.* **2006**, *106*, 1589–1615, DOI: 10.1021/cr040426m.
- (63) Miller, W. H. Quantum dynamics of complex molecular systems. *Proceedings of the National Academy of Sciences* **2005**, *102*, 6660–6664, DOI: 10.1073/pnas.0408043102.
- (64) Khait, Y. G.; Panin, A. I.; Averyanov, A. S. Search for stationary points of arbitrary index by augmented Hessian method. *International Journal of Quantum Chemistry* **1995**, *54*, 329–336, DOI: 10.1002/qua.560540602.
- (65) Pradhan, R.; Lourderaj, U. Can reactions follow non-traditional second-order saddle pathways avoiding transition states? *Physical Chemistry Chemical Physics* **2019**, *21*, 12837–12842, DOI: 10.1039/c9cp02431j.
- (66) Heidrich, D.; Quapp, W. Saddle points of index 2 on potential energy surfaces and their role in theoretical reactivity investigations. *Theoretica Chimica Acta* **1986**, *70*, 89–98, DOI: 10.1007/bf00532206.

Bibliography

- (67) Yin, J.; Zhang, L.; Zhang, P. High-Index Optimization-Based Shrinking Dimer Method for Finding High-Index Saddle Points. *SIAM Journal on Scientific Computing* **2019**, *41*, A3576–A3595, DOI: 10.1137/19m1253356.
- (68) Yang, C.-H.; Bhattacharyya, S.; Liu, L.; Fang, W.-h.; Liu, K. Real-time tracking of the entangled pathways in the multichannel photodissociation of acetaldehyde. *Chemical Science* **2020**, DOI: 10.1039/d0sc00063a.
- (69) Fukui, K. The path of chemical reactions - the IRC approach. *Accounts of Chemical Research* **1981**, *14*, 363–368, DOI: 10.1021/ar00072a001.
- (70) Simons, J.; Joergensen, P.; Taylor, H.; Ozment, J. Walking on potential energy surfaces. *The Journal of Physical Chemistry* **1983**, *87*, 2745–2753, DOI: 10.1021/j100238a013.
- (71) JÓNSSON, H.; MILLS, G.; JACOBSEN, K. W. In *Classical and Quantum Dynamics in Condensed Phase Simulations*, WORLD SCIENTIFIC: 1998, DOI: 10.1142/9789812839664_0016.
- (72) E, W.; Ren, W.; Vanden-Eijnden, E. String method for the study of rare events. *Physical Review B* **2002**, *66*, DOI: 10.1103/physrevb.66.052301.
- (73) Quapp, W.; Bofill, J. M. A comment to the nudged elastic band method. *Journal of Computational Chemistry* **2010**, NA–NA, DOI: 10.1002/jcc.21540.
- (74) Müller, K.; Brown, L. D. Location of saddle points and minimum energy paths by a constrained simplex optimization procedure. *Theoret. Chim. Acta* **1979**, *53*, 75–93, DOI: 10.1007/bf00547608.
- (75) Schlegel, H. B. Optimization of equilibrium geometries and transition structures. *Journal of Computational Chemistry* **1982**, *3*, 214–218, DOI: 10.1002/jcc.540030212.
- (76) Birkholz, A. B.; Schlegel, H. B. Path optimization by a variational reaction coordinate method. I. Development of formalism and algorithms. *The Journal of Chemical Physics* **2015**, *143*, 244101, DOI: 10.1063/1.4937764.
- (77) Birkholz, A. B.; Schlegel, H. B. Path optimization by a variational reaction coordinate method. II. Improved computational efficiency through internal coordinates and surface interpolation. *The Journal of Chemical Physics* **2016**, *144*, 184101, DOI: 10.1063/1.4948439.
- (78) Quapp, W.; Bofill, J. M. Mechanochemistry on the Müller-Brown surface by Newton trajectories. *Int J Quantum Chem* **2017**, *118*, e25522, DOI: 10.1002/qua.25522.

- (79) Koistinen, O.-P.; Dagbjartsdóttir, F. B.; Ásgeirsson, V.; Vehtari, A.; Jónsson, H. Nudged elastic band calculations accelerated with Gaussian process regression. *The Journal of Chemical Physics* **2017**, *147*, 152720, DOI: 10.1063/1.4986787.
- (80) Unke, O. T.; Brickel, S.; Meuwly, M. Sampling reactive regions in phase space by following the minimum dynamic path. *J. Chem. Phys.* **2019**, *150*, 074107, DOI: 10.1063/1.5082885.
- (81) Denzel, A.; Haasdonk, B.; Kästner, J. Gaussian Process Regression for Minimum Energy Path Optimization and Transition State Search. *J. Phys. Chem. A* **2019**, *123*, 9600–9611, DOI: 10.1021/acs.jpca.9b08239.
- (82) Dewyer, A. L.; Argüelles, A. J.; Zimmerman, P. M. Methods for exploring reaction space in molecular systems. *WIREs Comput Mol Sci* **2017**, *8*, e1354, DOI: 10.1002/wcms.1354.
- (83) Gonzalez, C.; Schlegel, H. B. Reaction path following in mass-weighted internal coordinates. *The Journal of Physical Chemistry* **1990**, *94*, 5523–5527, DOI: 10.1021/j100377a021.
- (84) Schlegel, H. B. Geometry optimization. *WIREs Computational Molecular Science* **2011**, *1*, 790–809, DOI: 10.1002/wcms.34.
- (85) Ásgeirsson, V.; Jónsson, H. In *Handbook of Materials Modeling*; Springer International Publishing: 2020, pp 689–714, DOI: 10.1007/978-3-319-44677-6_28.
- (86) Richter, M.; Marquetand, P.; Gonzalez-Vazquez, J.; Sola, I.; Gonzalez, L. SHARC: ab Initio Molecular Dynamics with Surface Hopping in the Adiabatic Representation Including Arbitrary Couplings. *J. Chem. Theory Comput.* **2011**, *7*, 1253–1258, DOI: 10.1021/ct1007394.
- (87) Zhang, L.; Roither, S.; Xie, X.; Kartashov, D.; Schöffler, M.; Xu, H.; Iwasaki, A.; Gräfe, S.; Okino, T.; Yamanouchi, K.; Baltuska, A.; Kitzler, M. Path-selective investigation of intense laser-pulse-induced fragmentation dynamics in triply charged 1,3-butadiene. *J. Phys. B: At. Mol. Opt. Phys.* **2012**, *45*, 085603, DOI: 10.1088/0953-4075/45/8/085603.
- (88) Mai, S.; Richter, M.; Marquetand, P.; Gonzalez, L. The DNA nucleobase thymine in motion – Intersystem crossing simulated with surface hopping. *Chemical Physics* **2017**, *482*, 9–15, DOI: 10.1016/j.chemphys.2016.10.003.

Bibliography

- (89) Gonzalez, L.; Marquetand, P.; Richter, M.; Gonzalez-Vazquez, J.; Sola, I. In *Springer Series in Chemical Physics*; Springer International Publishing: 2014, pp 145–170, DOI: 10.1007/978-3-319-02051-8_7.
- (90) Koch, A.; Kinzel, D.; Dröge, F.; Gräfe, S.; Kupfer, S. Photochemistry and Electron Transfer Kinetics in a Photocatalyst Model Assessed by Marcus Theory and Quantum Dynamics. *The Journal of Physical Chemistry C* **2017**, *121*, 16066–16078, DOI: 10.1021/acs.jpcc.7b02812.
- (91) Staniszewska, M.; Kupfer, S.; Guthmuller, J. Theoretical Investigation of the Electron-Transfer Dynamics and Photodegradation Pathways in a Hydrogen-Evolving Ruthenium-Palladium Photocatalyst. *Chem. Eur. J.* **2018**, *24*, 11166–11176, DOI: 10.1002/chem.201801698.
- (92) Staniszewska, M.; Kupfer, S.; Guthmuller, J. Effect of the Catalytic Center on the Electron Transfer Dynamics in Hydrogen-Evolving Ruthenium-Based Photocatalysts Investigated by Theoretical Calculations. *J. Phys. Chem. C* **2019**, *123*, 16003–16013, DOI: 10.1021/acs.jpcc.9b03621.
- (93) Toniolo, A.; Olsen, S.; Manohar, L.; Martinez, T. J. Conical intersection dynamics in solution: The chromophore of Green Fluorescent Protein. *Faraday Discuss.* **2004**, *127*, 149–163, DOI: 10.1039/b401167h.
- (94) Worth, G. A.; Cederbaum, L. S. BEYOND BORN-OPPENHEIMER: Molecular Dynamics Through a Conical Intersection. *Annu. Rev. Phys. Chem.* **2004**, *55*, 127–158, DOI: 10.1146/annurev.physchem.55.091602.094335.
- (95) Galvan, I. F.; Delcey, M. G.; Pedersen, T. B.; Aquilante, F.; Lindh, R. Analytical State-Average Complete-Active-Space Self-Consistent Field Nonadiabatic Coupling Vectors: Implementation with Density-Fitted Two-Electron Integrals and Application to Conical Intersections. *J. Chem. Theory Comput.* **2016**, *12*, 3636–3653, DOI: 10.1021/acs.jctc.6b00384.
- (96) Tuna, D.; Sobolewski, A. L.; Domcke, W. Conical-Intersection Topographies Suggest That Ribose Exhibits Enhanced UV Photostability. *J. Phys. Chem. B* **2016**, *120*, 10729–10735, DOI: 10.1021/acs.jpcc.6b09048.
- (97) Polli, D.; Altoe, P.; Weingart, O.; Spillane, K. M.; Manzoni, C.; Brida, D.; Tomasello, G.; Orlandi, G.; Kukura, P.; Mathies, R. A.; Garavelli, M.; Cerullo, G. Conical intersection dynamics of the primary photoisomerization event in vision. *Nature* **2010**, *467*, 440–443, DOI: 10.1038/nature09346.

- (98) Soto, J.; Otero, J. C.; Avila, F. J.; Pelaez, D. Conical intersections and intersystem crossings explain product formation in photochemical reactions of aryl azides. *Phys. Chem. Chem. Phys.* **2019**, *21*, 2389–2396, DOI: 10.1039/c8cp06974c.
- (99) Barbatti, M.; Ruckebauer, M.; Szymczak, J. J.; Aquino, A. J. A.; Lischka, H. Nonadiabatic excited-state dynamics of polar π -systems and related model compounds of biological relevance. *Phys. Chem. Chem. Phys.* **2008**, *10*, 482–494, DOI: 10.1039/b709315m.
- (100) Marian, C. M. Spin-orbit coupling and intersystem crossing in molecules. *WIREs Comput Mol Sci* **2011**, *2*, 187–203, DOI: 10.1002/wcms.83.
- (101) Penfold, T. J.; Gindensperger, E.; Daniel, C.; Marian, C. M. Spin-Vibronic Mechanism for Intersystem Crossing. *Chem. Rev.* **2018**, *118*, 6975–7025, DOI: 10.1021/acs.chemrev.7b00617.
- (102) Noda, H.; Nakanotani, H.; Adachi, C. Excited state engineering for efficient reverse intersystem crossing. *Sci. Adv.* **2018**, *4*, eaao6910, DOI: 10.1126/sciadv.aao6910.
- (103) Wada, Y.; Nakagawa, H.; Matsumoto, S.; Wakisaka, Y.; Kaji, H. Organic light emitters exhibiting very fast reverse intersystem crossing. *Nat. Photonics* **2020**, *14*, 643–649, DOI: 10.1038/s41566-020-0667-0.
- (104) Kaila, V. R. I.; Send, R.; Sundholm, D. The Effect of Protein Environment on Photoexcitation Properties of Retinal. *J. Phys. Chem. B* **2012**, *116*, 2249–2258, DOI: 10.1021/jp205918m.
- (105) Kiefer, H. V.; Gruber, E.; Langeland, J.; Kusocek, P. A.; Bochenkova, A. V.; Andersen, L. H. Intrinsic photoisomerization dynamics of protonated Schiff-base retinal. *Nat Commun* **2019**, *10*, DOI: 10.1038/s41467-019-09225-7.
- (106) Zgrablić, G.; Novello, A. M.; Parmigiani, F. Population Branching in the Conical Intersection of the Retinal Chromophore Revealed by Multipulse Ultrafast Optical Spectroscopy. *J. Am. Chem. Soc.* **2011**, *134*, 955–961, DOI: 10.1021/ja205763x.
- (107) Nathans, J. Determinants of visual pigment absorbance: role of charged amino acids in the putative transmembrane segments. *Biochemistry* **1990**, *29*, 937–942, DOI: 10.1021/bi00456a013.
- (108) Andersen, L. H.; Nielsen, I. B.; Kristensen, M. B.; Ghazaly, M. O. A. E.; Haacke, S.; Nielsen, M. B.; Petersen, M. A. Absorption of Schiff-Base Retinal Chromophores in Vacuo. *J. Am. Chem. Soc.* **2005**, *127*, 12347–12350, DOI: 10.1021/ja051638j.

Bibliography

- (109) Coughlan, N. J. A.; Adamson, B. D.; Gamon, L.; Catani, K.; Bieske, E. J. Retinal shows its true colours: photoisomerization action spectra of mobility-selected isomers of the retinal protonated Schiff base. *Phys. Chem. Chem. Phys.* **2015**, *17*, 22623–22631, DOI: 10.1039/c5cp03611a.
- (110) Knudsen, J. L.; Kluge, A.; Bochenkova, A. V.; Kiefer, H. V.; Andersen, L. H. The UV-visible action-absorption spectrum of all-*trans* and 11-*cis* protonated Schiff base retinal in the gas phase. *Physical Chemistry Chemical Physics* **2018**, *20*, 7190–7194, DOI: 10.1039/c7cp07512j.
- (111) Polli, D.; Altoè, P.; Weingart, O.; Spillane, K. M.; Manzoni, C.; Brida, D.; Tomasello, G.; Orlandi, G.; Kukura, P.; Mathies, R. A.; Garavelli, M.; Cerullo, G. Conical intersection dynamics of the primary photoisomerization event in vision. *Nature* **2010**, *467*, 440–443, DOI: 10.1038/nature09346.
- (112) Arshavsky, V. Y.; Lamb, T. D.; Pugh, E. N. G Proteins and Phototransduction. *Annual Review of Physiology* **2002**, *64*, 153–187, DOI: 10.1146/annurev.physiol.64.082701.102229.
- (113) Garavelli, M. Computational Organic Photochemistry: Strategy, Achievements and Perspectives. *Theor Chem Acc* **2006**, *116*, 87–105, DOI: 10.1007/s00214-005-0030-z.
- (114) Persico, M.; Granucci, G., *Photochemistry*; Springer International Publishing: 2018, DOI: 10.1007/978-3-319-89972-5.
- (115) Hill, N. S.; Coote, M. L. In *Annual Reports in Computational Chemistry*; Elsevier: 2019, pp 203–285, DOI: 10.1016/bs.arcc.2019.08.008.
- (116) Francés-Monerris, A.; Gros, P. C.; Assfeld, X.; Monari, A.; Pastore, M. Toward Luminescent Iron Complexes: Unravelling the Photophysics by Computing Potential Energy Surfaces. *ChemPhotoChem* **2019**, *3*, 666–683, DOI: 10.1002/cptc.201900100.
- (117) Loos, P.-F.; Jacquemin, D. Evaluating 0–0 Energies with Theoretical Tools: A Short Review. *ChemPhotoChem* **2019**, *3*, 684–696, DOI: 10.1002/cptc.201900070.
- (118) Plasser, F. Visualisation of Electronic Excited-State Correlation in Real Space. *ChemPhotoChem* **2019**, *3*, 702–706, DOI: 10.1002/cptc.201900014.
- (119) Mai, S.; Gonzalez, L. Molecular Photochemistry: Recent Developments in Theory. *Angew. Chem. Int. Ed.* **2020**, *59*, 16832–16846, DOI: 10.1002/anie.201916381.

- (120) Westermayr, J.; Marquetand, P. Machine Learning for Electronically Excited States of Molecules. *Chem. Rev.* **2020**, DOI: 10.1021/acs.chemrev.0c00749.
- (121) Neese, F. Software update: the ORCA program system version 4.0. *WIREs Computational Molecular Science* **2017**, *8*, DOI: 10.1002/wcms.1327.
- (122) Furche, F.; Ahlrichs, R.; Hättig, C.; Klopper, W.; Sierka, M.; Weigend, F. Turbomole. *Wiley Interdisciplinary Reviews: Computational Molecular Science* **2013**, *4*, 91–100, DOI: 10.1002/wcms.1162.
- (123) Balasubramani, S. G. et al. TURBOMOLE: Modular program suite for ab initio quantum-chemical and condensed-matter simulations. *J. Chem. Phys.* **2020**, *152*, 184107, DOI: 10.1063/5.0004635.
- (124) Larsen, A. H. et al. The atomic simulation environment—a Python library for working with atoms. *Journal of Physics: Condensed Matter* **2017**, *29*, 273002, DOI: 10.1088/1361-648x/aa680e.
- (125) Kloss, F.; Neuwirth, T.; Haensch, V. G.; Hertweck, C. Metal-Free Synthesis of Pharmaceutically Important Biaryls by Photosplicing. *Angewandte Chemie* **2018**, *130*, 14684–14689, DOI: 10.1002/ange.201805961.
- (126) Mustroph, H. Potential-Energy Surfaces, the Born-Oppenheimer Approximations, and the Franck-Condon Principle: Back to the Roots. *ChemPhysChem* **2016**, *17*, 2616–2629, DOI: 10.1002/cphc.201600243.
- (127) Klahn, B.; Bingel, W. A. The convergence of the Rayleigh-Ritz Method in quantum chemistry. *Theoretica Chimica Acta* **1977**, *44*, 9–26, DOI: 10.1007/bf00548026.
- (128) Pauli, W. The Connection Between Spin and Statistics. *Physical Review* **1940**, *58*, 716–722, DOI: 10.1103/physrev.58.716.
- (129) Hartree, D. R. The Wave Mechanics of an Atom with a Non-Coulomb Central Field. Part I. Theory and Methods. *Mathematical Proceedings of the Cambridge Philosophical Society* **1928**, *24*, 89–110, DOI: 10.1017/s0305004100011919.
- (130) Shiozaki, T.; Hirata, S. Grid-based numerical Hartree-Fock solutions of polyatomic molecules. *Physical Review A* **2007**, *76*, DOI: 10.1103/physreva.76.040503.
- (131) Morrison, J. C.; Kobus, J. In *Novel Electronic Structure Theory: General Innovations and Strongly Correlated Systems*; Elsevier: 2018, pp 103–116, DOI: 10.1016/bs.aiq.2017.06.001.

Bibliography

- (132) Lehtola, S. Fully numerical Hartree-Fock and density functional calculations. II. Diatomic molecules. *International Journal of Quantum Chemistry* **2019**, *119*, DOI: 10.1002/qua.25944.
- (133) Jiao, L. G.; Ma, J.; Ho, Y. K. Development of the numerical Hartree-Fock method for screened atoms with Debye-Hückel potential. *Journal of Physics: Conference Series* **2020**, *1412*, 132018, DOI: 10.1088/1742-6596/1412/13/132018.
- (134) Electronic wave functions - I. A general method of calculation for the stationary states of any molecular system. *Proceedings of the Royal Society of London. Series A. Mathematical and Physical Sciences* **1950**, *200*, 542-554, DOI: 10.1098/rspa.1950.0036.
- (135) Electronic wave functions II. A calculation for the ground state of the beryllium atom. *Proceedings of the Royal Society of London. Series A. Mathematical and Physical Sciences* **1950**, *201*, 125-137, DOI: 10.1098/rspa.1950.0047.
- (136) Huzinaga, S. Gaussian-Type Functions for Polyatomic Systems. I. *The Journal of Chemical Physics* **1965**, *42*, 1293-1302, DOI: 10.1063/1.1696113.
- (137) Gill, P. M. In *Advances in Quantum Chemistry*; Elsevier: 1994, pp 141-205, DOI: 10.1016/s0065-3276(08)60019-2.
- (138) Shavitt, I. The History and Evolution of Gaussian Basis Sets. *Israel Journal of Chemistry* **1993**, *33*, 357-367, DOI: 10.1002/ijch.199300044.
- (139) Silverstone, H. J. On the Evaluation of Two-Center Overlap and Coulomb Integrals with Noninteger-n Slater-Type Orbitals. *The Journal of Chemical Physics* **1966**, *45*, 4337-4341, DOI: 10.1063/1.1727493.
- (140) Jones, H. W. Computer-generated formulas for overlap integrals of slater-type orbitals. *International Journal of Quantum Chemistry* **1980**, *18*, 709-713, DOI: 10.1002/qua.560180306.
- (141) Guseinov, I. I. Evaluation of two-center overlap and nuclear-attraction integrals for Slater-type orbitals. *Physical Review A* **1985**, *32*, 1864-1866, DOI: 10.1103/physreva.32.1864.
- (142) Jones, H. W. Comprehensive strategy for the calculation of overlap integrals with Slater-type orbitals. *International Journal of Quantum Chemistry* **1997**, *61*, 881-889, DOI: 10.1002/(sici)1097-461x(1997)61:6<881::aid-qual>3.0.co;2-s.

- (143) Guseinov, I.; Mamedov, B. Computation of molecular integrals over Slater type orbitals I. Calculations of overlap integrals using recurrence relations. *Journal of Molecular Structure: THEOCHEM* **1999**, *465*, 1–6, DOI: 10.1016/s0166-1280(98)00129-8.
- (144) Guseinov, I.; Mamedov, B. Evaluation of overlap integrals with integer and noninteger n Slater-type orbitals using auxiliary functions. *Journal of Molecular Modeling* **2002**, *8*, 272–276, DOI: 10.1007/s00894-002-0098-5.
- (145) Stewart, R. F. Small Gaussian Expansions of Slater-Type Orbitals. *The Journal of Chemical Physics* **1970**, *52*, 431–438, DOI: 10.1063/1.1672702.
- (146) Hariharan, P. C.; Pople, J. A. The influence of polarization functions on molecular orbital hydrogenation energies. *Theoretica Chimica Acta* **1973**, *28*, 213–222, DOI: 10.1007/bf00533485.
- (147) McLean, A. D.; Chandler, G. S. Contracted Gaussian basis sets for molecular calculations. I. Second row atoms, Z=11-18. *The Journal of Chemical Physics* **1980**, *72*, 5639–5648, DOI: 10.1063/1.438980.
- (148) Weigend, F.; Furche, F.; Ahlrichs, R. Gaussian basis sets of quadruple zeta valence quality for atoms H–Kr. *The Journal of Chemical Physics* **2003**, *119*, 12753–12762, DOI: 10.1063/1.1627293.
- (149) Martin, J. M.; El-Yazal, J.; François, J.-P. Basis set convergence and performance of density functional theory including exact exchange contributions for geometries and harmonic frequencies. *Molecular Physics* **1995**, *86*, 1437–1450, DOI: 10.1080/00268979500102841.
- (150) Helgaker, T.; Klopper, W.; Tew, D. P. Quantitative quantum chemistry. *Molecular Physics* **2008**, *106*, 2107–2143, DOI: 10.1080/00268970802258591.
- (151) Hall, G. G. The molecular orbital theory of chemical valency VIII. A method of calculating ionization potentials. *Proceedings of the Royal Society of London. Series A. Mathematical and Physical Sciences* **1951**, *205*, 541–552, DOI: 10.1098/rspa.1951.0048.
- (152) Roothaan, C. C. J. New Developments in Molecular Orbital Theory. *Reviews of Modern Physics* **1951**, *23*, 69–89, DOI: 10.1103/revmodphys.23.69.
- (153) Hohenberg, P.; Kohn, W. Inhomogeneous Electron Gas. *Physical Review* **1964**, *136*, B864–B871, DOI: 10.1103/physrev.136.b864.
- (154) Sahni, V. In *Quantal Density Functional Theory*; Springer Berlin Heidelberg: 2004, pp 99–123, DOI: 10.1007/978-3-662-09624-6_4.

Bibliography

- (155) Wang, Y. A.; Carter, E. A. In *Theoretical Methods in Condensed Phase Chemistry*; Kluwer Academic Publishers, pp 117–184, DOI: 10.1007/0-306-46949-9_5.
- (156) Lignères, V. L.; Carter, E. A. In *Handbook of Materials Modeling*; Springer Netherlands: 2005, pp 137–148, DOI: 10.1007/978-1-4020-3286-8_9.
- (157) Xia, J.; Huang, C.; Shin, I.; Carter, E. A. Can orbital-free density functional theory simulate molecules? *The Journal of Chemical Physics* **2012**, *136*, 084102, DOI: 10.1063/1.3685604.
- (158) Karasiev, V. V.; Trickey, S. B. In *Advances in Quantum Chemistry*; Elsevier: 2015, pp 221–245, DOI: 10.1016/bs.aiq.2015.02.004.
- (159) Meyer, R.; Weichselbaum, M.; Hauser, A. W. Machine Learning Approaches toward Orbital-free Density Functional Theory: Simultaneous Training on the Kinetic Energy Density Functional and Its Functional Derivative. *Journal of Chemical Theory and Computation* **2020**, *16*, 5685–5694, DOI: 10.1021/acs.jctc.0c00580.
- (160) Golub, P.; Manzhos, S. CONUNDrum: A program for orbital-free density functional theory calculations. *Computer Physics Communications* **2020**, *256*, 107365, DOI: 10.1016/j.cpc.2020.107365.
- (161) Kohn, W.; Sham, L. J. Self-Consistent Equations Including Exchange and Correlation Effects. *Physical Review* **1965**, *140*, A1133–A1138, DOI: 10.1103/physrev.140.a1133.
- (162) Becke, A. D. Perspective: Fifty years of density-functional theory in chemical physics. *The Journal of Chemical Physics* **2014**, *140*, 18A301, DOI: 10.1063/1.4869598.
- (163) Becke, A. D. Density-functional exchange-energy approximation with correct asymptotic behavior. *Physical Review A* **1988**, *38*, 3098–3100, DOI: 10.1103/physreva.38.3098.
- (164) Dirac, P. A. M. Note on Exchange Phenomena in the Thomas Atom. *Mathematical Proceedings of the Cambridge Philosophical Society* **1930**, *26*, 376–385, DOI: 10.1017/s0305004100016108.
- (165) Perdew, J. P.; Burke, K.; Ernzerhof, M. Generalized Gradient Approximation Made Simple. *Physical Review Letters* **1996**, *77*, 3865–3868, DOI: 10.1103/physrevlett.77.3865.

- (166) Becke, A. D. Density-functional thermochemistry. III. The role of exact exchange. *The Journal of Chemical Physics* **1993**, *98*, 5648–5652, DOI: 10.1063/1.464913.
- (167) Lee, C.; Yang, W.; Parr, R. G. Development of the Colle-Salvetti correlation-energy formula into a functional of the electron density. *Physical Review B* **1988**, *37*, 785–789, DOI: 10.1103/physrevb.37.785.
- (168) Curtiss, L. A.; Raghavachari, K.; Trucks, G. W.; Pople, J. A. Gaussian-2 theory for molecular energies of first- and second-row compounds. *The Journal of Chemical Physics* **1991**, *94*, 7221–7230, DOI: 10.1063/1.460205.
- (169) Perdew, J. P.; Kurth, S.; Zupan, A.; Blaha, P. Accurate Density Functional with Correct Formal Properties: A Step Beyond the Generalized Gradient Approximation. *Physical Review Letters* **1999**, *82*, 2544–2547, DOI: 10.1103/physrevlett.82.2544.
- (170) Adamo, C.; Ernzerhof, M.; Scuseria, G. E. The meta-GGA functional: Thermochemistry with a kinetic energy density dependent exchange-correlation functional. *The Journal of Chemical Physics* **2000**, *112*, 2643–2649, DOI: 10.1063/1.480838.
- (171) Grimme, S.; Neese, F. Double-hybrid density functional theory for excited electronic states of molecules. *The Journal of Chemical Physics* **2007**, *127*, 154116, DOI: 10.1063/1.2772854.
- (172) Goerigk, L.; Grimme, S. Efficient and Accurate Double-Hybrid-Meta-GGA Density Functionals—Evaluation with the Extended GMTKN30 Database for General Main Group Thermochemistry, Kinetics, and Noncovalent Interactions. *Journal of Chemical Theory and Computation* **2010**, *7*, 291–309, DOI: 10.1021/ct100466k.
- (173) Neese, F. A critical evaluation of DFT, including time-dependent DFT, applied to bioinorganic chemistry. *JBIC Journal of Biological Inorganic Chemistry* **2006**, *11*, 702–711, DOI: 10.1007/s00775-006-0138-1.
- (174) Maitra, N. T.; Zhang, F.; Cave, R. J.; Burke, K. Double excitations within time-dependent density functional theory linear response. *The Journal of Chemical Physics* **2004**, *120*, 5932–5937, DOI: 10.1063/1.1651060.
- (175) Elliott, P.; Goldson, S.; Canahui, C.; Maitra, N. T. Perspectives on double-excitations in TDDFT. *Chemical Physics* **2011**, *391*, 110–119, DOI: 10.1016/j.chemphys.2011.03.020.

Bibliography

- (176) Sagredo, F.; Burke, K. Accurate double excitations from ensemble density functional calculations. *The Journal of Chemical Physics* **2018**, *149*, 134103, DOI: 10.1063/1.5043411.
- (177) Loos, P.-F.; Boggio-Pasqua, M.; Scemama, A.; Caffarel, M.; Jacquemin, D. Reference Energies for Double Excitations. *Journal of Chemical Theory and Computation* **2019**, *15*, 1939–1956, DOI: 10.1021/acs.jctc.8b01205.
- (178) Tawada, Y.; Tsuneda, T.; Yanagisawa, S.; Yanai, T.; Hirao, K. A long-range-corrected time-dependent density functional theory. *The Journal of Chemical Physics* **2004**, *120*, 8425–8433, DOI: 10.1063/1.1688752.
- (179) Yanai, T.; Tew, D. P.; Handy, N. C. A new hybrid exchange–correlation functional using the Coulomb-attenuating method (CAM-B3LYP). *Chemical Physics Letters* **2004**, *393*, 51–57, DOI: 10.1016/j.cplett.2004.06.011.
- (180) Gerber, I. C.; Ángyán, J. G. Hybrid functional with separated range. *Chemical Physics Letters* **2005**, *415*, 100–105, DOI: 10.1016/j.cplett.2005.08.060.
- (181) Vydrov, O. A.; Scuseria, G. E. Assessment of a long-range corrected hybrid functional. *The Journal of Chemical Physics* **2006**, *125*, 234109, DOI: 10.1063/1.2409292.
- (182) Gerber, I. C.; Angyan, J. G.; Marsman, M.; Kresse, G. Range separated hybrid density functional with long-range Hartree-Fock exchange applied to solids. *The Journal of Chemical Physics* **2007**, *127*, 054101, DOI: 10.1063/1.2759209.
- (183) Mardirossian, N.; Head-Gordon, M. ω B97X-V: A 10-parameter, range-separated hybrid, generalized gradient approximation density functional with nonlocal correlation, designed by a survival-of-the-fittest strategy. *Physical Chemistry Chemical Physics* **2014**, *16*, 9904, DOI: 10.1039/c3cp54374a.
- (184) Jaramillo, J.; Scuseria, G. E.; Ernzerhof, M. Local hybrid functionals. *The Journal of Chemical Physics* **2003**, *118*, 1068–1073, DOI: 10.1063/1.1528936.
- (185) Maier, T. M.; Arbuznikov, A. V.; Kaupp, M. Local hybrid functionals: Theory, implementation, and performance of an emerging new tool in quantum chemistry and beyond. *Wiley Interdisciplinary Reviews: Computational Molecular Science* **2018**, *9*, e1378, DOI: 10.1002/wcms.1378.
- (186) Haasler, M.; Maier, T. M.; Grotjahn, R.; Gückel, S.; Arbuznikov, A. V.; Kaupp, M. A Local Hybrid Functional with Wide Applicability and Good Balance between (De)Localization and Left–Right Correlation. *Journal of Chemical Theory and Computation* **2020**, *16*, 5645–5657, DOI: 10.1021/acs.jctc.0c00498.

- (187) Runge, E.; Gross, E. K. U. Density-Functional Theory for Time-Dependent Systems. *Physical Review Letters* **1984**, *52*, 997–1000, DOI: 10.1103/physrevlett.52.997.
- (188) Gross, E. K. U.; Dobson, J. F.; Petersilka, M. In *Topics in Current Chemistry*; Springer-Verlag, pp 81–172, DOI: 10.1007/bfb0016643.
- (189) Jensen, F., *Introduction to Computational Chemistry*; Wiley: 2017.
- (190) Lopata, K.; Govind, N. Modeling Fast Electron Dynamics with Real-Time Time-Dependent Density Functional Theory: Application to Small Molecules and Chromophores. *Journal of Chemical Theory and Computation* **2011**, *7*, 1344–1355, DOI: 10.1021/ct200137z.
- (191) Fischer, S. A.; Cramer, C. J.; Govind, N. Excited State Absorption from Real-Time Time-Dependent Density Functional Theory. *Journal of Chemical Theory and Computation* **2015**, *11*, 4294–4303, DOI: 10.1021/acs.jctc.5b00473.
- (192) Goings, J. J.; Lestrangé, P. J.; Li, X. Real-time time-dependent electronic structure theory. *WIREs Computational Molecular Science* **2017**, *8*, DOI: 10.1002/wcms.1341.
- (193) Müller, C.; Sharma, M.; Sierka, M. Real-time time-dependent density functional theory using density fitting and the continuous fast multipole method. *Journal of Computational Chemistry* **2020**, *41*, 2573–2582, DOI: 10.1002/jcc.26412.
- (194) CASIDA, M. E. In *Recent Advances in Density Functional Methods*; WORLD SCIENTIFIC: 1995, pp 155–192, DOI: 10.1142/9789812830586_0005.
- (195) Casida, M.; Huix-Rotllant, M. Progress in Time-Dependent Density-Functional Theory. *Annual Review of Physical Chemistry* **2012**, *63*, 287–323, DOI: 10.1146/annurev-physchem-032511-143803.
- (196) Giuliani, G.; Vignale, G., *Quantum Theory of the Electron Liquid*; Cambridge University Press: 2005, DOI: 10.1017/cbo9780511619915.
- (197) Ullrich, C. A., *Time-Dependent Density-Functional Theory*; Oxford University Press: 2011, DOI: 10.1093/acprof:oso/9780199563029.001.0001.
- (198) Furche, F.; Ahlrichs, R. Adiabatic time-dependent density functional methods for excited state properties. *The Journal of Chemical Physics* **2002**, *117*, 7433–7447, DOI: 10.1063/1.1508368.

Bibliography

- (199) Abraham, M. J.; Murtola, T.; Schulz, R.; Pall, S.; Smith, J. C.; Hess, B.; Lindahl, E. GROMACS: High performance molecular simulations through multi-level parallelism from laptops to supercomputers. *SoftwareX* **2015**, *1-2*, 19–25, DOI: 10.1016/j.softx.2015.06.001.
- (200) Eastman, P.; Swails, J.; Chodera, J. D.; McGibbon, R. T.; Zhao, Y.; Beauchamp, K. A.; Wang, L.-P.; Simmonett, A. C.; Harrigan, M. P.; Stern, C. D.; Wiewiora, R. P.; Brooks, B. R.; Pande, V. S. OpenMM 7: Rapid development of high performance algorithms for molecular dynamics. *PLOS Computational Biology* **2017**, *13*, ed. by Gentleman, R., e1005659, DOI: 10.1371/journal.pcbi.1005659.
- (201) Kutzner, C.; Pall, S.; Fechner, M.; Esztermann, A.; Groot, B. L.; Grubmüller, H. More bang for your buck: Improved use of GPU nodes for GROMACS 2018. *Journal of Computational Chemistry* **2019**, *40*, 2418–2431, DOI: 10.1002/jcc.26011.
- (202) Thiel, W. Semiempirical quantum–chemical methods. *Wiley Interdisciplinary Reviews: Computational Molecular Science* **2013**, *4*, 145–157, DOI: 10.1002/wcms.1161.
- (203) Akimov, A. V.; Prezhdo, O. V. Large-Scale Computations in Chemistry: A Bird’s Eye View of a Vibrant Field. *Chemical Reviews* **2015**, *115*, 5797–5890, DOI: 10.1021/cr500524c.
- (204) Koskinen, P.; Mäkinen, V. Density-functional tight-binding for beginners. *Computational Materials Science* **2009**, *47*, 237–253, DOI: 10.1016/j.commatsci.2009.07.013.
- (205) Elstner, M.; Seifert, G. Density functional tight binding. *Philosophical Transactions of the Royal Society A: Mathematical, Physical and Engineering Sciences* **2014**, *372*, 20120483, DOI: 10.1098/rsta.2012.0483.
- (206) Hourahine, B. et al. DFTB+, a software package for efficient approximate density functional theory based atomistic simulations. *The Journal of Chemical Physics* **2020**, *152*, 124101, DOI: 10.1063/1.5143190.
- (207) Gaus, M.; Cui, Q.; Elstner, M. DFTB3: Extension of the Self-Consistent-Charge Density-Functional Tight-Binding Method (SCC-DFTB). *Journal of Chemical Theory and Computation* **2011**, *7*, 931–948, DOI: 10.1021/ct100684s.

- (208) Porezag, D.; Frauenheim, T.; Köhler, T.; Seifert, G.; Kaschner, R. Construction of tight-binding-like potentials on the basis of density-functional theory: Application to carbon. *Physical Review B* **1995**, *51*, 12947–12957, DOI: 10.1103/physrevb.51.12947.
- (209) Elstner, M.; Porezag, D.; Jungnickel, G.; Elsner, J.; Haugk, M.; Frauenheim, T.; Suhai, S.; Seifert, G. Self-consistent-charge density-functional tight-binding method for simulations of complex materials properties. *Physical Review B* **1998**, *58*, 7260–7268, DOI: 10.1103/physrevb.58.7260.
- (210) Brandenburg, J. G.; Grimme, S. Accurate Modeling of Organic Molecular Crystals by Dispersion-Corrected Density Functional Tight Binding (DFTB). *The Journal of Physical Chemistry Letters* **2014**, *5*, 1785–1789, DOI: 10.1021/jz500755u.
- (211) Caldeweyher, E.; Bannwarth, C.; Grimme, S. Extension of the D3 dispersion coefficient model. *The Journal of Chemical Physics* **2017**, *147*, 034112, DOI: 10.1063/1.4993215.
- (212) Bannwarth, C.; Ehlert, S.; Grimme, S. GFN2-xTB—An Accurate and Broadly Parametrized Self-Consistent Tight-Binding Quantum Chemical Method with Multipole Electrostatics and Density-Dependent Dispersion Contributions. *Journal of Chemical Theory and Computation* **2019**, *15*, 1652–1671, DOI: 10.1021/acs.jctc.8b01176.
- (213) Caldeweyher, E.; Ehlert, S.; Hansen, A.; Neugebauer, H.; Spicher, S.; Bannwarth, C.; Grimme, S. A generally applicable atomic-charge dependent London dispersion correction. *The Journal of Chemical Physics* **2019**, *150*, 154122, DOI: 10.1063/1.5090222.
- (214) Gaus, M.; Goez, A.; Elstner, M. Parametrization and Benchmark of DFTB3 for Organic Molecules. *Journal of Chemical Theory and Computation* **2012**, *9*, 338–354, DOI: 10.1021/ct300849w.
- (215) Jenness, G. R.; Bresnahan, C. G.; Shukla, M. K. Adventures in DFTB: Toward an Automatic Parameterization Scheme. *Journal of Chemical Theory and Computation* **2020**, *16*, 6894–6903, DOI: 10.1021/acs.jctc.0c00842.
- (216) Grimme, S.; Bannwarth, C.; Shushkov, P. A Robust and Accurate Tight-Binding Quantum Chemical Method for Structures, Vibrational Frequencies, and Noncovalent Interactions of Large Molecular Systems Parametrized for All spd-Block Elements ($Z = 1-86$). *Journal of Chemical Theory and Computation* **2017**, *13*, 1989–2009, DOI: 10.1021/acs.jctc.7b00118.

Bibliography

- (217) Bannwarth, C.; Caldeweyher, E.; Ehlert, S.; Hansen, A.; Pracht, P.; Seibert, J.; Spicher, S.; Grimme, S. Extended tight-binding quantum chemistry methods. *WIREs Computational Molecular Science* **2020**, DOI: 10.1002/wcms.1493.
- (218) Closser, K. D.; Gessner, O.; Head-Gordon, M. Simulations of the dissociation of small helium clusters with ab initio molecular dynamics in electronically excited states. *The Journal of Chemical Physics* **2014**, *140*, 134306, DOI: 10.1063/1.4869193.
- (219) Li, J.-H.; Chai, J.-D.; Guo, G.-Y.; Hayashi, M. The quantified NTO analysis for the electronic excitations of molecular many-body systems. *Chemical Physics Letters* **2011**, *514*, 362–367, DOI: 10.1016/j.cplett.2011.08.066.
- (220) Li, J.-H.; Chai, J.-D.; Guo, G.-Y.; Hayashi, M. Significant role of the DNA backbone in mediating the transition origin of electronic excitations of B-DNA – implication from long range corrected TDDFT and quantified NTO analysis. *Physical Chemistry Chemical Physics* **2012**, *14*, 9092, DOI: 10.1039/c2cp23676a.
- (221) Plasser, F. TheoDORE: A toolbox for a detailed and automated analysis of electronic excited state computations. *The Journal of Chemical Physics* **2020**, *152*, 084108, DOI: 10.1063/1.5143076.
- (222) Song, H.; Fischer, S. A.; Zhang, Y.; Cramer, C. J.; Mukamel, S.; Govind, N.; Tretiak, S. First Principles Nonadiabatic Excited-State Molecular Dynamics in NWChem. *Journal of Chemical Theory and Computation* **2020**, *16*, 6418–6427, DOI: 10.1021/acs.jctc.0c00295.
- (223) García, J. S.; Boggio-Pasqua, M.; Ciofini, I.; Campetella, M. Excited state tracking during the relaxation of coordination compounds. *Journal of Computational Chemistry* **2019**, *40*, 1420–1428, DOI: 10.1002/jcc.25800.
- (224) Campetella, M.; García, J. S. Following the evolution of excited states along photochemical reaction pathways. *Journal of Computational Chemistry* **2020**, DOI: 10.1002/jcc.26162.
- (225) Plasser, F.; Ruckebauer, M.; Mai, S.; Oppel, M.; Marquetand, P.; González, L. Efficient and Flexible Computation of Many-Electron Wave Function Overlaps. *Journal of Chemical Theory and Computation* **2016**, *12*, 1207–1219, DOI: 10.1021/acs.jctc.5b01148.
- (226) Sapunar, M.; Piteša, T.; Davidović, D.; Došlić, N. Highly Efficient Algorithms for CIS Type Excited State Wave Function Overlaps. *Journal of Chemical Theory and Computation* **2019**, *15*, 3461–3469, DOI: 10.1021/acs.jctc.9b00235.

- (227) Martin, R. L. Natural transition orbitals. *The Journal of Chemical Physics* **2003**, *118*, 4775–4777, DOI: 10.1063/1.1558471.
- (228) Plasser, F.; Lischka, H. Analysis of Excitonic and Charge Transfer Interactions from Quantum Chemical Calculations. *Journal of Chemical Theory and Computation* **2012**, *8*, 2777–2789, DOI: 10.1021/ct300307c.
- (229) Shepard, R. In *Modern Electronic Structure Theory*; World Scientific Publishing Company: 1995, pp 345–458, DOI: 10.1142/9789812832108_0007.
- (230) Sorensen, D. C. Newton’s Method with a Model Trust Region Modification. *SIAM Journal on Numerical Analysis* **1982**, *19*, 409–426, DOI: 10.1137/0719026.
- (231) Banerjee, A.; Adams, N.; Simons, J.; Shepard, R. Search for stationary points on surfaces. *The Journal of Physical Chemistry* **1985**, *89*, 52–57, DOI: 10.1021/j100247a015.
- (232) Bakken, V.; Helgaker, T. The efficient optimization of molecular geometries using redundant internal coordinates. *The Journal of Chemical Physics* **2002**, *117*, 9160–9174, DOI: 10.1063/1.1515483.
- (233) Asmundis, R. D.; di Serafino, D.; Riccio, F.; Toraldo, G. On spectral properties of steepest descent methods. *IMA Journal of Numerical Analysis* **2013**, *33*, 1416–1435, DOI: 10.1093/imanum/drs056.
- (234) *Numerical Optimization*; Springer New York: 2006, DOI: 10.1007/978-0-387-40065-5.
- (235) Broyden, C. G. The Convergence of a Class of Double-rank Minimization Algorithms 1. General Considerations. *IMA Journal of Applied Mathematics* **1970**, *6*, 76–90, DOI: 10.1093/imamat/6.1.76.
- (236) Fletcher, R. A new approach to variable metric algorithms. *The Computer Journal* **1970**, *13*, 317–322, DOI: 10.1093/comjnl/13.3.317.
- (237) Goldfarb, D. A family of variable-metric methods derived by variational means. *Mathematics of Computation* **1970**, *24*, 23–23, DOI: 10.1090/s0025-5718-1970-0258249-6.
- (238) Shanno, D. F. Conditioning of quasi-Newton methods for function minimization. *Mathematics of Computation* **1970**, *24*, 647–647, DOI: 10.1090/s0025-5718-1970-0274029-x.

Bibliography

- (239) Birkholz, A. B.; Schlegel, H. B. Exploration of some refinements to geometry optimization methods. *Theoretical Chemistry Accounts* **2016**, *135*, DOI: 10.1007/s00214-016-1847-3.
- (240) Bofill, J. M. Updated Hessian matrix and the restricted step method for locating transition structures. *Journal of Computational Chemistry* **1994**, *15*, 1–11, DOI: 10.1002/jcc.540150102.
- (241) Lindh, R.; Bernhardsson, A.; Karlström, G.; Malmqvist, P. A. On the use of a Hessian model function in molecular geometry optimizations. *Chemical Physics Letters* **1995**, *241*, 423–428, DOI: 10.1016/0009-2614(95)00646-1.
- (242) Fischer, T. H.; Almlof, J. General methods for geometry and wave function optimization. *The Journal of Physical Chemistry* **1992**, *96*, 9768–9774, DOI: 10.1021/j100203a036.
- (243) Swart, M.; Bickelhaupt, F. M. Optimization of strong and weak coordinates. *International Journal of Quantum Chemistry* **2006**, *106*, 2536–2544, DOI: 10.1002/qua.21049.
- (244) Vreven, T.; Morokuma, K.; Farkas, Ö.; Schlegel, H. B.; Frisch, M. J. Geometry optimization with QM/MM, ONIOM, and other combined methods. I. Microiterations and constraints. *Journal of Computational Chemistry* **2003**, *24*, 760–769, DOI: 10.1002/jcc.10156.
- (245) Farkas, Ö.; Schlegel, H. B. Methods for optimizing large molecules. II. Quadratic search. *The Journal of Chemical Physics* **1999**, *111*, 10806–10814, DOI: 10.1063/1.480484.
- (246) Eckert, F.; Pulay, P.; Werner, H.-J. Ab initio geometry optimization for large molecules. *Journal of Computational Chemistry* **1997**, *18*, 1473–1483, DOI: 10.1002/(sici)1096-987x(199709)18:12<1473::aid-jcc5>3.0.co;2-g.
- (247) Polak, E.; Ribiere, G. Note sur la convergence de méthodes de directions conjuguées. *ESAIM: Mathematical Modelling and Numerical Analysis-Modélisation Mathématique et Analyse Numérique* **1969**, *3*, 35–43.
- (248) Polyak, B. The conjugate gradient method in extremal problems. *USSR Computational Mathematics and Mathematical Physics* **1969**, *9*, 94–112, DOI: 10.1016/0041-5553(69)90035-4.

- (249) Hager, W. W.; Zhang, H. A New Conjugate Gradient Method with Guaranteed Descent and an Efficient Line Search. *SIAM Journal on Optimization* **2005**, *16*, 170–192, DOI: 10.1137/030601880.
- (250) Koslover, E. F.; Wales, D. J. Geometry optimization for peptides and proteins: Comparison of Cartesian and internal coordinates. *The Journal of Chemical Physics* **2007**, *127*, 234105, DOI: 10.1063/1.2807227.
- (251) Nocedal, J. Updating quasi-Newton matrices with limited storage. *Mathematics of Computation* **1980**, *35*, 773–773, DOI: 10.1090/s0025-5718-1980-0572855-7.
- (252) Baysal, C.; Meirovitch, H.; Navon, I. M. Performance of efficient minimization algorithms as applied to models of peptides and proteins. *Journal of Computational Chemistry* **1999**, *20*, 354–364, DOI: 10.1002/(sici)1096-987x(199902)20:3<354::aid-jcc7>3.0.co;2-8.
- (253) Das, B.; Meirovitch, H.; Navon, I. M. Performance of hybrid methods for large-scale unconstrained optimization as applied to models of proteins. *Journal of Computational Chemistry* **2003**, *24*, 1222–1231, DOI: 10.1002/jcc.10275.
- (254) Powell, M. J. D. Algorithms for nonlinear constraints that use lagrangian functions. *Mathematical Programming* **1978**, *14*, 224–248, DOI: 10.1007/bf01588967.
- (255) Goldfarb, D.; Ren, Y.; Bahamou, A. Practical Quasi-Newton Methods for Training Deep Neural Networks, 2020.
- (256) Besalú, E.; Bofill, J. M. On the automatic restricted-step rational-function-optimization method. *Theoretical Chemistry Accounts: Theory Computation, and Modeling (Theoretica Chimica Acta)* **1998**, *100*, 265–274, DOI: 10.1007/s002140050387.
- (257) Moré, J. J.; Thuente, D. J. Line Search Algorithms with Guaranteed Sufficient Decrease. *ACM Trans. Math. Softw.* **1994**, *20*, 286–307, DOI: 10.1145/192115.192132.
- (258) Császár, P.; Pulay, P. Geometry optimization by direct inversion in the iterative subspace. *Journal of Molecular Structure* **1984**, *114*, 31–34, DOI: 10.1016/s0022-2860(84)87198-7.
- (259) Farkas, Ö.; Schlegel, H. B. Methods for optimizing large molecules. Part III. An improved algorithm for geometry optimization using direct inversion in the iterative subspace (GDIIS). *Phys. Chem. Chem. Phys.* **2002**, *4*, 11–15, DOI: 10.1039/b108658h.

Bibliography

- (260) Li, X.; Frisch, M. J. Energy-Represented Direct Inversion in the Iterative Subspace within a Hybrid Geometry Optimization Method. *Journal of Chemical Theory and Computation* **2006**, *2*, 835–839, DOI: 10.1021/ct050275a.
- (261) Baker, J.; Hehre, W. J. Geometry optimization in cartesian coordinates: The end of the Z-matrix? *Journal of Computational Chemistry* **1991**, *12*, 606–610, DOI: 10.1002/jcc.540120510.
- (262) Sellers, H.; Klimkowski, V.; Schäfer, L. Normal coordinate ab initio force relaxation. *Chemical Physics Letters* **1978**, *58*, 541–544, DOI: 10.1016/0009-2614(78)80014-1.
- (263) Boür, P.; Keiderling, T. A. Partial optimization of molecular geometry in normal coordinates and use as a tool for simulation of vibrational spectra. *The Journal of Chemical Physics* **2002**, *117*, 4126–4132, DOI: 10.1063/1.1498468.
- (264) Pulay, P.; Fogarasi, G. Geometry optimization in redundant internal coordinates. *The Journal of Chemical Physics* **1992**, *96*, 2856–2860, DOI: 10.1063/1.462844.
- (265) Peng, C.; Ayala, P. Y.; Schlegel, H. B.; Frisch, M. J. Using redundant internal coordinates to optimize equilibrium geometries and transition states. *Journal of Computational Chemistry* **1996**, *17*, 49–56, DOI: 10.1002/(sici)1096-987x(19960115)17:1<49::aid-jcc5>3.0.co;2-0.
- (266) Baiardi, A.; Bloino, J.; Barone, V. General formulation of vibronic spectroscopy in internal coordinates. *The Journal of Chemical Physics* **2016**, *144*, 084114, DOI: 10.1063/1.4942165.
- (267) Fogarasi, G.; Zhou, X.; Taylor, P. W.; Pulay, P. The calculation of ab initio molecular geometries: efficient optimization by natural internal coordinates and empirical correction by offset forces. *Journal of the American Chemical Society* **1992**, *114*, 8191–8201, DOI: 10.1021/ja00047a032.
- (268) Baker, J. Techniques for geometry optimization: A comparison of cartesian and natural internal coordinates. *Journal of Computational Chemistry* **1993**, *14*, 1085–1100, DOI: 10.1002/jcc.540140910.
- (269) Von Arnim, M.; Ahlrichs, R. Geometry optimization in generalized natural internal coordinates. *The Journal of Chemical Physics* **1999**, *111*, 9183–9190, DOI: 10.1063/1.479510.

- (270) Baker, J.; Kessi, A.; Delley, B. The generation and use of delocalized internal coordinates in geometry optimization. *The Journal of Chemical Physics* **1996**, *105*, 192–212, DOI: 10.1063/1.471864.
- (271) Billeter, S. R.; Turner, A. J.; Thiel, W. Linear scaling geometry optimisation and transition state search in hybrid delocalised internal coordinates. *Physical Chemistry Chemical Physics* **2000**, *2*, 2177–2186, DOI: 10.1039/a909486e.
- (272) Wang, L.-P.; Song, C. Geometry optimization made simple with translation and rotation coordinates. *The Journal of Chemical Physics* **2016**, *144*, 214108, DOI: 10.1063/1.4952956.
- (273) Hoy, A.; Mills, I.; Strey, G. Anharmonic force constant calculations. *Molecular Physics* **1972**, *24*, 1265–1290, DOI: 10.1080/00268977200102361.
- (274) Jackels, C. F.; Gu, Z.; Truhlar, D. G. Reaction-path potential and vibrational frequencies in terms of curvilinear internal coordinates. *The Journal of Chemical Physics* **1995**, *102*, 3188–3201, DOI: 10.1063/1.468630.
- (275) Chuang, Y.-Y.; Truhlar, D. G. Reaction-path dynamics with harmonic vibration frequencies in curvilinear internal coordinates: H+trans-N₂H₂→N₂H+H 2. *The Journal of Chemical Physics* **1997**, *107*, 83–89, DOI: 10.1063/1.474377.
- (276) Lee, S.-H.; Palmo, K.; Krimm, S. New out-of-plane angle and bond angle internal coordinates and related potential energy functions for molecular mechanics and dynamics simulations. *Journal of Computational Chemistry* **1999**, *20*, 1067–1084, DOI: 10.1002/(sici)1096-987x(19990730)20:10<1067::aid-jcc9>3.0.co;2-v.
- (277) Németh, K.; Challacombe, M.; Veenendaal, M. V. The choice of internal coordinates in complex chemical systems. *Journal of Computational Chemistry* **2010**, NA–NA, DOI: 10.1002/jcc.21494.
- (278) Wilson, E. B.; Decius, J. C.; Cross, P. C., *Molecular vibrations: the theory of infrared and Raman vibrational spectra*; Courier Corporation: 1980.
- (279) Baker, J.; Bergeron, D. Constrained optimization in cartesian coordinates. *J. Comput. Chem.* **1993**, *14*, 1339–1346, DOI: 10.1002/jcc.540141111.
- (280) Baker, J. Constrained optimization in delocalized internal coordinates. *J. Comput. Chem.* **1997**, *18*, 1079–1095, DOI: 10.1002/(sici)1096-987x(199706)18:8<1079::aid-jcc12>3.0.co;2-8.

Bibliography

- (281) Kruse, H.; Spöner, J. Towards biochemically relevant QM computations on nucleic acids: controlled electronic structure geometry optimization of nucleic acid structural motifs using penalty restraint functions. *Phys. Chem. Chem. Phys.* **2015**, *17*, 1399–1410, DOI: 10.1039/c4cp04680c.
- (282) Palenik, M. C. Initial estimate for minimum energy pathways and transition states using velocities in internal coordinates. *Chemical Physics* **2021**, *542*, 111046, DOI: 10.1016/j.chemphys.2020.111046.
- (283) Rybkin, V. V.; Ekström, U.; Helgaker, T. Internal-to-Cartesian back transformation of molecular geometry steps using high-order geometric derivatives. *Journal of Computational Chemistry* **2013**, *34*, 1842–1849, DOI: 10.1002/jcc.23327.
- (284) Golub, G. H., *Matrix Computations (Johns Hopkins Studies in the Mathematical Sciences)*; Johns Hopkins University Press: 2013.
- (285) Goodfellow, I.; Bengio, Y.; Courville, A., *Deep Learning*, <http://www.deeplearningbook.org>; MIT Press: 2016.
- (286) Mones, L.; Ortner, C.; Csányi, G. Preconditioners for the geometry optimisation and saddle point search of molecular systems. *Scientific Reports* **2018**, *8*, DOI: 10.1038/s41598-018-32105-x.
- (287) Packwood, D.; Kermode, J.; Mones, L.; Bernstein, N.; Woolley, J.; Gould, N.; Ortner, C.; Csányi, G. A universal preconditioner for simulating condensed phase materials. *The Journal of Chemical Physics* **2016**, *144*, 164109, DOI: 10.1063/1.4947024.
- (288) Jiang, L.; Byrd, R. H.; Eskow, E.; Schnabel, R. B. *A preconditioned L-BFGS algorithm with application to molecular energy minimization*; tech. rep.; COLORADO UNIV AT BOULDER DEPT OF COMPUTER SCIENCE, 2004.
- (289) Rappe, A. K.; Casewit, C. J.; Colwell, K. S.; Goddard, W. A.; Skiff, W. M. UFF, a full periodic table force field for molecular mechanics and molecular dynamics simulations. *Journal of the American Chemical Society* **1992**, *114*, 10024–10035, DOI: 10.1021/ja00051a040.
- (290) Heyden, A.; Bell, A. T.; Keil, F. J. Efficient methods for finding transition states in chemical reactions: Comparison of improved dimer method and partitioned rational function optimization method. *The Journal of Chemical Physics* **2005**, *123*, 224101, DOI: 10.1063/1.2104507.

- (291) Neese, F.; Wennmohs, F.; Hansen, A.; Becker, U. Efficient approximate and parallel Hartree–Fock and hybrid DFT calculations. A ‘chain-of-spheres’ algorithm for the Hartree–Fock exchange. *Chemical Physics* **2009**, *356*, 98–109, DOI: 10.1016/j.chemphys.2008.10.036.
- (292) Bykov, D.; Petrenko, T.; Izsák, R.; Kossmann, S.; Becker, U.; Valeev, E.; Neese, F. Efficient implementation of the analytic second derivatives of Hartree–Fock and hybrid DFT energies: a detailed analysis of different approximations. *Molecular Physics* **2015**, *113*, 1961–1977, DOI: 10.1080/00268976.2015.1025114.
- (293) Ayala, P. Y.; Schlegel, H. B. A combined method for determining reaction paths minima, and transition state geometries. *The Journal of Chemical Physics* **1997**, *107*, 375–384, DOI: 10.1063/1.474398.
- (294) Henkelman, G.; Jónsson, H. Improved tangent estimate in the nudged elastic band method for finding minimum energy paths and saddle points. *The Journal of Chemical Physics* **2000**, *113*, 9978–9985, DOI: 10.1063/1.1323224.
- (295) Peters, B.; Heyden, A.; Bell, A. T.; Chakraborty, A. A growing string method for determining transition states: Comparison to the nudged elastic band and string methods. *The Journal of Chemical Physics* **2004**, *120*, 7877–7886, DOI: 10.1063/1.1691018.
- (296) Smidstrup, S.; Pedersen, A.; Stokbro, K.; Jónsson, H. Improved initial guess for minimum energy path calculations. *The Journal of Chemical Physics* **2014**, *140*, 214106, DOI: 10.1063/1.4878664.
- (297) Halgren, T. A.; Lipscomb, W. N. The synchronous-transit method for determining reaction pathways and locating molecular transition states. *Chemical Physics Letters* **1977**, *49*, 225–232, DOI: 10.1016/0009-2614(77)80574-5.
- (298) Govind, N.; Petersen, M.; Fitzgerald, G.; King-Smith, D.; Andzelm, J. A generalized synchronous transit method for transition state location. *Computational Materials Science* **2003**, *28*, 250–258, DOI: 10.1016/s0927-0256(03)00111-3.
- (299) Behn, A.; Zimmerman, P. M.; Bell, A. T.; Head-Gordon, M. Incorporating Linear Synchronous Transit Interpolation into the Growing String Method: Algorithm and Applications. *Journal of Chemical Theory and Computation* **2011**, *7*, 4019–4025, DOI: 10.1021/ct200654u.

Bibliography

- (300) Zimmerman, P. M. Growing string method with interpolation and optimization in internal coordinates: Method and examples. *The Journal of Chemical Physics* **2013**, *138*, 184102, DOI: 10.1063/1.4804162.
- (301) Zhu, X.; Thompson, K. C.; Martínez, T. J. Geodesic interpolation for reaction pathways. *The Journal of Chemical Physics* **2019**, *150*, 164103, DOI: 10.1063/1.5090303.
- (302) E, W.; Ren, W.; Vanden-Eijnden, E. Simplified and improved string method for computing the minimum energy paths in barrier-crossing events. *The Journal of Chemical Physics* **2007**, *126*, 164103, DOI: 10.1063/1.2720838.
- (303) Maragakis, P.; Andreev, S. A.; Brumer, Y.; Reichman, D. R.; Kaxiras, E. Adaptive nudged elastic band approach for transition state calculation. *The Journal of Chemical Physics* **2002**, *117*, 4651–4658, DOI: 10.1063/1.1495401.
- (304) Zhu, T.; Li, J.; Samanta, A.; Kim, H. G.; Suresh, S. Interfacial plasticity governs strain rate sensitivity and ductility in nanostructured metals. *Proceedings of the National Academy of Sciences* **2007**, *104*, 3031–3036, DOI: 10.1073/pnas.0611097104.
- (305) Zhang, J.; Zhang, H.; Ye, H.; Zheng, Y. Free-end adaptive nudged elastic band method for locating transition states in minimum energy path calculation. *The Journal of Chemical Physics* **2016**, *145*, 094104, DOI: 10.1063/1.4962019.
- (306) Sheppard, D.; Terrell, R.; Henkelman, G. Optimization methods for finding minimum energy paths. *The Journal of Chemical Physics* **2008**, *128*, 134106, DOI: 10.1063/1.2841941.
- (307) Herbol, H. C.; Stevenson, J.; Clancy, P. Computational Implementation of Nudged Elastic Band Rigid Rotation, and Corresponding Force Optimization. *Journal of Chemical Theory and Computation* **2017**, *13*, 3250–3259, DOI: 10.1021/acs.jctc.7b00360.
- (308) Melander, M.; Laasonen, K.; Jónsson, H. Removing External Degrees of Freedom from Transition-State Search Methods using Quaternions. *Journal of Chemical Theory and Computation* **2015**, *11*, 1055–1062, DOI: 10.1021/ct501155k.
- (309) Henkelman, G.; Uberuaga, B. P.; Jónsson, H. A climbing image nudged elastic band method for finding saddle points and minimum energy paths. *The Journal of Chemical Physics* **2000**, *113*, 9901–9904, DOI: 10.1063/1.1329672.

- (310) Zarkevich, N. A.; Johnson, D. D. Nudged-elastic band method with two climbing images: Finding transition states in complex energy landscapes. *The Journal of Chemical Physics* **2015**, *142*, 024106, DOI: 10.1063/1.4905209.
- (311) Henkelman, G.; Jónsson, H. A dimer method for finding saddle points on high dimensional potential surfaces using only first derivatives. *The Journal of Chemical Physics* **1999**, *111*, 7010–7022, DOI: 10.1063/1.480097.
- (312) Kästner, J.; Sherwood, P. Superlinearly converging dimer method for transition state search. *The Journal of Chemical Physics* **2008**, *128*, 014106, DOI: 10.1063/1.2815812.
- (313) Shang, C.; Liu, Z.-P. Constrained Broyden Minimization Combined with the Dimer Method for Locating Transition State of Complex Reactions. *Journal of Chemical Theory and Computation* **2010**, *6*, 1136–1144, DOI: 10.1021/ct9005147.
- (314) Schaefer, B.; Mohr, S.; Amsler, M.; Goedecker, S. Minima hopping guided path search: An efficient method for finding complex chemical reaction pathways. *The Journal of Chemical Physics* **2014**, *140*, 214102, DOI: 10.1063/1.4878944.
- (315) Baker, J.; Chan, F. The location of transition states: A comparison of Cartesian, Z-matrix, and natural internal coordinates. *Journal of Computational Chemistry* **1996**, *17*, 888–904, DOI: 10.1002/(sici)1096-987x(199605)17:7<888::aid-jcc12>3.0.co;2-7.
- (316) Fukui, K.; Kato, S.; Fujimoto, H. Constituent analysis of the potential gradient along a reaction coordinate. Method and an application to methane + tritium reaction. *Journal of the American Chemical Society* **1975**, *97*, 1–7, DOI: 10.1021/ja00834a001.
- (317) Ishida, K.; Morokuma, K.; Komornicki, A. The intrinsic reaction coordinate. An ab initio calculation for $\text{HNC} \rightarrow \text{HCN}$ and $\text{H} + \text{CH}_4 \rightarrow \text{CH}_3 + \text{H}$. *The Journal of Chemical Physics* **1977**, *66*, 2153–2156, DOI: 10.1063/1.434152.
- (318) Maeda, S.; Harabuchi, Y.; Ono, Y.; Taketsugu, T.; Morokuma, K. Intrinsic reaction coordinate: Calculation bifurcation, and automated search. *International Journal of Quantum Chemistry* **2014**, *115*, 258–269, DOI: 10.1002/qua.24757.
- (319) Unke, O. T.; Brickel, S.; Meuwly, M. Sampling reactive regions in phase space by following the minimum dynamic path. *The Journal of Chemical Physics* **2019**, *150*, 074107, DOI: 10.1063/1.5082885.

Bibliography

- (320) Baker, J.; Gill, P. M. W. An algorithm for the location of branching points on reaction paths. *Journal of Computational Chemistry* **1988**, *9*, 465–475, DOI: 10.1002/jcc.540090505.
- (321) Quapp, W.; Hirsch, M.; Heidrich, D. Bifurcation of reaction pathways: the set of valley ridge inflection points of a simple three-dimensional potential energy surface. *Theoretical Chemistry Accounts: Theory, Computation, and Modeling (Theoretica Chimica Acta)* **1998**, *100*, 285–299, DOI: 10.1007/s002140050389.
- (322) Quapp, W.; Hirsch, M.; Heidrich, D. An approach to reaction path branching using valley?ridge inflection points of potential-energy surfaces. *Theoretical Chemistry Accounts: Theory, Computation, and Modeling (Theoretica Chimica Acta)* **2004**, *112*, 40–51, DOI: 10.1007/s00214-003-0558-8.
- (323) Curtiss, C. F.; Hirschfelder, J. O. Integration of Stiff Equations. *Proceedings of the National Academy of Sciences* **1952**, *38*, 235–243, DOI: 10.1073/pnas.38.3.235.
- (324) Shampine, L. F. In *Numerische Behandlung von Differentialgleichungen*; Birkhäuser Basel: 1975, pp 287–301, DOI: 10.1007/978-3-0348-5532-7_18.
- (325) Hratchian, H. P.; Schlegel, H. B. Accurate reaction paths using a Hessian based predictor-corrector integrator. *The Journal of Chemical Physics* **2004**, *120*, 9918–9924, DOI: 10.1063/1.1724823.
- (326) Aguilar-Mogas, A.; Giménez, X.; Bofill, J. M. On the implementation of the Runge–Kutta–Fehlberg algorithm to integrate intrinsic reaction coordinate paths. *Chemical Physics Letters* **2006**, *432*, 375–382, DOI: 10.1016/j.cplett.2006.10.061.
- (327) Aguilar-Mogas, A.; Giménez, X.; Bofill, J. M. Implementation of an algorithm based on the Runge-Kutta-Fehlberg technique and the potential energy as a reaction coordinate to locate intrinsic reaction paths. *Journal of Computational Chemistry* **2010**, n/a–n/a, DOI: 10.1002/jcc.21539.
- (328) Melissas, V. S.; Truhlar, D. G.; Garrett, B. C. Optimized calculations of reaction paths and reaction-path functions for chemical reactions. *The Journal of Chemical Physics* **1992**, *96*, 5758–5772, DOI: 10.1063/1.462674.
- (329) Deng, L.; Ziegler, T. The determination of intrinsic reaction coordinates by density functional theory. *International Journal of Quantum Chemistry* **1994**, *52*, 731–765, DOI: 10.1002/qua.560520406.

- (330) Gonzalez, C.; Schlegel, H. B. Improved algorithms for reaction path following: Higher-order implicit algorithms. *The Journal of Chemical Physics* **1991**, *95*, 5853–5860, DOI: 10.1063/1.461606.
- (331) Gonzalez, C.; Schlegel, H. B. An improved algorithm for reaction path following. *The Journal of Chemical Physics* **1989**, *90*, 2154–2161, DOI: 10.1063/1.456010.
- (332) Hratchian, H. P.; Frisch, M. J.; Schlegel, H. B. Steepest descent reaction path integration using a first-order predictor–corrector method. *The Journal of Chemical Physics* **2010**, *133*, 224101, DOI: 10.1063/1.3514202.
- (333) Hratchian, H. P.; Frisch, M. J. Integrating steepest-descent reaction pathways for large molecules. *The Journal of Chemical Physics* **2011**, *134*, 204103, DOI: 10.1063/1.3593456.
- (334) Pechukas, P. On simple saddle points of a potential surface, the conservation of nuclear symmetry along paths of steepest descent, and the symmetry of transition states. *The Journal of Chemical Physics* **1976**, *64*, 1516–1521, DOI: 10.1063/1.432370.
- (335) Page, M.; McIver, J. W. On evaluating the reaction path Hamiltonian. *The Journal of Chemical Physics* **1988**, *88*, 922–935, DOI: 10.1063/1.454172.
- (336) Hratchian, H. P.; Schlegel, H. B. Using Hessian Updating To Increase the Efficiency of a Hessian Based Predictor-Corrector Reaction Path Following Method. *Journal of Chemical Theory and Computation* **2004**, *1*, 61–69, DOI: 10.1021/ct0499783.
- (337) Bulirsch, R.; Stoer, J. Fehlerabschätzungen und Extrapolation mit rationalen Funktionen bei Verfahren vom Richardson-Typus. *Numerische Mathematik* **1964**, *6*, 413–427, DOI: 10.1007/bf01386092.
- (338) Bulirsch, R.; Stoer, J. Numerical treatment of ordinary differential equations by extrapolation methods. *Numerische Mathematik* **1966**, *8*, 1–13, DOI: 10.1007/bf02165234.
- (339) Bulirsch, R.; Stoer, J. Asymptotic upper and lower bounds for results of extrapolation methods. *Numerische Mathematik* **1966**, *8*, 93–104, DOI: 10.1007/bf02163179.
- (340) Farwig, R. Rate of convergence of Shepard’s global interpolation formula. *Mathematics of Computation* **1986**, *46*, 577–577, DOI: 10.1090/s0025-5718-1986-0829627-0.

Bibliography

- (341) Farwig, R. In *Algorithms for Approximation*; Clarendon Press: USA, 1987, pp 193–211.
- (342) Ischtwan, J.; Collins, M. A. Molecular potential energy surfaces by interpolation. *The Journal of Chemical Physics* **1994**, *100*, 8080–8088, DOI: 10.1063/1.466801.
- (343) Thompson, K. C.; Jordan, M. J. T.; Collins, M. A. Molecular potential energy surfaces by interpolation in Cartesian coordinates. *The Journal of Chemical Physics* **1998**, *108*, 564–578, DOI: 10.1063/1.475419.
- (344) Bettens, R. P. A.; Collins, M. A. Learning to interpolate molecular potential energy surfaces with confidence: A Bayesian approach. *The Journal of Chemical Physics* **1999**, *111*, 816–826, DOI: 10.1063/1.479368.
- (345) Hratchian, H. P.; Kraka, E. Improved Predictor–Corrector Integrators For Evaluating Reaction Path Curvature. *Journal of Chemical Theory and Computation* **2013**, *9*, 1481–1488, DOI: 10.1021/ct301021y.
- (346) Meisner, J.; Markmeyer, M. N.; Bohner, M. U.; Kästner, J. Comparison of classical reaction paths and tunneling paths studied with the semiclassical instanton theory. *Physical Chemistry Chemical Physics* **2017**, *19*, 23085–23094, DOI: 10.1039/c7cp03722h.
- (347) Meisner, J. Theoretical investigations of atom tunneling in the interstellar medium, en, 2018, DOI: 10.18419/OPUS-9841.
- (348) IX. The approximate arithmetical solution by finite differences of physical problems involving differential equations, with an application to the stresses in a masonry dam. *Philosophical Transactions of the Royal Society of London. Series A, Containing Papers of a Mathematical or Physical Character* **1911**, *210*, 307–357, DOI: 10.1098/rsta.1911.0009.
- (349) VIII. The deferred approach to the limit. *Philosophical Transactions of the Royal Society of London. Series A, Containing Papers of a Mathematical or Physical Character* **1927**, *226*, 299–361, DOI: 10.1098/rsta.1927.0008.
- (350) Celik, I.; Li, J.; Hu, G.; Shaffer, C. Limitations of Richardson Extrapolation and Some Possible Remedies. *Journal of Fluids Engineering* **2005**, *127*, 795–805, DOI: 10.1115/1.1949646.
- (351) Monroe, J. L. Extrapolation and the Bulirsch-Stoer algorithm. *Physical Review E* **2002**, *65*, DOI: 10.1103/physreve.65.066116.

- (352) Hairer, E.; Wanner, G., *Solving Ordinary Differential Equations II*; Springer Berlin Heidelberg: 1996, DOI: 10.1007/978-3-642-05221-7.
- (353) Hajduk, P. J.; Bures, M.; Praestgaard, J.; Fesik, S. W. Privileged Molecules for Protein Binding Identified from NMR-Based Screening. *Journal of Medicinal Chemistry* **2000**, *43*, 3443–3447, DOI: 10.1021/jm000164q.
- (354) Michel, M. C.; Foster, C.; Brunner, H. R.; Liu, L. A Systematic Comparison of the Properties of Clinically Used Angiotensin II Type 1 Receptor Antagonists. *Pharmacological Reviews* **2013**, *65*, ed. by Perez, D. M., 809–848, DOI: 10.1124/pr.112.007278.
- (355) Kylmälä, T.; Tois, J.; Xu, Y.; Franzén, R. One step synthesis of Diflunisal using a Pd-diamine complex. *Open Chemistry* **2009**, *7*, DOI: 10.2478/s11532-009-0068-1.
- (356) Kuuloja, N.; Kylmälä, T.; Xu, Y.; Franzén, R. Synthesis of Xenbucin using Suzuki reaction catalyzed by Pd/C in water. *Open Chemistry* **2008**, *6*, DOI: 10.2478/s11532-008-0044-1.
- (357) Bringmann, G.; Menche, D. Stereoselective Total Synthesis of Axially Chiral Natural Products via Biaryl Lactones†. *Accounts of Chemical Research* **2001**, *34*, 615–624, DOI: 10.1021/ar000106z.
- (358) Turner, S. E.; Williams, C. M.; Iversen, L.; Whalley, B. J. In *Progress in the Chemistry of Organic Natural Products*; Springer International Publishing: 2017, pp 61–101, DOI: 10.1007/978-3-319-45541-9_3.
- (359) Fayez, S.; Bruhn, T.; Feineis, D.; Assi, L. A.; Awale, S.; Bringmann, G. Ancistrosecolines A–F Unprecedented seco-Naphthylisoquinoline Alkaloids from the Roots of *Ancistrocladus abbreviatus*, with Apoptosis-Inducing Potential against HeLa Cancer Cells. *Journal of Natural Products* **2020**, DOI: 10.1021/acs.jnatprod.9b01168.
- (360) Xiao, B.-B.; Xia, G.-Y.; Wang, L.-Y.; Qiu, B.-L.; Xia, H.; Zhong, W.-C.; Tian, G.-H.; Lin, S. (±)-Bicoryanhunine A dimeric benzyloquinoline alkaloid atropo-enantiomers from *Corydalis yanhusuo*. *Tetrahedron Letters* **2020**, 151890, DOI: 10.1016/j.tetlet.2020.151890.
- (361) Fayez, S.; Li, J.; Feineis, D.; Assi, L. A.; Kaiser, M.; Brun, R.; Anany, M. A.; Wajant, H.; Bringmann, G. A Near-Complete Series of Four Atropisomeric Jozimine A2-Type Naphthylisoquinoline Dimers with Antiplasmodial and Cytotoxic Activ-

- ities and Related Alkaloids from *Ancistrocladus abbreviatus*. *Journal of Natural Products* **2019**, *82*, 3033–3046, DOI: 10.1021/acs.jnatprod.9b00589.
- (362) Hirano, K.; Miura, M. Recent Advances in Copper-mediated Direct Biaryl Coupling. *Chemistry Letters* **2015**, *44*, 868–873, DOI: 10.1246/cl.150354.
- (363) Negishi, E.; King, A. O.; Okukado, N. Selective carbon-carbon bond formation via transition metal catalysis. 3. A highly selective synthesis of unsymmetrical biaryls and diarylmethanes by the nickel- or palladium-catalyzed reaction of aryl- and benzylzinc derivatives with aryl halides. *The Journal of Organic Chemistry* **1977**, *42*, 1821–1823, DOI: 10.1021/jo00430a041.
- (364) Guo, L.; Srimontree, W.; Zhu, C.; Maity, B.; Liu, X.; Cavallo, L.; Rueping, M. Nickel-catalyzed Suzuki–Miyaura cross-couplings of aldehydes. *Nature Communications* **2019**, *10*, DOI: 10.1038/s41467-019-09766-x.
- (365) Liao, G.; Zhou, T.; Yao, Q.-J.; Shi, B.-F. Recent advances in the synthesis of axially chiral biaryls via transition metal-catalysed asymmetric C–H functionalization. *Chemical Communications* **2019**, *55*, 8514–8523, DOI: 10.1039/c9cc03967h.
- (366) Shi, S.; Meng, G.; Szostak, M. Synthesis of Biaryls through Nickel-Catalyzed Suzuki–Miyaura Coupling of Amides by Carbon–Nitrogen Bond Cleavage. *Angewandte Chemie International Edition* **2016**, *55*, 6959–6963, DOI: 10.1002/anie.201601914.
- (367) Corrie, T. J. A.; Ball, L. T.; Russell, C. A.; Lloyd-Jones, G. C. Au-Catalyzed Biaryl Coupling To Generate 5- to 9-Membered Rings: Turnover-Limiting Reductive Elimination versus π -Complexation. *Journal of the American Chemical Society* **2016**, *139*, 245–254, DOI: 10.1021/jacs.6b10018.
- (368) Simonetti, M.; Cannas, D. M.; Larrosa, I. In *Advances in Organometallic Chemistry*; Elsevier: 2017, pp 299–399, DOI: 10.1016/bs.adomc.2017.03.002.
- (369) Konze, W. V.; Scott, B. L.; Kubas, G. J. C–H Activation and C–C Coupling of Arenes by Cationic Pt(II) Complexes. *Journal of the American Chemical Society* **2002**, *124*, 12550–12556, DOI: 10.1021/ja020798h.
- (370) Felpin, F.-X.; Sengupta, S. Biaryl synthesis with arenediazonium salts: cross-coupling CH-arylation and annulation reactions. *Chemical Society Reviews* **2019**, *48*, 1150–1193, DOI: 10.1039/c8cs00453f.

- (371) Elsler, B.; Schollmeyer, D.; Dyballa, K. M.; Franke, R.; Waldvogel, S. R. Metal- and Reagent-Free Highly Selective Anodic Cross-Coupling Reaction of Phenols. *Angewandte Chemie International Edition* **2014**, n/a–n/a, DOI: 10.1002/anie.201400627.
- (372) Kita, Y.; Morimoto, K.; Ito, M.; Ogawa, C.; Goto, A.; Dohi, T. Metal-Free Oxidative Cross-Coupling of Unfunctionalized Aromatic Compounds. *Journal of the American Chemical Society* **2009**, *131*, 1668–1669, DOI: 10.1021/ja808940n.
- (373) Chan, T. L.; Wu, Y.; Choy, P. Y.; Kwong, F. Y. A Radical Process towards the Development of Transition-Metal-Free Aromatic Carbon-Carbon Bond-Forming Reactions. *Chemistry - A European Journal* **2013**, *19*, 15802–15814, DOI: 10.1002/chem.201301583.
- (374) Yanagi, T.; Otsuka, S.; Kasuga, Y.; Fujimoto, K.; Murakami, K.; Nogi, K.; Yorimitsu, H.; Osuka, A. Metal-Free Approach to Biaryls from Phenols and Aryl Sulfoxides by Temporarily Sulfur-Tethered Regioselective C–H/C–H Coupling. *Journal of the American Chemical Society* **2016**, *138*, 14582–14585, DOI: 10.1021/jacs.6b10278.
- (375) Dohi, T.; Ito, M.; Itani, I.; Yamaoka, N.; Morimoto, K.; Fujioka, H.; Kita, Y. Metal-Free C–H Cross-Coupling toward Oxygenated Naphthalene-Benzene Linked Biaryls. *Organic Letters* **2011**, *13*, 6208–6211, DOI: 10.1021/o1202632h.
- (376) Morimoto, K.; Yamaoka, N.; Ogawa, C.; Nakae, T.; Fujioka, H.; Dohi, T.; Kita, Y. Metal-Free Regioselective Oxidative Biaryl Coupling Leading to Head-to-Tail Bithiophenes: Reactivity Switching a Concept Based on the Iodonium(III) Intermediate. *Organic Letters* **2010**, *12*, 3804–3807, DOI: 10.1021/o11101498r.
- (377) Morimoto, K.; Sakamoto, K.; Ohnishi, Y.; Miyamoto, T.; Ito, M.; Dohi, T.; Kita, Y. Metal-Free OxidativeparaCross-Coupling of Phenols. *Chemistry - A European Journal* **2013**, *19*, 8726–8731, DOI: 10.1002/chem.201301028.
- (378) Leroux, F. R.; Berthelot, A.; Bonnafoux, L.; Panossian, A.; Colobert, F. Transition-Metal-Free Atropo-Selective Synthesis of Biaryl Compounds Based on Arynes. *Chemistry - A European Journal* **2012**, *18*, 14232–14236, DOI: 10.1002/chem.201202739.
- (379) Morimoto, K.; Dohi, T.; Kita, Y. Metal-free Oxidative Cross-Coupling Reaction of Aromatic Compounds Containing Heteroatoms. *Synlett* **2017**, *28*, 1680–1694, DOI: 10.1055/s-0036-1588455.

Bibliography

- (380) Ali, M. A. Computational studies on the gas phase reaction of methylenimine (CH₂NH) with water molecules. *Scientific Reports* **2020**, *10*, DOI: 10.1038/s41598-020-67515-3.
- (381) Weigend, F.; Ahlrichs, R. Balanced basis sets of split valence triple zeta valence and quadruple zeta valence quality for H to Rn: Design and assessment of accuracy. *Physical Chemistry Chemical Physics* **2005**, *7*, 3297, DOI: 10.1039/b508541a.
- (382) Grimme, S.; Antony, J.; Ehrlich, S.; Krieg, H. A consistent and accurate ab initio parametrization of density functional dispersion correction (DFT-D) for the 94 elements H-Pu. *The Journal of Chemical Physics* **2010**, *132*, 154104, DOI: 10.1063/1.3382344.
- (383) Grimme, S.; Ehrlich, S.; Goerigk, L. Effect of the damping function in dispersion corrected density functional theory. *Journal of Computational Chemistry* **2011**, *32*, 1456–1465, DOI: 10.1002/jcc.21759.
- (384) Frisch, M. J. et al. Gaussian 16 Revision B.01, Gaussian Inc. Wallingford CT, 2016.
- (385) Paulechka, E.; Kazakov, A. Efficient DLPNO-CCSD(T)-Based Estimation of Formation Enthalpies for C-, H-, O-, and N-Containing Closed-Shell Compounds Validated Against Critically Evaluated Experimental Data. *The Journal of Physical Chemistry A* **2017**, *121*, 4379–4387, DOI: 10.1021/acs.jpca.7b03195.
- (386) Riplinger, C.; Neese, F. An efficient and near linear scaling pair natural orbital based local coupled cluster method. *The Journal of Chemical Physics* **2013**, *138*, 034106, DOI: 10.1063/1.4773581.
- (387) Riplinger, C.; Sandhoefer, B.; Hansen, A.; Neese, F. Natural triple excitations in local coupled cluster calculations with pair natural orbitals. *The Journal of Chemical Physics* **2013**, *139*, 134101, DOI: 10.1063/1.4821834.
- (388) Neese, F. Software update: the ORCA program system, version 4.0. *WIREs Computational Molecular Science* **2017**, *8*, DOI: 10.1002/wcms.1327.
- (389) Weigend, F. Accurate Coulomb-fitting basis sets for H to Rn. *Physical Chemistry Chemical Physics* **2006**, *8*, 1057, DOI: 10.1039/b515623h.
- (390) Hellweg, A.; Hättig, C.; Höfener, S.; Klopper, W. Optimized accurate auxiliary basis sets for RI-MP2 and RI-CC2 calculations for the atoms Rb to Rn. *Theoretical Chemistry Accounts* **2007**, *117*, 587–597, DOI: 10.1007/s00214-007-0250-5.

- (391) Barone, V.; Cossi, M. Quantum Calculation of Molecular Energies and Energy Gradients in Solution by a Conductor Solvent Model. *The Journal of Physical Chemistry A* **1998**, *102*, 1995–2001, DOI: 10.1021/jp9716997.
- (392) Cossi, M.; Rega, N.; Scalmani, G.; Barone, V. Energies, structures, and electronic properties of molecules in solution with the C-PCM solvation model. *Journal of Computational Chemistry* **2003**, *24*, 669–681, DOI: 10.1002/jcc.10189.
- (393) Liakos, D. G.; Sparta, M.; Kesharwani, M. K.; Martin, J. M. L.; Neese, F. Exploring the Accuracy Limits of Local Pair Natural Orbital Coupled-Cluster Theory. *Journal of Chemical Theory and Computation* **2015**, *11*, 1525–1539, DOI: 10.1021/ct501129s.
- (394) Pedregosa, F.; Varoquaux, G.; Gramfort, A.; Michel, V.; Thirion, B.; Grisel, O.; Blondel, M.; Prettenhofer, P.; Weiss, R.; Dubourg, V.; Vanderplas, J.; Passos, A.; Cournapeau, D.; Brucher, M.; Perrot, M.; Duchesnay, E. Scikit-learn: Machine Learning in Python. *Journal of Machine Learning Research* **2011**, *12*, 2825–2830.
- (395) Buitinck, L.; Louppe, G.; Blondel, M.; Pedregosa, F.; Mueller, A.; Grisel, O.; Niculae, V.; Prettenhofer, P.; Gramfort, A.; Grobler, J.; Layton, R.; VanderPlas, J.; Joly, A.; Holt, B.; Varoquaux, G. In *ECML PKDD Workshop: Languages for Data Mining and Machine Learning*, 2013, pp 108–122.
- (396) Mu, Y.; Nguyen, P. H.; Stock, G. Energy landscape of a small peptide revealed by dihedral angle principal component analysis. *Proteins: Structure, Function, and Bioinformatics* **2004**, *58*, 45–52, DOI: 10.1002/prot.20310.
- (397) Peach, M. J. G.; Benfield, P.; Helgaker, T.; Tozer, D. J. Excitation energies in density functional theory: An evaluation and a diagnostic test. *The Journal of Chemical Physics* **2008**, *128*, 044118, DOI: 10.1063/1.2831900.
- (398) Lu, T.; Chen, F. Multiwfn: A multifunctional wavefunction analyzer. *Journal of Computational Chemistry* **2011**, *33*, 580–592, DOI: 10.1002/jcc.22885.
- (399) Hawkins, P. C. D.; Skillman, A. G.; Warren, G. L.; Ellingson, B. A.; Stahl, M. T. Conformer Generation with OMEGA: Algorithm and Validation Using High Quality Structures from the Protein Databank and Cambridge Structural Database. *Journal of Chemical Information and Modeling* **2010**, *50*, 572–584, DOI: 10.1021/ci100031x.
- (400) O’Boyle, N. M.; Banck, M.; James, C. A.; Morley, C.; Vandermeersch, T.; Hutchison, G. R. Open Babel: An open chemical toolbox. *Journal of Cheminformatics* **2011**, *3*, DOI: 10.1186/1758-2946-3-33.

Bibliography

- (401) Hawkins, P. C. D.; Nicholls, A. Conformer Generation with OMEGA: Learning from the Data Set and the Analysis of Failures. *Journal of Chemical Information and Modeling* **2012**, *52*, 2919–2936, DOI: 10.1021/ci300314k.
- (402) Kanal, I. Y.; Keith, J. A.; Hutchison, G. R. A sobering assessment of small-molecule force field methods for low energy conformer predictions. *International Journal of Quantum Chemistry* **2017**, *118*, e25512, DOI: 10.1002/qua.25512.
- (403) Chan, L.; Hutchison, G. R.; Morris, G. M. Bayesian optimization for conformer generation. *Journal of Cheminformatics* **2019**, *11*, DOI: 10.1186/s13321-019-0354-7.
- (404) Grimme, S. Exploration of Chemical Compound, Conformer, and Reaction Space with Meta-Dynamics Simulations Based on Tight-Binding Quantum Chemical Calculations. *Journal of Chemical Theory and Computation* **2019**, *15*, 2847–2862, DOI: 10.1021/acs.jctc.9b00143.
- (405) De Vijver, R. V.; Zádor, J. KinBot: Automated stationary point search on potential energy surfaces. *Computer Physics Communications* **2020**, *248*, 106947, DOI: 10.1016/j.cpc.2019.106947.
- (406) Chandramouli, B.; Galdo, S. D.; Fusè, M.; Barone, V.; Mancini, G. Two-level stochastic search of low-energy conformers for molecular spectroscopy: implementation and validation of MM and QM models. *Physical Chemistry Chemical Physics* **2019**, *21*, 19921–19934, DOI: 10.1039/c9cp03557e.
- (407) Pracht, P.; Bohle, F.; Grimme, S. Automated exploration of the low-energy chemical space with fast quantum chemical methods. *Physical Chemistry Chemical Physics* **2020**, *22*, 7169–7192, DOI: 10.1039/c9cp06869d.
- (408) Hanson, K.; Roskop, L.; Djurovich, P. I.; Zahariev, F.; Gordon, M. S.; Thompson, M. E. A Paradigm for Blue- or Red-Shifted Absorption of Small Molecules Depending on the Site of π -Extension. *Journal of the American Chemical Society* **2010**, *132*, 16247–16255, DOI: 10.1021/ja1075162.
- (409) Chaitanya, K.; Ju, X.-H.; Heron, B. M. Can elongation of the π -system in triarylamine derived sensitizers with either benzothiadiazole and/or ortho-fluorophenyl moieties enrich their light harvesting efficiency? – a theoretical study. *RSC Advances* **2015**, *5*, 3978–3998, DOI: 10.1039/c4ra09914a.
- (410) Tsuneda, T.; Singh, R. K.; Nakata, A. Relationship between orbital energy gaps and excitation energies for long-chain systems. *Journal of Computational Chemistry* **2016**, *37*, 1451–1462, DOI: 10.1002/jcc.24357.

- (411) Giereth, R.; Reim, I.; Frey, W.; Junge, H.; Tschierlei, S.; Karnahl, M. Remarkably long-lived excited states of copper photosensitizers containing an extended π -system based on an anthracene moiety. *Sustainable Energy & Fuels* **2019**, *3*, 692–700, DOI: 10.1039/c8se00521d.
- (412) Kimber, P.; Plasser, F. Toward an understanding of electronic excitation energies beyond the molecular orbital picture. *Physical Chemistry Chemical Physics* **2020**, *22*, 6058–6080, DOI: 10.1039/d0cp00369g.
- (413) Van Rossum, G.; Drake Jr, F. L., *Python tutorial*; Centrum voor Wiskunde en Informatica Amsterdam: 1995; Vol. 620.
- (414) Van Rossum, G. et al. In *USENIX annual technical conference, 2007*; Vol. 41, p 36.
- (415) Kästner, J.; Carr, J. M.; Keal, T. W.; Thiel, W.; Wander, A.; Sherwood, P. DL-FIND: An Open-Source Geometry Optimizer for Atomistic Simulations†. *The Journal of Physical Chemistry A* **2009**, *113*, 11856–11865, DOI: 10.1021/jp9028968.
- (416) Denzel, A.; Kästner, J. Gaussian process regression for geometry optimization. *The Journal of Chemical Physics* **2018**, *148*, 094114, DOI: 10.1063/1.5017103.
- (417) Raggi, G.; Galvan, I. F.; Ritterhoff, C. L.; Vacher, M.; Lindh, R. Restricted-Variance Molecular Geometry Optimization Based on Gradient-Enhanced Kriging. *Journal of Chemical Theory and Computation* **2020**, *16*, 3989–4001, DOI: 10.1021/acs.jctc.0c00257.
- (418) Bannwarth, C.; Ehlert, S.; Grimme, S. GFN2-xTB—An Accurate and Broadly Parametrized Self-Consistent Tight-Binding Quantum Chemical Method with Multipole Electrostatics and Density-Dependent Dispersion Contributions. *Journal of Chemical Theory and Computation* **2019**, *15*, 1652–1671, DOI: 10.1021/acs.jctc.8b01176.
- (419) Murtagh, B. A. Computational experience with quadratically convergent minimisation methods. *The Computer Journal* **1970**, *13*, 185–194, DOI: 10.1093/comjnl/13.2.185.
- (420) POWELL, M. J. D. On the Convergence of the Variable Metric Algorithm. *IMA Journal of Applied Mathematics* **1971**, *7*, 21–36, DOI: 10.1093/imamat/7.1.21.

Bibliography

- (421) Galvan, I. F. et al. OpenMolcas: From Source Code to Insight. *Journal of Chemical Theory and Computation* **2019**, *15*, 5925–5964, DOI: 10.1021/acs.jctc.9b00532.
- (422) Aquilante, F. et al. Modern quantum chemistry with [Open]Molcas. *The Journal of Chemical Physics* **2020**, *152*, 214117, DOI: 10.1063/5.0004835.
- (423) Jurečka, P.; Šponer, J.; Černý, J.; Hobza, P. Benchmark database of accurate (MP2 and CCSD(T) complete basis set limit) interaction energies of small model complexes, DNA base pairs, and amino acid pairs. *Phys. Chem. Chem. Phys.* **2006**, *8*, 1985–1993, DOI: 10.1039/b600027d.
- (424) Takatani, T.; Hohenstein, E. G.; Malagoli, M.; Marshall, M. S.; Sherrill, C. D. Basis set consistent revision of the S22 test set of noncovalent interaction energies. *The Journal of Chemical Physics* **2010**, *132*, 144104, DOI: 10.1063/1.3378024.
- (425) Cremer, D. Møller–Plesset perturbation theory: from small molecule methods to methods for thousands of atoms. *WIREs Computational Molecular Science* **2011**, *1*, 509–530, DOI: <https://doi.org/10.1002/wcms.58>.
- (426) Ditchfield, R.; Hehre, W. J.; Pople, J. A. Self-Consistent Molecular-Orbital Methods. IX. An Extended Gaussian-Type Basis for Molecular-Orbital Studies of Organic Molecules. *J. Chem. Phys.* **1971**, *54*, 724–728, DOI: 10.1063/1.1674902.
- (427) Hariharan, P. C.; Pople, J. A. The influence of polarization functions on molecular orbital hydrogenation energies. *Theor. Chim. Acta* **1973**, *28*, 213–222, DOI: 10.1007/bf00533485.
- (428) Hehre, W. J.; Ditchfield, R.; Pople, J. A. Self-Consistent Molecular Orbital Methods. XII. Further Extensions of Gaussian-Type Basis Sets for Use in Molecular Orbital Studies of Organic Molecules. *J. Chem. Phys.* **1972**, *56*, 2257–2261, DOI: 10.1063/1.1677527.
- (429) Weigend, F.; Häser, M. RI-MP2: first derivatives and global consistency. *Theor. Chem. Acta* **1997**, *97*, 331–340, DOI: 10.1007/s002140050269.
- (430) Hättig, C. Optimization of auxiliary basis sets for RI-MP2 and RI-CC2 calculations. *Phys. Chem. Chem. Phys.* **2005**, *7*, 59–66, DOI: 10.1039/B415208E.
- (431) Munkres, J. Algorithms for the Assignment and Transportation Problems. *Journal of the Society for Industrial and Applied Mathematics* **1957**, *5*, 32–38, DOI: 10.1137/0105003.

- (432) Kuhn, H. W. The Hungarian method for the assignment problem. *Naval Research Logistics Quarterly* **1955**, *2*, 83–97, DOI: 10.1002/nav.3800020109.
- (433) Allen, W. J.; Rizzo, R. C. Implementation of the Hungarian Algorithm to Account for Ligand Symmetry and Similarity in Structure-Based Design. *Journal of Chemical Information and Modeling* **2014**, *54*, 518–529, DOI: 10.1021/ci400534h.
- (434) Wagner, A.; Himmel, H.-J. aRMSD: A Comprehensive Tool for Structural Analysis. *Journal of Chemical Information and Modeling* **2017**, *57*, 428–438, DOI: 10.1021/acs.jcim.6b00516.
- (435) Pettersen, E. F.; Goddard, T. D.; Huang, C. C.; Couch, G. S.; Greenblatt, D. M.; Meng, E. C.; Ferrin, T. E. UCSF Chimera?A visualization system for exploratory research and analysis. *Journal of Computational Chemistry* **2004**, *25*, 1605–1612, DOI: 10.1002/jcc.20084.
- (436) Coutsias, E. A.; Seok, C.; Dill, K. A. Using quaternions to calculate RMSD. *Journal of Computational Chemistry* **2004**, *25*, 1849–1857, DOI: 10.1002/jcc.20110.
- (437) Ahuja, K.; Green, W. H.; Li, Y.-P. Learning to Optimize Molecular Geometries Using Reinforcement Learning. *Journal of Chemical Theory and Computation* **2021**, DOI: 10.1021/acs.jctc.0c00971.
- (438) Helgaker, T. Transition-state optimizations by trust-region image minimization. *Chemical Physics Letters* **1991**, *182*, 503–510, DOI: 10.1016/0009-2614(91)90115-p.
- (439) Spicher, S.; Grimme, S. Single-Point Hessian Calculations for Improved Vibrational Frequencies and Rigid-Rotor-Harmonic-Oscillator Thermodynamics. *Journal of Chemical Theory and Computation* **2021**, DOI: 10.1021/acs.jctc.0c01306.
- (440) Hermes, E. D.; Sargsyan, K.; Najm, H. N.; Zador, J. Accelerated Saddle Point Refinement through Full Exploitation of Partial Hessian Diagonalization. *J. Chem. Theory Comput.* **2019**, *15*, 6536–6549, DOI: 10.1021/acs.jctc.9b00869.
- (441) Virtanen, P. et al. SciPy 1.0: fundamental algorithms for scientific computing in Python. *Nature Methods* **2020**, *17*, 261–272, DOI: 10.1038/s41592-019-0686-2.
- (442) Birkholz, A. B.; Schlegel, H. B. Using bonding to guide transition state optimization. *J. Comput. Chem.* **2015**, *36*, 1157–1166, DOI: 10.1002/jcc.23910.

Bibliography

- (443) Peng, C.; Schlegel, H. B. Combining Synchronous Transit and Quasi-Newton Methods to Find Transition States. *Isr. J. Chem.* **1993**, *33*, 449–454, DOI: 10.1002/ijch.199300051.
- (444) Ess, D. H. Transition-Structure Catalog of Organic Reactions. *J. Chem. Educ.* **2012**, *89*, 817–818, DOI: 10.1021/ed2005856.
- (445) Stewart, J. J. P. Optimization of parameters for semiempirical methods V: Modification of NDDO approximations and application to 70 elements. *J Mol Model* **2007**, *13*, 1173–1213, DOI: 10.1007/s00894-007-0233-4.
- (446) Vosko, S. H.; Wilk, L.; Nusair, M. Accurate spin-dependent electron liquid correlation energies for local spin density calculations: a critical analysis. *Can. J. Phys.* **1980**, *58*, 1200–1211, DOI: 10.1139/p80-159.
- (447) Lee, C.; Yang, W.; Parr, R. G. Development of the Colle-Salvetti correlation-energy formula into a functional of the electron density. *Physical Review B* **1988**, *37*, 785–789, DOI: 10.1103/physrevb.37.785.
- (448) Becke, A. D. Density-functional thermochemistry. III. The role of exact exchange. *The Journal of Chemical Physics* **1993**, *98*, 5648–5652, DOI: 10.1063/1.464913.
- (449) Stephens, P. J.; Devlin, F. J.; Chabalowski, C. F.; Frisch, M. J. Ab Initio Calculation of Vibrational Absorption and Circular Dichroism Spectra Using Density Functional Force Fields. *J. Phys. Chem.* **1994**, *98*, 11623–11627, DOI: 10.1021/j100096a001.
- (450) Iron, M. A.; Janes, T. Evaluating Transition Metal Barrier Heights with the Latest Density Functional Theory Exchange–Correlation Functionals: The MOBH35 Benchmark Database. *J. Phys. Chem. A* **2019**, *123*, 3761–3781, DOI: 10.1021/acs.jpca.9b01546.
- (451) Dohm, S.; Bursch, M.; Hansen, A.; Grimme, S. Semiautomated Transition State Localization for Organometallic Complexes with Semiempirical Quantum Chemical Methods. *J. Chem. Theory Comput.* **2020**, *16*, 2002–2012, DOI: 10.1021/acs.jctc.9b01266.
- (452) Shukla, M.; Mishra, P. A gas phase ab initio excited state geometry optimization study of thymine cytosine and uracil. *Chemical Physics* **1999**, *240*, 319–329, DOI: 10.1016/s0301-0104(98)00374-7.

- (453) Peon, J.; Zewail, A. H. DNA/RNA nucleotides and nucleosides: direct measurement of excited-state lifetimes by femtosecond fluorescence up-conversion. *Chemical Physics Letters* **2001**, *348*, 255–262, DOI: 10.1016/S0009-2614(01)01128-9.
- (454) Mennucci, B.; Toniolo, A.; Tomasi, J. Theoretical Study of the Photophysics of Adenine in Solution: Tautomerism Deactivation Mechanisms, and Comparison with the 2-Aminopurine Fluorescent Isomer. *The Journal of Physical Chemistry A* **2001**, *105*, 4749–4757, DOI: 10.1021/jp0045843.
- (455) Shukla, M. K.; Leszczynski, J. Interaction of Water Molecules with Cytosine Tautomers: An Excited-State Quantum Chemical Investigation. *The Journal of Physical Chemistry A* **2002**, *106*, 11338–11346, DOI: 10.1021/jp021317j.
- (456) Ismail, N.; Blancafort, L.; Olivucci, M.; Kohler, B.; Robb, M. A. Ultrafast Decay of Electronically Excited Singlet Cytosine via a π, π^* to n, π^* State Switch. *Journal of the American Chemical Society* **2002**, *124*, 6818–6819, DOI: 10.1021/ja0258273.
- (457) Malone, R. J.; Miller, A. M.; Kohler, B. Singlet Excited-state Lifetimes of Cytosine Derivatives Measured by Femtosecond Transient Absorption. *Photochemistry and Photobiology* **2007**, *77*, 158–164, DOI: 10.1562/0031-8655(2003)0770158sesloc2.0.co2.
- (458) Improta, R.; Santoro, F.; Blancafort, L. Quantum Mechanical Studies on the Photophysics and the Photochemistry of Nucleic Acids and Nucleobases. *Chemical Reviews* **2016**, *116*, 3540–3593, DOI: 10.1021/acs.chemrev.5b00444.
- (459) Taylor, J. S. Unraveling the Molecular Pathway from Sunlight to Skin Cancer. *Accounts of Chemical Research* **1994**, *27*, 76–82, DOI: 10.1021/ar00039a003.
- (460) Crespo-Hernández, C. E.; Cohen, B.; Hare, P. M.; Kohler, B. Ultrafast Excited-State Dynamics in Nucleic Acids. *Chemical Reviews* **2004**, *104*, 1977–2020, DOI: 10.1021/cr0206770.
- (461) Kleinerhanns, K.; Nachtigallová, D.; de Vries, M. S. Excited state dynamics of DNA bases. *International Reviews in Physical Chemistry* **2013**, *32*, 308–342, DOI: 10.1080/0144235x.2012.760884.
- (462) Richter, M.; Marquetand, P.; González-Vázquez, J.; Sola, I.; González, L. Femtosecond Intersystem Crossing in the DNA Nucleobase Cytosine. *The Journal of Physical Chemistry Letters* **2012**, *3*, 3090–3095, DOI: 10.1021/jz301312h.

Bibliography

- (463) Adamo, C.; Barone, V. Toward reliable density functional methods without adjustable parameters: The PBE0 model. *The Journal of Chemical Physics* **1999**, *110*, 6158–6170, DOI: 10.1063/1.478522.
- (464) Eichkorn, K.; Treutler, O.; Öhm, H.; Häser, M.; Ahlrichs, R. Auxiliary basis sets to approximate Coulomb potentials. *Chemical Physics Letters* **1995**, *240*, 283–290, DOI: 10.1016/0009-2614(95)00621-a.
- (465) Mustafa, A. K.; Gadalla, M. M.; Snyder, S. H. Signaling by Gasotransmitters. *Science Signaling* **2009**, *2*, re2–re2, DOI: 10.1126/scisignal.268re2.
- (466) Frostell, C.; Fratacci, M. D.; Wain, J. C.; Jones, R.; Zapol, W. M. Inhaled nitric oxide. A selective pulmonary vasodilator reversing hypoxic pulmonary vasoconstriction. *Circulation* **1991**, *83*, 2038–2047, DOI: 10.1161/01.cir.83.6.2038.
- (467) Williams, S. B.; Cusco, J. A.; Roddy, M.-A.; Johnstone, M. T.; Creager, M. A. Impaired nitric oxide-mediated vasodilation in patients with non-insulin-dependent diabetes mellitus. *Journal of the American College of Cardiology* **1996**, *27*, 567–574, DOI: 10.1016/0735-1097(95)00522-6.
- (468) Murad, F. Nitric Oxide and Cyclic GMP in Cell Signaling and Drug Development. *New England Journal of Medicine* **2006**, *355*, 2003–2011, DOI: 10.1056/nejmsa063904.
- (469) Bogdan, C. Nitric oxide and the immune response. *Nature Immunology* **2001**, *2*, 907–916, DOI: 10.1038/ni1001-907.
- (470) Stuehr, D. J.; Gross, S. S.; Sakuma, I.; Levi, R.; Nathan, C. F. Activated murine macrophages secrete a metabolite of arginine with the bioactivity of endothelium-derived relaxing factor and the chemical reactivity of nitric oxide. *The Journal of Experimental Medicine* **1989**, *169*, 1011–1020, DOI: 10.1084/jem.169.3.1011.
- (471) Divakaran, S.; Loscalzo, J. The Role of Nitroglycerin and Other Nitrogen Oxides in Cardiovascular Therapeutics. *Journal of the American College of Cardiology* **2017**, *70*, 2393–2410, DOI: 10.1016/j.jacc.2017.09.1064.
- (472) Steinhorn, B. S.; Loscalzo, J.; Michel, T. Nitroglycerin and Nitric Oxide — A Rondo of Themes in Cardiovascular Therapeutics. *New England Journal of Medicine* **2015**, *373*, 277–280, DOI: 10.1056/nejmsr1503311.

- (473) Carneiro, Z. A.; Biazotto, J. C.; Alexiou, A. D.; Nikolaou, S. Nitric oxide photorelease from a trinuclear ruthenium nitrosyl complex and its in vitro cytotoxicity against melanoma cells. *Journal of Inorganic Biochemistry* **2014**, *134*, 36–38, DOI: 10.1016/j.jinorgbio.2014.01.012.
- (474) Roose, M.; Sasaki, I.; Bukhanko, V.; Mallet-Ladeira, S.; Barba-Barba, R. M.; Ramos-Ortiz, G.; Enriquez-Cabrera, A.; Farfán, N.; Lacroix, P. G.; Malfant, I. Nitric oxide photo-release from a ruthenium nitrosyl complex with a 4,4'-bisfluorenyl-2,2'-bipyridine ligand. *Polyhedron* **2018**, *151*, 100–111, DOI: 10.1016/j.poly.2018.05.028.
- (475) Bukhanko, V.; Lacroix, P. G.; Sasaki, I.; Tassé, M.; Mallet-Ladeira, S.; Voitenko, Z.; Malfant, I. Mechanism and oxidation state involved in the nitric oxide (NO) photorelease in a terpyridine-bipyridine-based ruthenium nitrosyl complex. *Inorganica Chimica Acta* **2018**, *482*, 195–205, DOI: 10.1016/j.ica.2018.05.038.
- (476) De Lima, R. G.; Sauaia, M. G.; Bonaventura, D.; Tedesco, A. C.; Bendhack, L. M.; da Silva, R. S. Influence of ancillary ligand L in the nitric oxide photorelease by the [Ru(L)(tpy)NO]³⁺ complex and its vasodilator activity based on visible light irradiation. *Inorganica Chimica Acta* **2006**, *359*, 2543–2549, DOI: 10.1016/j.ica.2006.02.020.
- (477) De Lima, R. G.; Sauaia, M. G.; Bonaventura, D.; Tedesco, A. C.; Lopez, R. F. V.; Bendhack, L. M.; da Silva, R. S. Controlled nitric oxide photo-release from nitro ruthenium complexes: The vasodilator response produced by UV light irradiation. *Inorganica Chimica Acta* **2005**, *358*, 2643–2650, DOI: 10.1016/j.ica.2005.03.019.
- (478) Rose, M. J.; Mascharak, P. K. Fiat Lux: selective delivery of high flux of nitric oxide (NO) to biological targets using photoactive metal nitrosyls. *Current Opinion in Chemical Biology* **2008**, *12*, 238–244, DOI: 10.1016/j.cbpa.2008.02.009.
- (479) García, J. S.; Alary, F.; Boggio-Pasqua, M.; Dixon, I. M.; Heully, J.-L. Is photoisomerization required for NO photorelease in ruthenium nitrosyl complexes? *Journal of Molecular Modeling* **2016**, *22*, DOI: 10.1007/s00894-016-3138-2.
- (480) De Lima Batista, A. P.; de Oliveira-Filho, A. G. S.; Galembeck, S. E. Photophysical properties and the NO photorelease mechanism of a ruthenium nitrosyl model complex investigated using the CASSCF-in-DFT embedding approach. *Physical Chemistry Chemical Physics* **2017**, *19*, 13860–13867, DOI: 10.1039/c7cp01642e.

Bibliography

- (481) Roose, M.; Tassé, M.; Lacroix, P. G.; Malfant, I. Nitric oxide (NO) photo-release in a series of ruthenium–nitrosyl complexes: new experimental insights in the search for a comprehensive mechanism. *New Journal of Chemistry* **2019**, *43*, 755–767, DOI: 10.1039/c8nj03907k.
- (482) Giri, B.; Kumbhakar, S.; Selvan, K. K.; Muley, A.; Maji, S. Formation reactivity, photorelease, and scavenging of NO in ruthenium nitrosyl complexes. *Inorganica Chimica Acta* **2020**, *502*, 119360, DOI: 10.1016/j.ica.2019.119360.
- (483) González, L.; Boggio-Pasqua, M.; Talotta, F. Early relaxation dynamics in the photoswitchable trans-[RuCl(NO)(py)₄]²⁺. *Chemistry - A European Journal* **2020**, DOI: 10.1002/chem.202000507.
- (484) Sasaki, I.; Amabilino, S.; Mallet-Ladeira, S.; Tassé, M.; Sournia-Saquet, A.; Lacroix, P. G.; Malfant, I. Further studies on the photoreactivities of ruthenium–nitrosyl complexes with terpyridyl ligands. *New Journal of Chemistry* **2019**, *43*, 11241–11250, DOI: 10.1039/c9nj02398d.
- (485) Becke, A. D. A new mixing of Hartree–Fock and local density-functional theories. *The Journal of Chemical Physics* **1993**, *98*, 1372–1377, DOI: 10.1063/1.464304.
- (486) Hehre, W. J.; Ditchfield, R.; Pople, J. A. Self—Consistent Molecular Orbital Methods. XII. Further Extensions of Gaussian—Type Basis Sets for Use in Molecular Orbital Studies of Organic Molecules. *The Journal of Chemical Physics* **1972**, *56*, 2257–2261, DOI: 10.1063/1.1677527.
- (487) Spitznagel, G. W.; Clark, T.; von Ragué Schleyer, P.; Hehre, W. J. An evaluation of the performance of diffuse function-augmented basis sets for second row elements Na–Cl. *Journal of Computational Chemistry* **1987**, *8*, 1109–1116, DOI: 10.1002/jcc.540080807.
- (488) Clark, T.; Chandrasekhar, J.; Spitznagel, G. W.; Schleyer, P. V. R. Efficient diffuse function-augmented basis sets for anion calculations. III. The 3-21+G basis set for first-row elements Li–F. *Journal of Computational Chemistry* **1983**, *4*, 294–301, DOI: 10.1002/jcc.540040303.
- (489) T. H. Dunning, P. J. H., *In Modern Theoretical Chemistry*; Plenum: 1977.
- (490) Hay, P. J.; Wadt, W. R. Ab initio effective core potentials for molecular calculations. Potentials for the transition metal atoms Sc to Hg. *The Journal of Chemical Physics* **1985**, *82*, 270–283, DOI: 10.1063/1.448799.

- (491) Lu, T.; Chen, F. Multiwfn: A multifunctional wavefunction analyzer. *Journal of Computational Chemistry* **2011**, *33*, 580–592, DOI: 10.1002/jcc.22885.
- (492) Hanson, R. M. Jmol— a paradigm shift in crystallographic visualization. *Journal of Applied Crystallography* **2010**, *43*, 1250–1260, DOI: 10.1107/s0021889810030256.
- (493) Larsen, C. B.; van der Salm, H.; Shillito, G. E.; Lucas, N. T.; Gordon, K. C. Tuning the Rainbow: Systematic Modulation of Donor–Acceptor Systems through Donor Substituents and Solvent. *Inorganic Chemistry* **2016**, *55*, 8446–8458, DOI: 10.1021/acs.inorgchem.6b01039.
- (494) Shillito, G. E.; Hall, T. B. J.; Preston, D.; Traber, P.; Wu, L.; Reynolds, K. E. A.; Horvath, R.; Sun, X. Z.; Lucas, N. T.; Crowley, J. D.; George, M. W.; Kupfer, S.; Gordon, K. C. Dramatic Alteration of 3ILCT Lifetimes Using Ancillary Ligands in [Re(L)(CO)₃(phen-TPA)]ⁿ⁺ Complexes: An Integrated Spectroscopic and Theoretical Study. *Journal of the American Chemical Society* **2018**, *140*, 4534–4542, DOI: 10.1021/jacs.7b12868.
- (495) Kupfer, S.; Zedler, L.; Guthmuller, J.; Bode, S.; Hager, M. D.; Schubert, U. S.; Popp, J.; Gräfe, S.; Dietzek, B. Self-healing mechanism of metallopolymers investigated by QM/MM simulations and Raman spectroscopy. *Physical Chemistry Chemical Physics* **2014**, *16*, 12422, DOI: 10.1039/c4cp00562g.
- (496) Schindler, J.; Kupfer, S.; Zedler, L.; Wächtler, M.; Gräfe, S.; Ryan, A. A.; Senge, M. O.; Dietzek, B. Spectroelectrochemical Investigation of the One-Electron Reduction of Nonplanar Nickel(II) Porphyrins. *ChemPhysChem* **2016**, *17*, 3480–3493, DOI: 10.1002/cphc.201600698.
- (497) Reiher, M.; Salomon, O.; Hess, B. A. Reparameterization of hybrid functionals based on energy differences of states of different multiplicity. *Theoretical Chemistry Accounts: Theory Computation, and Modeling (Theoretica Chimica Acta)* **2001**, *107*, 48–55, DOI: 10.1007/s00214-001-0300-3.
- (498) Salomon, O.; Reiher, M.; Hess, B. A. Assertion and validation of the performance of the B3LYP* functional for the first transition metal row and the G2 test set. *The Journal of Chemical Physics* **2002**, *117*, 4729–4737, DOI: 10.1063/1.1493179.
- (499) Dolg, M.; Wedig, U.; Stoll, H.; Preuss, H. Ab initio pseudopotential study of the first row transition metal monoxides and iron monohydride. *The Journal of Chemical Physics* **1987**, *86*, 2123–2131, DOI: 10.1063/1.452110.

Bibliography

- (500) Mennucci, B.; Cappelli, C.; Guido, C. A.; Cammi, R.; Tomasi, J. Structures and Properties of Electronically Excited Chromophores in Solution from the Polarizable Continuum Model Coupled to the Time-Dependent Density Functional Theory. *The Journal of Physical Chemistry A* **2009**, *113*, 3009–3020, DOI: 10.1021/jp8094853.
- (501) Yanai, T.; Tew, D. P.; Handy, N. C. A new hybrid exchange–correlation functional using the Coulomb-attenuating method (CAM-B3LYP). *Chemical Physics Letters* **2004**, *393*, 51–57, DOI: 10.1016/j.cplett.2004.06.011.
- (502) GNU General Public License, version 3, Free Software Foundation, 2007.
- (503) Smith, D. et al. Psi4 1.4: Open-Source Software for High-Throughput Quantum Chemistry. **2020**, DOI: 10.26434/chemrxiv.11930031.v1.
- (504) Sun, Q.; Berkelbach, T. C.; Blunt, N. S.; Booth, G. H.; Guo, S.; Li, Z.; Liu, J.; McClain, J. D.; Sayfutyarova, E. R.; Sharma, S.; Wouters, S.; Chan, G. K.-L. PySCF: the Python-based simulations of chemistry framework. *WIREs Computational Molecular Science* **2017**, *8*, DOI: 10.1002/wcms.1340.
- (505) Eastman, P.; Swails, J.; Chodera, J. D.; McGibbon, R. T.; Zhao, Y.; Beauchamp, K. A.; Wang, L.-P.; Simmonett, A. C.; Harrigan, M. P.; Stern, C. D.; Wiewiora, R. P.; Brooks, B. R.; Pande, V. S. OpenMM 7: Rapid development of high performance algorithms for molecular dynamics. *PLoS Comput Biol Computational Biology* **2017**, *13*, ed. by Gentleman, R., e1005659, DOI: 10.1371/journal.pcbi.1005659.
- (506) Olsen, J. M. H.; Reine, S.; Vahtras, O.; Kjellgren, E.; Reinholdt, P.; Dundas, K. O. H.; Li, X.; Cukras, J.; Ringholm, M.; Hedegard, E. D.; Remigio, R. D.; List, N. H.; Faber, R.; Tenorio, B. N. C.; Bast, R.; Pedersen, T. B.; Rinkevicius, Z.; Sauer, S. P. A.; Mikkelsen, K. V.; Kongsted, J.; Coriani, S.; Ruud, K.; Helgaker, T.; Jensen, H. J. A.; Norman, P. Dalton Project: A Python platform for molecular- and electronic-structure simulations of complex systems. *J. Chem. Phys.* **2020**, *152*, 214115, DOI: 10.1063/1.5144298.
- (507) Herbst, M. F.; Scheurer, M.; Fransson, T.; Rehn, D. R.; Dreuw, A. adcc: A versatile toolkit for rapid development of algebraic-diagrammatic construction methods. *WIREs Comput Mol Sci Computational Molecular Science* **2020**, *10*, DOI: 10.1002/wcms.1462.
- (508) Harris, C. R. et al. Array programming with NumPy. *Nature* **2020**, *585*, 357–362, DOI: 10.1038/s41586-020-2649-2.

- (509) Stewart, J. J. P. MOPAC2016, 2016.
- (510) Smith, D.; Altarawy, D.; Burns, L.; Welborn, M.; Naden, L. N.; Ward, L.; Ellis, S.; Crawford, T. The MolSSI QCArchive Project: An Open-Source Platform to Compute Organize, and Share Quantum Chemistry Data. **2020**, DOI: 10.26434/chemrxiv.11908356.v1.
- (511) Valiev, M.; Bylaska, E.; Govind, N.; Kowalski, K.; Straatsma, T.; Dam, H. V.; Wang, D.; Nieplocha, J.; Apra, E.; Windus, T.; de Jong, W. NWChem: A comprehensive and scalable open-source solution for large scale molecular simulations. *Computer Physics Communications* **2010**, *181*, 1477–1489, DOI: 10.1016/j.cpc.2010.04.018.
- (512) Gordon, M. S.; Schmidt, M. W. In *Theory and Applications of Computational Chemistry*; Elsevier: 2005, pp 1167–1189, DOI: 10.1016/b978-044451719-7/50084-6.
- (513) Shao, Y. et al. Advances in molecular quantum chemistry contained in the Q-Chem 4 program package. *Molecular Physics* **2014**, *113*, 184–215, DOI: 10.1080/00268976.2014.952696.
- (514) For dynamic task scheduling, D. L. Dask Development Team, 2016.
- (515) Meurer, A. et al. SymPy: symbolic computing in Python. *PeerJ Computer Science* **2017**, *3*, e103, DOI: 10.7717/peerj-cs.103.
- (516) Ceriotti, M.; More, J.; Manolopoulos, D. E. i-PI: A Python interface for ab initio path integral molecular dynamics simulations. *Computer Physics Communications* **2014**, *185*, 1019–1026, DOI: 10.1016/j.cpc.2013.10.027.
- (517) Kapil, V. et al. i-PI 2.0: A universal force engine for advanced molecular simulations. *Computer Physics Communications* **2019**, *236*, 214–223, DOI: 10.1016/j.cpc.2018.09.020.
- (518) Giannozzi, P. et al. QUANTUM ESPRESSO: a modular and open-source software project for quantum simulations of materials. *J. Phys.: Condens. Matter* **2009**, *21*, 395502, DOI: 10.1088/0953-8984/21/39/395502.
- (519) Giannozzi, P.; Barone, O.; Bonfanti, P.; Brunato, D.; Car, R.; Carnimeo, I.; Cavazzoni, C.; de Gironcoli, S.; Delugas, P.; Ruffino, F. F.; Ferretti, A.; Marzari, N.; Timrov, I.; Urru, A.; Baroni, S. Quantum ESPRESSO toward the exascale. *J. Chem. Phys.* **2020**, *152*, 154105, DOI: 10.1063/5.0005082.

Bibliography

- (520) Artacho, E.; Anglada, E.; Dieguez, O.; Gale, J. D.; Garcia, A.; Junquera, J.; Martin, R. M.; Ordejon, P.; Pruneda, J. M.; Sanchez-Portal, D.; Soler, J. M. The SIESTA method – developments and applicability. *J. Phys.: Condens. Matter* **2008**, *20*, 064208, DOI: 10.1088/0953-8984/20/6/064208.
- (521) Apra, E. et al. NWChem: Past, present, and future. *J. Chem. Phys.* **2020**, *152*, 184102, DOI: 10.1063/5.0004997.
- (522) Meyer, M. Continuous Integration and Its Tools. *IEEE Software* **2014**, *31*, 14–16, DOI: 10.1109/ms.2014.58.
- (523) Jones, G. Make Dimer Method N-Vector Translationally Invariant, <https://github.com/eljost/pysisyphus/pull/116>, [Online; accessed at 2021-02-09], 2021.
- (524) Mloston, G.; Buday, P.; Seeber, P.; Neumann, C.; Abul-Futouh, H.; Görls, H.; Gräfe, S.; Matczak, P.; Kupfer, S.; Weigand, W. Iron(0) mediated stereoselective (3+2)-cycloaddition of thiochalcones via a diradical intermediate. *Chemistry - A European Journal* **2020**, DOI: 10.1002/chem.202001412.
- (525) eljost/pywfo, <https://github.com/eljost/pywfo>, Accessed on Wed, April 29, 2020.
- (526) Krekel, H.; Oliveira, B.; Pfannschmidt, R.; Bruynooghe, F.; Laughner, B.; Bruhin, F. pytest 6.2, 2004.
- (527) Hubertz, J. In *Softwaretests mit Python*; Springer Berlin Heidelberg: Berlin, Heidelberg, 2016, pp 117–169, DOI: 10.1007/978-3-662-48603-0_5.
- (528) Pajankar, A. In *Python Unit Test Automation : Practical Techniques for Python Developers and Testers*; Apress: Berkeley, CA, 2017, pp 87–100, DOI: 10.1007/978-1-4842-2677-3_5.
- (529) Hunt, J. In *Advanced Guide to Python 3 Programming*; Springer International Publishing: Cham, 2019, pp 175–186, DOI: 10.1007/978-3-030-25943-3_15.